Durham E-Theses

Electronic processes in electroluminescent device structures

Jones, R.E.

How to cite:

Jones, R.E. (1986) *Electronic processes in electroluminescent device structures*, Durham theses, Durham University. Available at Durham E-Theses Online: http://etheses.dur.ac.uk/7031/

Use policy

The full-text may be used and/or reproduced, and given to third parties in any format or medium, without prior permission or charge, for personal research or study, educational, or not-for-profit purposes provided that:

- a full bibliographic reference is made to the original source
- a link is made to the metadata record in Durham E-Theses
- the full-text is not changed in any way

The full-text must not be sold in any format or medium without the formal permission of the copyright holders.

Please consult the full Durham E-Theses policy for further details.

Academic Support Office, Durham University, University Office, Old Elvet, Durham DH1 3HP
e-mail: e-theses.admin@dur.ac.uk Tel: +44 0191 334 6107
http://etheses.dur.ac.uk

ELECTRONIC PROCESSES IN

ELECTROLUMINESCENT DEVICE STRUCTURES

by

R E JONES B.A.

The copyright of this thesis rests with the author.
No quotation from it should be published without
his prior written consent and information derived
from it should be acknowledged.

A Thesis Submitted for the
Degree of Doctor of Philosophy
in the University of Durham

May 1986

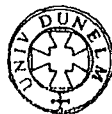

-8. OCT. 1986

ABSTRACT

Electronic processes in two different electroluminescent device structures, the forward biassed metal/thick insulator/semiconductor (MIS) diode and the high field metal/insulator/metal (MIM) panel, are investigated.

Models are produced to explain the behaviour of two particular MIS systems which have been studied experimentally. One of these systems is the Au/cadmium stearate/n-GaP structure, where the insulator is deposited using Langmuir-Blodgett (LB) technology. The other is the Au/i-ZnS/n-ZnS structure. In the MIS devices electroluminescence occurs as a result of the recombination of electrons and holes in the semiconductor and so it is necessary to have an efficient minority carrier (hole) injection mechanism. Attention is paid to the impact excitation of the electron gas in the metal by the electrons injected from the semiconductor because this has been proposed by other workers as a process for producing holes in the metal that are energetically capable of entering the semiconductor valence band, provided they can traverse the insulator. The characteristics of the LB film devices are found to be best described by assuming the minority carrier injection to be limited by the hole transport through the insulator. Hopping between interface states on the successive LB layers is proposed as the transport mechanism. However, the device incorporating a II-VI semi-insulator is shown to be more characteristic of hole transport in the insulator valence band and a minority carrier injection which is limited by the supply of holes from the metal.

In high field MIM panels the mechanism of electroluminescence is quite different with impurity centres being impact excited or impact ionised by injected electrons and subsequently luminescing. Such devices driven by a dc signal are susceptible to the formation of high current filaments which burn out and result in device failure. A model is developed which predicts that there is a voltage range over which the device can exist in either a low current state or two higher current states and the resultant instability is expected to be destructive. Current-voltage characteristics are produced using this model and their general features are found to be relatively insensitive to material and device parameters. In order to understand the evolution of the electrical state of the MIM device after switch-on, a time dependent theory of system behaviour is also developed. This is particularly important as the devices are usually driven by a pulsed signal. For an homogeneous system the current is found to converge to the lower current state of the steady state characteristic.

DECLARATION

I declare that the work reported in this Thesis, unless otherwise stated, was carried out by the candidate, that it has not previously been submitted for any degree and that it is not currently being submitted for any other degree.

STATEMENT OF COPYRIGHT

The copyright of this Thesis rests with the author. No quotation from it should be published without his prior written consent and information derived from it should be acknowledged.

ACKNOWLEDGEMENTS

I would like to take this opportunity to thank the many people who have helped to make my study in Durham, and the production of this Thesis, an enjoyable and rewarding experience. It was a pleasure to be part of the Department of Applied Physics and Electronics, which I found to be personable and friendly. I am grateful to my supervisor Dr R A Abram for his welcome support and encouragement, and also to the Semiconductor Theory Group, especially Mr G N Childs and Mr R I Taylor, for providing many contributions (and diversions) to my work. I am indebted to Ms K Cummins for her accurate production of the figures and diagrams.

The provision of an SERC CASE studentship in collaboration with Plessey Research (Caswell) is gratefully acknowledged. I would like to thank my industrial supervisor Dr D J Robbins and the members of the Theory Group at Caswell for their support and assistance.

On a more personal note, I would like to acknowledge the encouragement of my parents throughout my educational career. Finally, I would like thank my wife Chris (whom I love very much) for her constant support over the years spent in Durham. My thanks are also due to her for the typing and presentation of this Thesis.

CONTENTS

CHAPTER 1 - INTRODUCTION 1

CHAPTER 2 - THE PHYSICS OF SCHOTTKY BARRIERS AND METAL-INSULATOR-SEMICONDUCTOR DEVICES .. 5

2.1 INTRODUCTION 5
2.2 ELECTROLUMINESCENT STRUCTURES 5
2.2.1 The p-n Homojunction 5
2.2.2 Schottky Barriers 8
2.2.3 The MIS Diode 9
2.2.4 Panel Devices 11
2.3 SCHOTTKY BARRIER FORMATION 12
2.3.1 Schottky-Mott Theory 12
2.3.2 The Bardeen Model 13
2.4 SCHOTTKY BARRIER CURRENT MECHANISMS 15
2.4.1 Possible Mechanisms 15
2.4.2 The Diffusion Theory 16
2.4.3 Thermionic Emission Theory 19
2.4.4 Thermionic Emission - Diffusion Theory 22
2.5 SCHOTTKY BARRIER BEHAVIOUR 22
2.5.1 Image Charge Effects 22
2.5.2 Effect of Potential Step 25
2.5.3 Minority Carrier Injection 26
2.6 METAL-INSULATOR-SEMICONDUCTOR DEVICE THEORY .. 28
2.6.1 Current-Voltage Characteristics 30
2.6.2 Minority Carrier Injection 33
a) Thin Insulating Layer 33
b) Thick Insulating Layers 34
2.7 SUMMARY 37

CHAPTER 3 - A BRIEF REVIEW OF MIS LIGHT EMITTING DIODES 39

3.1 INTRODUCTION 39
3.2 'THICK INSULATOR' MIS DIODES 40
3.2.1 MIS Devices Incorporating II-VI Semiconductors 40
3.2.2 MIS Devices Incorporating Langmuir-Blodgett Films .. 42

CHAPTER 4 - HOLE CREATION IN THE METAL CONTACT OF AN MIS DIODE BY IMPACT IONISATION 45

4.1 INTRODUCTION 45
4.2 FREE ELECTRON GAS MODEL 46
4.2.1 Gold as a Free Electron Gas 46
4.2.2 Electron – Electron Interactions 47
4.3 MATRIX ELEMENTS 48
4.3.1 Initial and Final Wavefunctions 48

4.3.2 Evaluation of the Matrix Element 49
4.3.3 The Direct Matrix Element Term 50
4.3.4 The Matrix Element Including Exchange 52
4.4 HOLE CREATION 52
4.4.1 Direct Transitions.. 52
4.4.2 Transitions Including Exchange Effects 59
4.4.3 Distribution of Created Holes 65
4.5 TRANSPORT OF CREATED HOLE TO MI INTERFACE 67
4.5.1 Hole Recombination by an Auger Process 67
4.5.2 Calculation of the Probability of a Hole Reaching the MI Interface 69
4.5.3 Approximate Expression for the Probability of a Hole Reaching the Interface 73
4.5.4 Hole Flux at the MI Interface 74
4.6 SUMMARY.. 78

CHAPTER 5 - SEMICONDUCTOR BAND ALIGNMENT IN THE MIS DIODE 80
5.1 INTRODUCTION 80
5.2 DEVICE CHARACTERISTICS AT LOW BIASES.. 81
5.2.1 Semiconductor Barrier Height 81
5.2.2 Electric Field in the Semiconductor 83
5.2.3 Surface States 86
5.2.4 Change in Barrier Height 89
5.3 DEVICE CHARACTERISTICS AT HIGH BIASES 92
5.3.1 Electron Current 92
5.3.2 Model the Majority Carrier Current 93
5.3.3 Effective Barrier Height 96
5.3.4 Effect of the Potential Step 98
5.3.5 Current-Voltage Characteristics 99
5.3.6 Barrier Height Variations 102
5.4 SUMMARY AND CONCLUSIONS 103

CHAPTER 6 - CARRIER TRANSPORT THROUGH THE INSULATOR OF THE MIS DIODE 106
6.1 INTRODUCTION 106
6.2 TRAPPING OF ELECTRONS IN LANGMUIR-BLODGETT FILM INSULATORS 107
6.2.1 Interface States 107
6.2.2 The Trapping of Electrons 107
6.2.3 The Perturbing Potential 108
6.2.4 Transition Rate 109
6.2.5 Matrix Element 109
6.2.6 Mean Free Path of the Incident Electron 111
6.2.7 The Effect on the Majority Carrier Current.. 115
6.2.8 Trapping as a Possible Hole Creation Process 117
6.3 LANGMUIR-BLODGETT FILM HOLE TRANSPORT PROCESSES.. 119
6.3.1 Direct Tunnelling 119

6.3.2 Poole-Frenkel Conduction 123
6.3.3 Linear Conduction 125
6.4 HOLE TRANSPORT IN DIODES INCORPORATING II-VI SEMI-INSULATORS 129
6.4.1 Direct Tunnelling 129
6.4.2 Conduction via the Insulator Valence Band 130
6.5 SUMMARY 133

CHAPTER 7 - ELECTRICAL CHARACTERISTICS OF AN MIM ELECTROLUMINESCENT PANEL IN THE STEADY STATE 135
7.1 INTRODUCTION 135
7.2 MODELLING THE DEVICE 137
7.2.1 Band Alignment 137
7.2.2 Defining Equations 139
7.2.3 Method of Solution 140
7.2.4 Dead Space 143
7.2.5 Mn Electroluminescent Centre 145
7.3 CURRENT-VOLTAGE CHARACTERISTICS 146
7.3.1 Inclusion of Dead Space 147
7.3.2 Carrier Concentration Profiles 148
7.3.3 Effect of Temperature 149
7.3.4 Carrier Mobilities 150
7.3.5 Electron Barrier and Effective Mass 152
7.3.6 ZnS Thickness 152
7.3.7 Inclusion of an N_D+ Region at the Cathode 153
7.4 SUMMARY 154

CHAPTER 8 - TIME DEPENDENT CHARACTERISTICS OF AN MIM ELECTROLUMINESCENT PANEL 155
8.1 INTRODUCTION 155
8.2 TIME DEPENDENT MODEL 155
8.2.1 The External Circuit 155
8.2.2 Defining Equations 156
8.3 METHOD OF COMPUTATION 158
8.3.1 Method 1 - Current Continuity Implied in System of Equations 158
8.3.2 Method 2 - Current Continuity Explicit in System of Equations 161
8.3.3 The Choice Between Methods 162
8.3.4 Starting Conditions 163
8.3.5 Electroluminescent Centres 163
8.4 ANALYTICAL TREATMENT FOR NO CURRENT INJECTION .. 165
8.5 DEVELOPMENT OF SYSTEM WITH TIME 166
8.6 SUMMARY AND DISCUSSION 168

CHAPTER 9 - SUMMARY AND CONCLUSIONS 170

9.1 THE "THICK" MIS DIODE 170
9.2 MIM ELECTROLUMINSECENT PANEL 172

APPENDIX 1 - STANDARD INTEGRALS 174

REFERENCES 175

LIST OF FIGURES 181

CHAPTER ONE

INTRODUCTION

This thesis deals with electronic processes in two electroluminescent device structures; the forward biased metal/thick insulator/semiconductor (MIS) diode and the high field metal/insulator/metal (MIM) panel. The electroluminescent mechanism is different in the two cases. The MIS diode relies on the recombination of minority carriers injected into the semiconductor while the MIM structure uses electroluminescent centres which are excited by the majority (electron) current and subsequently de-excite radiatively.

The MIS device has been considered as a possible alternative to the light emitting p-n diode. Like the MIS diode the p-n homojunction relies on minority carrier injection for electroluminescence, and at this it is very efficient. However it is not possible to produce p-n homojunctions using the wide, direct bandgap II-VI materials, ZnS and ZnSe, because they are not amphoteric. This is unfortunate as they are efficient phosphors with light emission in the visible range. A number of workers have investigated the possibility of producing an LED based on a metal/thin insulator/semiconductor structure, the idea being that under forward bias some of the potential would be dropped across the insulating layer and as a result the valence band edge of the semiconductor would rise with respect to the metal Fermi level. The number of holes with sufficient energy to enter the valence band of the n type semiconductor would then increase rapidly with the rise in the valence band edge leading to an enhanced

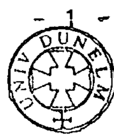

minority carrier injection ratio. This assumes that the insulator is thin enough to allow tunnelling with little attenuation. Figure 1.1 illustrates the re-alignment of bands under forward bias. However experimental devices fabricated using II-VI semi-insulators have been reported as giving maximum radiative efficiency at insulator thicknesses well in excess of tunnellable dimensions, and this suggests that hole transport is by some other mechanism. For example the hole transport could occur via the valence band of the semi-insulator. In this mode of transport the barrier to holes passing from the metal into the semiconductor remains unchanged with applied voltage and the minority carrier injection rate would be expected to remain negligibly small. However it was proposed by some workers that electrons injected into the metal (majority carrier current) would impact excite the electron gas in the metal, in a process similar to impact ionisation in a semiconductor, to produce a steady state hole population energetically capable of crossing the insulator. In this thesis, the process will be referred to as impact ionisation as is conventional when referring to carrier excitation in semiconductors.

MIS diodes have also been fabricated using Langmuir-Blodgett film technology to create insulating layers of highly controlled thicknesses in the range of ~25Å to ~500Å. Using materials such as cadmium stearate as the insulator it has been found that thicknesses for optimum radiative efficiency are well in excess of tunnellable dimensions.

The aim of this work has been to make a theoretical investigation of the various electronic processes that could occur in these thick insulator MIS structures. In particular two types of device fabricated in the Department of Applied Physics and Electronics at the Univeristy of Durham are

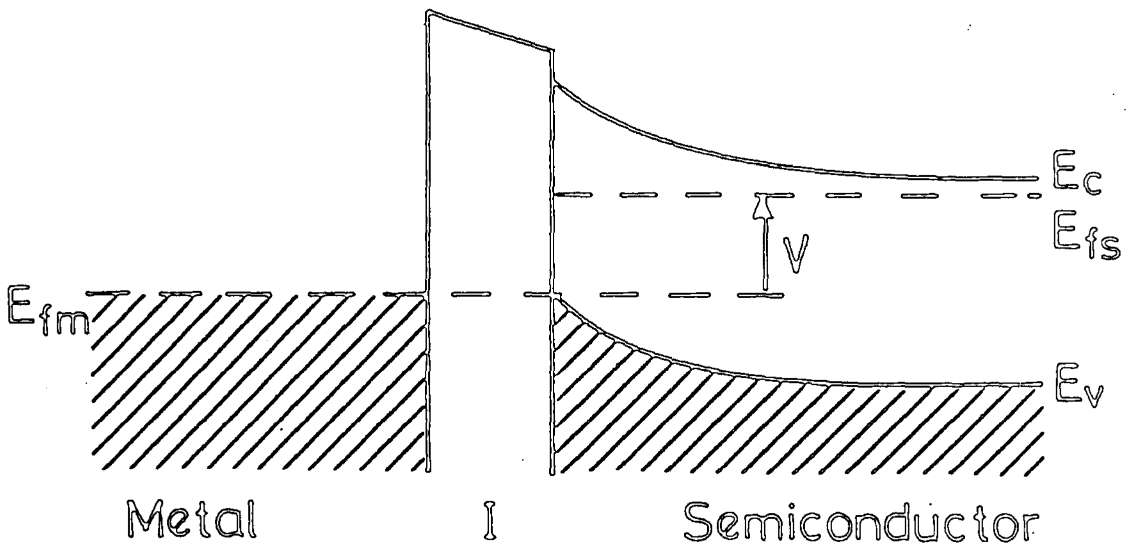

Fig. 1.1 : An MIS diode under forward bias.

considered. These two systems were Au/cadmium stearate/n-GaP and Au/i-ZnS/n-ZnS.

The basic physics of Schottky barriers and MIS diodes is reviewed in Chapter Two and Chapter Three. In Chapter Four, the impact ionisation process in the metal is considered in some detail. Calculations are reported which are intended to determine the probability of an energetic electron interacting toproduce a hole in the metal with a given wavevector. In particular, the distribution in energy of holes arriving at the metal-insulator interface is found and the significance of the impact ionisation process relative to normal thermal generation is assessed. In Chapter Five and Chapter Six the behaviour, under forward bias, of the "II-VI semi-insulator" and "Langmuir-Blodgett film" systems are considered. In particular a model is produced to explain the current-voltage characteristics of the Langmuir-Blodgett film device and to predict the band alignment under bias. With the framework of this model the possible hole transport mechanisms through the insulator are studied. The same model is then applied to the II-VI device and used to explain the experimentally observed results for the efficiency of these structures.

The remainder of the thesis deals with the second electroluminescent structure; the high field MIM panel. Such devices when driven by a dc signal are prone to the occurence of high current filaments, which quickly burn out and eventually lead to the destruction of the device. Theoretical research on this device was carried out whilst the author worked at Plessey Research (Caswell) Limited, during the spring of 1984. A simple model of the device was developed which predicts the existence, over a certain voltage range of three current states at any given voltage and hence a susceptibility to filament formation.

Current-voltage characteristics for the device are calculated for a range of possible materials parameters and the implications for real devices are discussed. To develop an understanding of the evolution of the device after switch-on, the time dependent behaviour is also considered. This is particularly relevant as such devices are usually driven by a pulsed signal.

CHAPTER TWO

THE PHYSICS OF SCHOTTKY BARRIERS AND METAL-INSULATOR-SEMICONDUCTOR DEVICES

2.1 INTRODUCTION

The purpose of this section is to fill in the basic background to the theory of MIS devices. This is intended to form a solid basis from which the particular devices of interest in this work (which will be reviewed in Chapter Three) can be investigated in more detail. It is also intended to refer back to this chapter, later in this work, to explain aspects of the theory which have already been covered by previous authors.

2.2 ELECTROLUMINESCENT STRUCTURES

The aim of this section is to give a brief introduction to the light emitting devices considered in the thesis. Althought the p-n junction is not a subject of the research reported here, it is the logical starting point for a discussion of electroluminescence and provides some useful background for the overall picture.

2.2.1 The p-n Homojunction

The p-n junction is the most widely used light emitting diode at

present and as such it is informative to briefly review the mechanism of its electroluminescence.

There is a movement of carriers between the n and p type regions of a homojunction to enable the Fermi levels to equalise and this leads to a depletion region where there is space charge due to uncompensated donor and acceptor impurities. By assuming a band edge density of states and using Boltzmann statistics it is relatively straightforward to show that the diffusion potential (or the barrier) produced by the carrier exchange is

$$V_d = \frac{kT}{|e|} \ln\left(\frac{n_n}{n_p}\right) \tag{2.1}$$

with n_n and n_p representing the bulk electron concentrations in the n type and p type semiconductors respectively. The band diagram is shown in Figure 2.1(a), where there is an effective barrier to minority carrier injection across the junction. In forward bias the bands of the n type semiconductor are raised with respect to those of the p type material and minority carrier injection occurs with the reduced barrier. As a result there is current flow (see Figure 2.1(b)). Almost all the applied voltage is dropped across the depletion region and in the bulk, where the electric field is small, diffusion is the dominant current mechanism. The current is given by the Schockley equation

$$J = |e|\left(\frac{D_n n_p}{L_n} + \frac{D_p p_n}{L_p}\right)\left(\exp\left(\frac{|e|V}{kT}\right) - 1\right) \tag{2.2}$$

where D and L are the diffusion constant and diffusion length of

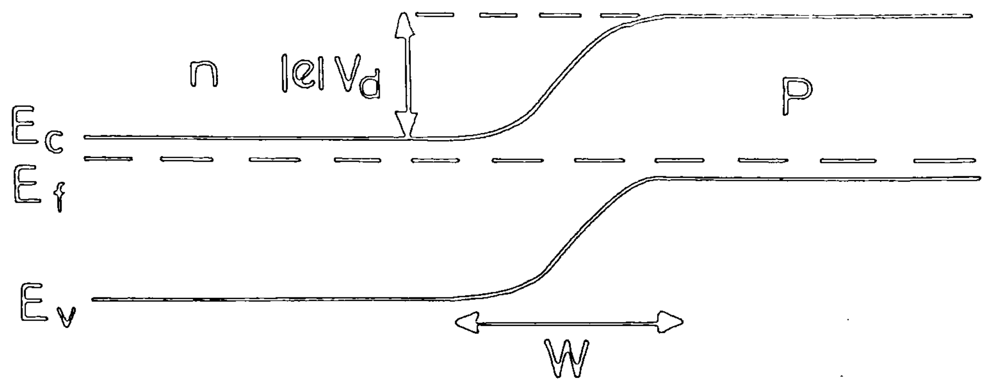

(a)

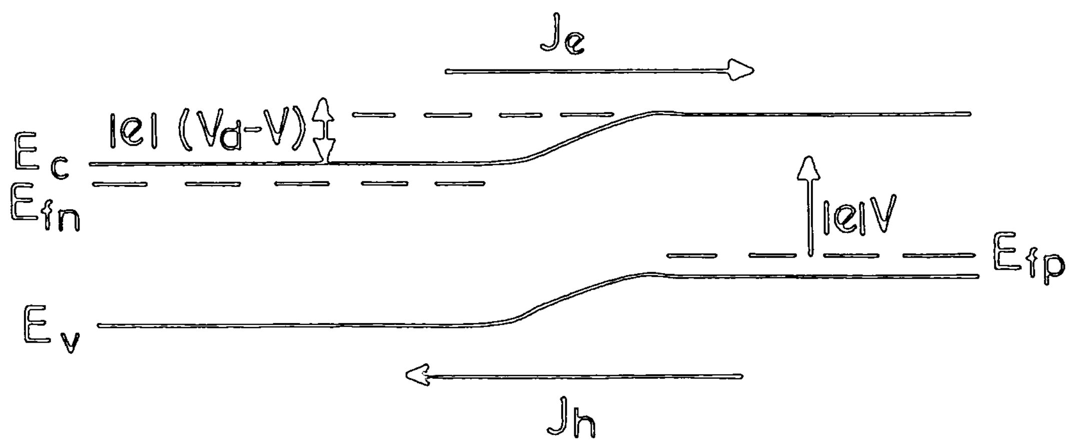

(b)

Fig. 2.1 : Schematic diagram of a p-n homojunction a) at zero bias; b) under forward bias.

the doped semiconductor and their subscripts follow the normal nomenclature. There can also be another component to the current due to recombination in the vicinity of the depletion region which will lead to a deviation from the ideal characteristics given by equation (2.2). Recombination through impurities is an undesirable effect as it causes loss of minority carriers with no light output. It can be minimised by avoiding the occurance of the defects which are good recombination centres. The recombination current usually represents the major part of any deviation from the ideal current-voltage characteristic, but other mechanisms may contribute. For example, interband tunnelling, where carriers in the conduction band of a degenerately doped n type semiconductor tunnel across the depletion region into empty states in the valence band of a degenerately doped p type material ; or the "high injection condition" where fields in the bulk mean that drift must also be taken into account; or image charge effects due to ionic charge in the vicinity of the semiconductor surface. However these effects are usually much smaller than those due to recombination current unless the specified special conditions prevail.

With the injection of minority carriers into a semiconductor, electroluminescence will be produced through radiative recombination. For direct bandgap semiconductors there is a high probability of an interband transition. However for indirect bandgap material, such as GaP, recombination centres need to be incorporated to improve radiative efficiency.

2.2.2 Schottky Barriers

Unfortunately it is not possible to produce p-n junctions with the wide bandgap II-VI compounds such as ZnS and ZnSe because low resistivity p type materials cannot be made. The Schottky barrier has therefore received a good deal of attention as an alternative method of incorporating II-VI materials into an efficient light emitting diode based on minority carrier injection.

In the ideal case a Schottky barrier will consist of an abrupt junction between a metal and semiconductor with the boundary free of interface states. If the situation in Figure 2.2(a) is first considered, with the metal and semiconductor separated, the difference in energy between the metal Fermi level and the semiconductor conduction band edge can be seen to be equal to the difference between the respective work function ϕ_m and electron affinity X_S. On bringing the metal and the semiconductor together there is a transfer of electrons from the semiconductor into the metal until Fermi level alignment is achieved. the band diagram becomes that shown in Figure 2.2(b) with negative charge at the metal surface being compensated for by the ionised donors in the depletion region. A fuller treatment of the barrier formation, including the effects of interface states, will be given in Section 2.3

Electroluminescence can be produced with the device in either forward or reverse bias. The reverse bias case is shown in Figure 2.3(a). Here light emission can be produced as a result of avalanche multiplication after field emission of electrons from the metal into the semiconductor conduction band and the excitation of luminescent

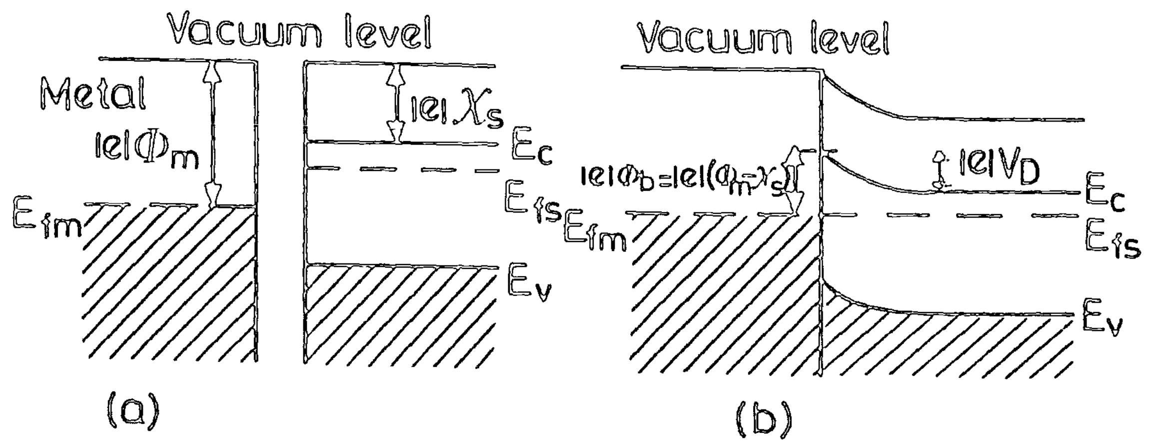

Fig. 2.2 : Formation of a Schottky barrier

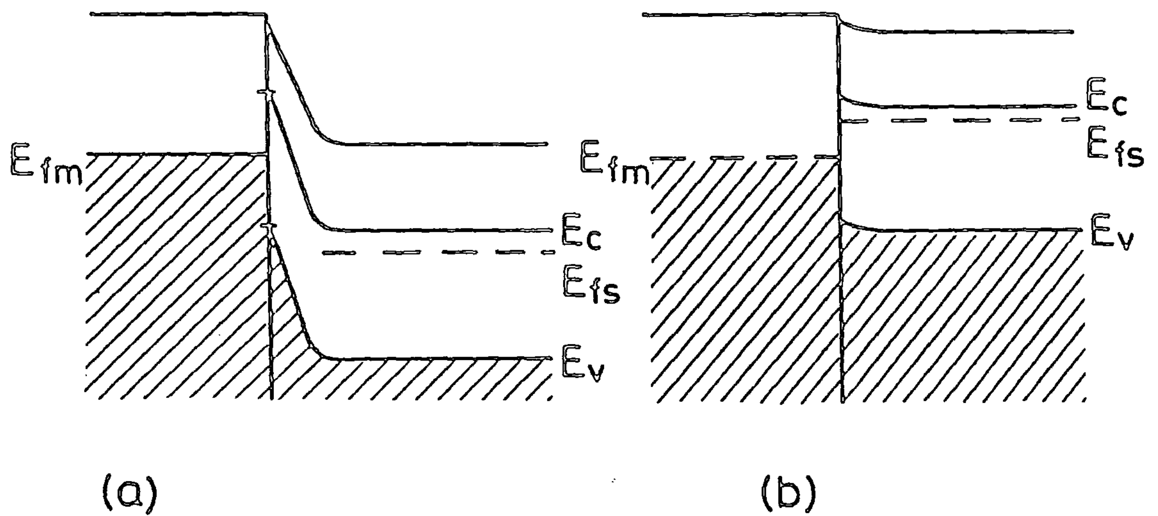

Fig. 2.3 : A Schottky barrier under a) reverse bias; b) forward bias.

centres by the electron current. Figure 2.3(b) shows a Schottky barrier in forward bias. The important electronic process here is the injection of holes from the metal into the valence band of the semiconductor, where they can recombine radiatively. Unfortunately the ratio of the hole current to the electron current is very low with typical values given by $\gamma \sim 10^{-4}$ compared with p-n junction values close to unity. This is a direct result of the relatively large barrier presented to the holes at the interface which is indicated in Figure 2.3(b). However in the next section it is shown how the inclusion of a thin insulating layer between the metal and the semiconductor can increase the value of γ.

2.2.3 The MIS Diode

If an insulator is incorporated between the metal and semiconductor in a Schottky barrier it is expected that some of the applied bias will be dropped across the insulator itself. Figure 2.4(a) shows an idealised band diagram of an MIS device under zero bias while Figure 2.4(b) shows the same device under forward bias. At zero bias it is expected that the semiconductor barrier height ϕ_b (the energy difference between the metal Fermi level and the semiconductor conductance band edge at the MI interface - see Figure 2.4(a)) will be smaller than it is in the simple Schottky barrier. If we consider the ideal case of no interface states then the field in the insulator is related to that at the surface of the semiconductor by the expression

$$\varepsilon_i F_i = \varepsilon_s F_s \qquad (2.3)$$

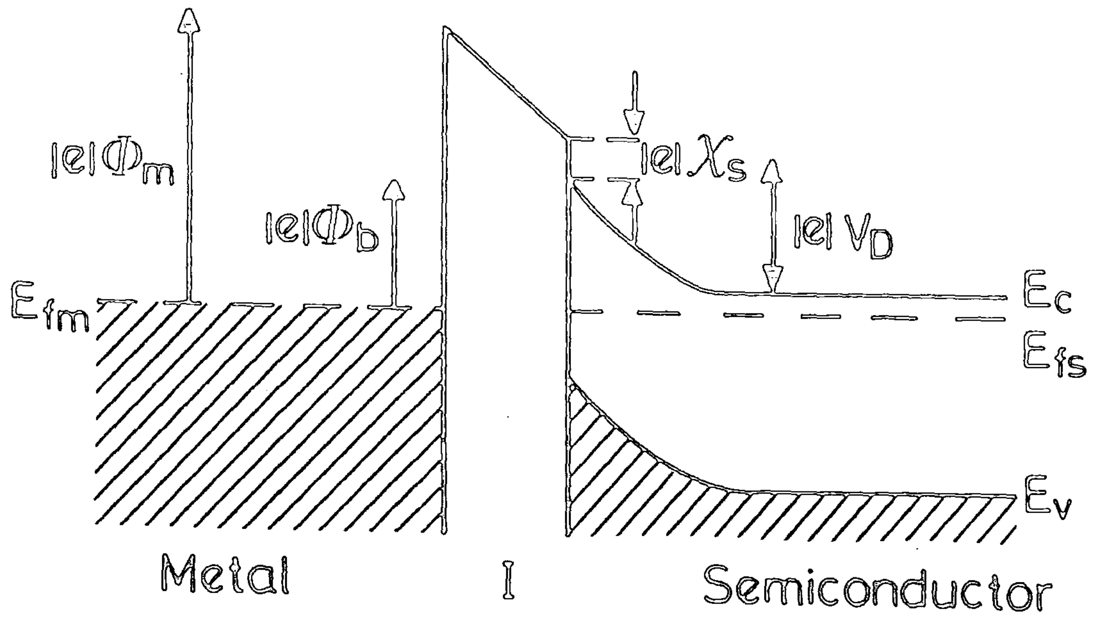

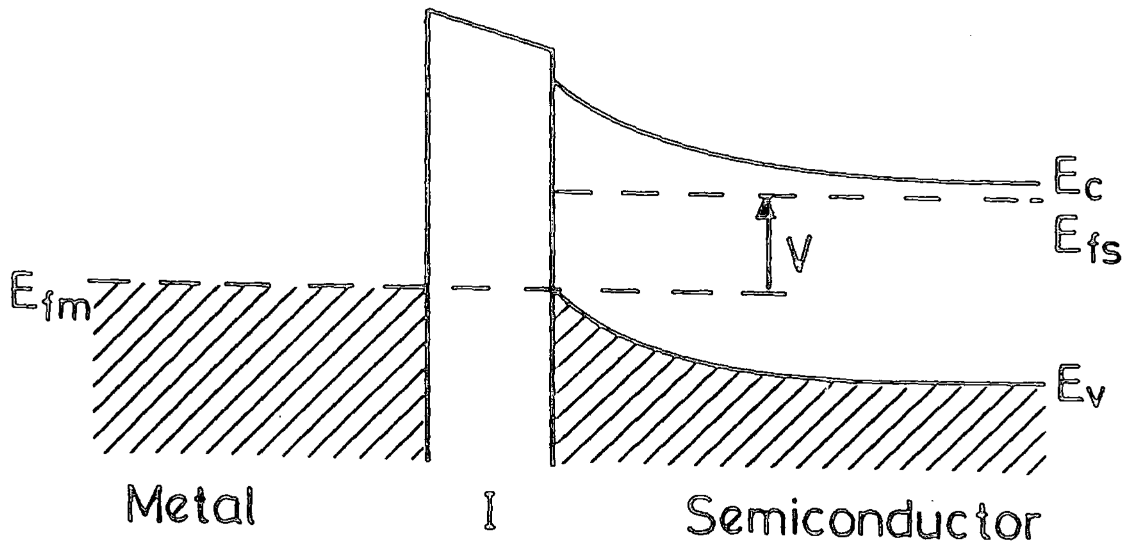

Fig. 2.4 : An MIS diode under a) zero bias; b) forward bias.

where ε_i and ε_s are the relative permittivities of the insulator and semiconductor respectively. A potential is developed across the insulator and hence the semiconductor barrier height is reduced to satisfy equation (2.3). When a forward bias is applied, as shown in Figure 2.4(b), some of the applied voltage is dropped across the insulator and the semiconductor barrier height increases as a result. Part of the bias will also be dropped across the semiconductor depletion region leading to less band bending. The result is that with increasing bias the valence band of the semiconductor is allowed to rise relative to the metal Fermi level. Assuming the insulator to be thin enough to allow significant tunnelling current or current by some other mechanism the rise in the valence band means that the electrons in that band will have more opportunity to tunnel into the metal's unoccupied states above or just below the metal Fermi level. With increasing bias the number of unoccupied states in the metal at the energy corresponding to the valence band edge increases rapidly until the point at which the valence band edge is close to the metal Fermi level. Then the rise in unoccupied electron states decreased becoming approximately linear with energy because virtually all the states above the metal Fermi level are unoccupied.

For a thin insulator that allows a large tunnelling current, whilst still supporting a potential difference, the increase in the number of elecrons able to enter the metal from the valence band (or equivalently, holes able to tunnel into the semiconductor) will increase the minority carrier injection ratio γ compared to the Schottky barrier. The theory of MIS devices incorporating thin, perfect insulators will be developed later in this chapter.

2.2.4 Panel Devices

Another form of electroluminescent device is the large area panel which uses a II-VI compound phosphor. Both ac and dc current devices have been produced with the difference being that in the ac structure the phosphor is enclosed between insulating layers and therefore capacitively coupled to the alternating applied bias. The dc device is directly connected to the voltage supply. The structures work under high fields, typically 10^8 Vm^{-1}, with the electroluminescence usually due to either impact ionisation or impact excitation of luminescent centres, normally transition metal ions. In the case of impact ionisation the centre is actually ionised with subsequent light emission on the capture of an electron, while in impact excitation a bound electron is excited to a higher bound state with light emission on the de-excitation. It has generally been found that the ac devices are the more stable because the insulating layers protect the phosphor from high current filament formation, which is responsible for the occurrence of "hot spots" in the dc devices.

These 'hot spots' quickly burn out and lead to the eventual failure of the whole device. Initially most of the work on these devices used phosphor powders interspersed in a dielectric medium as the electroluminescent layer[3]. Recently more attention has been paid to thin film devices and these are reviewed by Howard[4], Mach and Muller[5] and more generally by Vecht[6]. Figure 2.5(a) shows a schematic diagram of a typical ac device. The phosphor is nearly always ZnS as various wavelengths for the electroluminescence can be produced by suitable doping with luminescent impurities. The top electrode is typically aluminium while the transparent electrode is a material such as

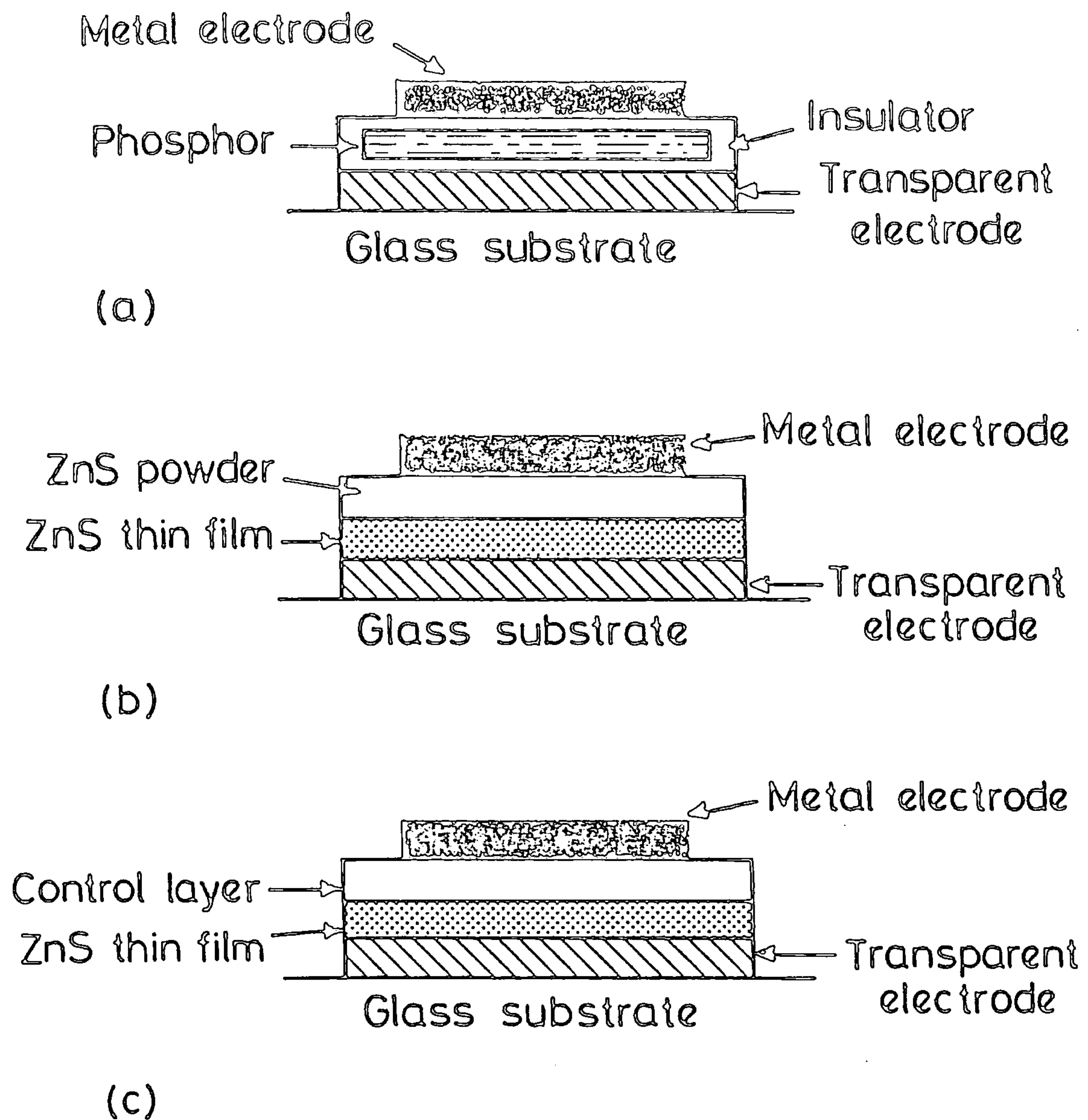

Fig. 2.5 : Various forms of electroluminescent panel devices a) ac device; b) composite thin film-powder dc device and c) dc thin film device.

cadmium stannate. The insulator may be silicon nitride or aluminium oxide.

In an effort to reduce high current filament formation in the dc structures composite devices incorporating both thin films and powders have been fabricated[6,7]. Figure 2.5(b) illustrates one of these. Being more resistive the powder layer takes most of the applied voltage and the electric field across the thin film is relatively small so avoiding filament formation. The film acts as the active electroluminescent component. Until recently it had proved difficult to provide dc panel devices with just thin films because of filament formation. Attempts to include some sort of control layer to limit filaments had produced little success[8]. However stable devices are now being produced[9] and such a structure is illustrated in Figure 2.5(c). The control layer acts to inhibit the spread of filaments but does not completely eliminate them. This particular device and some of the characteristics affects its stability, will be discussed in more detail in Chapter Seven and Chapter Eight.

In conclusion, it should be mentioned that, due to the high electric fields required, a bias of typically 100V to 200V is needed to drive these displays and this obviously is a limitation on their general applicability.

2.3 SCHOTTKY BARRIER FORMATION

2.3.1 Schottky-Mott Theory

It is clear from Figure 2.2(b) that the barrier height of an ideal Schottky barrier can be written as:

$$|e|\phi_b = |e|\,\phi_m - |e|X_e \qquad (2.4)$$

where $|e|\phi_m$ is the work function of the metal and $|e|\,X_s$ is the electron affinity of the semiconductor. In achieving this result several assumptions have been made. One of the most important of these has been mentioned in Section 2.2.2, that there is an absence of surface states. A second important assumption is that the surface dipole contributions to ϕ_m and X_s do not change when the metal and semiconductor are brought together.

In the simplest model of the Schottky barrier, the semiconductor is assumed to be homogeneous right up to the interface and this makes the application of the depletion approximation quite straightforward. Ignoring the effect of the 'transition region' at the edge of the depletion region, where the electron concentration is still within one order of magnitude of the donor concentration, the charge distribution is illustrated in Figure 2.6(a). The electric field and potential for this distribution are shown in Figures 2.6(b) and 2.6(c) respectively.

No matter what the shape of the barrier, the central result of Schottky-Mott theory is that the barrier height is given by equation (2.4). Measurement of ϕ_b[12] shows that this is not the case and that often there is little change in the barrier height for different metals with different work functions.

2.3.2 The Bardeen Model

In an attempt to explain the weak dependence of the barrier height ϕ_b

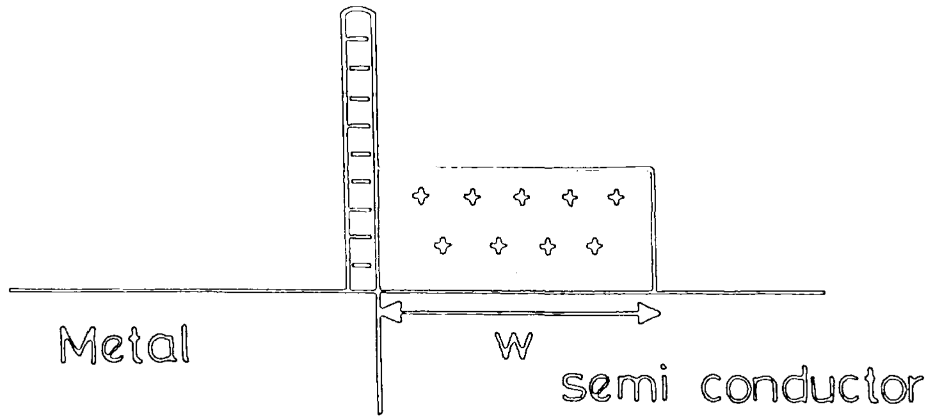

(a)

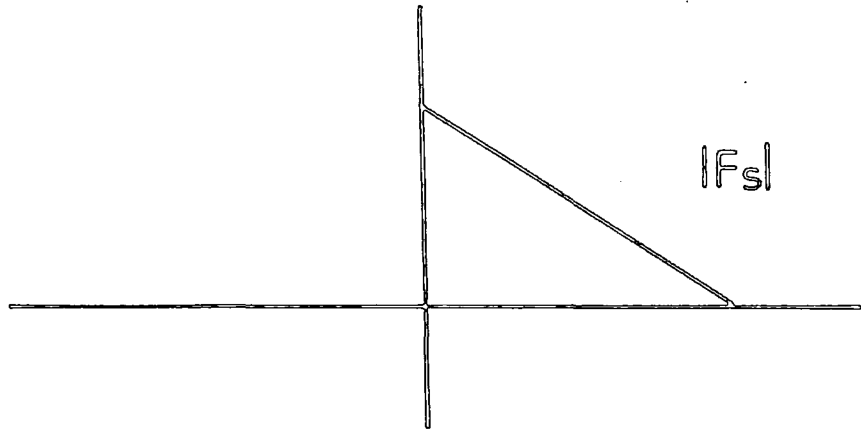

(b)

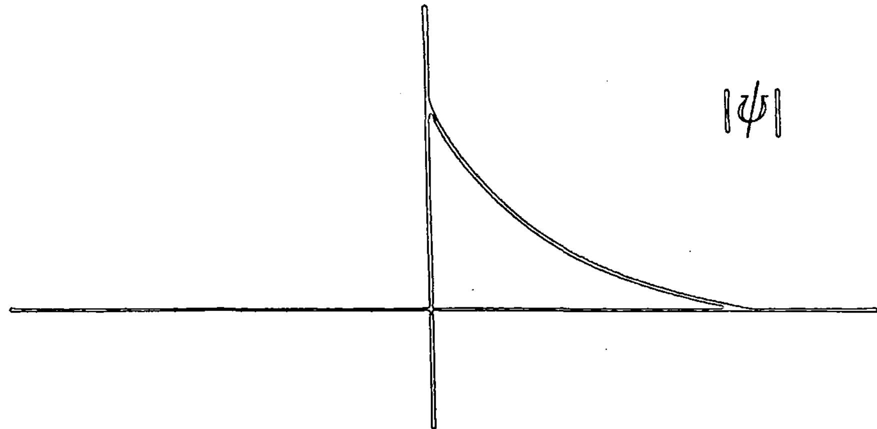

(c)

Fig. 2.6 : a) Charge distribution; b) field and c) potential in a Schottky barrier using the depletion approximation.

Bardeen[13] suggested that the discrepancy may be due to the effect of interface states.

Supposing that the metal and semiconductor were separated by a thin insulating layer, Bardeen suggested that there was a distribution of surface states across the semiconductor energy gap and defined a so called neutral level of ϕ_0. When states were filled up to this level it was proposed that the net surface charge was zero. The effect of a high surface state density is then to pin ϕ_b close to the value corresponding to the situation in which ϕ_o is at the same energy as the Fermi level E_f. This can be explained if we analyse the Bardeen model using Figure 2.7. The insulating layer is considered thin enough to allow unimpeded electron flow but capable of withstanding a field. The surface state density D_{ss} is assumed constant across the energy gap. The value of ϕ_m will be dependent on the particular metal used. The fields at the insulator-semiconductor interface are related by:

$$\varepsilon_i \varepsilon_o F_i = \varepsilon_s \varepsilon_o F_s - Q_{ss} \qquad (2.5)$$

Where Q_{ss} is the net surface charge. As electrons can readily tunnel through the thin insulator their surface states will be in strong communication with the metal. Communication with the semiconductor is weaker because activated transitions are required for carrier transfer. Taking this into account it can be stated (using the zero temperature approximation) that all the surface states below E_{fm} are occupied while those above are empty. This is important when the device is under bias and the Fermi levels misaligned.

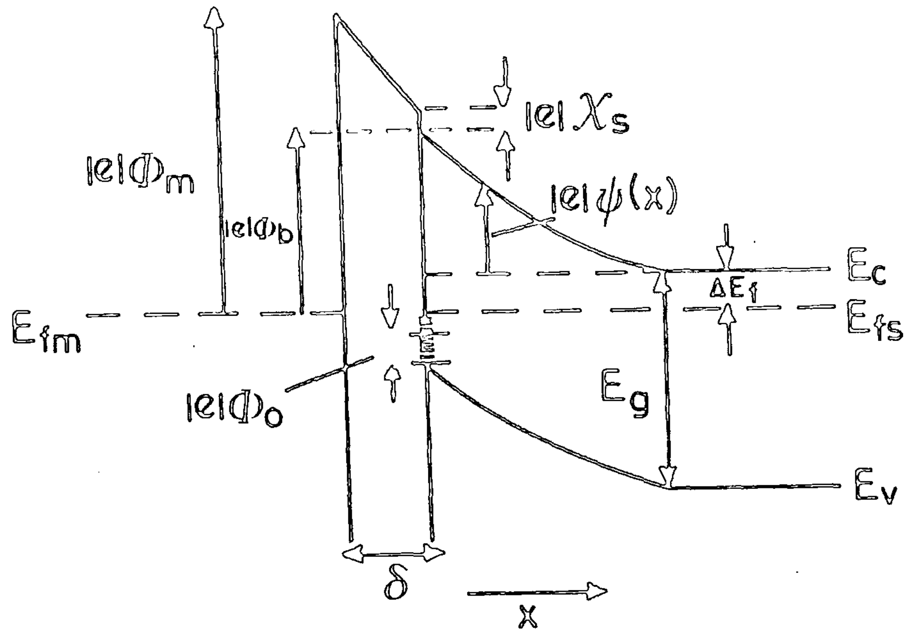

Fig. 2.7 : A Schottky barrier incorporating a thin interfacial layer.

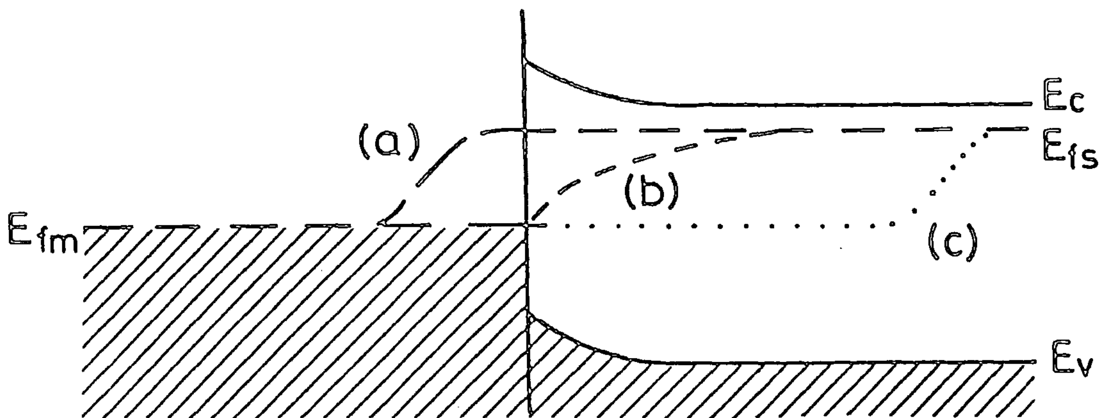

Fig. 2.8 : Quasi Fermi levels proposed to explain current mechanisms in a Schottky barrier a) thermionic emission of electrons; b) diffusion of electrons and c) diffusion of holes.

Referring to Figure 2.7 we can write the relationships:

$$Q_{ss} = D_{ss}|e| \left(\phi_b - \left(\frac{E_g}{|e|} - \phi_o\right)\right)$$

and
$$F_i = ((\phi_b + X_s) - \phi_m)/\delta \qquad (2.6)$$

Substituting these expressions into equation (2.5) and rearranging, it is now possible to write

$$\phi_b = \alpha\left(\phi_m - X_s + \frac{\varepsilon_s}{\varepsilon_i}\delta F_s\right) + (1-\alpha)\left(\frac{E_g}{|e|} - \phi_b\right) \qquad (2.7)$$

where
$$\alpha = \frac{\varepsilon_i \varepsilon_o}{\varepsilon_i \varepsilon_o + |e|\delta D_{ss}}$$

In the limiting case of $D_{ss} \rightarrow \infty$, α tends to zero and ϕ_b tends to the Bardeen limit of $E_g - \phi_o$, or the neutral level ϕ_o aligns with E_{fm}. In this limit ϕ_b is independent of the properties of the metal. This analysis was first carried out by Crowell and Sze[14] except that these authors took the flat band condition with F_s in equation (2.7) set to zero.

2.4 SCHOTTKY BARRIER CURRENT MECHANISMS

2.4.1 Possible Mechanisms

For an n type Schottky barrier in forward bias (by convention that is with the semiconductor at a higher potential energy) the majority carriers travelling from the semiconductor bulk into the metal must

cross the potential barrier formed by the depletion region.

In heavily doped materials at low temperatures tunnelling has been observed in the forms of both field emission and thermionic field emissions[16]. However at higher temperatures and with "normally" doped semiconductors the barrier region is too wide for an appreciable tunnelling current and thermionic emission over the barrier is favoured.

To explain current emissions over the barrier, two main theories have been put forward. First Wagner[17] and then Schottky and Spenk[18] proposed that the diffusion of carriers through the depletion region would be the limiting factor to the current, while Bethe[19] suggested that it would in fact be the thermionic emission over the barrier which was dominant in controlling the current. Figure 2.8 illustrates the difference between the two mechanisms in terms of the effect it has on the quasi Fermi level for electrons in the system. With the diffusion theory the Fermi level must fall off as it approaches the interface, in order that there is some diffusion current. However, in the thermionic emission theory, where the barrier height is the limiting factor, the Fermi level will be at a constant energy right up to the interface.

These two mechanisms will now be considered separately in more details.

2.4.2 The Diffusion Theory

The Diffusion Theory's main assumption is that the current from the semiconductor into the metal is limited by the normal processes of drift and diffusion and is given by the standard transport equation:

$$J_n(x) = |e|\, n(x)\, \mu_e F_s(x) + |e|\, D_e \frac{dn}{dx}(x) \qquad (2.8)$$

where D_e is the diffusion constant for electrons, $n(x)$ is their concentration and the other symbols are as previously defined in the chapter.

In his treatment of this theory, Rhoderick[20] points out that, as the top of the barrier is reached, the value of the field $F_s(x)$ is high ($\sim 10^7 Vm^{-1}$). Under such fields the concept of a mobility and diffusion constant independent of the field is dubious. Taking account of these effects means that the analysis becomes much more complicated so no correction is made although there is some reservation about the ultimate accuracy of the method.

Introducing the quasi-Fermi level $\xi(x)$, defined by

$$n(x) = N_c \exp\left(\frac{-|e|\,(E_c(x) - \xi(x))}{kT}\right) \qquad (2.9)$$

Where N_c is the effective density of states for the conduction band, $E_c(x)$ is the energy of the band edge and Boltzmann statistics have been used. Equation (2.8) can be re-arranged into the form:

$$-J_n(x) = kT\mu_e N_c \exp\left(\frac{-|e|E_c(x)}{kT}\right) \frac{d}{dx} \exp\left(\frac{|e|\,\xi(x)}{kT}\right) \qquad (2.10)$$

Making use of the depletion approximation the variation of $E_c(x)$ in

the depletion region is given by:

$$E_c(x) = \phi_b + \frac{|e|N_D}{2\varepsilon_s\varepsilon_o}(x^2 - 2wx) \qquad (2.11)$$

where N_D is the donor concentration and w is the depletion region length. Substituting equation (2.11) into equation(2.10) and integrating over the depletion region, an expression for the current is found, given by:

$$J_n = \frac{|e|N_c\mu_e F_s(0)}{2aw\, I(aw)} \times \exp\left(\frac{-|e|\phi_b}{kT}\right)\left[\exp\left(\frac{|e|V}{kT}\right) - 1\right] \qquad (2.12)$$

where $a = \left(\frac{|e|^2 N_D}{2\varepsilon_s\varepsilon_o\, kT}\right)^{\frac{1}{2}}$

and I(aw) is Dawson's integral. For almost all cases of physical interest $aw > 2$ and I(aw) is close to its assymtotic value of $(2aw)^{-1}$. Hence

$$J_n = |e|N_c\mu_e F_s(0)\exp\left(\frac{-|e|\phi_b}{kT}\right)\left[\exp\left(\frac{|e|V}{kT}\right) - 1\right] \qquad (2.13)$$

or

$$J_n = J_d\left[\exp\left(\frac{|e|V}{kT}\right) - 1\right]$$

2.4.3 Thermionic Emission Theory

The basis of this theory is that the major impediment to current is the probability that a carrier will have sufficient energy to get over the electron barrier. It is assumed that drift and diffusion are negligible. In his treatment, Henisch[21] sets an imaginery boundary a distance λ_B inside the semiconductor, where λ_B is the barrier width. This is to avoid the effect of high fields near the MS interface. By assuming that the electron mean free path is equivilent to, or greater than this distance, it is argued that electrons crossing this barrier will also cross the depletion region into the metal.

Using standard kinetic gas theory with Boltzman statistics, the number of electrons impinging on the imaginary boundary at $x = \lambda_B$ with their x component of velocity in the range v_x to $v_x + dv_x$ is given by:

$$dR_e = n(\lambda_B)\, v_x \left(\frac{m_e}{2\pi kT}\right)^{\frac{1}{2}} \exp\left(\frac{-m_e v_x^2}{2kT}\right) dv_x \qquad (2.14)$$

The potential barrier just impedes transport in the x direction, so it is the energy associated with motion in the x direction that must be larger than the potential barrier in the depletion region. For an applied voltage of V and a barrier height of ϕ_b the minimum value of v_x for emission over the barrier is given by:

$$v_{x_{min}}^2 = \frac{2}{m_e} \left(|e| \left(\phi_b - V - \frac{\Delta E_f}{|e|} - \psi(\lambda_B)\right)\right) \qquad (2.15)$$

where ΔE_f and $\psi(x)$ are defined by Figure 2.7. To determine the curent crossing the interface from the semiconductor into the metal, it is necessary to find the rate at which electrons impinge on the boundary $x = \lambda_B$ with velocities greater than $v_{x_{min}}$. Integrating equation (2.14) between the limits of $v_{x_{min}}$ and ∞ and multiplying by $|e|$:

$$J_{sm} = n(\lambda_B)\ |e| \left(\frac{kT}{2\pi m_e}\right)^{\frac{1}{2}} \exp\left[\frac{-|e|}{kT}\left(\phi_b - V - \frac{\Delta E_f}{|e|} - \psi(\lambda_B)\right)\right] \tag{2.16}$$

The subscript sm indicates that the current is from the semiconductor to the metal.

There will be a current in the opposite direction independent of bias because the barrier to electrons in the metal ϕ_m remains unchanged by applied bias. At zero bias there is no net current so:

$$J_{ms} = - J_{sm}(V=0) \tag{2.17}$$

The electron concentration $n_e(\lambda_B)$ can be written using the effective density of states:

$$n(\lambda_B) = N_c \exp\left[\frac{-|e|}{kT}\left(\frac{\Delta E_f}{|e|} + \psi(\lambda_B)\right)\right] \tag{2.18}$$

Combining equations (2.16), (2.17) and (2.18) to give the total current:

$$J_n = A^*T^2 \exp\left(\frac{-|e|\phi_b}{kT}\right)\left[\exp\left(\frac{|e|V}{kT}\right) - 1\right] \quad (2.19)$$

where A* is the Richardson constant defined as

$$A^* = \frac{4\pi|e|m_e k^2}{h^3} \quad (2.20)$$

Further refinements can be introduced with the inclusion of an ideality factor n from the following argument.

In Section 2.3.2 the idea of a thin insulating layer between the metal and the semiconductor was introduced and with it the possibility that ϕ_b can rise with applied voltage. Assuming this change with bias is linear we can write the bias dependent barrier height as:

$$\phi_b(V) = \phi_b(0) \left(1 - \frac{1}{n}\right)V \quad (2.21)$$

Substituting for ϕ_b in equation (2.19) using equation (2.21) the revised expression for the current is:

$$J_n \approx A^*T^2 \exp\left(\frac{-|e|\phi_b(0)}{kT}\right)\left[\exp\left(\frac{|e|V}{nkT}\right) - 1\right] \quad (2.22)$$

Obviously the value of n will depend on the method of preparation of the device, but it is possible to fabricate structures with values of n very close to unity.

2.4.4 Thermionic Emission - Diffusion Theory

Although thermionic emission theory, on its own, accurately describes most Schottky barriers, Crowell and Sze[22] combined the theories related in the last two sections to produce an expression for the current density given by:

$$J_n = \left(\frac{|e| N_c v_r}{1 + v_r/v_d} \right) \exp\left(\frac{-|e|\phi_b}{kT} \right) \left[\exp\left(\frac{|e|V}{kT} \right) - 1 \right] \tag{2.24}$$

where v_r is an effective recombination velocity at the potential barrier maximum and v_d is an effective diffusion velocity for electrons in the depletion region.

2.5 SCHOTTKY BARRIER BEHAVIOUR

2.5.1 Image Charge Effects

The requirements that an electric field must be perpendicular to a metal surface[23] leads to an effect in Schottky barriers known as the Schottky Effect. In approaching the metal from the semiconductor, an electron a distance x from the interface will induce a charge distribution at the metal surface equivalent in effect to placing a single charge of $|e|$ the same distance x inside the metal[23]. Due to this induced charge the electron experiences an additional force of mangitude $|e|^2/4\pi\varepsilon_s\varepsilon_0(2x)^2$, attracting it towards the surface of the metal. The field due to the image charge is of opposite sign to the field across

the depletion region created in the barrier formation. Including the effects of image charge therefore leads to a revised electric field

$$F_s'(x) = F_s(x) + \frac{|e|}{4\pi\varepsilon_s\varepsilon_o(2x)^2} \quad (2.25)$$

where $F_s(x)$ is the field due to the Schottky barrier and is negative. Integrating equation (2.25) from ∞ to x will give the revised diffusion potential at x as

$$\psi'(x) = \psi(x) - \frac{|e|}{16\pi\varepsilon_s\varepsilon_o x} \quad (2.26)$$

The inclusion of image charge can therefore be seen to reduce the barrier height. Figure 2.9 shows the profile of the resultant barrier when the Schottky effect is included. It can be seen, both from this figure and equation (2.26) that the effect is most significant near the MS interface. It is a reasonable approximation, therefore, to set the value of F(x) equal to its maximum value, which occurs at the interface.

Assuming F(x) to be constant at the value of F(0), the maximum height of the revised barrier profile will occur when the fields are equal and opposite:

$$|F(0)| = \frac{|e|}{16\pi\varepsilon_s\varepsilon_o x_{max}^2} \quad (2.27)$$

which gives the position of the potential maximum as

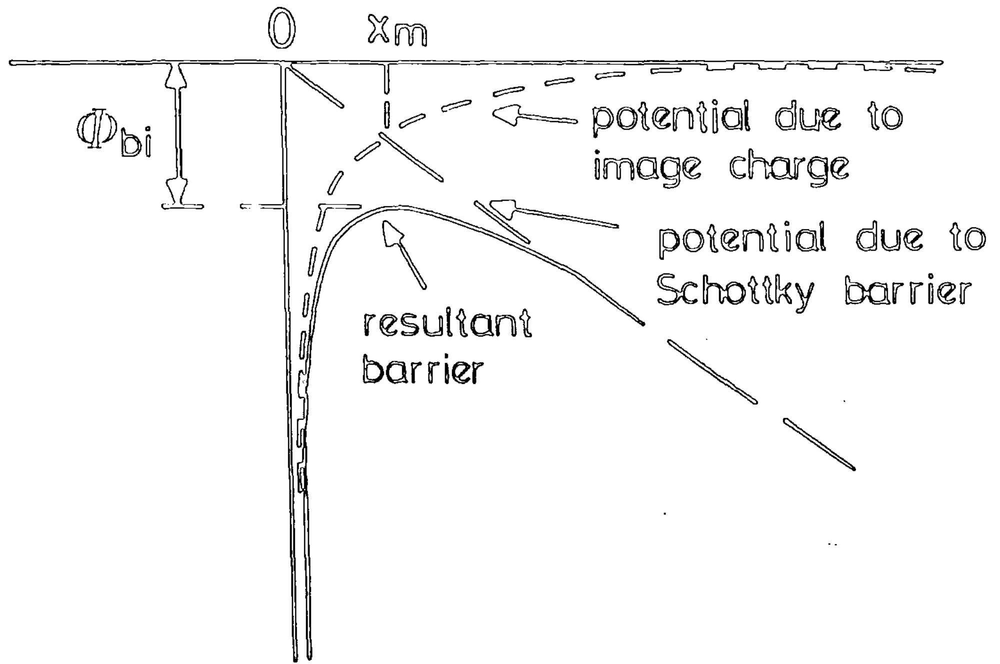

Fig. 2.9 : The effect of image charge on the electron barrier of a Schottky diode.

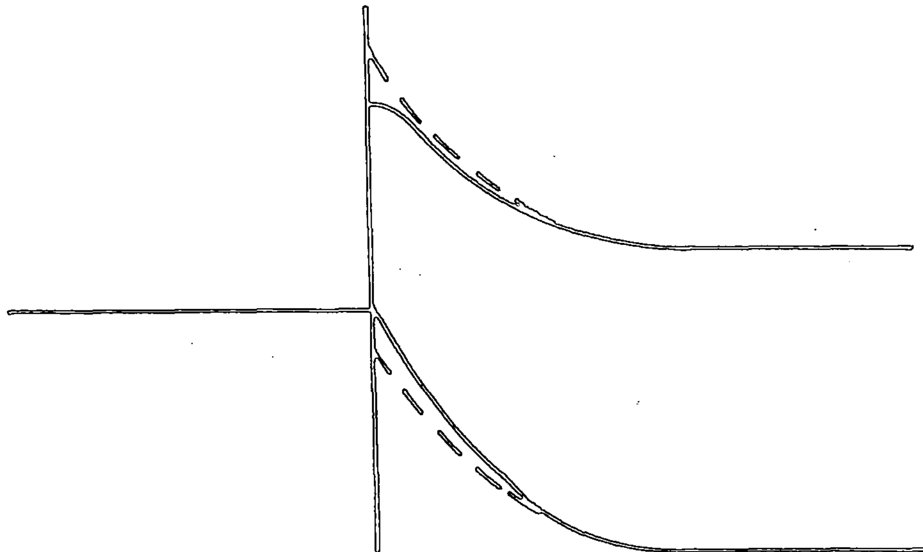

Fig. 2.10 : The influence of the Schottky effect on the bandgap at the metal-semiconductor interface.

$$x_m = \left(\frac{|e|}{16\pi\varepsilon_s\varepsilon_o \, |F(o)|} \right)^{\frac{1}{2}} \qquad (2.28)$$

The reduction in barrier height is given by:

$$\Delta\phi_{bi} = \psi(o) - \psi' \, (x_m) \qquad (2.29)$$

We can also write

$$\psi(x_m) = \psi(o) - xF(o) \qquad (2.30)$$

so substituting for $\psi'(x_m)$ in equation (2.29) using equations (2.28) and (2.26) then substituting for $\psi(o)$ using equation (2.30), yields a final expression for the barrier lowering

$$\Delta\phi_{bi} = \left(\frac{|e|F(o)}{4\pi\varepsilon_s\varepsilon_o} \right)^{\frac{1}{2}} \qquad (2.31)$$

Care must be taken on the value of ε_s used. As the electrons are moving at thermal velocities ($10^5 ms^{-1}$) ε_s should be the appropriate dynamic value of the relative permittivity rather than the static value.

For typical values of the parameters in equation (2.31) the barrier lowering is quite small (0.01 to 0.05eV). However, even a small effect like that can affect the Schottky barrier characteristics, especially the current emission mechanisms, with their exponential dependence on barrier height. The Schottky effect can be incorporated into the theory of thermionic emission by simply replacing ϕ_b by $\phi_b - \Delta\phi_{bi}$. The problem

that ϕ_{bi} is also dependent on the applied bias can be incorporated into the theory by a suitable choice of ideality factor n.

It should also be pointed out that holes in the semiconductor will experience a similar effect. However, in this case the image charge will be negative and its field will be of the same sign as the Schottky barrier field leading to an additional rise in the valence band edge. This effect is illustrated in Figure 2.10.

2.5.2 Effect of Potential Step

When an electron crosses the interface from the semiconductor into the metal, the energy associated with its motion in the x direction, that is normal to the boundary, is increased by amount equivalent to the barrier height $|e|\phi_b$. This sets a minimum value for the x component of velocity in the metal given by:

$$v_{x_{min}}^2 = \frac{2|e|\phi_b}{m} \tag{2.32}$$

The component of velocity parallel to the interface will not be affected in moving from the semiconductor into the metal. The angle at which the injected electron will travel to the normal is simply defined by:

$$\tan\theta = \frac{v_{\parallel}}{v_x} \tag{2.33}$$

so if an elelctron of a particular energy is considered, there is a maximum value of θ, corresponding to the case where the velocity is

initially parallel to the interface, given by:

$$\theta_{max} = \tan^{-1}\left(\frac{|v|}{v_{x_{min}}}\right) \quad (2.34)$$

Assuming a Maxwellian distribution of electrons crossing the interface and using typical values for a Schottky barrier, equation (2.34) can be used to obtain a value of $\theta_{max} = 5°$. Therefore it can be expected that electrons injected from the semiconductor into the metal will be funnelled into a cone, 5° to the interface normal.

2.5.3 Minority Carrier Injection

In considering the minority carrier current in a Schottky barrier, we must look at the process by which holes will be able to travel from the metal into the semiconductor valence band. Assuming that the diffusion length for holes in the semiconductor is larger than the depletion region, and that as a result the hole quasi Fermi level is constant there (Rhoderick[25]), it is possible to calculate the hole injection rate using standard p-n junction theory. This can be understood by virtue of the fact that, with the constant quasi Fermi level, the actual shape of the depletion region is irrelevant and it is the magnitude of the potential barrier to holes that is important. Figure 2.8 illustrates the behaviour of the hole quasi Fermi level believed to occur in the Schottky barrier. Comparison to a p-n junction can be made using Figure 2.1(b).

With reference to equation (2.2) the hole injection current can be written as:

$$J_p = \frac{|e|D_p p_n}{L_p}\left[\exp\left(\frac{|e|V}{kT}\right) - 1\right] \qquad (2.35)$$

where D_p is the hole diffusion constant, L_p is the hole diffusion length, and p_n the bulk hole concentration in the n type semiconductor.

The contribution of the hole injection to the total current can be readily found by introducing the minority carrier injection ratio defined by:

$$\gamma = \frac{J_p}{J_p + J_n}$$

$$\gamma \approx \frac{J_p}{J_n} \quad \text{if } J_n \gg J_p \qquad (2.36)$$

Using thermionic emission theory to describe the majority carrier current, J_n is given by equation (2.19). Substituting for J_n and J_p in equation (2.36) and writing $p_n = n_i^2/N_D$, we obtain:

$$\gamma = \frac{|e|D_p n_i^2}{N_D L_p A^* T^2 \exp\left(\frac{-|e|\phi_b}{kT}\right)} \qquad (2.37)$$

where A* is the Richardson Constant (defined in equation (2.19)), T is the temperature and n_i is the intrinsic electron concentration of the semiconductor.

At low current densities Yu and Snow[26] found that equation (2.37) described well the minority carrier injection ratio in Au/Si devices. However they also noticed that, at higher currents, γ began to rise with the total current J. This followed to some degree, the prediction of Scharfetter[27] that, due to the drift component in the hole current, γ would rise with J once it approached a critical value defined by:

$$J_c = \frac{|e| D_N N_D}{L_n} \tag{2.38}$$

However, they did not go to sufficiently high currents to see whether Scharfetter's[27] further prediction that γ would vary linearly with J was experimentally verifiable. In elaborating on Scharfetter's [27] theory, Green and Schewchum[28] deduced that that there would be a limit to the growth of γ due to partly to high level injection effects and partly to a limit in the supply of holes at the interface. Unfortunately the results of Yu and Snow[26] were in the wrong range to test the validity of this theory as well.

However, the effects described by Scharfetter[27] and Green and Schewchum[28] are unlikely to be observed in the majority of devices as the value of J_c is very high, being of the order of $10^6 Am^{-2}$. It is therefore to be expected that the minority carrier injection ratio will be of the form of equation (2.37)

2.6 METAL-INSULATOR-SEMICONDUCTOR DEVICE THEORY

In introducing the MIS diode in Section 2.2.3 it was mentioned that

with the inclusion of an insulator between the metal and the semiconductor, part of the applied bias would be dropped across the insulator, leading to a rise in the semiconductor barrier height ϕ_b. Figure 2.11 illustrates the band diagram expected for an MIS device under forward bias, with the applied voltage leading to a reduction in both the diffusion potential V_D and the potential across the insulator Δ. A consequence of having an appreciable insulating layer is that any semiconductor surface states will not be able to communicate so easily with the metal and any pinning of the surface neutral point ϕ_o (see Section 2.3.2) will not be as strong. The value of ϕ_b will vary more freely with the applied bias. At the other extreme if all the interface states communicate solely with the semiconductor then it is to be expected that ϕ_o will follow the semiconductor Fermi level and vary linearly with the applied voltage V.

The analysis of the MIS diode will, therefore, differ from that of the Bardeen model for the Schottky barrier in a number of respects. Compared to the Schottky barrier, the insulating layer of the MIS diode will be thicker. This will necessitate the inclusion of carrier transport through the insulator in the theory as well as considering the behaviour of the surface states. Also, even if there is good communication between the surface states and the metal, the larger insulator thickness will lead to values of Δ which are not negligible in contrast to the Schottky barrier case.

The behaviour of an ideal MIS diode has been considered by a number of authors[29, 31,32,35], whose work will be reviewed in the following sections. The term "ideal" is used to indicate that current transport through the insulators is by quantum mechanical tunnelling and that in

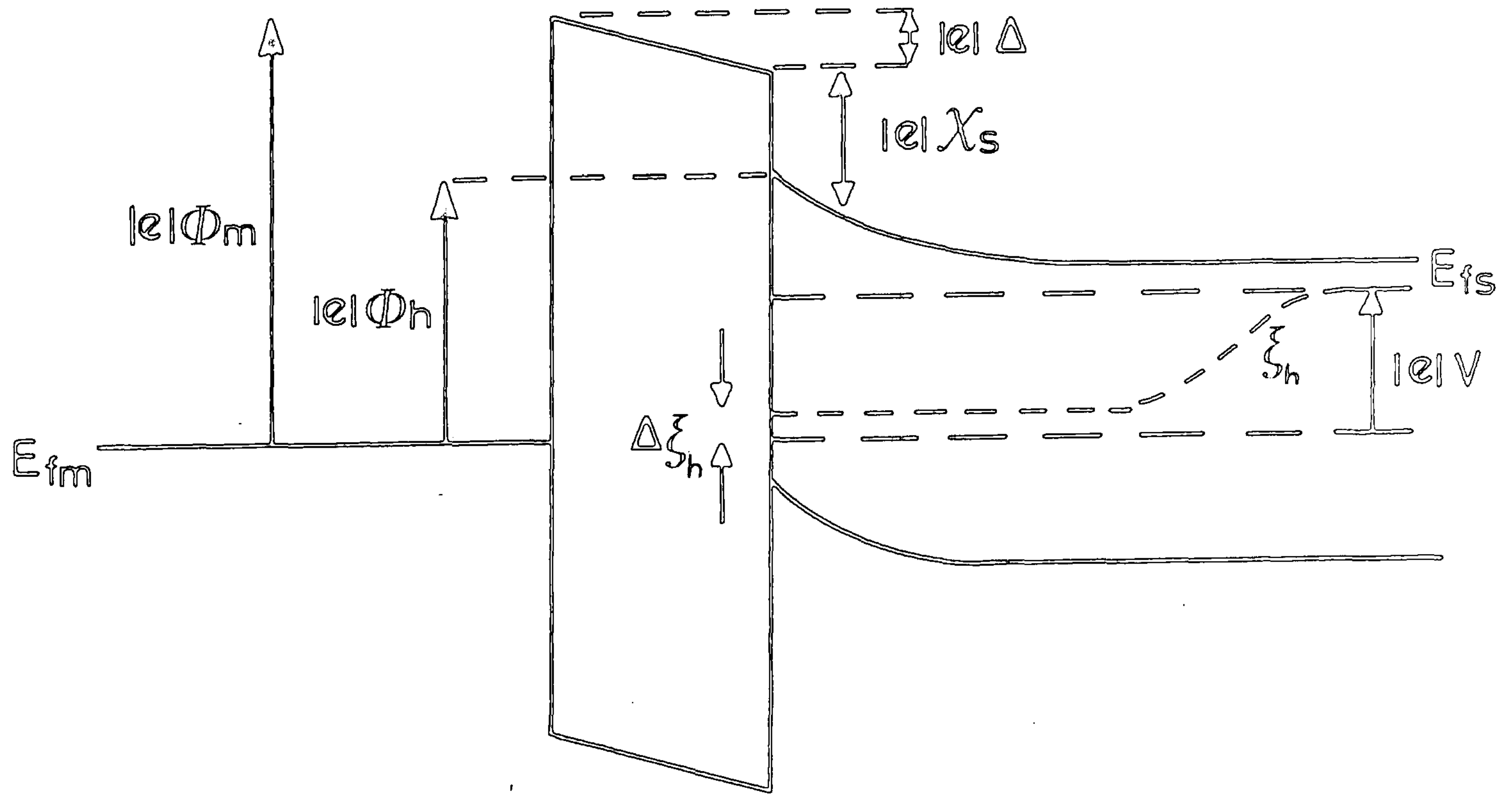

Fig. 2.11 : The MIS diode under forward bias.

all respects the insulator is perfect. This naturally means that the insulator, although being thick enough to affect the system and in particular the band alignment, must also be thin enough to allow a significant tunnelling current. This last point will restrict insulator thicknesses to values less than approximately 100Å.

2.6.1 Current-Voltage Characteristics

When an insulator is present, the transmission coefficient of carriers through the insulator must be also included in any theory of current-voltage characteristics. Card and Rhoderick[29] considered this problem and, by using the approximation of a rectangular insulator barrier, produced an expression for the current, which is in effect a modification of the thermionic emission equation for a Schottky barrier (equation (2.22)).

$$J_n = A^*T^2 \exp(-X^{\frac{1}{2}}\delta) \exp\left(\frac{-|e|\phi_b}{kT}\right)\left[\exp\left(\frac{|e|V}{nkT}\right) - 1\right] \qquad (2.39)$$

where X is the average height of the insulator barrier to electrons (measured in eV) given by

$$X = \tfrac{1}{2}((\phi_m - \phi_b) + X_s) \qquad (2.40)$$

and δ is the insulator thickness (measured in Angstoms). The use of these units is essential as there is a constant (of dimensions $eV^{-1}Å^{-1}$) in the relevant exponential term, which has been omitted as it is approximately unity in these units.

It is of interest here to point out that the approximation to a rectangular barrier used above is not completely necessary. Using the WKB approximation, as Card and Rhoderick[29] did in their argument, the tunnelling transmission coefficient can be written as:

$$T = \exp\left[-2 \int_{0}^{\delta} \left(\frac{2m|e|X'(x)}{h^2} \right) dx \right] \qquad (2.41)$$

where $X'(x)$ is the height of the barrier to electrons at a distance x from the semiconductor-insulator interface. The integral in equation (2.41) is straightforward and gives:

$$T = \exp\left[-2 \left(\frac{2m|e|}{h^2} \right)^{\frac{1}{2}} \frac{2}{3} \left[\frac{(\phi_m - \phi_b)^{3/2} - X_s^{\,3/2}}{\phi_m - \phi_b - X_s} \right] \delta \right] \qquad (2.42)$$

If δ is expressed in Angstroms, this can be re-written as

$$T \sim \exp\left(\frac{-2}{3} \left[\frac{(\phi_m - \phi_b)^{3/2} - X_s^{\,3/2}}{\phi_m - \phi_b - X_s} \right] \delta \right) \qquad (2.43)$$

It would seem, therefore, that rather than use equation (2.40) to define X, it would be more accurate to write:

$$X^{\frac{1}{2}} = \frac{2}{3} \left[\frac{(\phi_m - \phi_b)^{3/2} - X_s^{\,3/2}}{\phi_m - \phi_b - X_s} \right] \qquad (2.44)$$

As mentioned in the introduction to this section, it is to be expected that the dependence of the barrier height ϕ_b on voltage will be affected by the inclusion of the insulating layer. Card and Rhoderick[29]

also addressed this problem. To account for the fact that the communication of surface states with the semiconductor Fermi level would now be relatively more important (due to the insulator impeding transport to and from the metal) they divided the interface states into two species. The first, of density D_{sa}, communicated only with the metal, and the second, of density D_{sb}, only with the semiconductor. Using the differential form of equation (2.21)

$$\frac{d}{dV} (\phi_b(V) - \phi_b(o)) = \frac{1}{n} - 1 \tag{2.45}$$

Card and Rhoderick[29] found the theoretical ideality factor for electrons to be of the form:

$$n_e = 1 + \frac{(\delta/\varepsilon_i \varepsilon_o)(\varepsilon_s \varepsilon_o/W + |e|D_{sb})}{1 + (\delta/\varepsilon_i \varepsilon_o)|e|D_{sa}} \tag{2.46}$$

where W is the width of the depletion region. Two limiting cases for this expression are $D_{sb} >> D_{sa}$ for thick insulators. In the first case the ideality factor reduces to:

$$n_e \sim 1 + \frac{\delta \varepsilon_s \varepsilon_o}{W (\varepsilon_i \varepsilon_o + \delta|e|D_{sa})} \tag{2.47}$$

while for the thick insulating layer

$$n_e \sim 1 + \frac{\delta}{\varepsilon_i \varepsilon_o} \left(\frac{\varepsilon_s \varepsilon_o}{W} + |e| D_{sb} \right) \tag{2.48}$$

2.6.2 Minority Carrier Injection

Minority carrier injection was also considered, in some detail, by Card and Rhoderick[35] who found that their theory corresponded well with their experimental results from Au/SiO_2/Si MIS diodes. Their analysis covered two cases. The first was concerned with very thin insulators and the second with thicker oxide layers. We will deal with these two cases separtely.

a) Thin Insulating Layer

The term "thin" is used to denote insulators through which holes (and electrons) can readily tunnel. This being the case, the minority carrier injection current is limited by the diffusion rate of holes into the semiconductor bulk.. The situation is therefore very similar to minority carrier injection in a simple Schottky barrier (see Section 2.5.3). The major difference in this case is that a significant change in the value of the quasi hole Fermi level can be expected across the insulator. This is depicted in Figure 2.11. For very thin insulators, the difference $\Delta\xi_p$ will be small because of the high tunnelling transmission constant ($\sim$1). However if the insulator thickness δ is increased, the value of $\Delta\xi_p$ will become significant.

Taking account of the change in the hole quasi Fermi level across the insulator a revised form of equation (2.35) is found:

$$J_p = \frac{|e|D_p p_n}{L_p}\left[\exp\left(\frac{|e|V - \Delta\xi_p}{kT}\right) - 1\right] \qquad (2.49)$$

By assuming that $\Delta\xi_p$ varies linearly with V, Card and Rhoderick[35] re-wrote this in the form:

$$J_p = \frac{|e|D_p p_n}{L_p}\left[\exp\left(\frac{|e|V}{n_h kT}\right) - 1\right] \qquad (2.50)$$

where now an ideality factor for holes, n_h, has been introduced. For thin insulators, therefore, the MIS diode acts very much like an imperfect Schottky diode, the minority carrier injection ratio for which has already been given in Section 2.5.3.

b) Thick Insulating Layers

For thicker insulators the tunnelling rate through the insulating layer will be the limiting factor for hole injection into the semiconductor assuming no other transport mechanism exists. Stratton's equation for the tunnelling current through an MIM barrier gives:

$$J_p = \left(\frac{4\pi m_h |e|}{h^3}\right)\int_{-\infty}^{\infty}[f_m(E) - f_s(E)]\int_0^E T(E_x)\, dE_x dE \qquad (2.51)$$

where $f_m(E)$ and $f_s(E)$ are the occupancy functions in the metal and semiconductor respectively, $T(E_x)$ is the tunnelling transmission coefficient and E_x is the energy associated with motion in the x direction. The x direction is defined as being normal to the barrier interface. Following the procedure used to analyse the majority carrier current[29] (reviewed here in Section 2.6.1) Card and Rhoderick[35] approximated the insulator barrier to a rectangular barrier by using an average barrier height to holes χ_h. Using this approximation the hole current

density can be written as :

$$J_p = \left(\frac{4\pi m_h |e|}{h^3}\right) \exp\left(-X_h^{\frac{1}{2}}\delta\right) \int_0^{\infty} E\left(f_s(-E) - f_m(-E)\right) dE \qquad (2.52)$$

As was pointed out in Section 2.6.1, the use of the average value X_h is unnecessary. Using a WKB approximation for the sloping barrier, illustrated in Figure 2.11, and following the same procedure as Section 2.6.1, an effective value for X_h can be found:

$$X_h = \frac{2}{3}\left(\frac{(E_{gi} - E_g - X_s)^{3/2} - (E_{gi} - E_g - \phi_m + \phi_b)^{3/2}}{\phi_m - \phi_b - X_s}\right) \qquad (2.53)$$

where E_{gi} is the band gap of the insulator in units of eV.

Card and Rhoderick[35] observed that equation (2.52) cannot be solved in closed form and considered equation (2.52) in three separate cases. With V_h being defined as the bias required to raise the semiconductor valence band edge to the same energy as the metal Fermi level, expressions for the hole current density were obtained for the conditions 1) $V < V_h$; 2) $V = V_h$ and 3) $V > V_h$. Using equations (2.39) to give the electron current, equation (2.36) was used to give the majority carrier injection ratio as:

1) $$\gamma = \left(\frac{|e| D_p N_v}{L_p A^*}\right) \exp\ (-\chi^{\frac{1}{2}}\ \delta)\ \exp\left(\frac{|e|(\phi_b - V_h)}{kT}\right)$$

$$\times\ \exp\left[\ |e| V \left(\frac{1}{n_h} - \frac{1}{n_e}\right) \Big/ kT \right]$$

$(V < V_h)$

2) $$\gamma = \frac{m_h}{m_e} \exp\ ((\chi^{\frac{1}{2}} - \chi_h^{\frac{1}{2}})\ \delta)\ \exp\left(\frac{|e|\phi_b}{kT}\right)$$

$$\times\ F_{\ell}\left(\frac{|e|\ (V - V_h)}{kT}\right)$$

where $$F_j(x) = \frac{1}{\Gamma(j+1)} \int_0^{\infty} \frac{y^j}{1 + \exp\ (y - x)}\ dy$$

$(V \doteq V_h)$

3) $$\gamma = \frac{m_h}{2m_e} \left(\frac{|e|}{kT}\right)^2 \exp\ (\chi^{\frac{1}{2}}\delta_e - \chi_h^{\frac{1}{2}}\delta_h)$$

$$\times\ \exp\left(\frac{|e|\phi_b}{kT}\right)\ (V - V_h)^2 \qquad (2.54)$$

$(V > V_h)$

Effective barrier thicknesses for holes and electons (δ_h and δ_e) were introduced in Case 3 as it was argued that under high biases the electron would not have to tunnel across the whole barrier. For $\phi_b > \phi_m$ the electrons would just tunnel across part of the barrier and then enter the insulator conduction band.

The analysis of Card and Rhoderick[35] must be treated with some caution as it assumes that the insulator is perfect and the only carrier tranport process through it is quantum mechanical tunnelling. For a less than perfect insulator, this will not be the case. There will be the possibility of other current mechanisms due to, for example, defect states. it is also likely that the alternative current mechanisms will not be as sensitive to insulator thickness. In testing their theory by experiment, Card and Rhoderick[35] found that Au/sputtered SiO_2/Si diodes underwent a forming process, leading to an irreversible rise in current at a threshold voltage of around 1.5eV. The largest value of γ for such devices was obtained at insulator thicknesses of around 80Å compared with 30Å for similar devices[35] where the oxide layer was produced thermally. The efficiency of the sputtered devices was also observed to be less dependent on insulator thickness than those with thermally grown oxides. Card and Rhoderick's theory for the MIS diode[29.35] must, therefore, be treated with some degree of caution, when applying it to particular devices, as tunnelling might not be the dominant transport process across the insulator.

2.7 SUMMARY

Chapter Two forms a basic introduction to the Schottky barrier and MIS diode. After a brief introduction to the various forms of electroluminescent device, the Schottky barrier was reviewed in some detail and, in particular, the Bardeen model and thermionic emission were discussed. This theory was then extended to take into account the inclusion of an

insulating layer to produce an MIS diode. It was shown that the MIS structure could be used to obtain an enhanced minority carrier injection ratio and hence a greater electroluminescent efficiency. It was observed, however, that this part of the theory would not be accurate if a less than ideal insulator were used. This point will be raised again later in the work, particularly in Chapters Five and Six.

CHAPTER THREE

A BRIEF REVIEW OF MIS LIGHT EMITTING DIODES

3.1 INTRODUCTION

In Chapter Two the theory developed by Card and Rhoderick[1], to model the behaviour of an MIS diode, and in particular to describe the minority carrier injection ratio, was discussed. However, the idea of using a thin insulating layer between the metal and the semiconductor of a Schottky barrier had been used well before the work of Card and Rhoderick[1,2]. Electroluminescence was first reported in MIS devices by Fischer and Moss[3], and Jaklevic et al[4].. These devices, which both used CdS as the semiconductor, incorporated insulators of tunnellable dimensions. It was Jaklevic et al[4] who proposed tunnel-injection of minority carriers to explain their results.

In fabricating their Au/SiO_2/Si devices Card and Rhoderick[1] employed two different methods of producing the insulator. The tunnelling injection theory of the authors was successful in explaining the behaviour of their diodes when the insulator was produced thermally, by making the sample in dry oxygen. An optimum minority carrier injection ratio was found at an insulator thickness of ~ 40Å. In contrast, for r.f. sputtered films, they found that the effect of changing the insulator thickness has much less effect on the minority carrier injection ratio and that an optimum insulator thickness was then found to be ~ 80Å. This behaviour was attributed to an alternative hole transport mechanism, which was

associated with a 'forming' process taking place in the insulating film.

Since the work of Fischer and Moss[3] and Jaklevic et al[4] there have been numerous reports of the fabrication of MIS diodes[5-10], the characteristics of which have all been explained in terms of an enhanced minority carrier injection due to the ability of the semiconductor valence band to move with respect to the metal Fermi level. However, it has been found, that it is possible to produce diodes with optimum insulator thickness much in excess of those allowing significant direct tunnelling[11-18, 22-25]. These devices are of particular interest to this work and are dealt with here in more detail.

3.2 'THICK INSULATOR' MIS DIODES

3.2.1 MIS Devices Incorporating II-VI Semiconductors

Diodes incorporating II-VI semiconductors have been fabricated which seem to behave according to Card and Rhoderick's theory of tunnel injection. However, there have been a number of devices produced using II-VI materials whose behaviour cannot be explained using the same model. Livingstone et al[11] produced an Au/ZnO/ZnS device which had an enhanced quantum efficiency at insulator thicknesses in excess of 500 Å (Figure 3.1) Driving their device at a constant current of 20mA (a current density of approximately 500Am^{-2}), they found the quantum efficiency rose sharply as the insulator thickness was increased to ~500 Å. After this point however, the efficiency stayed on a plateau with any further increase in insulator thickness appearing to have little effect.

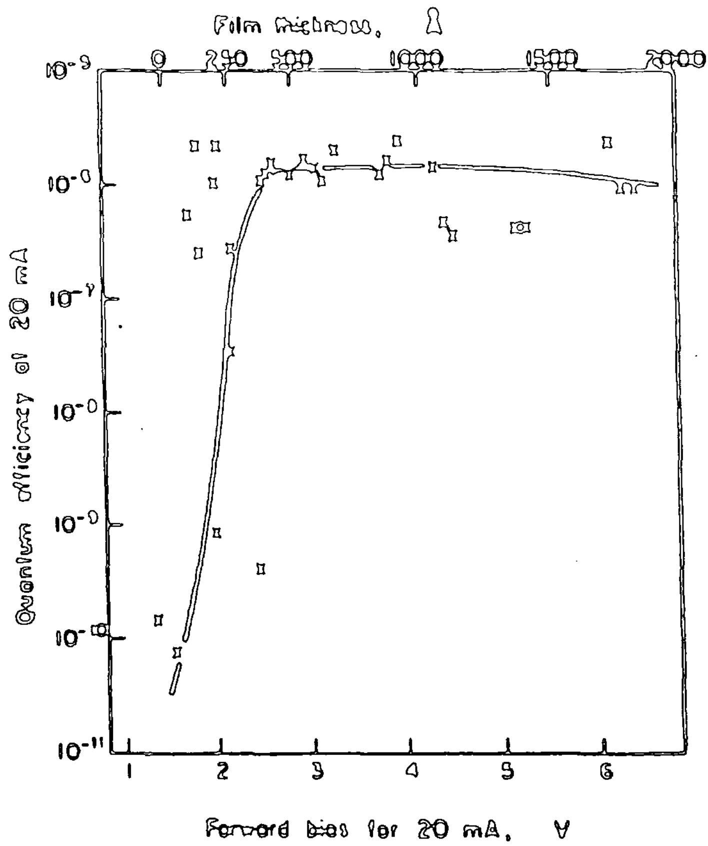

Fig. 3.1 : The variation of quantum efficiency with insulator thickness in Au/ZnO/ZnSe diodes (Reference 11).

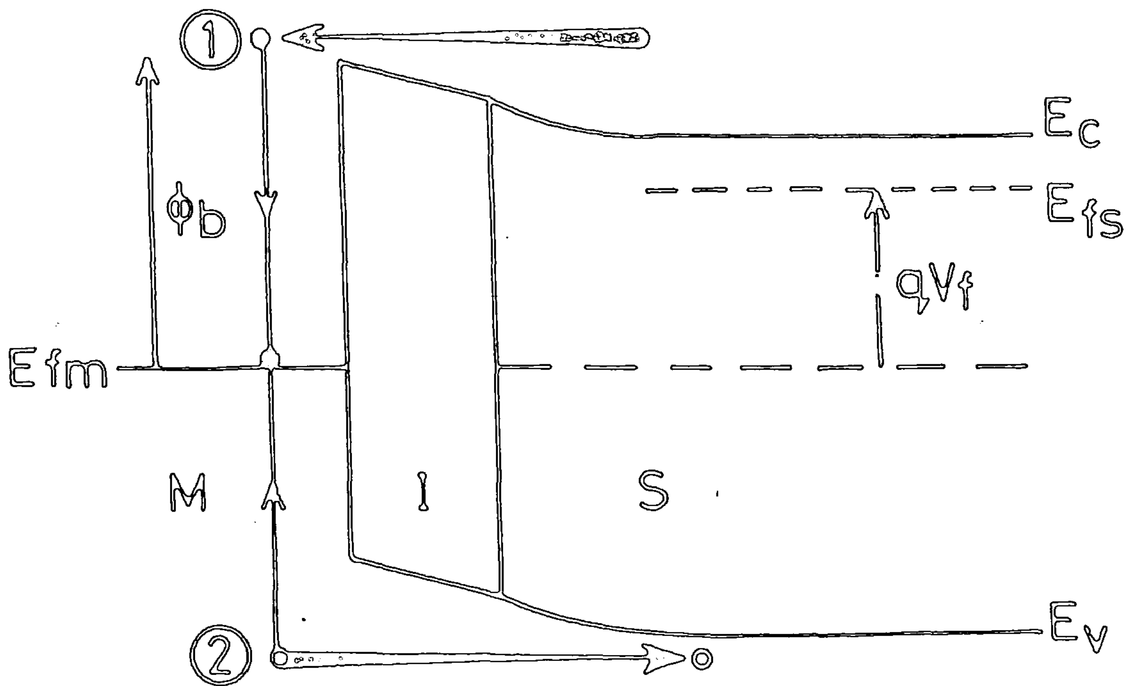

Fig. 3.2 : The hole creation mechanism proposed for II-VI MIS diodes.

Following Livingstone et al[11], similar observations were made by different groups[12-16]. working with II-VI materials. For constant current a plateau or broad peak in the efficiency of the devices was found for insulator thicknesses of the order of several hundred Angstroms. An explanation for this idea was first put put forward by Fischer[17] and later by Watanabe et al[12]. The argument rested on the fact that the insulators used in the fabrication of these devices had bandgaps which were not much larger than the semiconductor bandgaps. In some cases[16], the same material was used for both the semiconductor and the insulator by suitable doping. Such a device, under forward bias is illustrated in Figure 3.2. The basic mechanisms proposed concerned the ability of electrons (semiconductor majority carriers), injected from the semiconductor into the metal, to excite electrons from below the metal Fermi level - essentially an impact ionisation process. It was suggested that this mechanism would lead to a relatively large hole population below the metal Fermi level some of which could pass via the insulator valence band into the semiconductor valence band. In the semiconductor valence band, the holes would recombine radiatively with majority carrier electrons. The idea of holes travelling unimpeded through the insulator valence band explained the relative insensitivity of the efficiency with insulator thickness after a certain threshold.

Further support for this model was given by the observation[16] that the efficiency of devices was dependent on the height of the metal-insulator barrier. With this in mind, the novel material polymeric sulphur nitride ($(SN)_x$) has been used as the metal[18]. (SN_x), which acts as a quasi 1D metal[19], produces barrier heights $\sim$ 0.75eV greater than conventional diodes incorporating gold or ZnS. Experiments have shown that a 10^2 increase in the electroluminescent efficiency

accompanies the use of (SN_x). Even with this improvement, however, the quantum efficiencies obtained have only been of the order of 10^{-4}. The reason for this being attributed to the basic inefficiency of the hole creation mechanism.

It appears that, in the II-VI MIS diodes discussed in this section, the main limitation to a good majority carrier injection ratio is the hole creation mechanism itself. Despite the fact that impact ionisation has been proposed as the hole creation mechanism, nobody has actually attempted to calculate the hole creation rate by this process. In the next chapter this impact ionisation process is examined in some detail. In particular the probability of an injected elelctron creating a hole below a certain energy (say the insulator valence band edge) is calculated.

3.2.2 MIS Devices Incorporating Langmuir-Blodgett Films

Langmuir-Blodgett films[20] can be utilised to produced high quality thin insulating layers of uniform thickness. There are a number of applications of these films, which have been reviewed by Vincett and Roberts[21]. However, of particular relevance to this work is the use of Langmuir-Blodgett films as the insulator in an electroluminescent MIS diode[22-25].

MIS diodes incorporating a number of different materials, in the form of Langmuir-Blodgett films, have been produced[22-25]. The initial work[22] was carried out using cadmium stearate and ω-tricosenoic acid in an Au/Langmuir-Blodgett film/n-GaP device.

The idea behind this methodwas that, with good insulating film

uniformity, tunnelling MIS diodes (described by the theory of Card and Rhoderick[1,2]) of high quality would be produced. However, measurements of the d.c. power conversion ratio, indicate that this was not the case. Figure 3.3 is taken from reference 23 and shows the relative efficiency of a device, incorporating cadmium stearate monolayers, driven at a constant current of 200mA. It is clear that the optimum insulator thickness occurs at about 8 monoloayers, or approximately 200Å , a value too large for direct tunnelling. Figure 3.4 shows the power conversion efficiency for a similar device reported in reference 24. Again, the optimum thickness is too large to consider direct tunnelling as a viable transport mechanism through the insulator. Batey et al[23] suggested that their results might be due to the impact ionisation process proposed in the last section for II-VI devices[12,17]. They also suggested[24] that the minority carrier transport through the insulator could instead be via traps which are known to dominate bulk transport properties of Langmuir-Blodgett films[21].

Although for both II-VI and Langmuir-Blodgett film insulators the thicknesses are greater than those allowing direct tunnelling, it should be stressed that there is little similarity in the insulators used in the two cases. The II-VI insulators have a well defined semiconductor type band structure with a relatively small bandgap. This makes minority carrier transport via the insulator valence band a distinct possibility. The band structures of Langmuir-Blodgett films are, on the otherhand, unknown. Even if some valence band does exist, the bandgap may be too large to allow its use in the hole transport mechanisms. For this reason, the minority carrier mechanism could be very different from that in II-VI insulators. In Chapter Six, possible hole transport

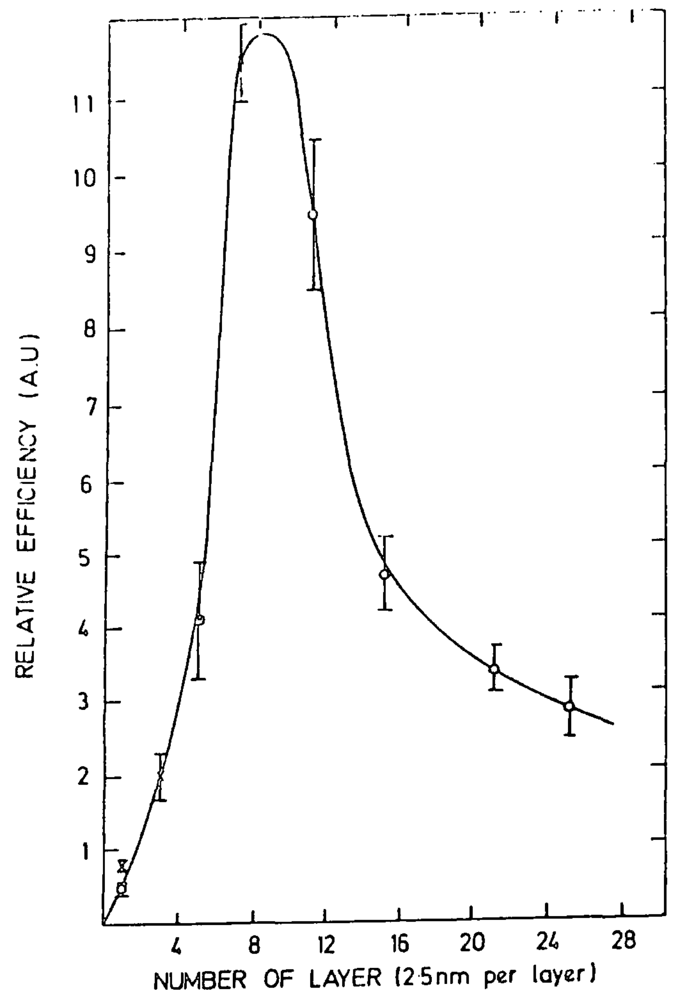

Fig. 3.3 : dc power conversion ratio versus insulator thickness for $Au/CdSt_2/GaP$ MIS diodes (Reference 23).

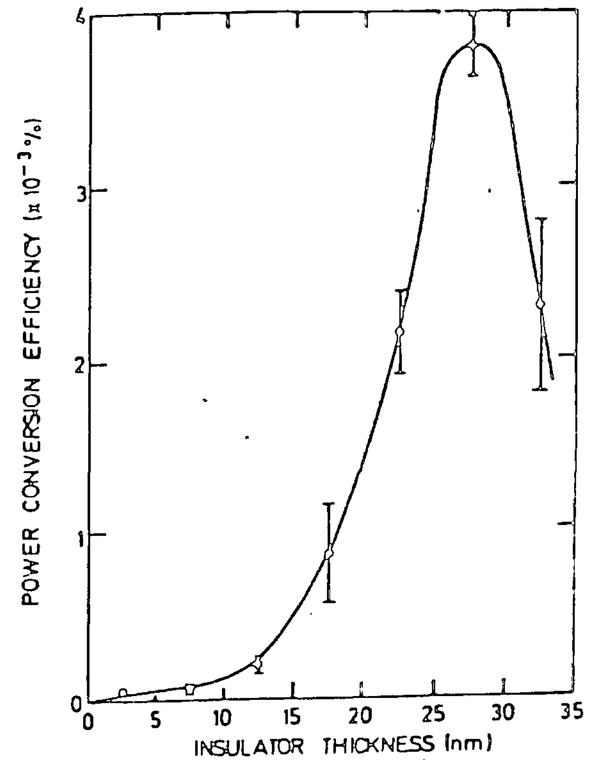

Fig. 3.4 : dc power conversion ratio versus insulator thickness for $Au/CdSt_2/GaP$ MIS diodes (Reference 24).

mechanisms, for both the Langmuir-Blodgett film and II-VI device will be investigated. Models for minority carrier injection in the respective MIS diodes will then be proposed.

CHAPTER FOUR

HOLE CREATION IN THE METAL CONTACT OF AN MIS DIODE BY IMPACT IONISATION

4.1 INTRODUCTION

The purpose of this chapter is to investigate impact ionisation between the electrons of the metal and the electrons (semiconductor majority carriers) injected into the metal when the MIS structure is under forward bias. As already mentioned in Chapter Three the impact ionisation process has been proposed by Watanabe[1] and Lawther and Woods[2] as a possible hole creation process with the injected electrons exciting some of the electrons of the metal to unoccupied states above the Fermi level and in the process leaving holes in states below the Fermi level. The energy of the incident electron relative to the Fermi level gives a limit to the range of possible hole states as energy must be conserved and the incident particle can only be scattered to a state which is initially unoccupied (ie above the Fermi level). This consideration sets a maximum possible energy transfer between the electrons and in the particular device we are considering with the majority of the electrons injected from the semiconductor into the metal, having just enough energy to surmount the barrier, holes can only be created in this fashion at a maximum energy below the Fermi level equivalent to the barrier height. In this chapter the created hole distribution over the allowed energy range is calculated using perturbation theory. A

particular result obtained is the probability of hole production within a certain energy range and direction. The interaction of a hot electron in a Fermi gas has been investigated before by Ritchie[3], Quinn[4], and Ashley and Ritchie[5]. However none of these authors have looked specifically at the hole creation process and its dependence on hole energy and wavevector. This knowledge facilitated the calculation of the probability of an electron injected into the metal producing a hole in a particular energy range which is able to travel back to the injection interface. It turns out that the hole flux due to this impact ionisation mechanism is significant in the system which we are looking at for states more than 0.5eV below the Fermi level, but for smaller energies the holes created thermally will dominate.

4.2 FREE ELECTRON GAS MODEL

4.2.1 Gold as a Free Electron Gas

Gold is used extensively in the fabrication of Schottky barriers and the MIS devices reviewed in Chapter Three, and in particular is the metal incorporated into the devices considered in this work.

Being a monovalent metal, gold has one of the simpler Fermi surfaces enclosing a volume of k space which contains just one electron per atom. Distinguishing between the noble and the alkali metals it is the latter which have the less complex surfaces and they can be described very accurately using the Sommerfeld free electron model. The noble metals are more complex, but again the Fermi surface is essentially spherical with a distortion in the 111 direction where

the Fermi surface makes contact with the Brillouin zone face. The important point is that the Fermi surface is sufficiently spherical to make it possible, at least in the first approximation, to model its electronic behaviour using free electron theory.

4.2.2 Electron-Electron Interactions

The electrons in the Fermi gas of a metal will have Coulombic interactions with each other and with electrons injected into the metal. If we consider the interaction between two particular electrons, immersed in a background sea of other electrons, the interaction between the two can be thought of as a small perturbation $\nu(\underline{r})$ to the overall potential. Using standard perturbation theory it is possible to show that given the electrons are in a particular state described by the wavefunction $\psi(\underline{r})$ at time zero, the probability that they occupy the states represented by $\psi'(\underline{r})$ after a time t is given by:

$$\text{Prob} = \frac{2\pi t}{\hbar} |\langle\psi'(\underline{r})|\ \nu(\underline{r})|\ \psi(\underline{r})\rangle|^2\ \delta(E - E') \tag{4.1}$$

where E and E' in the Dirac delta function represent the initial and final energies of the two particle system. The transition rate for this particular interaction can now be found by differentiating equation (4.1) with respect to time to yield:

$$TR = \frac{2\pi}{\hbar} |\langle\psi'(\underline{r})|\ \nu(\underline{r})|\ \psi(\underline{r})\rangle|^2\ \delta(E - E') \tag{4.2}$$

which is known as Fermi's Golden Rule Number 2.

In the next section the matrix element $\langle \psi'(\underline{r}) | \nu(\underline{r}) | \psi(\underline{r}) \rangle$ is considered in more detail for the two electron systems we are investigating.

4.3 MATRIX ELEMENTS

4.3.1 Initial and Final Wavefunctions

Before the transition takes place consider the two interacting electrons at positions $\underline{r}_1$ and $\underline{r}_2$, to be in electron states 1 and 2 with associated spins σ_{s1} and σ_{s2}. The initial wavefunction for the system must be expressed as an antisymmetrical combination of the two possible states. Hence

$$\psi = \frac{1}{\sqrt{2}} \left(\phi_1(\underline{r}_1)\, \sigma_{s1}(1)\, \phi_2(\underline{r}_2)\sigma_{s2}(2) - \phi_1(\underline{r}_2)\, \sigma_{s1}(2)\, \phi_2(\underline{r}_1)\, \sigma_{s2}(1) \right) \tag{4.3}$$

where $\phi_1(\underline{r}_1)$ represents the spatial wavefunction of an electron in state 1 at position $\underline{r}_1$ and $\sigma_{s1}(1)$ describes its z component of spin ($s_1 \equiv \uparrow$ or $\downarrow$). An identical convention holds for the rest of the terms.

Using a similar argument for the scattered electrons the final wavefunction for the system is:

$$\psi' = \frac{1}{\sqrt{2}} \left(\phi_{1'}(\underline{r}_{1'})\sigma_{s1'}(1)\phi_{2'}(\underline{r}_{2'})\sigma_{s2'}(2) - \phi_{1'}(\underline{r}_{2'})\sigma_{s1'}(2)\,\phi_{2'}(\underline{r}_{1'})\,\sigma_{s2'}(1) \right) \tag{4.4}$$

4.3.2 Evaluation of the Matrix Element

By using equations (4.3) and (4.4) in the matrix element the expression obtained is

$$M = \frac{1}{2}\int \left(\phi^*_{1'}(\underline{r}_1)\phi^*_{2'}(\underline{r}_2)\sigma_{s1'}(1)\sigma_{s2'}(2) - \phi^*_{1'}(\underline{r}_2)\phi^*_{2'}(\underline{r}_1)\sigma_{s1'}(2)\sigma_{s2'}(1)\right)^*$$
$$\times\ \nu(\underline{r})\left(\phi_1(\underline{r}_1)\ \phi_2(\underline{r}_2)\sigma_{s1}(1)\sigma_{s2}(2) - \phi_1(\underline{r}_2)\phi_2(\underline{r}_1)\sigma_{s1}(2)\sigma_{s2}(1)\right)$$
$$\times\ d^3\underline{r}_1\, d^3\underline{r}_2 \tag{4.5}$$

where the nature of the perturbing potential $\nu(\underline{r})$ has not yet been specified. Using the orthogonality of the spin functions

$$M = M_D - M_{ex} \tag{4.6}$$

where

$$M_D = \int \phi_{1'}{}^*(\underline{r}_1)\,\phi_{2'}{}^*(\underline{r}_2)\,\nu(\underline{r})\phi_1(\underline{r}_1)\phi_2(\underline{r}_2)\delta_{s1's1}\,\delta_{s2's2}\, d^3\underline{r}_1\, d^3\underline{r}_2 \tag{4.7}$$

and

$$M_{ex} = \int \phi_{1'}{}^*(\underline{r}_2)\,\phi_{2'}{}^*(\underline{r}_1)\nu(\underline{r})\phi_1(\underline{r}_2)\phi_2(\underline{r}_1)\delta_{s1's2}\,\delta_{s2's1}\, d^3\underline{r}_1\, d^3\underline{r}_2 \tag{4.8}$$

The subscripts D and ex standing for direct and exchange. The reason for this nomenclature is that M_D is identical to the expression

for the matrix element that would be obtained if the electrons were treated as distinguishable particles and we could completely specify the properties of each particle, whilst M_{ex} can be seen as an extra term resulting from the inclusion of exchange effects. We are now in a position to integrate equation (4.6) over space.

4.3.3 The Direct Matrix Element Term

As the evaluation of the M_D is a distinct part of the overall calculation of M, it is treated separately in this section.

The wavefunction of an electron in a free electron gas is simply a travelling wave given by:

$$\phi(r) = \frac{1}{\Omega^{\frac{1}{2}}} \exp(i\underline{k}.\underline{r}) \tag{4.9}$$

where $\underline{k}$ is its wavevector and Ω is the normalisation volume, so by using this form in equation (4.7) and introducing a Coulombic perturbing potential it becomes

$$M_D = \iint \phi^*_{1'}(\underline{r}_1)\phi^*_{2'}(\underline{r}_2) \frac{|e|^2}{4\pi\varepsilon\varepsilon_0|\underline{r}_1 - \underline{r}_2|} \phi_1(\underline{r}_1)\phi_2(\underline{r}_2) \times \delta_{s1's1}\delta_{s2's2} d^3\underline{r}_1 d^3\underline{r}_2 \tag{4.10}$$

The perturbing potential can be expressed in terms of its Fourier integral and the expression then integrated over $\underline{r}_1$ and $\underline{r}_2$ to produce

$$M_D \doteq \frac{|e|^2}{4\pi\varepsilon_o \Omega^2} \delta_{s_1's_1} \delta_{s_2's_2} \int \frac{4\pi}{\varepsilon(q)\ q^2} \delta(\underline{k}_{1'} - \underline{k}_1 - \underline{q})(2\pi)^3 \delta(\underline{k}_{2'} - \underline{k}_2 + \underline{q}) d^3\underline{q}$$

(4.11)

In this system the Coulombic potential varies slowly with respect to the electron wavelength and also the transition energies (of about 2eV) are much less than the plasmon energy (~10eV) so the electron gas can respond to the perturbation and the frequency dependent part of any screening is negligible. It is therefore adequate , in this case, to represent the screening in the form of the zero frequency Thomas-Fermi dielectric constant[8,9]

$$\varepsilon(q) = 1 + \frac{\lambda^2}{q^2} \qquad (4.12)$$

where λ is the Thomas-Fermi screening length which is defined as

$$\lambda^2 = \frac{a_o}{4}\left(\frac{\pi}{3n}\right)^{1/3} \qquad (4.13)$$

with a_o being the Bohr radius and n the electron concentration. So by substituting equation (4.12) into equation (4.11) and integrating over $\underline{q}$ we obtain our final expression for the direct matrix element

$$M_D = \frac{(2\pi)^3\ |e|^2}{\varepsilon_o\ \Omega^2} \frac{1}{(|\underline{k}_{1'} - \underline{k}_1|^2 + \lambda^2)} \delta(\underline{k}_{1'} + \underline{k}_{2'} - \underline{k}_1 - \underline{k}_2) \delta_{s_1's_1} \delta_{s_2's_2}$$

(4.14)

4.3.4 The Matrix Element Including Exchange

The term M_{ex} in equation (4.6) and defined by equation (4.8) can be evaluated in an identical manner to that for M_D in the last section and to avoid repetition the result will simply be quoted here as:

$$M_{ex} = \frac{(2\pi)^3|e|^2}{\varepsilon_o \Omega^2} \frac{1}{(|\underline{k}_{2'}-\underline{k}_1|^2 + \lambda^2)} \delta(\underline{k}_{1'}+\underline{k}_{2'}-\underline{k}_1-\underline{k}_2)\delta_{s2's1}\delta_{s1's2} \tag{4.15}$$

This can be immediately combined with equation (4.14) to give the total matrix element as:

$$M = \frac{|e|^2}{\varepsilon_o} \frac{(2\pi)^3}{\Omega^2} \left[\frac{\delta_{s1's1}\delta_{s2's2}}{|\underline{k}_{1'}-\underline{k}_1|^2+\lambda^2} - \frac{\delta_{s1's2}\delta_{s2's1}}{|\underline{k}_{2'}-\underline{k}_1|^2+\lambda^2} \right] \delta(\underline{k}_{1'}+\underline{k}_{2'}-\underline{k}_1-\underline{k}_2) \tag{4.16}$$

4.4 HOLE CREATION

4.4.1 Direct Transitions

The square of the modulus of the matrix element is actually needed to calculate the transition rate.

$$|M|^2 = M_D{}^2 + M_{ex}{}^2 - 2M_D M_{ex} \tag{4.17}$$

It can be seen that, with $M_D{}^2$ as the first term, the direct transition rate is produced as a distinct part of the overall rate and

so in this section it will be treated separately. There are in fact two reasons for this, apart from it being an integral part of the overall procedure it will enable the effects of exchange in the overall process to be observed and also let us compare results obtained in this method to previously published work by Quinn[4] which only considers direct transitions.

It is now possible to produce an expression for the probability of an incident electron on the metal producing a hole of particular energy and direction by finding the probability of an electron being excited from that state in the Fermi sphere.

Substituting the direct transition matrix element, given by equation (4.14) into equation (4.2) the transition rate is written as

$$TR = \left(\frac{|e|^2}{\varepsilon_0}\right)^2 \frac{(2\pi)^4}{\hbar\Omega^3} \frac{\delta_{s1's1}\delta_{s2's2}}{(|\underline{k}_{1'}-\underline{k}_1|^2+\lambda^2)^2} \delta(\underline{k}_{1'}+\underline{k}_{2'}-\underline{k}_1-\underline{k}_2)$$

$$\times\delta\left[\frac{\hbar^2}{2m}(\underline{k}_{1'}^{\,2}+\underline{k}_{2'}^{\,2}-\underline{k}_1^{\,2}-\underline{k}_2^{\,2})\right] \qquad (4.18)$$

This expression gives the transition rate between specified states. To find the total transition rate for an electron of wavevector $\underline{k}_1$ we need to sum over all possible $\underline{k}_{2'}$, $\underline{k}_2$ and $\underline{k}_{1'}$ states and all spin states, taking into account the occupancy of the states. We are concerned with finding the probability of a definite incident electron undergoing some interaction so its spin s1 is fixed, and by taking other spins into account equation (4.17) is simply multiplied by two

as states 2 and 2' can be either both up or both down, while 1' must be the same as 1. The Dirac delta function in $\underline{k}$ ensures that one summation over wavevector is trivial and then by converting the remaining wavevector summations to integrals and dividing by the incident electrons velocity, given by $\hbar k_1/m$, we have an expression for the inverse mean free path of that electron

$$\lambda_{DII} = 2\left\{\frac{2\pi m}{k_1}\left(\frac{|e|^2}{\hbar\varepsilon_0}\right)^2 \frac{1}{(2\pi)^6}\right\}\iint_{\underline{k}_{1'},\underline{k}_2} \frac{1}{(|\underline{k}_{1'} - \underline{k}_1|^2 + \lambda^2)^2}$$

$$\times\ \delta\left[\frac{\hbar^2}{2m}(\underline{k}_1{}^2 + \underline{k}_2{}^2 - \underline{k}_{1'}{}^2 - (\underline{k}_1 + \underline{k}_2 - \underline{k}_{1'})^2)\right] d^3\underline{k}_{1'} d^3\underline{k}_2 \qquad (4.19)$$

Where the subscript to λ refers to direct impact ionisation interactions.

If D is used to denote the term in the curly brackets and the substitutions

$$\underline{g} = \underline{k}_{1'} - \underline{k}_1 \quad \text{and} \quad \underline{h} = \underline{k}_{1'} - \underline{k}_2$$

made the differential inverse mean free path with respect to $\underline{k}_2$ is

$$\frac{d^3\lambda^{-1}_{DII}}{d^3\underline{k}} = 2D\int_{\underline{k}_{1'}} \frac{1}{(g^2 + \lambda^2)^2}\ \delta\left[\frac{\hbar^2}{m}\ \underline{h}\cdot\underline{g}\right] d^3\underline{k}_1 \qquad (4.20)$$

Because of the delta functions, it can be seen that the integral is only non-zero when the scalar product $\underline{h}\cdot\underline{g}$ is zero, or in other words

when $\underline{h}$ and $\underline{g}$ are orthogonal. This means that, in $\underline{k}$ space, $\underline{k}_1$, $\underline{k}_2$ and $\underline{k}_{1'}$ all lie on the surface of a sphere of diameter $|\underline{k}_1 - \underline{k}_2|$ centred at $\frac{1}{2}|\underline{k}_1 + \underline{k}_2|$. This has been illustrated in Figure 4.1. If $\underline{k}_2$ is kept constant initially, it is reasonable to exploit the symmetry of the situation by moving the origin of the integration from the centre of the Fermi sphere to $\frac{1}{2}|\underline{k}_1 + \underline{k}_2|$, as shown in Figure 4.1, so with

$$\underline{q} = \underline{k}_{1'} - \tfrac{1}{2}(\underline{k}_1 + \underline{k}_2)$$

we can produce the identities

$$\underline{h}\cdot\underline{g} = q^2 - \frac{k^2}{4}$$

$$g^2 = q^2 + \frac{k^2}{4} + \underline{q}\cdot\underline{k}$$

and

$$d^3\underline{k} = d^3\underline{q} \qquad (4.21)$$

where

$$\underline{k} = \underline{k}_2 - \underline{k}_1$$

To express $\underline{q}$ in terms of spherical polar co-ordinates we set a z axis in the direction $\underline{k}_1 + \underline{k}_2$ then

$$\underline{q}\cdot\underline{k} = qk\gamma$$

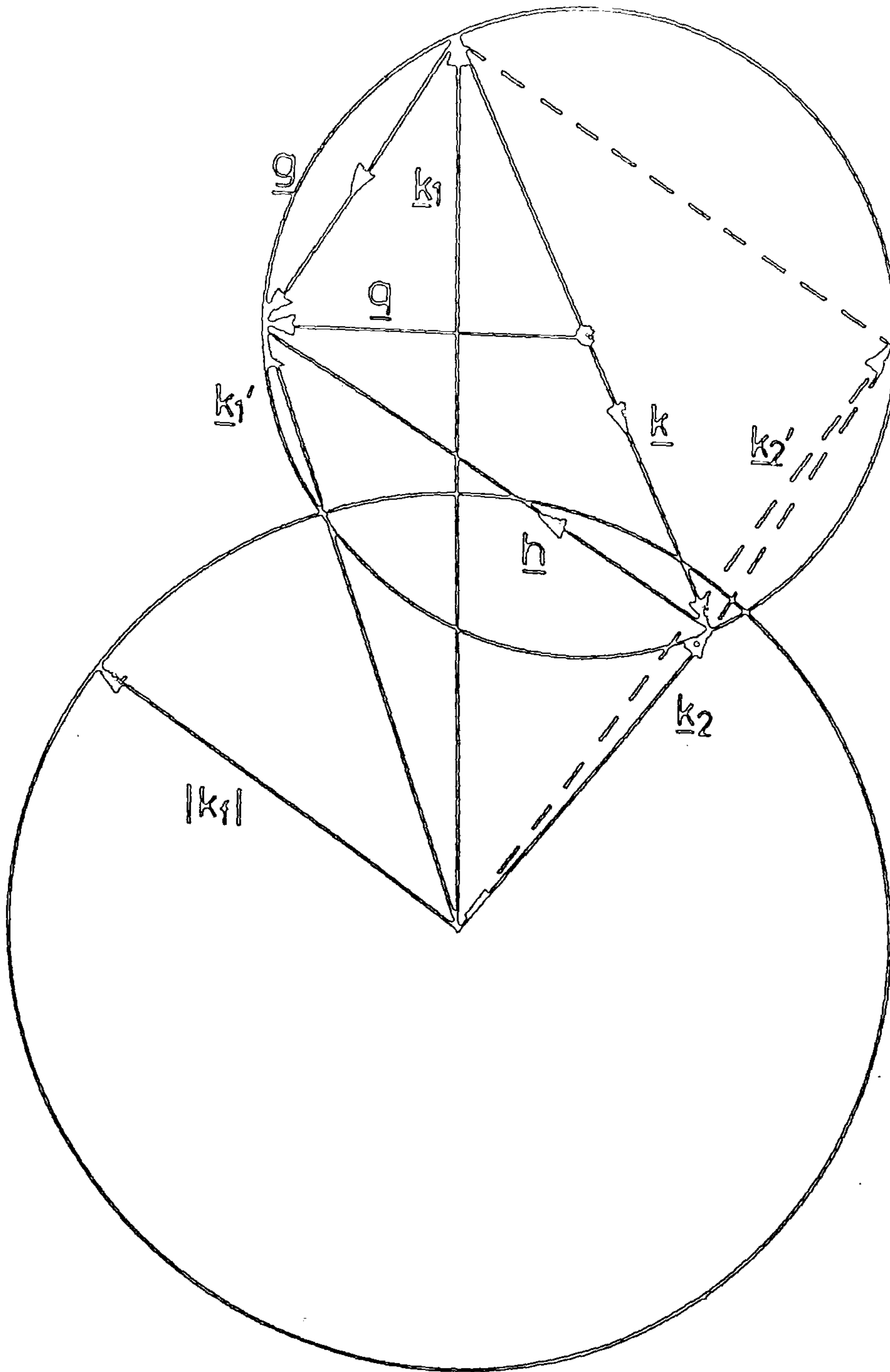

Fig. 4.1 : The final (1' and 2') and initial (1 and 2) states of the impact ionisation process in relation to the Fermi sphere.

where

$$\gamma = \cos\theta\cos\theta_k + \sin\theta\sin\theta_k\cos(\phi - \phi_k)$$

and the angles are defined in Figures 4.2 and 4.3. Combining these with equations (4.21), equation (4.20) becomes

$$\frac{d^3\lambda^{-1}_{DII}}{d^3\underline{k}_2} = 2D\int_{\underline{q}} \frac{1}{\left(q^2+\frac{k^2}{4}+qk\ +\lambda^2\right)^2}\,\delta\left[\frac{\hbar^2}{m}\left(q^2-\frac{k^2}{4}\right)\right] q^2\sin\theta\, d\theta\, d\phi\, dq \qquad (4.22)$$

Again the delta function requires that $\underline{q}$ must be on the small sphere of Figure 4.1. Integrating over q gives

$$\frac{d^3\lambda^{-1}_{DII}}{d^3\underline{k}_2} = \frac{Dmk}{2\hbar^2}\int_{\theta,\phi} \frac{\sin\theta\, d\theta\, d\phi}{\left[\frac{k^2}{2}+\lambda^2 + \frac{k^2}{2}(\cos\theta\cos\theta_k+\sin\theta\sin\theta_k\cos(\phi-\phi_k))\right]^2} \qquad (4.23)$$

In this expression 1' and 2' states must be above the Fermi surface (see Figure 4.1). If either, or both of them, are beneath the surface then they will be already filled and no transition to them will be possible. The upper limit to θ will exist at the condition shown in Figure 4.4(a) when $\underline{k}_{1'}$ lies on the Fermi surface or when

$$\cos\theta = \frac{2k_f^2 - k_1^2 - k_2^2}{|\underline{k}_1 + \underline{k}_2|\ |\underline{k}_2 - \underline{k}_1|} = -L$$

while the lower limit, illustrated by Figure 4.4(b), will correspond to

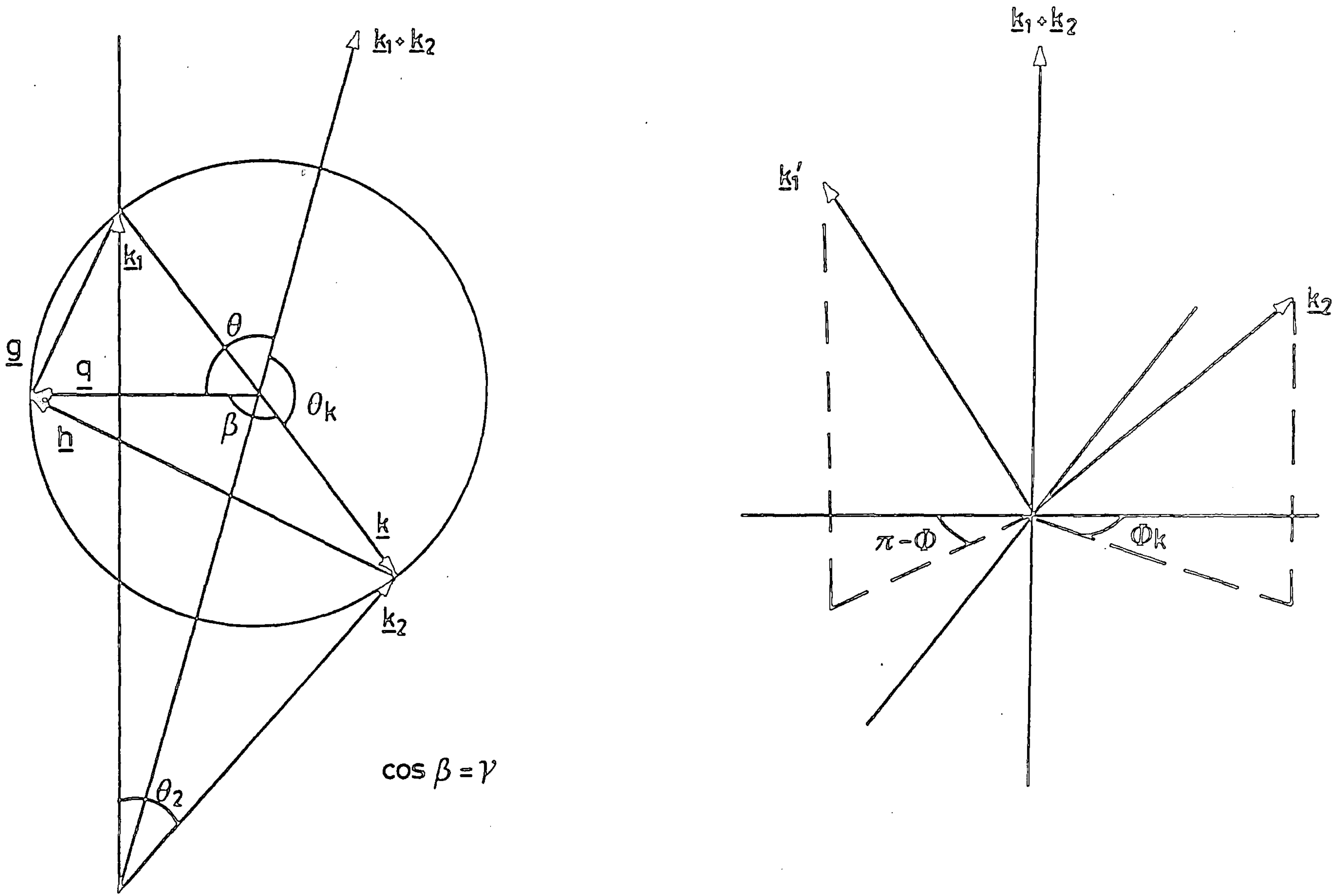

Fig. 4.2 and Fig. 4.3 : Illustration of variables used in impact ionisation transition rate calculations.

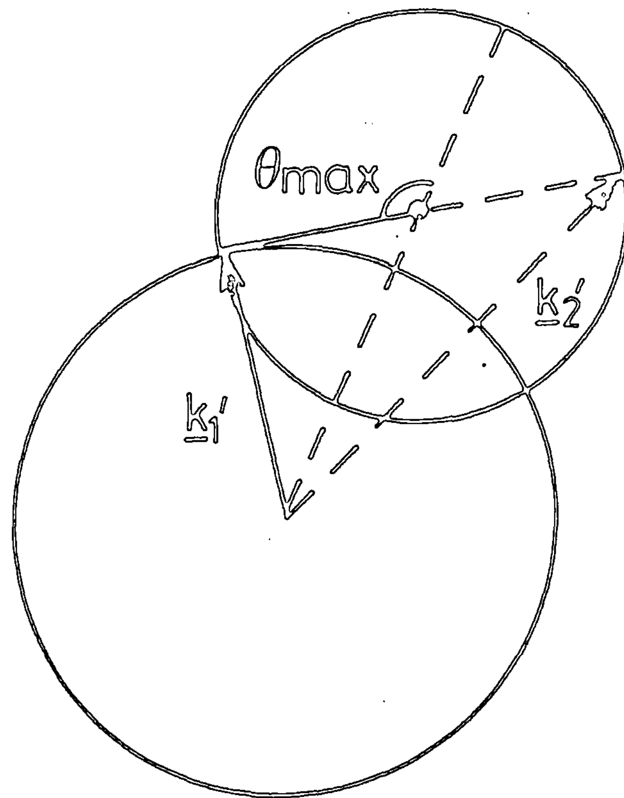

Fig. 4.4a) : Maximum value of θ_1, corresponding to $\underline{k}_1$, lying on the Fermi surface.

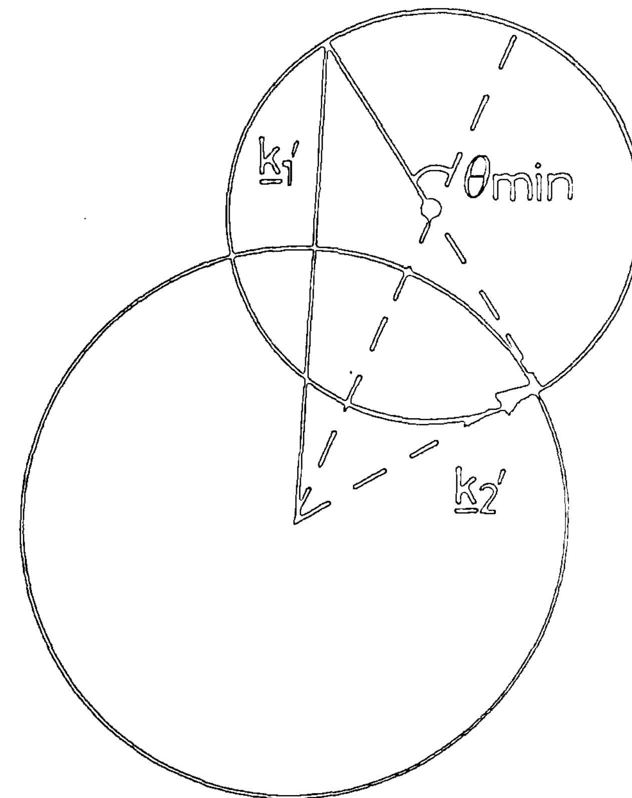

Fig. 4.4b) : Minimum value of θ_1, corresponding to $\underline{k}_2$, lying on the Fermi surface.

$\underline{k}_2$, lying on the surface or when

$$\cos\theta = \frac{k_1^2 + k_2^2 - 2k_f}{|\underline{k}_1 + \underline{k}_2|\ |\underline{k}_2 - \underline{k}_1|} = L$$

Integrating over ϕ (using standard integral A1.1) gives

$$\frac{d^3\lambda_{DII}^{-1}}{d^3\underline{k}_2} = \frac{D\pi mk}{\hbar^2}\int_{-L}^{L}\frac{\left(\frac{k^2}{2}+\lambda^2+\frac{k^2}{2}\cos\theta\cos\theta_k\right)\,d\cos\theta}{\left[\left(\frac{k^2}{2}+\lambda^2+\frac{k^2}{2}\cos\theta\cos\theta_k\right)^2-\left(\frac{k^2}{2}\sin\theta\sin\theta_k\right)^2\right]^{3/2}} \tag{4.24}$$

The denominator can be arranged into the form

$$R^{3/2} = (A + B\cos\theta + C\cos^2\theta)^{3/2}$$

where

$$A = \lambda^4 + k^2\lambda^2 + \frac{k^4}{4}\cos^2\theta_k$$

$$B = \left(\lambda^2 k^2 + \frac{k^4}{2}\right)\cos\theta_k$$

and

$$C = \frac{k^4}{4} \tag{4.25}$$

Integrating over $\cos\theta$ (using standard integrals A1.2 and A1.3) gives

$$\frac{d^3\lambda_{DII}^{-1}}{d^3\underline{k}_2} = \frac{D\pi mk}{\hbar^2}\left[\frac{2}{\Delta}\left(\frac{k^2}{2}+\lambda^2\right)\left(\frac{2CL+B}{\sqrt{R_1}}+\frac{2CL-B}{\sqrt{R_2}}\right) - \frac{k^2\cos\theta_k}{\Delta}\left(\frac{2A+BL}{\sqrt{R_1}}-\frac{2A-BL}{\sqrt{R_2}}\right)\right] \tag{4.26}$$

where

$$\Delta = \lambda^2 k^4 (\lambda^2 + k^2)(1 - \cos^2\theta_k)$$

$$R_1 = A + BL + CL^2$$

and

$$R_2 = A - BL + CL^2$$

We require information about the energy and wavevector of state 2 (the state in which a hole is created). It is convenient to express $\underline{k}_2$ in terms of spherical polar co-ordinates using $\underline{k}_1$ as the z direction, then

$$\begin{aligned} d^3\underline{k}_2 &= 2\pi \sin\theta_2 d\theta_2 k_2^2 dk_2 \\ &= -2\pi \frac{m}{\hbar^2} d(\cos\theta_2) k_2 dE_2 \end{aligned}$$

and substituting this into equation (4.26) gives

$$\frac{d^3\lambda_{DII}^{-1}}{dE_2 d\cos\theta_2} = \frac{2D\pi^2 m^2 k k_2}{\hbar^4}\left[\frac{k^2\cos\theta_k}{\Delta}\left(\frac{2A + BL}{\sqrt{R_1}} - \frac{2A - BL}{\sqrt{R_2}}\right) - \frac{2}{\Delta}\left(\frac{k^2}{2} + \lambda^2\right)\left(\frac{2CL + B}{\sqrt{R_1}} + \frac{2CL - B}{\sqrt{R_2}}\right)\right] \quad (4.27)$$

Finally we can define $\cos\theta_k$ using the relationship

$$k_2^2 - k_1^2 = |\underline{k}_1 + \underline{k}_2|\ |\underline{k}_2 - \underline{k}_1| \cos\theta_k$$

to give

$$\cos\theta_k = \frac{k_2^2 - k_1^2}{|\underline{k}_1 + \underline{k}_2|\ |\underline{k}_2 - \underline{k}_1|} \qquad (4.28)$$

Equation (4.27) now gives the information required about the probability of an electron being excited from a particular state as it gives the inverse mean free path, or a number of transitions per unit length, for interactions in which the incident electron excites another from the range E_2 to E_2+dE_2 and $\cos\theta_2$ to $\cos\theta_2 + d\cos\theta_2$ to a state above the Fermi surface.

4.4.2 Transitions Including Exchange Effects

By using the full expression, in equation (4.16), for the matrix element in equation (4.2), the transition rate is given as

$$TR = \left(\frac{|e|^2}{\varepsilon_0}\right)^2 \frac{(2\pi)^4}{\hbar\Omega^3}\left[\frac{\delta_{s1's1}\,\delta_{s2's2}}{|\underline{k}_{1'}-\underline{k}_1|^2+\lambda^2} - \frac{\delta_{s2's1}\,\delta_{s1's2}}{|\underline{k}_{2'}-\underline{k}_1|^2+\lambda^2}\right]^2$$

$$\times\ \delta(\underline{k}_{1'} + \underline{k}_{2'} - \underline{k}_1 - \underline{k}_2)\,\delta\left[\frac{\hbar^2}{2m}(k_{1'}^2 + k_{2'}^2 - k_1^2 - k_2^2)\right] \qquad (4.29)$$

and summing over the spin states s1', s2 and s2', the expression can be split into three parts

$$TR = I_1 + I_2 - I_3 \qquad (4.30)$$

where

$$I_1 = 2\left(\frac{|e|^2}{\varepsilon_0}\right)^2 \frac{(2\pi)^4}{\hbar\Omega^3} \frac{1}{(|\underline{k}_{1'}-\underline{k}_1|^2+\lambda^2)^2} \delta(\underline{k}_{1'}+\underline{k}_{2'}-\underline{k}_1-\underline{k}_2)\delta\left[\frac{\hbar^2}{2m}(k_{1'}^2+k_{2'}^2-k_1^2-k_2^2)\right]$$

$$I_2 = 2\left(\frac{|e|^2}{\varepsilon_0}\right)^2 \frac{(2\pi)^4}{\hbar\Omega^3} \frac{1}{(|\underline{k}_{2'}-\underline{k}_1|^2+\lambda^2)^2} \delta(\underline{k}_{1'}+\underline{k}_{2'}-\underline{k}_1-\underline{k}_2)\delta\left[\frac{\hbar^2}{2m}(k_{1'}^2+k_{2'}^2-k_1^2-k_2^2)\right]$$

and

$$I_3 = 2\left(\frac{|e|^2}{\varepsilon_0}\right)^2 \frac{(2\pi)^4}{\hbar\Omega^3} \frac{1}{(|\underline{k}_{1'}-\underline{k}_1|^2+\lambda^2)(|\underline{k}_{2'}-\underline{k}_1|^2+\lambda^2)}$$

$$\times \quad \delta(\underline{k}_{1'}+\underline{k}_{2'}-\underline{k}_1-\underline{k}_2)\delta\left[\frac{\hbar^2}{2m}(k_{1'}^2+k_{2'}^2-k_1^2-k_2^2)\right]$$

To find the inverse mean free path we divide by the incident electron velocity and sum over all possible $\underline{k}_{2'}$, $\underline{k}_2$ and $\underline{k}_{1'}$ states. So, by converting the summations to integrals we have

$$\lambda_{II}^{-1} = \lambda_1^{-1} + \lambda_2^{-1} - \lambda_3^{-1} \tag{4.31}$$

$$= \frac{\Omega^3}{(2\pi)^9}\iiint I_1 d^3\underline{k}_2 d^3\underline{k}_{2'} d^3\underline{k}_{1'} + \frac{\Omega^3}{(2\pi)^9}\iiint I_2 d^3\underline{k}_2 d^3\underline{k}_{2'} d^3\underline{k}_{1'}$$

$$- \frac{\Omega^3}{(2\pi)^9}\iiint I_3 d^3\underline{k}_2 d^3\underline{k}_{2'} d^3\underline{k}_{1'} \; .$$

As already mentioned at the beginning of the last section, the expression for λ_1^{-1} is identical to the direct transition case (shown in equation (4.18))so we can move directly to the result that

$$\frac{d^3\lambda_1^{-1}}{d^3\underline{k}_2} = \frac{d^3\lambda_{DII}^{-1}}{d^3\underline{k}_2} \tag{4.32}$$

The integral of λ_2^{-1} is similar to λ_{DII}^{-1}, the difference being that 1' and 2' are interchanged. This make no difference to the calculation other than changing the order of integration, as the limits for $\underline{k}_{2'}$ are the sames as for $\underline{k}_{1'}$, therefore we can write:

$$\frac{d^3\lambda_2^{-1}}{d^3\underline{k}_2} = \frac{d^3\lambda_{DII}^{-1}}{d^3\underline{k}_2} \qquad (4.33)$$

So now by differentiating equation (4.31) with respect to $\underline{k}_2$ and using equations (4.32) and (4.33)

$$\frac{d^3\lambda_{II}^{-1}}{d^3\underline{k}_2} = 2\,\frac{d^3\lambda_{DII}^{-1}}{d^3\underline{k}_2} - \frac{d^3\lambda_3^{-1}}{d^3\underline{k}_2} \qquad (4.34)$$

with

$$\frac{d^3\lambda_3^{-1}}{d^3\underline{k}_2} = \frac{\Omega^3}{(2\pi)^9}\iint I_3\, d^3\underline{k}_{2'}\, d^3\underline{k}_{1'} \qquad (4.35)$$

Following the procedure in Section 4.4.1 and integrating over $k_{2'}$, gives:

$$\frac{d^3\lambda_3^{-1}}{d^3\underline{k}_2} = 2D\int \frac{1}{(g^2+\lambda^2)(h^2+\lambda^2)}\,\delta\left[\frac{\hbar^2}{m}\,\underline{h}.\underline{g}\right] d^3\underline{k}_{1'} \qquad (4.36)$$

where

$$\underline{g} = \underline{k}_{1'} - \underline{k}_1 \,, \qquad \underline{h} = \underline{k}_{1'} - \underline{k}_2$$

and

$$D = \frac{2\pi m}{k_1}\left(\frac{|e|^2}{\hbar\varepsilon_o}\right)^2 \frac{1}{(2\pi)^6}$$

As explained previously the delta function imposes the condition that $\underline{k}_{1'}$, $\underline{k}_1$ and $\underline{k}_2$ must lie on the surface of a sphere of diameter $|\underline{k}_1 - \underline{k}_2|$, so, following the method used in the direct transition case, a variable q is introduced from the centre of the sphere to $\underline{k}_1$ in order to exploit the symmetry of the sphere. This is illustrated in Figure 4.1. Using the co-ordinate system used in Figures 4.2 and 4.3, originally developed for the preceding section and employing the relationships

$$\underline{h} \cdot \underline{g} = q^2 - \frac{k^2}{4}$$

$$h^2 = q^2 + \frac{k^2}{4} - \underline{q} \cdot \underline{k}$$

and

$$g^2 = q^2 + \frac{k^2}{4} + \underline{q} \cdot \underline{k} \tag{4.37}$$

where

$$\underline{k} = \underline{k}_2 - \underline{k}_1$$

equation (4.36) can be rewritten as

$$\frac{d^3\lambda_3^{-1}}{d^3\underline{k}_2} = 2D \int_{\underline{k}_{1'}} \frac{1}{(q^2+\frac{k^2}{4}-qk\gamma+\lambda^2)(q^2+\frac{k^2}{4}+qk\gamma+\lambda^2)}$$

$$\times \delta\left[\frac{\hbar^2}{m}\left(q^2-\frac{k^2}{4}\right)\right] q^2 \sin\theta d\theta d\phi dq \tag{4.38}$$

where

$$\gamma = \cos\theta\cos\theta_k + \sin\theta\sin\theta_k\cos(\phi-\phi_k)$$

Integrating over q and assuming at present, that both $\underline{k}_{1'}$ and $\underline{k}_{2'}$ are above the Fermi surface, equation (4.38) becomes

$$\frac{d^3\lambda_3^{-1}}{d^3\underline{k}_2} = \frac{Dmk}{2\hbar^2}\int_{\theta,\phi} \frac{\sin\theta\, d\theta\, d\phi}{\left(\frac{k^2}{2} + \lambda^2 + \frac{k^2\gamma}{2}\right)\left(\frac{k^2}{2} + \lambda^2 - \frac{k^2\gamma}{2}\right)} \tag{4.39}$$

Both states 1' and 2' must initially be empty and this leads to a maximum value of θ, corresponding to $\underline{k}_1$, lying on the Fermi surface (illustrated by Figure 4.4(a)) and given by

$$\cos\theta = \frac{2k_f^2 - k_1^2 - k_2^2}{|\underline{k}_1+\underline{k}_2||\underline{k}_2-\underline{k}_1|} = -L$$

and a minimum value, corresponding to $\underline{k}_2$ lying on the Fermi surface (Figure 4.4(b)) defined by

$$\cos\theta = \frac{k_1{}^2 + k_2{}^2 - 2k_f^2}{|\underline{k}_1+\underline{k}_2||\underline{k}_2-\underline{k}_1|} = L$$

Factorising equation (4.39), and using the standard integral A1.1, we integrate over ϕ to obtain:

$$\frac{d^3\lambda_3^{-1}}{d^3\underline{k}_2} = \frac{D\pi mk}{\hbar^2}\int_{\theta,\phi} \frac{1}{(k^2+2\lambda^2)}\left[\frac{1}{\sqrt{A + B\cos\theta + C\cos^2\theta}} + \frac{1}{\sqrt{A - B\cos\theta + C\cos^2\theta}}\right] d(\cos\theta) \tag{4.40}$$

where

$$A = \lambda^4 + k^2\lambda^2 + \frac{k^4\cos^2\theta_k}{4}$$

$$B = k^2\left(\lambda^2 + \frac{k^2}{2}\right)\cos\theta_k$$

and

$$C = \frac{k^4}{4}$$

The final integral is performed using A1.4 and yields

$$\frac{d^3\lambda_3^{-1}}{d^3\underline{k}_2} = \frac{D\pi mk}{\hbar^2}\left[\frac{1}{\sqrt{C}(k^2+2\lambda^2)} \ln\frac{(2\sqrt{CR_1}+2CL+B)(2\sqrt{CR_2}-2CL-B)}{(2\sqrt{CR_2}-2CL+B)(2\sqrt{CR_1}+2CL-B)}\right] \tag{4.41}$$

where

$$R_1 = A + BL + CL^2$$

and

$$R_2 = A - BL + CL^2$$

This is the final term of the equation (4.34). Taking equation (4.34), expressing $\underline{k}_2$ in spherical polar co-ordinates with the direction of the incident electron as the z axis and integrating over ϕ_2 gives

$$\frac{d^3\lambda_{II}^{-1}}{dE_2 d\cos\theta_2} = 2\frac{d^2\lambda_{DII}^{-1}}{dE_2 d\cos\theta_2} + \frac{2\pi mk_2}{\hbar^2}\frac{d^3\lambda_3^{-1}}{d^3\underline{k}_2} \tag{4.42}$$

Combining equations (4.27), (4.41) and (4.42) we can then write the full expression for the transition rate/unit length of the incident electron exciting an electron from a state in the range E_2 to E_2+dE_2 and $\cos\theta_2$ to $\cos\theta_2 + d\cos\theta_2$.

$$\frac{d^2\lambda_{II}^{-1}}{dE_2 d\cos\theta_2} = \frac{2\pi^2 m^2 k k_2}{\hbar^4} D\left[\frac{2k^2\cos\theta_k}{\Delta}\left(\frac{2A+BL}{\sqrt{R_1}} - \frac{2A-BL}{\sqrt{R_2}}\right)\right.$$

$$-\frac{4}{\Delta}\left(\frac{k^2}{2}+\lambda^2\right)\left(\frac{2CL+B}{\sqrt{R_1}} + \frac{2CL-B}{\sqrt{R_2}}\right)$$

$$\left.+\frac{1}{\sqrt{C}(k^2+2\lambda^2)} \ln\left(\frac{(2\sqrt{CR_1}+2CL+B)(2\sqrt{CR_2}+2CL-B)}{(2\sqrt{CR_2}-2CL+B)(2\sqrt{CR_2}-2CL-B)}\right)\right]$$

(4.43)

where

$$\Delta = \lambda^2 k\,(\lambda^2 + k^2)(1 - \cos^2\theta_k^4)$$

and

$$\cos\theta_k = \frac{k_2^2 - k_1^2}{|\underline{k}_1 + \underline{k}_2||\underline{k}_2 - \underline{k}_1|}$$

4.4.3 Distribution of Created Holes

When an electron is excited to a state above the Fermi level its original state is left occupied by a hole, which means that when we find the probability of an electron, of particular energy and direction, being excited to above the Fermi surface we are also finding the probability of creating a hole with the same velocity as that electron. It should be pointed out here that we use the convention of labelling hole states by the energy of the replaced electron, therefore equations (4.27) and (4.43) give that transition rate per unit length that a hole is produced, in the range E_2 to $E_2 + dE_2$ and $\cos\theta_2$ to $\cos\theta_2 + d\cos\theta_2$, for direct transitions alone and for the complete direct and exchange transition respectively.

Figures 4.5 and 4.6 illustrate the angular distribution of holes for an incident electron 1.4eV above the Fermi energy. The value 1.4eV is intended to be close to the barrier height of a n-GaP/Au Schottky barrier and is regarded as typical of the barrier heights of the MIS devices in which we are chiefly interested. Figure 4.5 shows the hole distribution at the surface of the Fermi sphere while Figure 4.6 is for holes at 4.45eV, that is 1.05eV below the Fermi level. It can be seen that the curves are similar for both direct and exchange expressions with difference being more pronounced in the range $\pi/2$ to π. Both graphs show that the hole is more likely to be created travelling in the opposite direction to the incident electron. This preference is stronger at energies nearer the Fermi level as illustrated in Figure 4.7. This trend can be explained diagrammatically.

If we first consider the hole at the Fermi surface, Figure 4.8 shows the case where the hole travels in the same direction as the incident electron, while Figure 4.9 shows the opposite case. Due to energy and momentum conservation the only allowed states for the scattered electrons lie on the sphere represented by the solid line. It can be seen that the much larger sphere in Figures 4.9 will provide more possible final states enhancing the chances of this particular interaction. Figures 4.10 and 4.11 show the same interactions for a hole created well below the Fermi surface. We now have an additional constraint to acceptable $\underline{k}_1$, and $\underline{k}_2$, states because the sphere has part of its surface inside the Fermi sphere and these states are therefore already filled. This means that the only available states will be on the thickly drawn part of the sphere. It is evident that the increase in available states between Figures 4.10 and 4.11 is not as great as between Figures 4.8 and 4.9, hence the

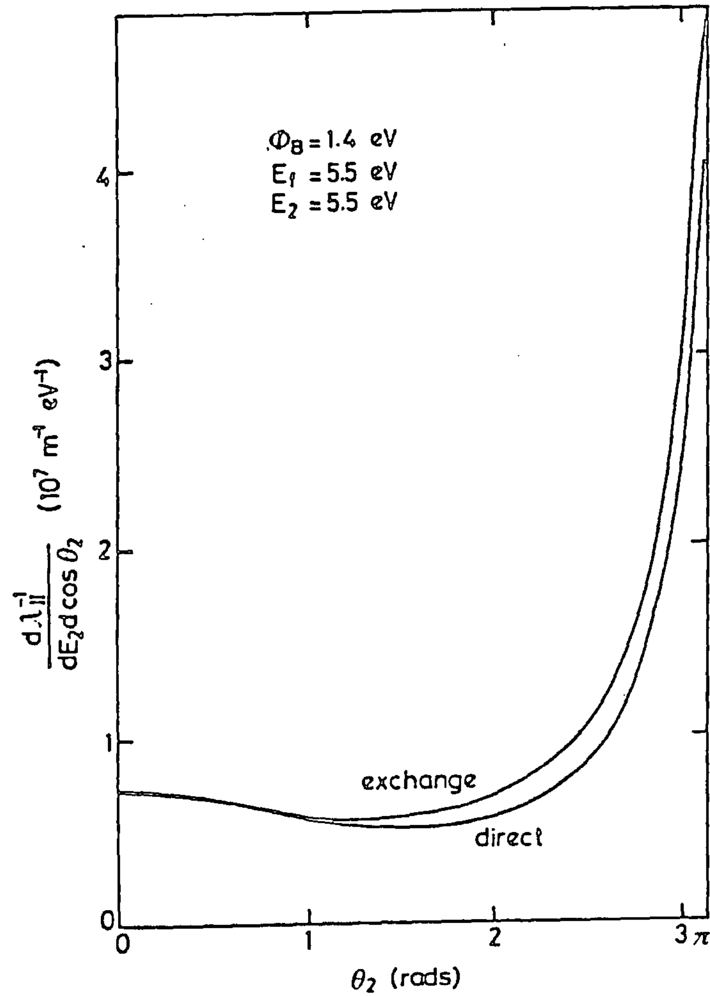

Fig. 4.5 : Hole distribution over θ_2, for an incident electron of energy E_F+1.4eV, at the Fermi surface.

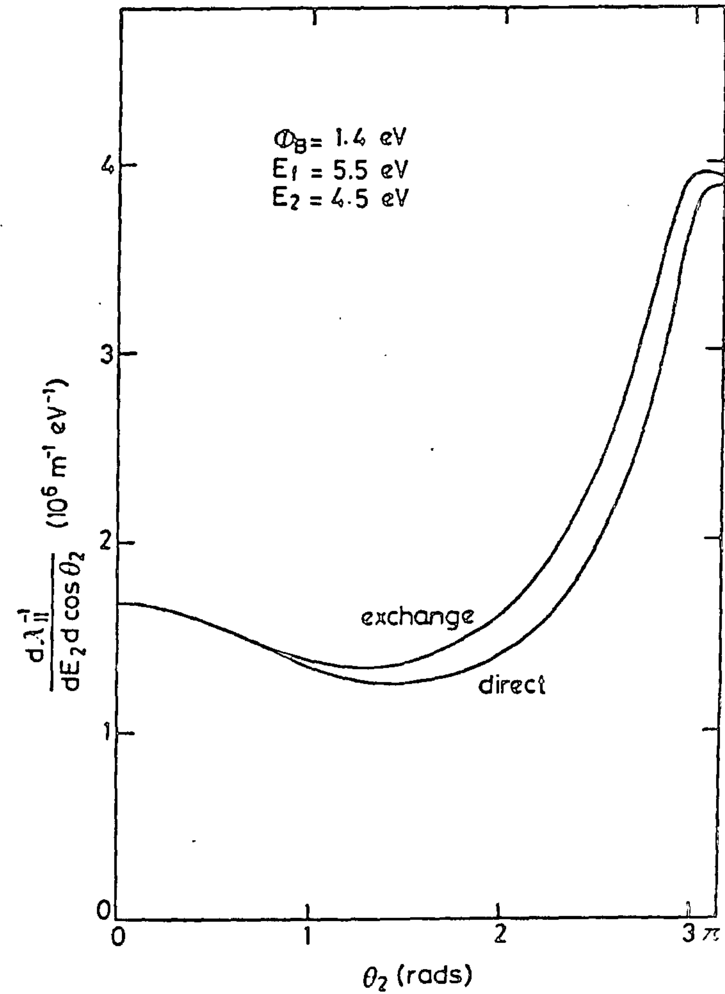

Fig. 4.6 : Hole distribution over θ_2, for an incident electron of energy E_F+1.4eV, at an energy of E_F-1.05eV.

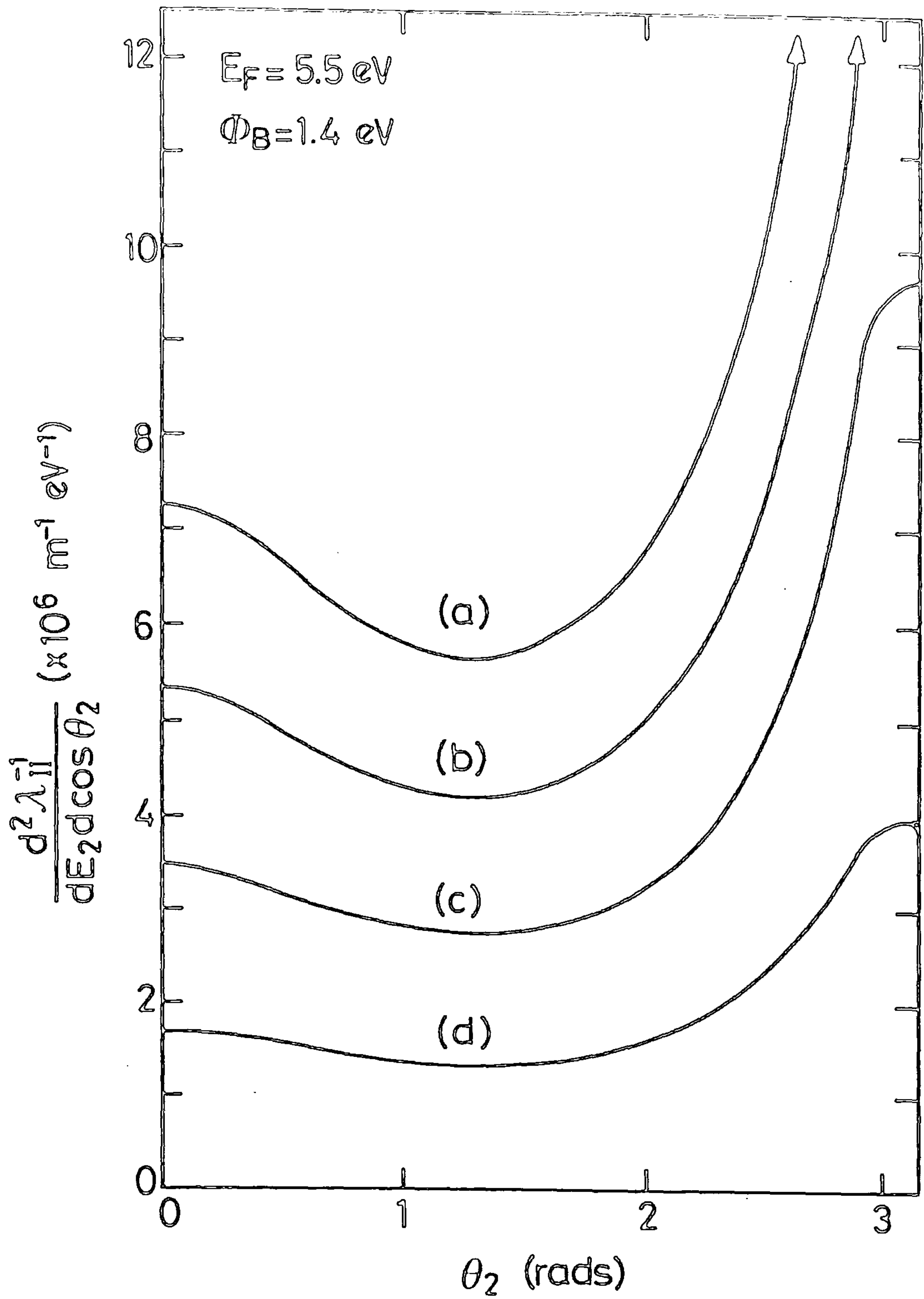

Fig. 4.7 : Hole distribution over θ_2, for an incident electron of energy E_F+1.4eV, at energies of: a) 5.5eV; b) 5.15eV; c) 4.8eV and d) 4.45eV.

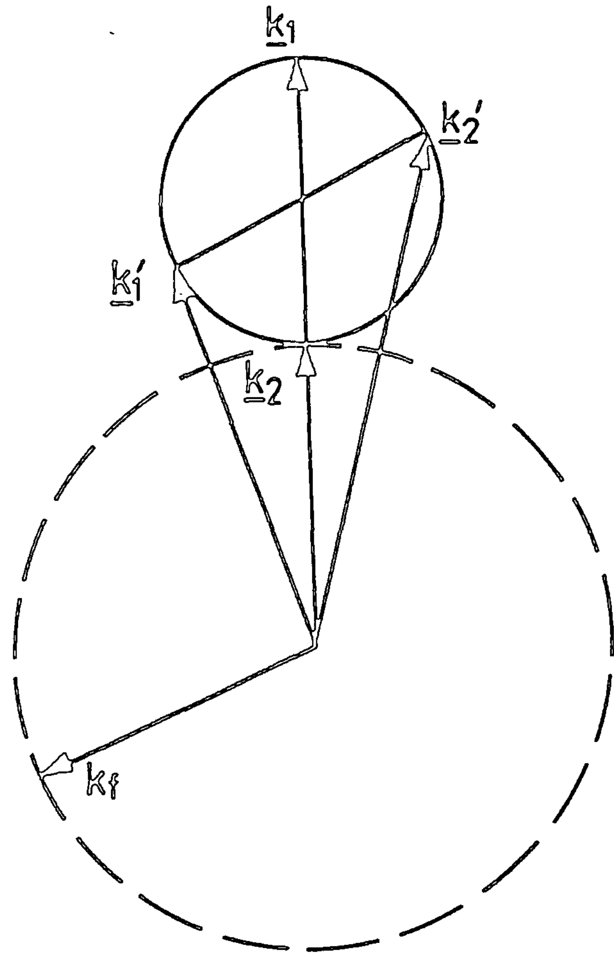

Fig. 4.8 : Available scattering states for hole creation at the Fermi surface with $\theta_2 = 0$.

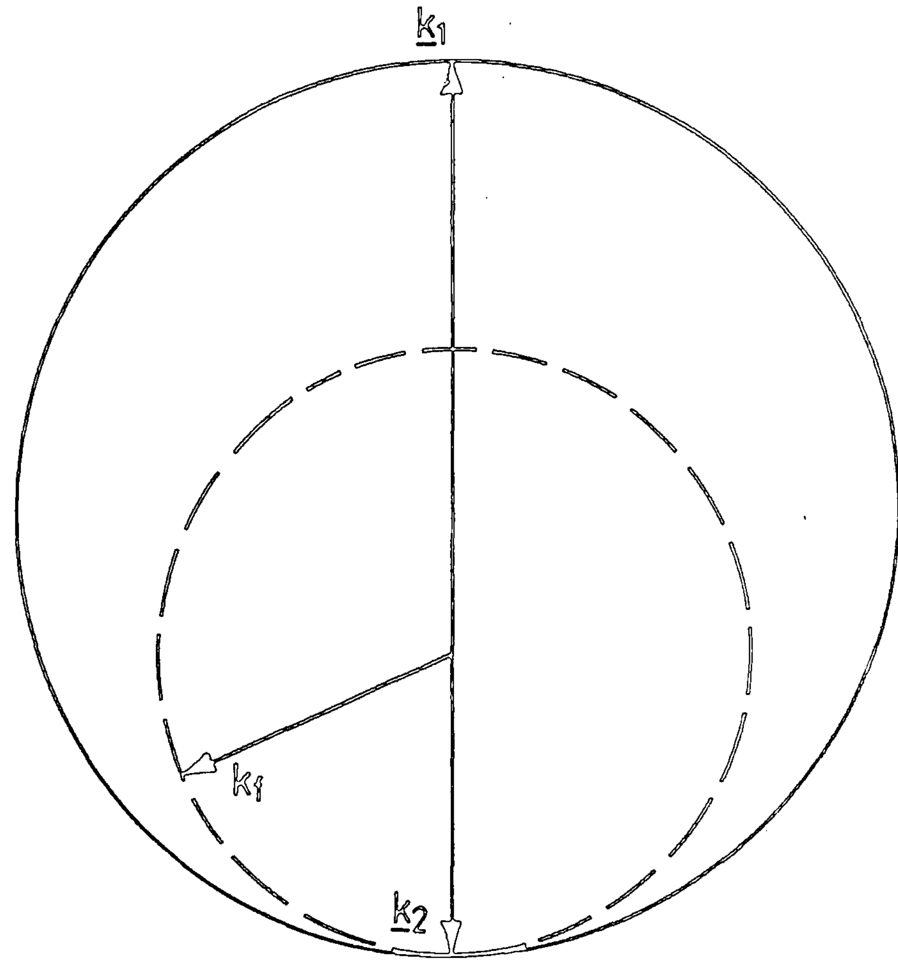

Fig. 4.9 : Available scattering states for hole creation at the Fermi surface with $\theta_2 = \pi$.

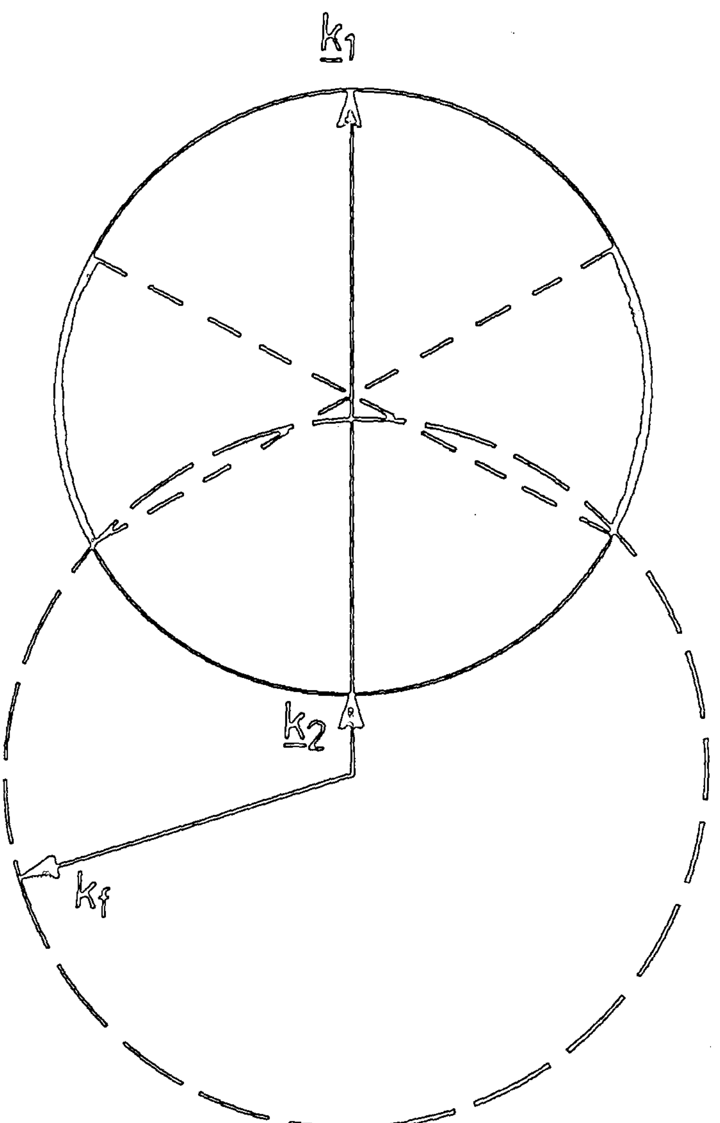

Fig. 4.10 : Available scattering states for hole creation creation below the Fermi surface with $\theta_2 = 0$.

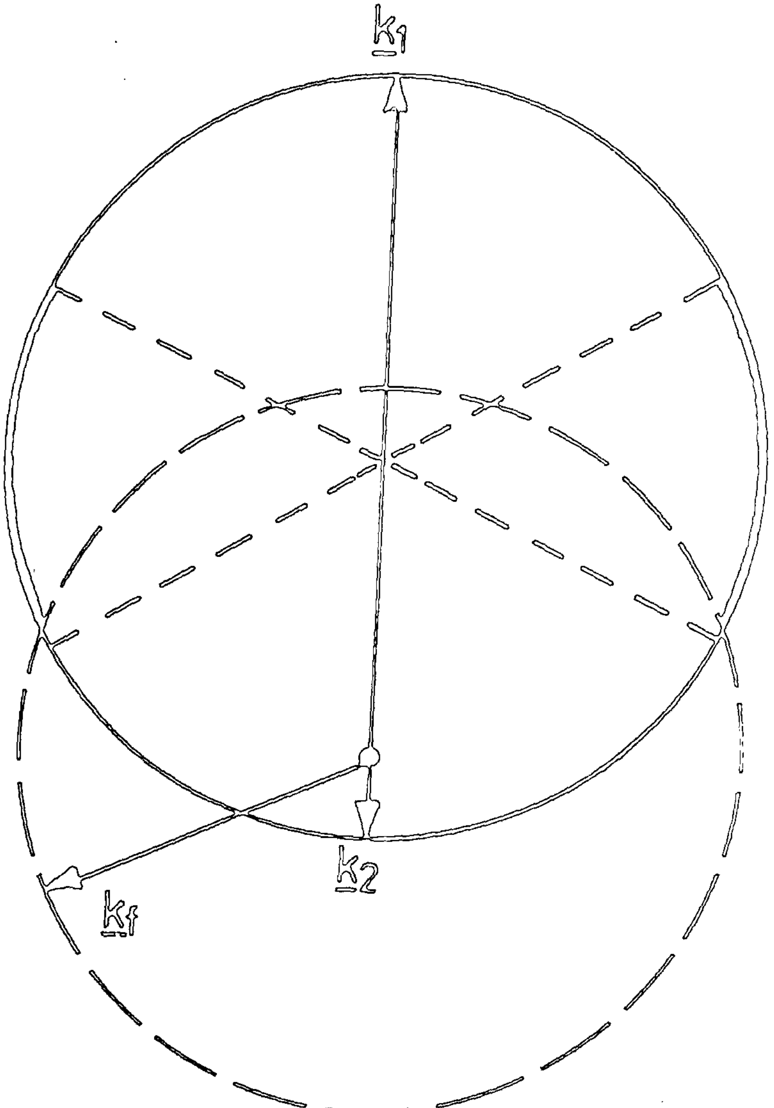

Fig. 4.11 : Available scattering states for hole creation below the Fermi surface with $\theta_2 = \pi$.

less pronounced preference to a scattering angle of π . This tendency is further underlined by Figure 4.12. The two curves are for the differential probability at $\theta_2 = 0$ and π over the whole range of E_2. The largest difference between the rates is, as expected, at the Fermi surface and the ratio between them then decreases as we move towards lower energies. These graphs seem to show that in all impact ionisation processes the preferred direction of the hole will be in the opposite direction to that of the incident electron.

4.5 TRANSPORT OF CREATED HOLE TO MI INTERFACE

4.5.1 Hole Recombination by an Auger Process

Once a hole has been produced at some level below the Fermi surface there is always the possibility that an electron from a higher level will be scattered into the hole state by an Auger process. This is simply the reverse of impact ionisation and if we use the same labelling of states to describe the situation we have two electrons initially in states 1' and2' being scattered to states 1 and 2 (see Figure 4.13).

Drawing parallels between this process and the impact ionisation process in the previous sections we can write an expression for the inverse mean free path of the hole:

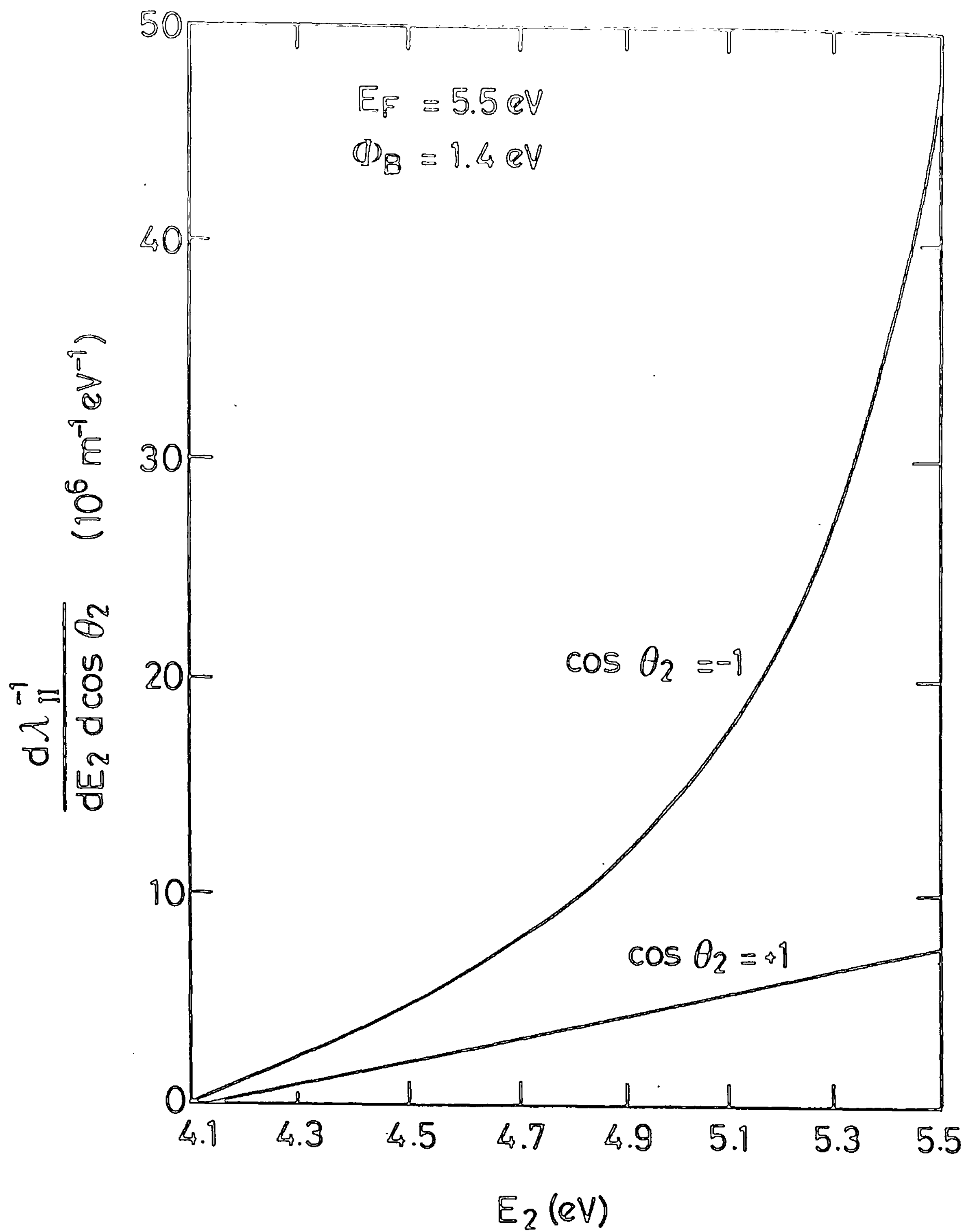

Fig. 4.12 : Hole distribution over E_2, for an incident electron of energy E_F+1.4eV, at θ = 0 and π.

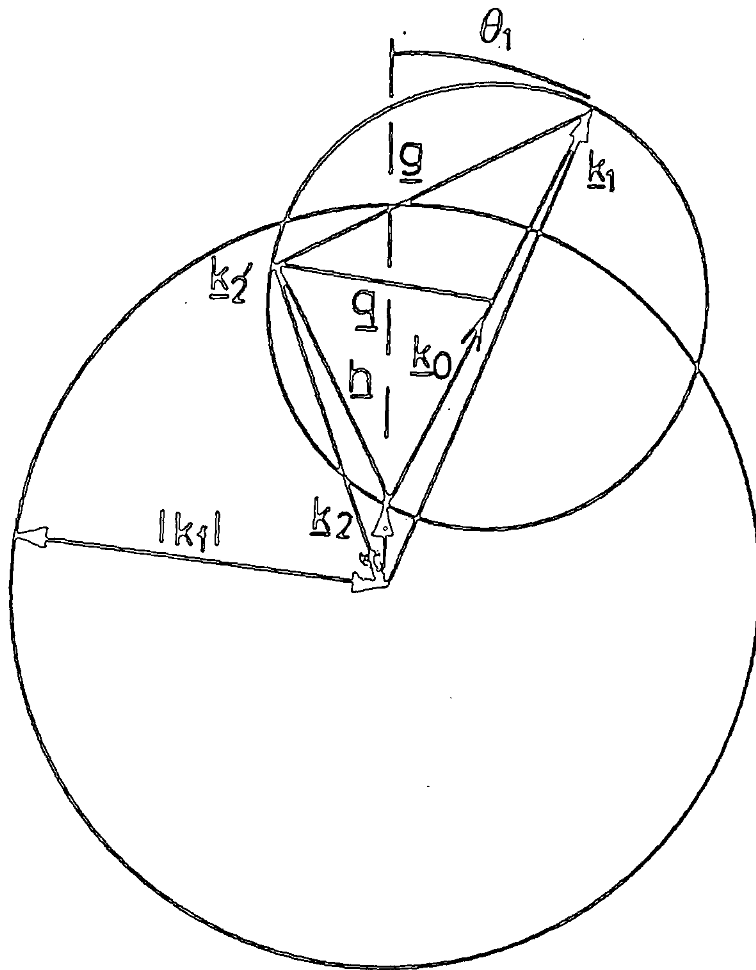

Fig. 4.13 : The initial and final wavevectors for an Auger-type transition.

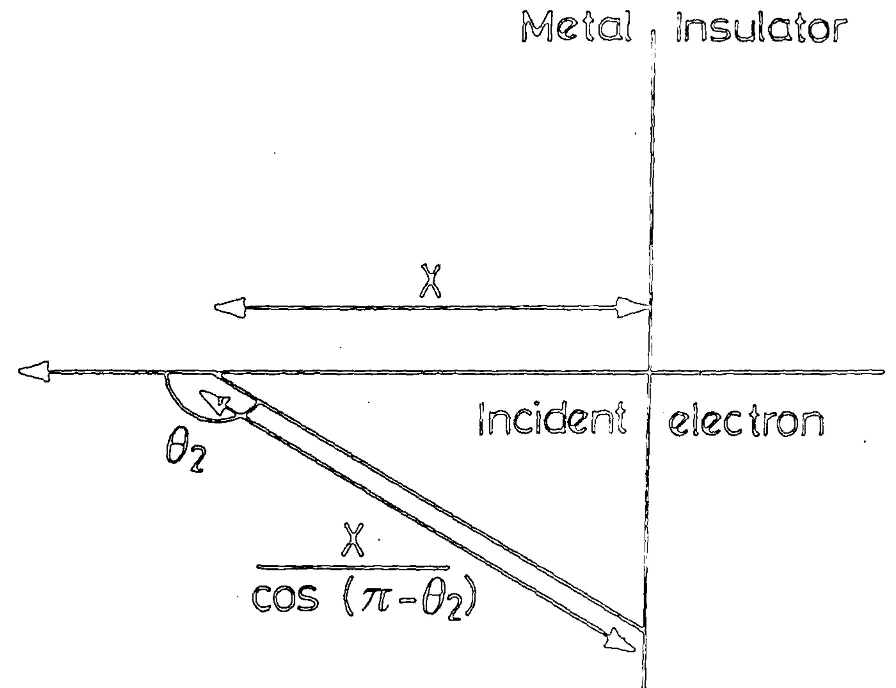

Fig. 4.14 : The path of a hole created in an impact ionisation process.

$$\lambda_{hA}^{-1} = 2\left\{\frac{2\pi m}{k_2}\left(\frac{|e|^2}{\hbar\varepsilon_0}\right)^2 \frac{1}{(2\pi)^6}\right\}\int_{\underline{k}_{2'}}\int_{\underline{k}_1}\left[\frac{1}{((\underline{k}_{2'}-\underline{k}_2)^2+\lambda^2)^2} + \frac{1}{((\underline{k}_2-\underline{k}_1)^2+\lambda^2)^2} - \frac{1}{((\underline{k}_{2'}-\underline{k}_2)^2+\lambda^2)((\underline{k}_{2'}-\underline{k}_1)^2+\lambda^2)}\right]$$

$$\times\,\delta\left[\frac{\hbar^2}{2m}(k_1^2 + k_2^2 - k_{2'}^2 - (\underline{k}_1+\underline{k}_2-\underline{k}_{2'})^2)\right] d^3\underline{k}_{2'}d^3\underline{k}_1 \qquad (4.44)$$

With the subscript 'hA' referring to holes and Auger.

The method used to carry out the integration is identical to that used in Sections 4.4.1 and 4.4.2 and to avoid repetition we move directly to the result equivalent to equation (4.43).

$$\frac{d^2\lambda_{hA}^{-1}}{dE_1 d\cos\theta_1} = \frac{2\pi^2 m^2 k k_1 D}{\hbar^4}\left[\frac{4}{\Delta}\left(\frac{k^2+\lambda^2}{2}\right)\left(\frac{2CL+B}{\sqrt{R_1}} + \frac{2CL-B}{\sqrt{R_2}}\right) - \frac{2k^2\cos\theta_k}{\Delta}\left(\frac{2A+BL}{\sqrt{R_1}} - \frac{2A-BL}{\sqrt{R_2}}\right) - \frac{1}{\sqrt{C(k^2+2\lambda^2)}}\ln\left(\frac{(2\sqrt{CR_1}+2CL+B)(2\sqrt{CR_2}+2CL-B)}{(2\sqrt{CR_2}-2CL+B)(2\sqrt{CR_1}-2CL-B)}\right)\right] \qquad (4.45)$$

where

$$R_1 = A + BL + CL^2$$

$$R_2 = A - BL + CL^2$$

$$A = \lambda^4 + k^2\lambda^2 + \frac{k^4}{4}\cos^2\theta_k$$

$$B = k^2\left(\frac{k^2}{4} + \lambda^2\right)\cos\theta_k$$

$$C = \frac{k^4}{4}$$

$$L = \frac{k_1^2 + k_2^2 - 2k_f^2}{|\underline{k}_1 + \underline{k}_2||\underline{k}_1 - \underline{k}_2|}$$

$$\Delta = \lambda^2 k^2(\lambda^2 + k^2)(1 - \cos^2\theta_k)$$

and

$$\cos\theta_k = \frac{k_2^2 - k_1^2}{|\underline{k}_1 + \underline{k}_2||\underline{k}_1 - \underline{k}_2|}$$

This is the probability that an electron will be scattered above the Fermi surface in the range E_1 to E_1+dE_1 and $\cos\theta_1$ to $\cos\theta_1+d\cos\theta_1$, where θ_1 is the angle between $\underline{k}_1$ and $\underline{k}_2$. Information on the final state of the scattered electron is not required but we do need the probability of a hole in a given state being involved in the interaction. The right hand side of equation (4.45) is therefore integrated over all E_1 and $\cos\theta_1$ to find λ_{hA}^{-1}. This integration has to be done numerically and will be considered in Section 4.5.4.

4.5.2 Calculation of the Probability of a Hole Reaching the MI Interface

As explained in Chapter Two it is expected that an electron which has been injected into the metal from the semiconductor will be travelling in a narrow cone, perpendicular to the metal-insulator interface. This means that if the direction of a created hole relative to the incident electron is known, its direction relative to the interface normal is also known to reasonable accuracy. To find the probability

of a hole reaching the interface it is necessary to know the distance from the interface at which it was created. If $P_{ec}(x)$ is the probability of an event within distance x then the probability of the event occuring in the interval x to x+dx is

$$dP_{ec}(x) = (1 - P_{ec}(x))\, \alpha\, dx \tag{4.47}$$

where α is the transition rate per unit length.

Solving this differential equation gives us

$$\ln(1 - P_{ec}(x)) = -\alpha x \tag{4.48}$$

or

$$1 - P_{ec}(x) = e^{-\alpha x} \tag{4.49}$$

Equation (4.49) gives the result that the probability of an electron not being scattered falls off exponentially with distance and is described by a mean free path give by $1/\alpha$. We obtain the probability of the interaction being in the range x to x+dx by combining equations (4.47) and (4.49) and substituting the mean free path λ_e for $1/\alpha$

$$dP_{ec}(x) = \frac{1}{\lambda_e} e^{-x/\lambda_e} dx \tag{4.50}$$

So far we have assumed that impact ionisation transitions are the only interactions possible. This is obviously not the case and there will be scattering due to other mechanisms such as phonon interaction and impurities. Equations (4.47) and (4.49) are still valid for any

scattering event, however, provided that it is realised that they deal with all interactions and not just impact ionisation. In this case λ_e will be a general mean free path covering all interactions expressed by

$$\frac{1}{\lambda_e} = \alpha = \frac{1}{\lambda_{II}} + \frac{1}{\lambda_P} + \frac{1}{\lambda_{IM}} + \ldots \qquad (4.51)$$

where λ_{II} λ_P and λ_{IM} are the mean free paths for impact ionisation, phonon and impurity scattering respectively, and are various functions of energy. In calculating the probability that the incident electron will travel a distance x without undergoing an interaction, all possible scattering mechanisms must be taken into account, but then to find the probability of an impact ionisation transition, in which a hole is produced, in a further distance dx we should only use the mean free path for impact ionisation events. By using the revised mean free path given by equation (4.51) in equation (4.49), then using λ_{II} in equation (4.47) and combining these two equations, the probability of impact ionisation in the range x to x+dx is given by:

$$dP_{ec}(x) = \frac{1}{\lambda_{II}} e^{-x/\lambda e} dx \qquad (4.52)$$

The probability per unit length that a hole is produced at x to x+dx, of energy E_2 to E_2+dE_2 and of direction $\cos\theta_2$ to $\cos\theta_2+d\cos\theta_2$, is hence

$$dP_{ec}(x) = \left[\frac{d\lambda_{II}^{-1}}{dE_2 d\cos\theta_2}\right] e^{-x/\lambda_e} \quad dE_2 d\cos\theta_2 dx \tag{4.53}$$

Having the probability of producing a hole at a particular position, the next step is to find the probability of this hole reaching the metal-insulator interface. As can be seen from Figure 4.14 the distance the hole has to travel is $x/\cos(\pi - \theta_2)$. The probability of the hole not undergoing an interaction before it reaches the interface is therefore

$$1 - P_{hc}(x/\cos(\pi - \theta_2)) = e^{x/\cos\theta_2 \lambda_h} \tag{4.54}$$

where $P_{hc}(x/\cos(\pi - \theta_2))$ is the probability of an interaction and λ_h is the mean free path for the hole which will be dependent on the hole energy and the scattering processes present, eg Auger, phonons, impurities etc. So, the probability that a hole created at x to x+dx reached the interface is

$$(1-P_{hc}(x/\cos(\pi - \theta_2))dP_{ec}(x) = \frac{d^2\lambda_{II}^{-1}}{dE_2 d\cos\theta_2} \exp\left[-\left(\frac{x}{\lambda_e} - \frac{x}{\lambda_h \cos\theta_2}\right)\right] dE_2 d\cos\theta_2 dx \tag{4.55}$$

Integrating over all x gives:

$$dP(E_2, \theta_2) = \left[\frac{d^2\lambda_{II}^{-1}}{dE_2 d\cos\theta_2}\right] \left(\frac{1}{\lambda_e} - \frac{1}{\lambda_h \cos\theta_2}\right)^{-1} dE_2 d\cos\theta_2 \tag{4.56}$$

Thus the probability that an injected electron will produce a hole in the range E_2 to E_2+dE_2 and $\cos\theta_2$ to $\cos\theta_2+d\cos\theta_2$ which will reach the interface, is obtained. It must be remembered that it has been assumed in this calculation that if the incident electron is scattered by anything other than an impact ionisation event, then it is removed from the system. In reality this would not always be the case because the electron could well still possess sufficient energy to produce a hole, but the calculation serves to give a lower limit to the probability. To obtain the probability over a range of energy and angle we integrate over these quantities. Substituting for $d^2\lambda_{II}/dE_2d\cos\theta_2$ in equation (4.56) using equation (4.43) gives an expression that can only be integrated numerically. We shall return to this numerical calculation in Section 4.5.4.

4.5.3 Approximate Expression for the Probability of a Hole Reaching the Interface

It is possible to produce an approximate probability for an incident electron producing a hole that reaches the interface by assuming the scattered hole distribution to be isotropic over θ_2 and for all value of E_2. In such a case, the mean free path λ_{II} will be independent of E_2 and λ_2 and instead of using equation (4.43) it will be possible to write

$$\frac{d^2\lambda_{II}^{-1}}{dE_2 d\cos\theta_2} = \frac{\lambda_{II}^{-1}}{2(E_1 - E_f)} \qquad (4.57)$$

If we make the further approximation that λ_h is the same as λ_e, and substitute equation (4.57) into equation (4.56) we obtain

$$dP(E_2,\theta_2) = \frac{1}{2(E_1 - E_f)} \left(\frac{\cos\theta_2}{\cos\theta_2 - 1} \right) dE_2 d\cos\theta_2 \qquad (4.58)$$

With this expression it is straighforward to integrate over E_2 and $\cos\theta_2$ to produce a result for the probability of a hole in a particular range of E_2 and θ_2 reaching the interface

$$P = \frac{E_{max} - E_{min}}{2(E_1 - E_f)} \left(\ln \left(\frac{1 - \cos\theta_{min}}{1 - \cos\theta_{max}} \right) + \cos\theta_{min} - \cos\theta_{max} \right) \qquad (4.59)$$

where E_{min} and E_{max}, and θ_{min} and θ_{max} are the minimum and maximum values of E_2 and θ_2 for the particular ranges chosen. The probability of any hole reaching the interface is given by taking the limits $\pi/2 < \theta_2 < \pi$ and $2E_f - E_1 < E_2 < E_f$. The value obtained with these limits is $P = 0.153$, which means that as many as 15% of incident electrons will produce holes capable of reaching the metal-insulator interface. This result will be useful to compare with the numerical values of the next section.

4.5.4 Hole Flux at the MI Interface

Using the full expression for $d^2\lambda_{||}^{-1} / dE_2 d\cos\theta_2$ in equation (4.56) means that numerical techniques are required when we integrate over E_2 and $\cos\theta_2$. Also in distinguishing between λ_e and λ_h these quantities will no longer cancel out and their values must be specified. $1/\lambda_e$ consists of the terms shown in equation (4.51). The impact

ionisation term can be found by integrating either equation (4.27) (direct) or equation (4.43) (direct and exchange). The results are compared with previous theoretical and experimental results in Figure 4.15, which shows the variation of the calculated, mean free path, obtained by just considering direct transitions, with the energy of the incident electron. The figure also shows similar results obtained by Quinn[4] using a self-consistent dielectric approach and several experimental values. The theoretical curves show very good agreement while comparison to experiment shows a reasonable match.

In considering the other terms in equation (4.51) we follow the suggestion of Crowell and Sze[10] and combine the expressions of Wilson[11] for electron-phonon scattering, and Mott[12,13] for impurity scattering to produce a general mean free path for lattice related interactions.

$$\lambda_L = \lambda_\sigma (E_1/E_f)^2 \tag{4.60}$$

λ_σ is the mean free path for electrons at the Fermi level and can be obtained experimentally from conductivity measurements. λ_h is determined by Auger scattering and lattice scattering.

To put the results obtained for the hole flux due to impact ionisation into perspective, it is worthwhile considering the flux of holes created thermally at the interface. Using Boltzmann statistics, the hole density at energy E is

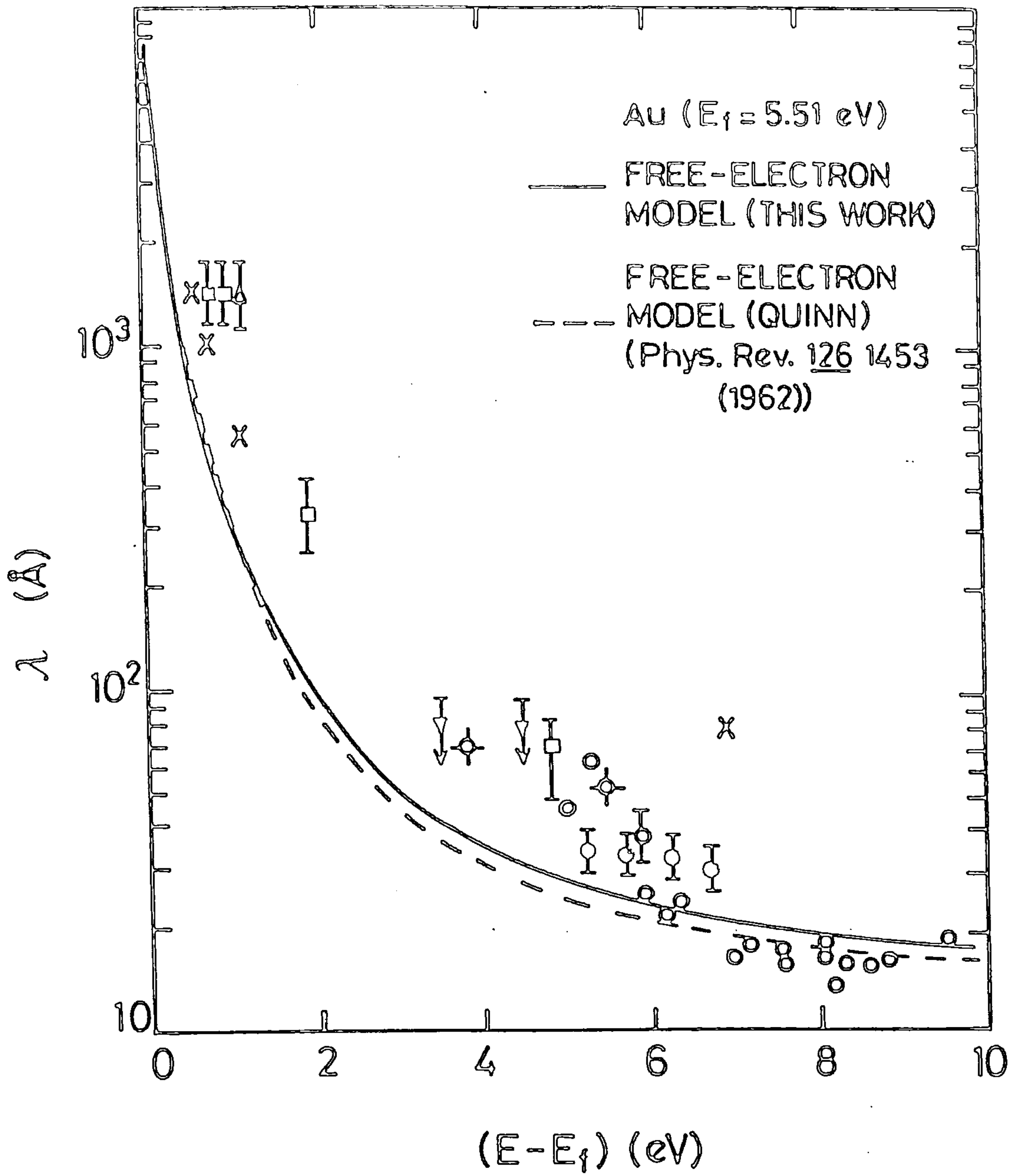

Fig. 4.15 : The variation of the mean free path of the incident electron over energy for direct transitions only, compared to previous theoretical and experimental results (from Reference 10).

$$p(E) = N(E) \exp\left(\frac{E - E_f}{kT}\right) \tag{4.61}$$

and if $\tau(E)$ is the lifetime of a hole then the creation rate $R_{th}(E)$ is given by

$$dR_{th}(E) = \frac{p(E)}{\tau(E)} dE \tag{4.62}$$

Given that the thermal creation of holes will be isotropic, we can write that the probability of a hole travelling at an angle θ to $\theta + d\theta$ to the normal of the interface is given by $\frac{1}{2}\sin\theta d\theta$, and that the probability of it being created at a distance x to x+dx from the interface is dx/L where L is the metal thickness. Combining these results with equation (4.54), which gives the probability of a hole reaching the interface, and integrating over x and θ the rate of holes reaching the interface over the range E to E+dE per unit area is found to correspond to a standard result of kinetic theory

$$dR_{th}(E) = \frac{p(E)v(E)dE}{4L} \tag{4.63}$$

where p(E) is given in equation (4.61), and v(E), the hole velocity, is given by $(2E/m)^{\frac{1}{2}}$. This expression can now be compared to the rate for impact ionisation created holes to see if the impact ionisation process is significant.

If we just consider holes approaching the interface in a 5° cone about

the normal, the distribution in energy of incident holes due to an electron current of $10^4 Am^{-2}$ (which is a typical driving current for the MIS devices incorporating Langmuir-Blodgett films), is shown in Figure 4.16. A limited cone angle is chosen because it is assumed that if the holes were energetically capable of getting under some hole barrier, then holes outside some narrow cone would be reflected back. This mechanism is more fully explained in Chapter Two. There are four curves for hole distribution versus energy in Figure 4.16, three for different values of λ_σ and one using the isotropic distribution approximation of Section 4.5.3. Curve (b) is for a typical value of λ_σ while curves (a) and (c) are for the two extreme cases of no lattice scattering (a), and for a value of λ_p substantially less than the typical value (c).

To find the thermal hole flux restricted to the 5° cone, equation (4.63) is multiplied by a constant equal to (1-cos(5°)). The distribution of thermal holes is compared to that of holes created by impact ionisation in Figure 4.17 and the total differential rate is shown in Figure 4.18. It can be seen that the thermal rate dominates over the higher energies with the alternative source of holes only being significant below approximately 4.9eV. If we consider holes reaching the interface at all angles, then we get the curves shown in Figures 4.19. There is an overall rise of about two orders of magnitude but again it is only at the lower energies that the impact ionisation becomes important. If there were some kind of barrier to the holes at a sufficiently low level to filter out the thermal holes but provide little impedance to the holes under the barrier travelling through the insulator, then the impact

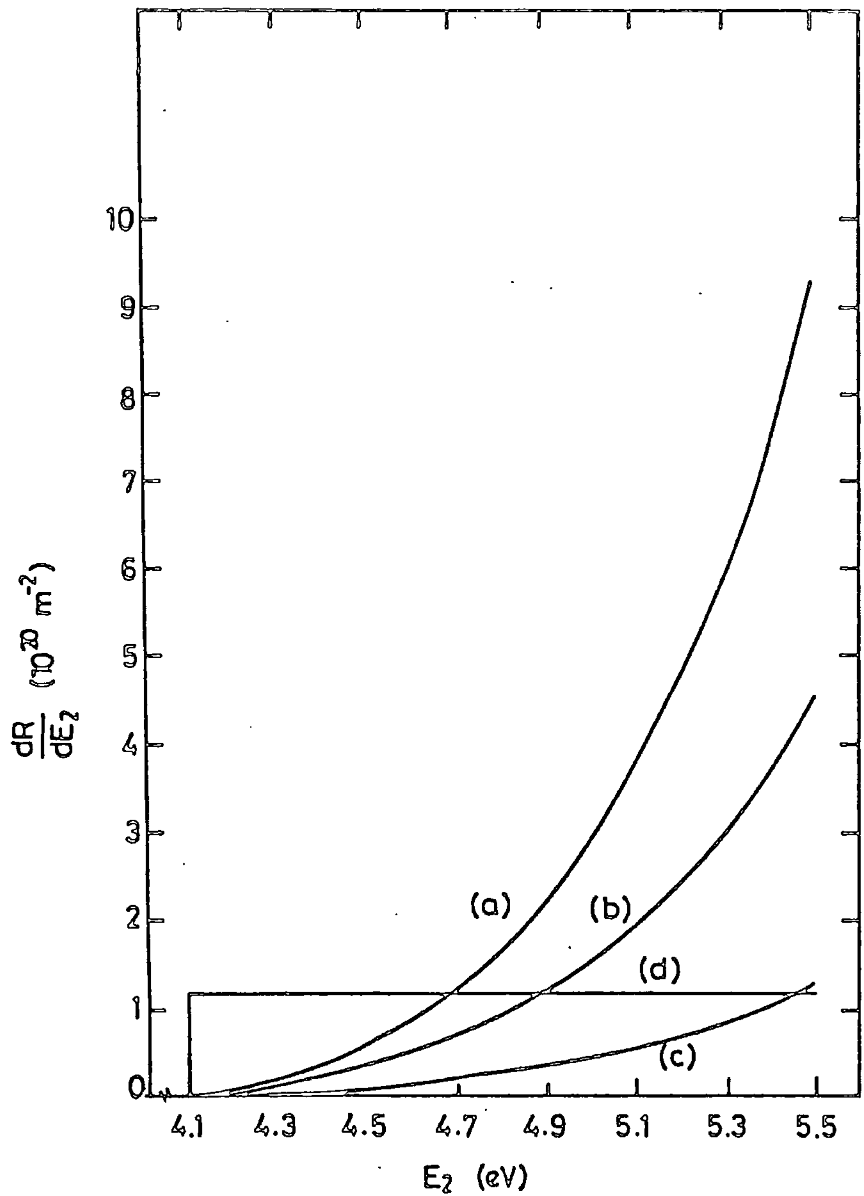

Fig. 4.16 : Distribution, over E_2, of holes incident at the metal-insulator interface in a 5° cone to the normal assuming an injection current of 10^4 Am^{-2} and a) $\lambda_p = \infty$; b) λ_p = 300Å; c) λ_p = 50Å and d) isotropic scattering with $\lambda_e = \lambda_h$.

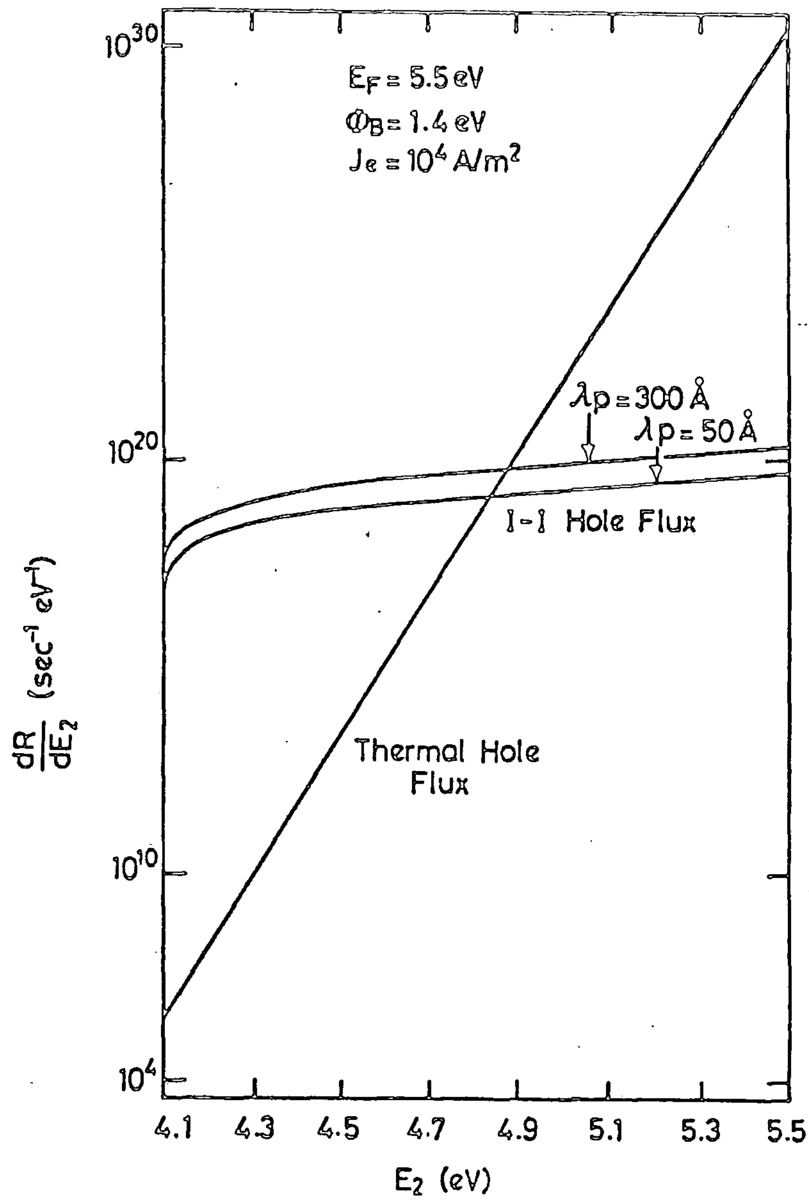

Fig. 4.17 : Distribution, over E_2, of holes incident at the metal-insulator interface in a 5° cone for an injection current of $10^4\ Am^{-2}$ compared to the thermal hole flux.

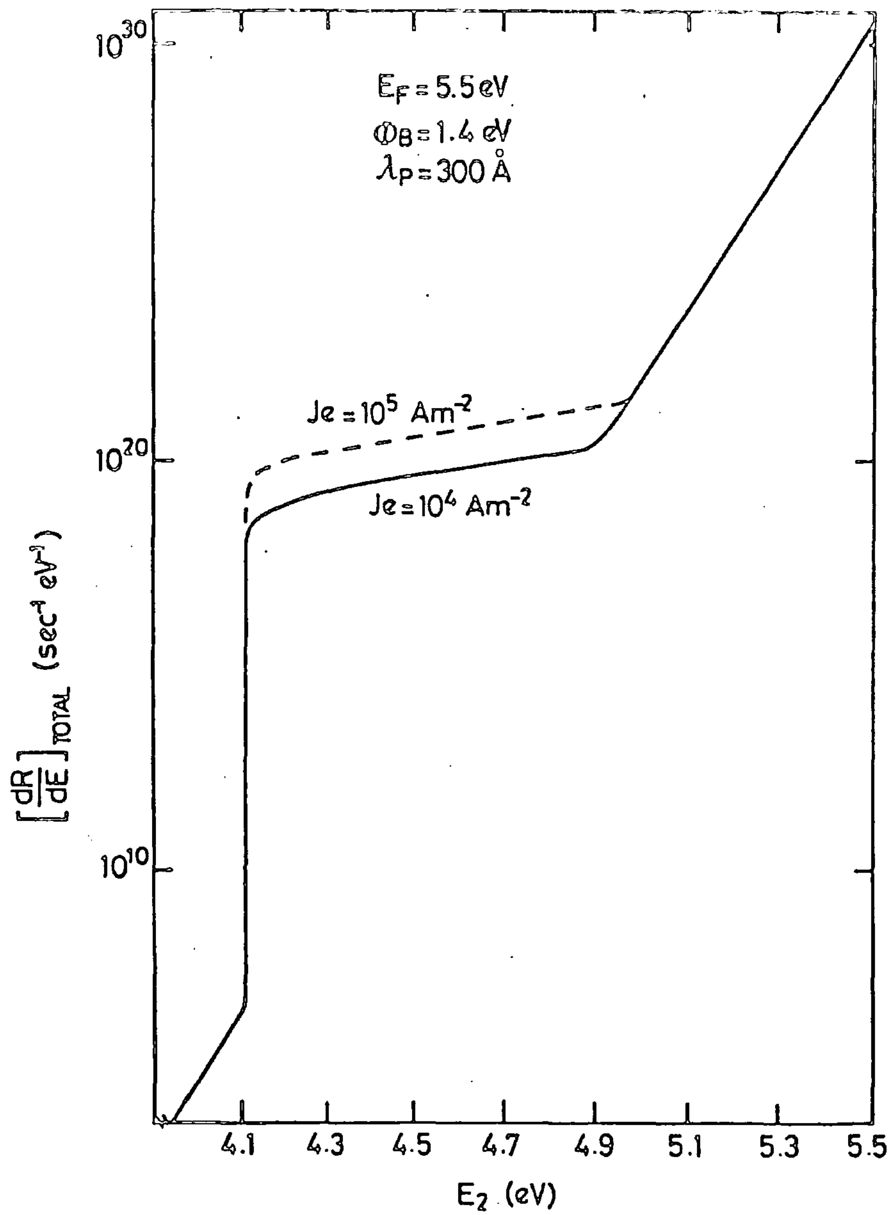

Fig. 4.18 : The total distribution, over E_2, of holes incident at the metal-insulator interface in a 5° cone.

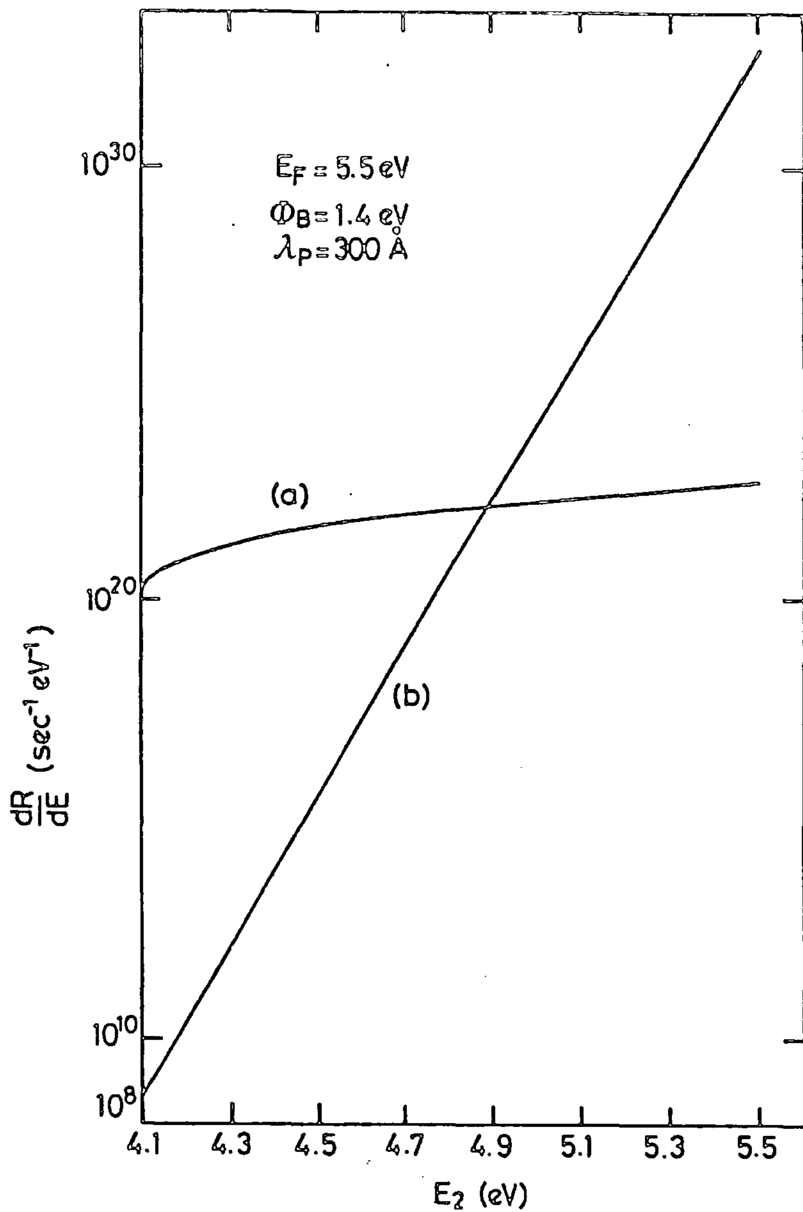

Fig. 4.19 : The distribution, over E_2, of holes incident at the metal-insulator interface at all angles: a) created by impact ionisation; b) created thermally.

ionisation process would indeed be significant.

Figures 4.20 and 4.21 give the probability that an incident electron 1.4eV above the Fermi level of 5.5eV, will produce a hole that will reach the interface below a certain energy. The probability over all energies is 18.5%, which compares well with the value of 16.3% obtained using the isotropic scattering approximation in equation (4.59). The difference in these values at the Fermi energy will be due to the difference in the general mean free paths for the holes and electrons, and the distribution over θ_2 as well as the isotropic distribution over energy by itself. At the lower energies, although hole production is less favoured, there is a significant hole rate with about 5% of the incident holes more than 1.0eV below the Fermi level.

4.6 SUMMARY

The creation of holes in gold by an impact ionisation process, in which an incident electron excites another from below the Fermi surface to leave a hole in its old state, has been investigated and results obtained giving the distribution of such holes over the energy and direction.

Using this information, it has proved possible to model the process in which an energetic electron, injected into the metal, produces a hole which can return to the surface without recombining, and the probability of such events occuring can be obtained.

Comparing the hole flux at the interface due to this process, for currents typical of the devices which we are considering, to that for

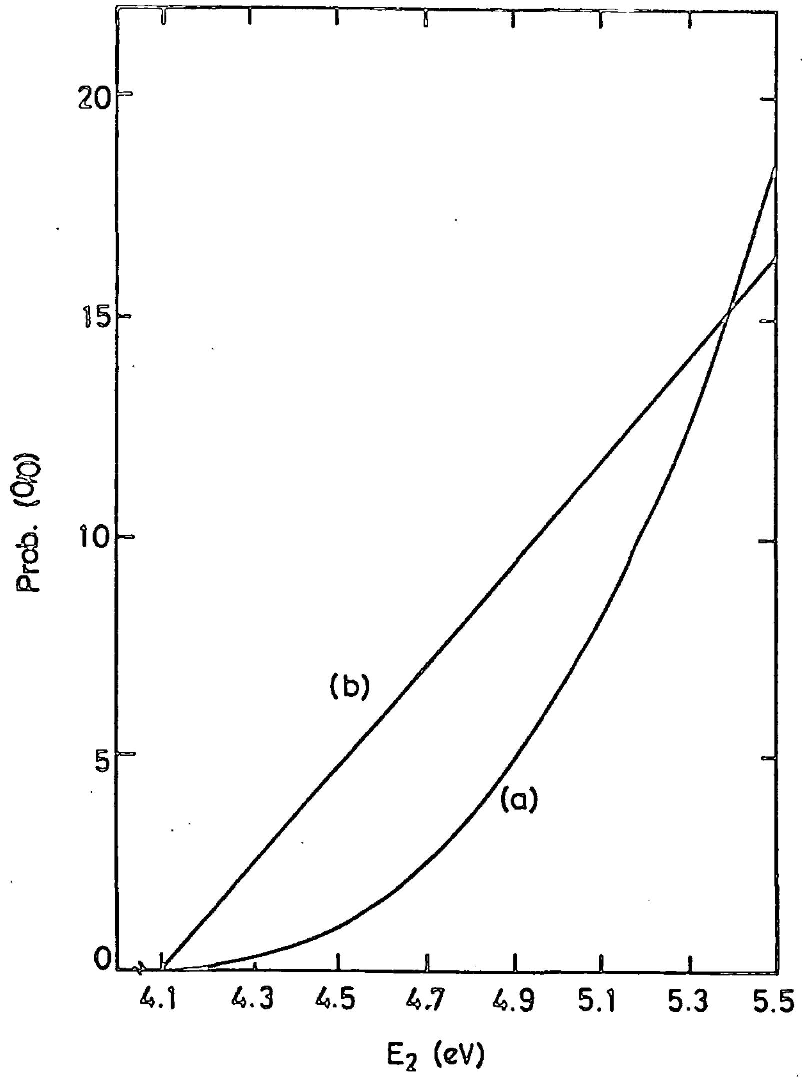

Fig. 4.20 : The probability of an incident electron of energy E_F+1.4eV creating a hole capable of reaching the interface below energy E_2(a) compared to the results for isotropic scattering (b).

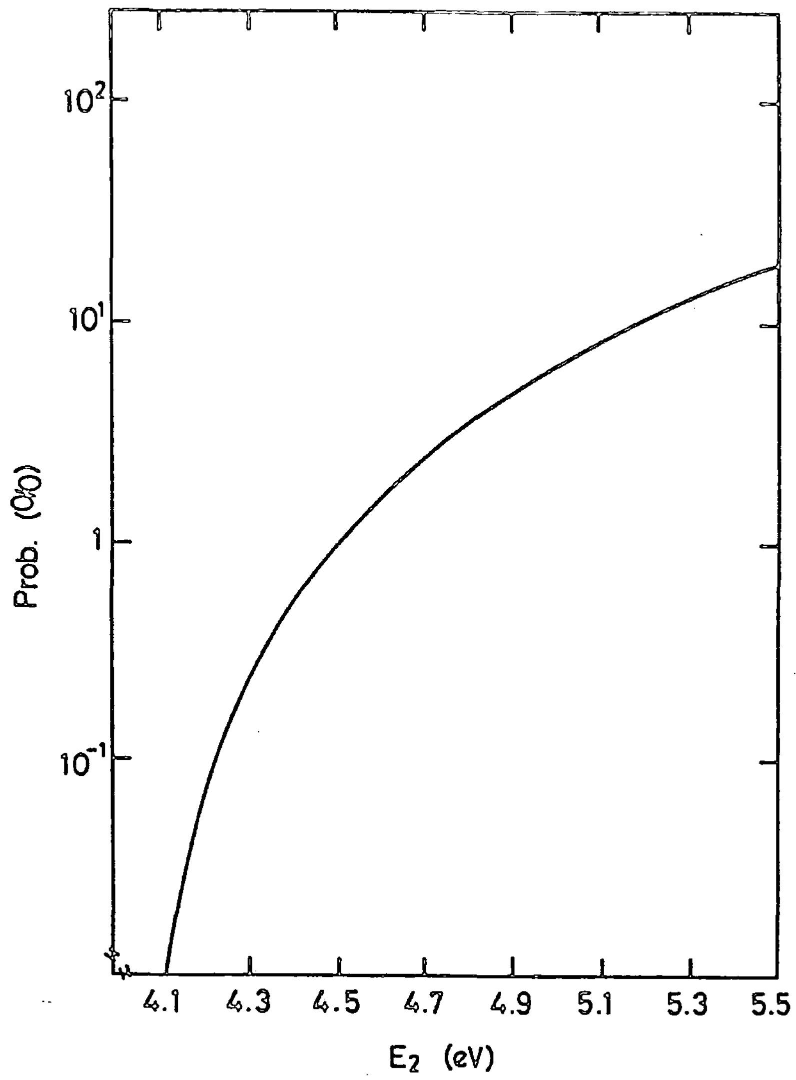

Fig. 4.21 : Curve (a) in Fig. 4.20 using a logarithmic scale.

holes created thermally, it was shown that the impact ionisation process was only significant at energies less than about 0.5eV below the Fermi level. The subsequent transport of the holes through the insulator into the semiconductor will be discussed in Chapter Six.

CHAPTER FIVE

SEMICONDUCTOR BAND ALIGNMENT IN THE MIS DIODE

5.1 INTRODUCTION

Gaining an understanding of the behaviour of the electric field in the semiconductor depletion region and in the bulk at higher voltages, when the device is under forward bias, is an important step in modelling the overall behaviour of the MIS device. The main aim of the work on MIS structures reported in this thesis is to investigate the mechanism by which holes are introduced into the valence band of the semiconductor. However the holes are minority carriers and are expected to constitute only a small fraction of the total current and have little effect on the total current-voltages characteristics. Bearing this in mind, we attempt to describe here the majority electron current in terms of the realignment of the semiconductor bands under forward bias. In the process particular attention will be paid to the behaviour of the Au/Langmuir-Blodgett Film/n-GaP diodes fabricated by Batey et al[1,2,3]. This allows a direct comparison of theory and experiment. The calculations of the alignment of the bands also gives the change with bias of the potential across the insulating region and this is important for assessing the various possibilities for the hole conduction mechanism between the metal and the semiconductor through the insulator.

5.2 DEVICE CHARACTERISTICS AT LOW BIASES

5.2.1 Semiconductor Barrier Height

An understanding of the behaviour of the semiconductor barrier height is important for two reasons. First, any change in barrier height is also the change in the level of the semiconductor valence band edge relative to the metal Fermi level. If hole transport into the semiconductor is through the barrier presented by the insulator rather than by excitation under it*, then the realignment of bands will be significant in that it alters the electric field across the insulator and increases the number of holes incident on the metal-insulator interface at energies below the valence band.

The second reason is that a rise in the barrier height will affect the majority carrier current from the semiconductor into the metal.

From Figure 5.1, showing the band diagram of the device, it is straightforward to write an expression for the metal-insulator barrier height ϕ_m.

$$\phi_m = \phi_b(V) + X_s + \Delta(V) \qquad (5.1)$$

where $\phi_b(V)$ is the semiconductor barrier height, $\Delta(V)$ is the voltage drop across the insulator and X_s is the difference in the electron affinities of the semiconductor and the insulator.

---

* By hole conduction under the barrier it is meant that the holes are able to travel across the insulator via some valence band

Fig. 5.1 : Schematic energy band diagram for an MIS diode under a small forward bias.

It is assumed that the insulator does have some band structure, and has a conventional conduction band, as indeed is the case for devices incorporating II-VI compounds as semi-insulators. Batey[3] also reports the devices including insulating Langmuir-Blodgett films show current-voltage characteristics typical of the thermionic emission over an aggregate barrier presented by both the semiconductor and the insulator, with ideality factors very close to unity. Batey argues that the majority carriers must be travelling throughthe insulator by either a conduction band or some conduction level.

We can relate the electric fields in the insulator and semiconductor using Gauss' Law

$$\varepsilon_o \varepsilon_s F_s(V) = \varepsilon_o \varepsilon_i F_i(V) + Q_{ss}(V) \qquad (5.2)$$

with $Q_{ss}(V)$ being the surface charge at the semiconductor-insulator interface. The potential drop across the insulator $\Delta(V)$ is also given by $-F_i(V)\,\delta$, where δ is the insulator thickness. So using $F_i(V)$ from equation (5.2) in equation (5.1) we can now write

$$\phi_b(V) = \phi_m - X_s + \frac{\delta}{\varepsilon_o \varepsilon_i}\left[\varepsilon_o \varepsilon_s F_s(V) - Q_{ss}(V)\right] \qquad (5.3)$$

and for the special case of zero bias we have

$$\phi_b(0) = \phi_m - X_s + \frac{\delta}{\varepsilon_o \varepsilon_i}\left[\varepsilon_o \varepsilon_s F_s(0) - Q_{ss}(0)\right] \qquad (5.4)$$

From equation (5.3)

$$\phi_b(V) - \phi_b(0) = \frac{\delta}{\varepsilon_o \varepsilon_i} \left[\varepsilon_o \varepsilon_s (F_s(V) - F_s(0)) - (Q_{ss}(0) - Q_{ss}(V)) \right] \qquad (5.5)$$

Some of the MIS devices studied experimentally were driven at relatively high current densities ($10^5 Am^{-2}$). This, coupled with the existence of an insulator layer, means that the semiconductor is likely to approach a flat band condition and possibly have a negative diffusion potential $\psi_s(V)$ leading to an accumulation of electrons (negative charge) at the interface. Under these conditions it is clearly inappropriate to use the depletion approximation.

5.2.2 Electric Field in the Semiconductor

To find the electric field $F_s(V)$ in the semiconductor at the semiconductor-insulator barrier Poisson's Equation is solved in the semiconductor. At a point in the semiconductor corresponding to a diffusion potential ψ the charge density is given by:

$$\rho(\psi) = |e| \, (N_D^+ - N_A^- + p(\psi) - n(\psi)) \qquad (5.6)$$

where N_D^+ and N_A^- are the concentrations of ionised donor sites and occupied acceptor sites respectively. $p(\psi)$ and $n(\psi)$ are the hole and electron concentrations which can be expressed using Fermi-Dirac statistics as

$$p(\psi) = \frac{N_v}{1 + \exp\left[\dfrac{E_g - \Delta E_f - |e|\psi}{kT}\right]} \qquad (5.7)$$

and

$$n(\psi) = \frac{N_c}{1 + \exp\left[\dfrac{E_f + |e|\psi}{kT}\right]} \qquad (5.8)$$

N_c and N_v are the band edge density of states for the conduction and valence bands respectively and ΔE_f, as illustrated in Figure 5.1, is the difference in potential between the Fermi level and the conduction band edge. E_g is the bandgap of the semicondutor.

In the bulk of the semiconductor, where ψ is zero, the charge due to the free carriers is equal in magnitude but opposite in sign to that due to the donor and acceptor centres. Making use of this to re-express N_D^+ and N_A^- in terms of p(0) and n(0) using equations (5.7) and (5.8) for $p(\psi)$ and $n(\psi)$, Poissons' equations for the semiconductor can be written as

$$\frac{d^2\psi}{dx^2} = \frac{|e|}{\varepsilon_s\varepsilon_o}\left[N_c\left(\frac{1}{1 + \exp\left[\dfrac{\Delta E_f}{kT}\right]} - \frac{1}{1 + \exp\left[\dfrac{E_f + |e|\psi}{kT}\right]}\right) - N_v\left(\frac{1}{1 + \exp\left[\dfrac{E_g - \Delta E_f}{kT}\right]} - \frac{1}{1 + \exp\left[\dfrac{E_g - \Delta E_f - |e|\psi}{kT}\right]}\right)\right] \qquad (5.9)$$

Restricting our attention to n type materials, ΔE_f will be small and coupled with the fact that the bandgap E_g is in the region of 1eV or more for typical semiconductors, (GaP has a bandgap of 2.2eV), the last two terms can be ignored as they are negligible compared to the other terms over all values of ψ. Of the two remaining terms, the first dominates near to the interface for low biases, but in the bulk and at higher voltages it can be significant. If it were omitted then charge neutrality in the bulk would not be predicted. To solve equations (5.9) it is integrated over ψ from the bulk. To do this the left hand side of the equation can be written as

$$\int \left(\frac{d^2\psi}{dx^2}\right) d\psi = \int \left(\frac{d\psi}{dx}\right) d\left(\frac{d\psi}{dx}\right)$$

then carrying out the integration, the square of the electric field at the point corresponding to $\psi = \psi'$ is found to be

$$F_s^2(\psi') = \left(\frac{d\psi'}{dx}\right)^2 = \frac{2|e|N_c}{\varepsilon_s\varepsilon_o}\left[\frac{kT}{|e|}\ln\left(1+\exp\left[\frac{\Delta E_f+|e|\psi'}{kt}\right]\right) - \frac{\psi'}{1+\exp\left[\frac{-\Delta E_f}{kT}\right]} - \frac{kT}{|e|}\ln\left(1+\exp\left[\frac{\Delta E_f}{kT}\right]\right)\right] \qquad (5.10)$$

and the field at the semiconductor surface $F_s(V)$ is found by setting ψ' equal to the diffusion potential ψ_s and taking the square root. It is clear from the band diagram (Figure 5.1) that the sign of the field will be determined by the sign of ψ_s, if ψ_s is positive then $F_s(\psi_s)$ is negative and vice versa. Figure 5.2 shows the variation of

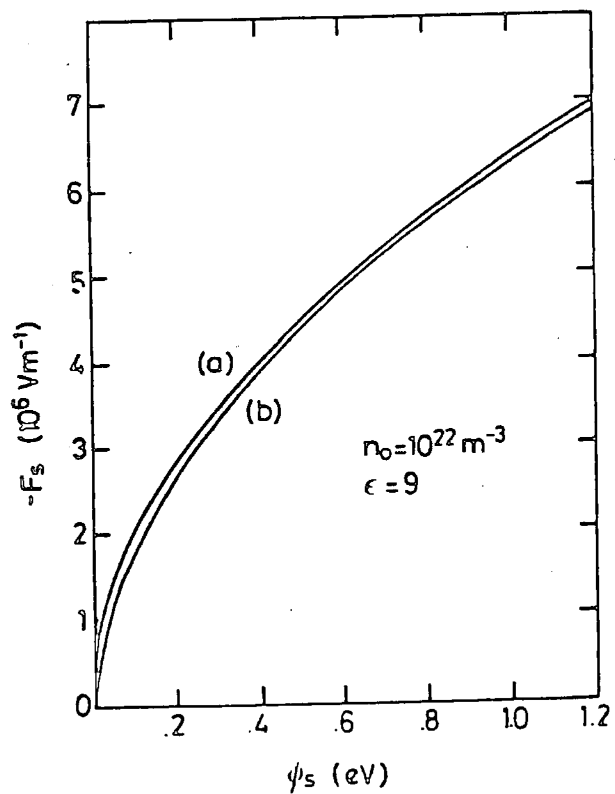

Fig. 5.2 : $F_s(0)$ plotted against diffusion potential for $N_D = 10^{22} m^3$;
a) depletion approximation;
b) equation (5.10).

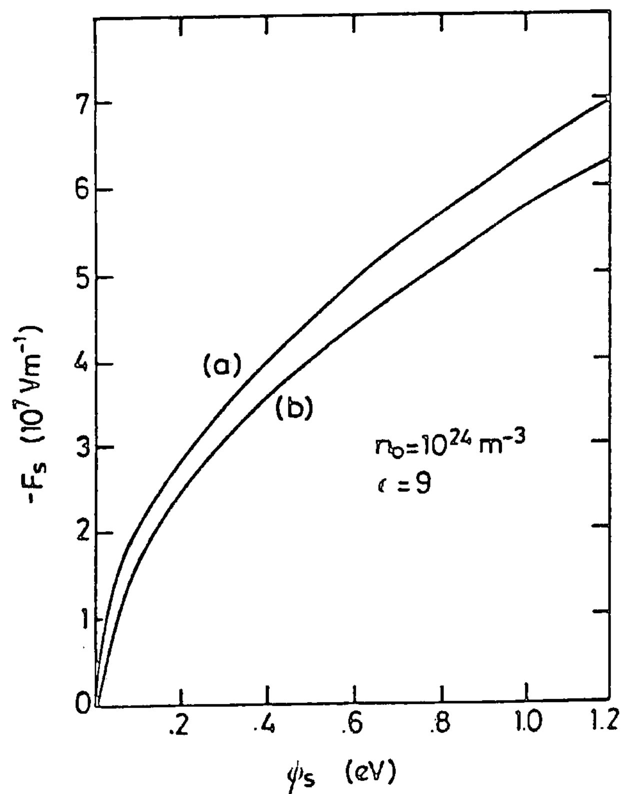

Fig. 5.3 : $F_s(0)$ versus diffusion potential for $N_D = 10^{24} m^{-3}$
a) depletion approximation;
b) equation (5.10).

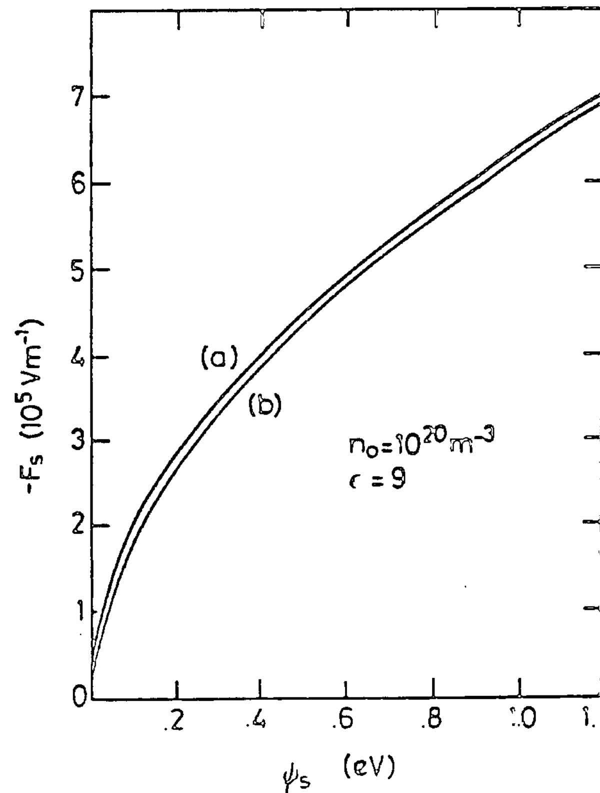

Fig. 5.4 : $F_s(0)$ versus diffusion potential for $N_D = 10^{20}$
a) depletion approximati
b) equation (5.10).

the field over different values of ψ_s. The chosen values for ε_s and the concentration of carriers are 9.0 and $10^{22}m^{-3}$ respectively, which are typical of the GaP used in the Langmuir-Blodgett film devices. The two curves, curve (a) for the depletion approximation and curve (b) obtained from equation (5.10), show a good degree of similarity with, as expected, a larger error at the lower values of diffusion potential. On this evidence the depletion approximation is a very good one with agreement to three significant figures at the higher values of ψ_s. Figures 5.3 and 5.4 show similar curves for different carrier concentrations and again the agreement with the depletion approximation is good.

5.2.3 Surface States

Surface states will be present at the semiconductor-insulator interface and also on successive molecular layers of a Langmuir-Blodgett film when this is used to form the insulator. Just as surface states on the semiconductor might lead to pinning of the Fermi level these "insulator-insulator" interface states might affect the behaviour of the barrier height under bias. Batey et al[2,3] has shown that, for various thicknesses of insulator in Au/Langmuir- Blodgett film/n-GaP devices, the semiconductor barrier height is essentially constant. This can be explained if it is assumed that the surface state is sufficiently high that the change in field, which must take place across the insulator with increasing thickness, is the result of a change in surface charge due to a slight variation in the semiconductor barrier height. If the insulator field were to remain constant with thickness then the semiconductor barrier height would be forced down, however

in doing this there would also be an increase in negative charge at the interface with more occupied surface states which would in turn act to reduce the field. If the surface state density is sufficiently large it is possible that the semiconductor barrier height need only drop a slight amount before an "equilibrium" position is found. The most dramatic change happens in going from one monolayer to three (in the fabrication process it is not possible to produce just two monolayers) as the ratio of the final to initial insulator thicknesses is the greatest. The actual change in field is dependent on the value of Δ (shown in figure 5.1). To produce a change in barrier height of less than 0.01eV, which is less than the accuracy of experimental measurements, the density of surface states has to be approximately $(4\times10^{18}) \times \Delta\, m^{-2}eV^{-1}$. If we take Batey's value of 1.6eV for the aggregate barrier height and 1.4eV for the semiconductor barrier height, then Δ is presumably of the order of 0.1eV, hence the required surface state density needs to be of the order of $10^{17}\ m^{-2}eV^{-1}$, which is by no means an exceptionally high value, and compares well with values for the surface state density obtained for various layer thicknesses from C^2-V by Batey[3].

One surprising result from Batey's data is that even at quite large insulator thicknesses the proportion of surface states which communicate with the metal is still quite large and with as many as 25 monolayers (~610Å) the ratio of states in communication with the metal to those in communication with the semiconductor is measured to be 1.7. This separation of surface states into two distinct species follows the work of Card and Rhoderick[5] described in Chapter Two.

Without any information about the distribution of those surface states at present, it is reasonable to assume a constant density across the band gap. It is also necessary to account for the relative communication of these states with the metal and semiconductor. To obtain an estimate of the relative numbers of these states, it is possible to fit a decaying exponential curve over thickness to known results[3] with some accuracy to give the ratio:

$$\frac{D_{sm}}{D_{ss}} = 8.93 \exp(-0.067N) \qquad (5.11)$$

where D_{sm} and D_{ss} are the densities of surface states in communication with the metal and the semiconductor respectively and N is the number of monolayers. The total density of surface states is of course given by $D_s = D_{sm} + D_{ss}$.

Returning to equation (5.5), it is now possible to make an estimate of the change in the surface charge with the change in barrier height. With the "metal states" an increase in semiconductor barrier height means that more states are above the Fermi level, as shown in Figure 5.5(a), and as these are now empty the change is positive and given by

$$Q_{ssm}(V) - Q_{ssm}(0) = |e| D_{sm}(\phi_b(V) - \phi_b(0)) \qquad (5.12)$$

The change due to the "semiconductor states" is rather more difficult to explain.

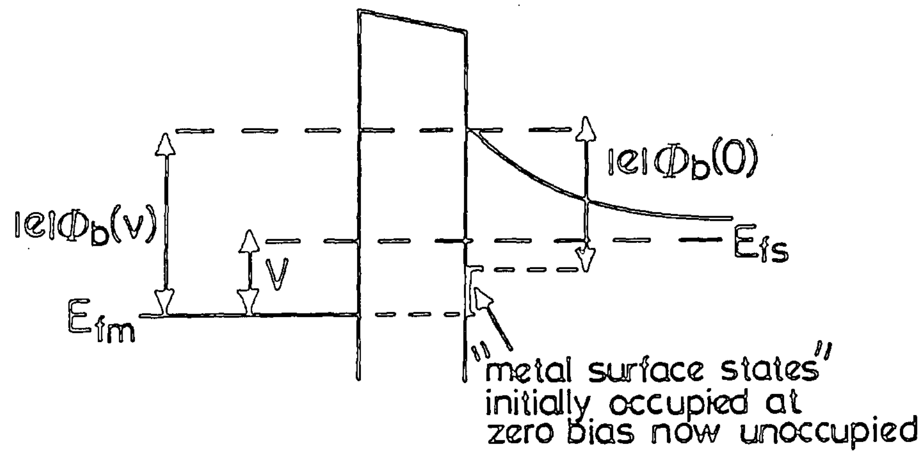

Fig. 5.5a) : Communication between surface states and the metal.

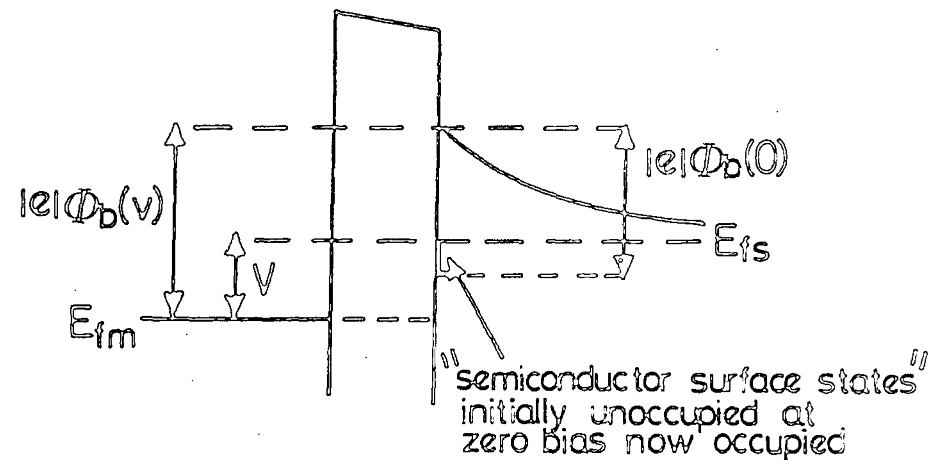

Fig. 5.5b) : Communication between surface states and the semiconductor.

The rise in the semiconductor Fermi level with voltage means that more states are filled but this is offset by the rise in the semiconductor barrier height. The rise in Fermi level with voltage is always greater than that for the barrier height as the voltage is also dropped across the depletion region so the overall change in surface charge will be negative with more states being occupied. This is shown diagrammatically in Figure 5.5.(b).

$$Q_{sss}(V) - Q_{sss}(0) = -|e|D_{ss}(V - (\phi_b(V) - \phi_b(0))) \tag{5.13}$$

Adding the changes described in equations (5.12) and (5.13) gives the overall change in the surface charge.

$$Q_{ss}(V) - Q_{ss}(0) = |e|D_s (\phi_b(V) - \phi_b(0)) - |e|D_{ss}V \tag{5.14}$$

5.2.4 Change in Barrier Height

Combining equations (5.14) and (5.5) gives an equation relating the change in semiconductor barrier height to applied voltage.

$$\phi_b(V)-\phi_b(0) = \frac{1}{\left(\frac{\varepsilon_i \varepsilon_o}{\delta} - |e|D_s\right)}\left[\varepsilon_s \varepsilon_o(F_s(0) - F_s(V)) + |e|D_{ss}V\right] \tag{5.15}$$

Unfortunately, with F_s from equation (5.10) it is not possible to produce an analytical expression for $\phi_b(V)-\phi_b(0)$ due to the equation's

transcendential nature, however it is relatively straightforward to find $\phi_b(V)-\phi_b(0)$ numerically using the Newton-Raphson iterative technique. Figure 5.6 shows the variation of $\phi_b(V)$ with V for a number of different insulator thicknesses with a total surface state density of $10^{17}m^{-2}eV^{-1}$ and Figure 5.7 is a similar set of curves for a smaller surface density of $10^{16}m^{-2}eV^{-1}$.

These results must be viewed with a certain amount of caution as the insulator has been treated as perfect when considering the distribution of electric field across the barrier and yet in allowing the communication of surface states with the metal Fermi level electrical conduction is implied. Provided that charge transport is small enough not to affect the electric fields in the device, it is a good approximation to treat the insulator as perfect.

The transport to and from the interface states does not have to be large and is unlikely to be so, however the majority carrier transport over the insulator barrier will become significant at higher voltages as the diffusion potential is reduced. The results in Figures 5.6 and 5.7 are therefore less trustworthy as the voltage increases and completely unreliable at the top end of the scale where diffusion potentials are of the order of -2.0eV. Also the field across the insulator becomes very high at the larger voltages ($\sim 10^8 Vm^{-1}$) and there is the additional problem of dielectric breakdown.

Despite the reservations expressed above, Figures 5.6 and 5.7 do serve to give some idea of the behaviour of the bands, at least at the

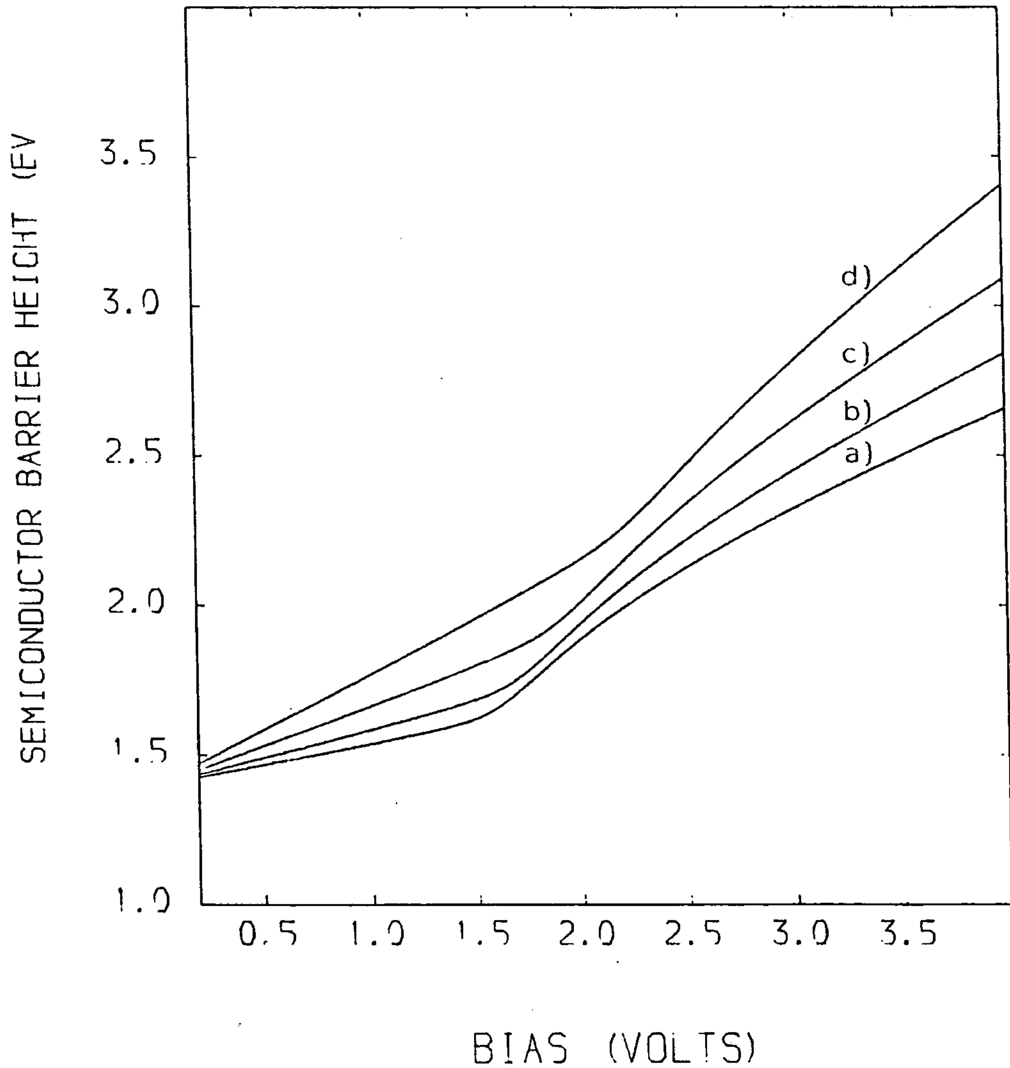

Fig. 5.6 : Variation of ϕ_b with V for $N_D = 10^{22} m^{-3}$ and $D_s = 10^{17} eV^{-1} m^{-2}$ assuming no injection current a) 125Å; b) 275Å; c) 375Å and d) 525Å.

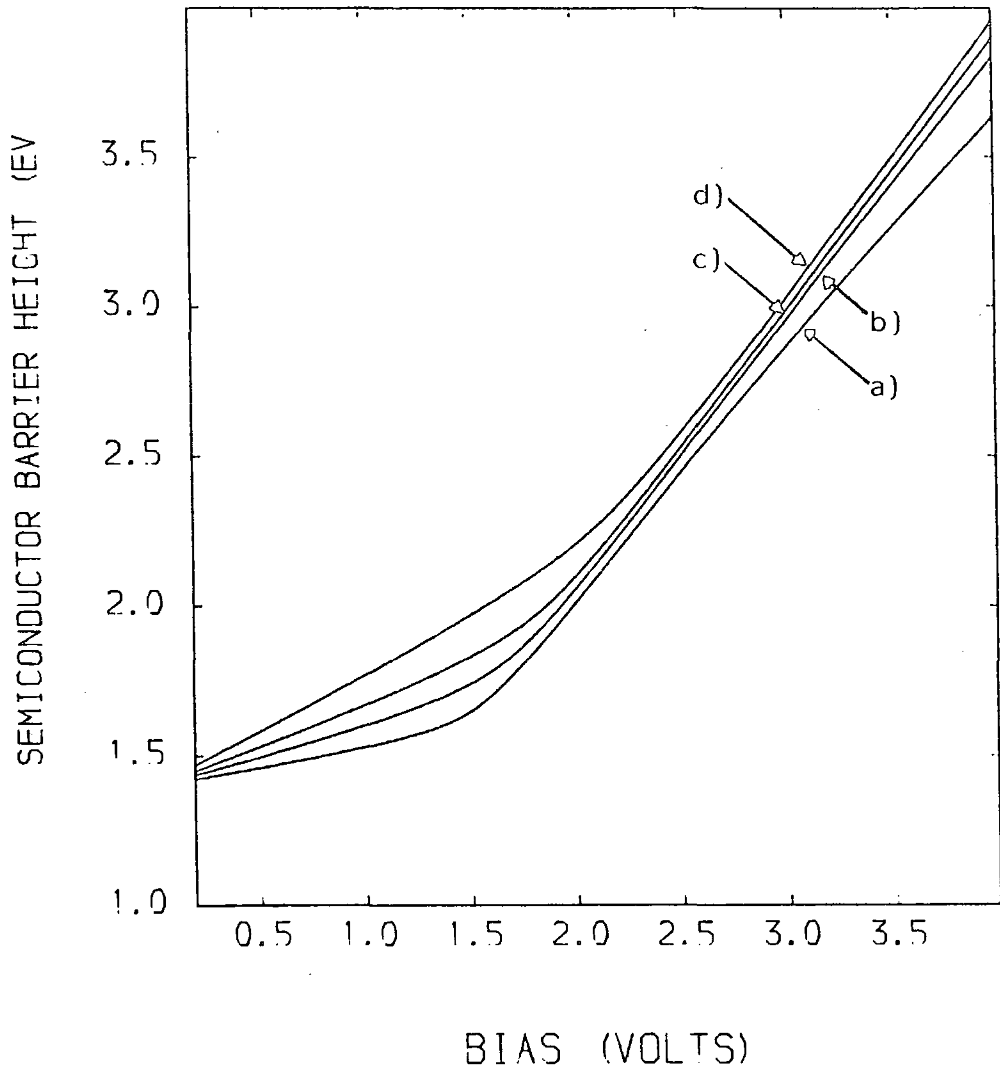

Fig. 5.7 : Variation of ϕ_b with V for $N_D = 10^{22} m^{-3}$ and $D_s = 10^{16} eV^{-1} m^{-2}$ assuming no injection current a) 125Å; b) 275Å; c) 375Å and d) 525Å.

lower voltages. Even at the lower surface state density the semiconductor barrier height is effectvely pinned at a particular value by the interface charge for the thinner samples. It is not until the diffusion potential approaches zero at a bias around 1.5V, that there is any real change. However it is at this point, with the conduction band edge of the semiconductor approaching the height of the aggregate barrier, that the current due to electrons emitted over the barrier starts to become too large to be ignored. For one thing, the bulk resistance due to the semiconductor and its substrate starts to have an effect on the general characteristics.

At large insulator thicknesses the pinning is naturally less pronounced as a large proportion of the surface states communicate with the semiconductor as opposed to the metal,and the barrier rises with the voltage and the semiconductor Fermi level. The behaviour of the semiconductor barrier height against insulator thickness is shown in Figure 5.8. Results for two voltages are shown. The first set is for a bias of 1 Volt which means that the conduction band edge is still about 0.5eV below the top of the estimated insulator barrier of 1.6eV. The current due to the thermionic emission over the barrier is still fairly small and the effects of the semiconductor bulk are negligible.

Figure 5.8 is not exactly comparable with Figures 5.6 and 5.7 because in the latter the exact experimental values of D_{sm}/D_{ss} for the different insulator thicknesses have been used whereas equation (5.11) has been used in Figure 5.8. However any difference is slight.

One apparently strange feature is that, at 1V, the change in ϕ_b is

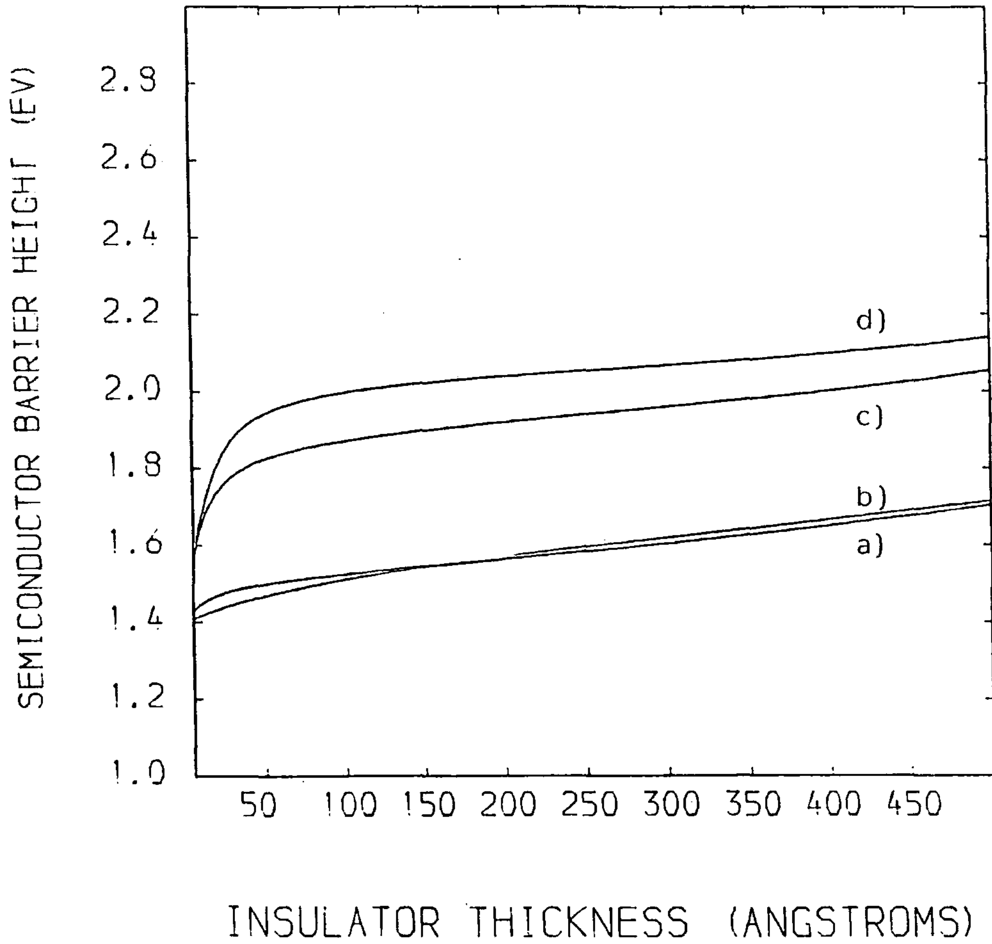

Fig. 5.8 : Variation of ϕ_b over insulator thickness for $N_D = 10^{22} m^{-3}$ and applied voltage and D_s of a) IV and $10^{17} eV^{-1} m^{-2}$, b) 1V and $10^{16} eV^{-1} m^{-2}$; c) 2V and $10^{17} eV^{-1} m^{-2}$ and d) 2V and $10^{16} eV^{-1} m^{-2}$.

less for the lower surface state density at the lower thicknesses. At first the opposite might be expected to be the case as in standard Schottky barrier theory. However, it is necessary to take the smaller number of surface states communicating with the semiconductor into account. These states are important because the semiconductor Fermi level rises faster than the barrier height with increasing bias and a much larger proportion of the "semiconductor surface states" are affected compared to the "metal surface states".

The effect of the surface states in communication with the semiconductor rather than the metal is a steady rise in semiconductor barrier height with voltage. This is because the surface state pinning level follows the semiconductor level, so the "semiconductor surface states" act to push up the barrier height opposing the effect of the "metal surface states". At a bias of 1 Volt the "semiconductor surface states" seem to dominate slightly so the increase in surface state density will lead to a small rise in barrier height.

The curve in Figure 5.8 for a bias of 2 Volts illustrates another aspect of the effect of surface state communication with semiconductor. In this case the field $F_s(\psi)$ at the interface is now inverted and the effect on the surface state is also reversed. The larger surface state density leads to a lower semiconductor barrier height.

5.3 DEVICE CHARACTERISTICS AT HIGH BIASES

5.3.1 Electron Current

So far, a negligible electron current from the semiconductor into the

metal has been assumed. At higher voltages this is not the case and some devices have been driven at current densities in the region of $10^5 Am^{-2}$ with external voltages of around 2 and 3 volts. Figures 5.9 and 5.10 show current-voltage characterisitics obtained by Batey[3] for Au/Langmuir-Blodgett film/n-GaP devices incorporating Cadmium Stearate and ω-Tricosenoic acid respectively as insulators. In the characteristics three separate regions can be discerned.

The first, region (a), is quite typical of thermionic emission, being linear in a Log J vs V plot, while region (c) is expected due to bulk resistance effects in the semiconductor and is typical of the behaviour of curves for Schottky barriers at higher voltages. Region (b), however, is a departure from Schottky barrier behaviour. It has been suggested[3] that this behaviour is due to the conduction mechanism in the Langmuir-Blodgett films. It is, however, very noticeable that Figures 5.9 and 5.10 corresponding to different Langmuir-Blodgett films are very similar and this suggests that is it the semiconductor which controls the current in region (b).

5.3.2 Modelling the Majority Carrier Current

The nature of the curve in region (a) of Figure 5.9 and 5.10 indicates thermionic emission and it is reasonable to attempt to describe the electron current into the metal using thermionic emission theory in the presence of a finite insulator barrier. It must be recognised that the current flows through the semiconductor and therefore part of the external voltage will be dropped across the semiconductor bulk. The current is small at low biases but as the bias approaches the barrier

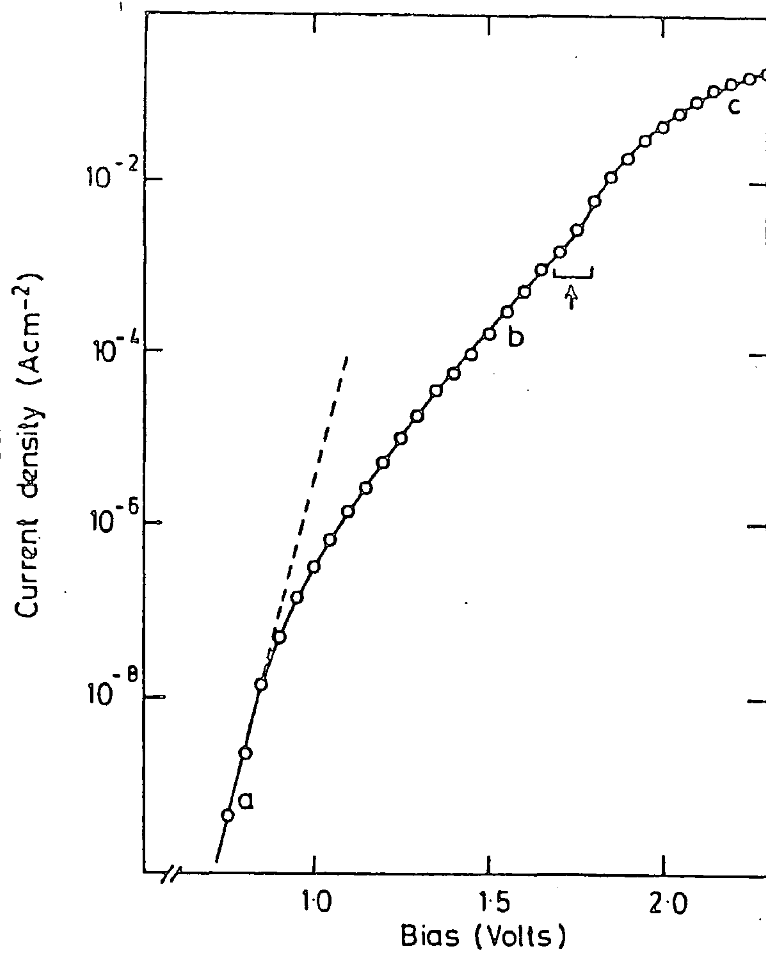

Fig. 5.9 : Experimental J-V characteristic for a 5 monolayer Au/Cadmium Stearate/n-GaP MIS diode (Reference 3.)

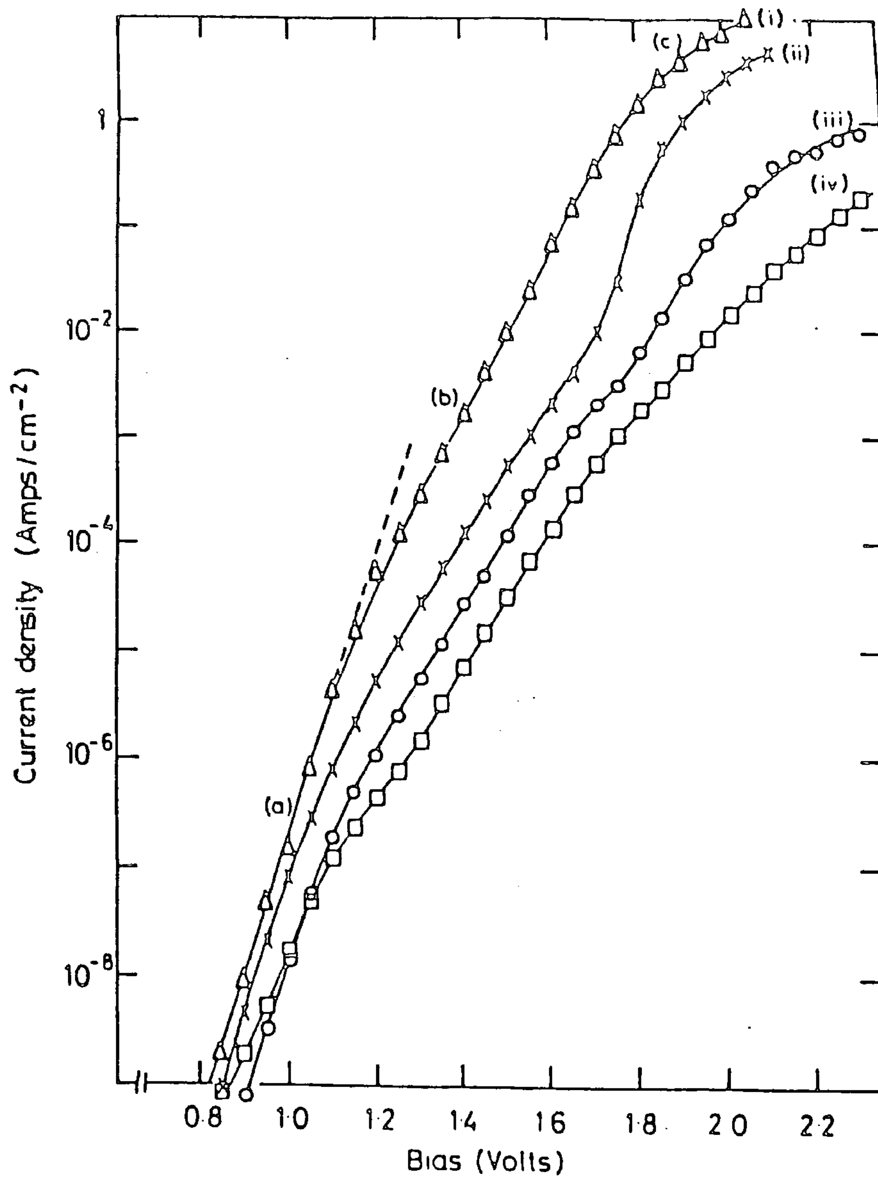

Fig. 5.10 : Experimental J-V characteristic for an Au/ω-Tricosenoic Acid/n-GaP MIS diode incorporating i) one; ii) five; iii) seven and iv) nine monolayers (Reference 3).

height the current becomes substantial and bulk resistance effects are expected theoretically, and observed experimentally.

With some of the applied voltages across the semiconductor it is necessary to use the thermionic emission theory with some care, taking account of the rise in the conduction band edge. It is also necessary to consider the effect on the electric field at the insulator-semiconductor interface due to the non-zero field in the bulk. The voltage drop in the bulk implies an electric field which is assumed to be constant over the whole length of the semiconductor. The situation illustrated in Figure 5.1 with flat bands in the bulk is changed to either that shown in Figure 5.11 when there is still some depletion, or to that shown in Figure 5.12 for electron accumulation at the interface. Splitting the potential of the conduction band edge into two components, one due to the bulk field and the other due to the band bending at the barrier, the total change in potential with distance x from the interface is given by :

$$\frac{dE_c}{dx}(x) = F(x) = \frac{d\psi}{dx} + F_B \qquad (5.16)$$

where F_B is the constant bulk field and ψ is again the diffusion potential but is now defined in respect to the semiconductor Fermi level which is assumed to be sloping at some constant gradient. Also by bearing in mind the sloping Fermi level, equations (5.7) and (5.8) can be used to express the carrier concentrations. So by solving Poissons equations (equation (5.9)) the field due to the band bending, $d\psi/dx$, as a function of ψ is given by equation (5.10). Substituting into equation (5.16), the

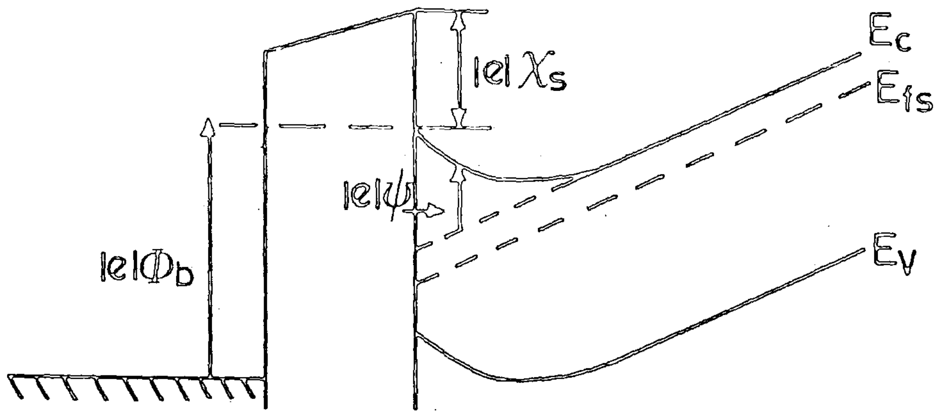

Fig. 5.11 : Schematic diagram of an MIS diode under high bias with depletion at the insulator-semiconductor interface.

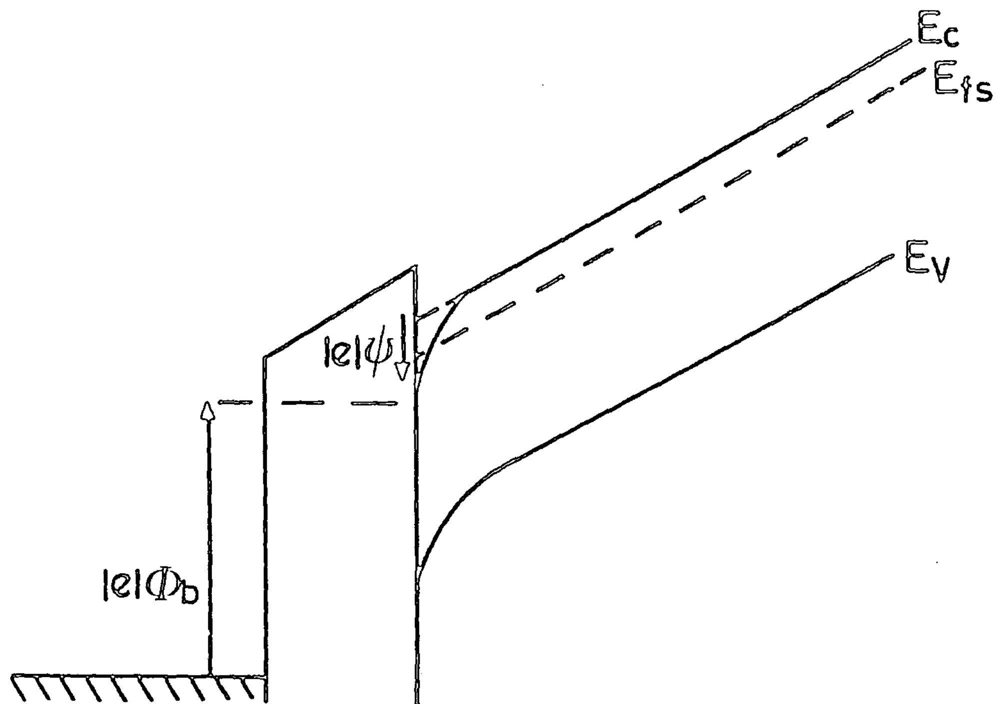

Fig. 5.12 : Schematic diagram of an MIS diode under high bias with accumulation in the semiconductor.

total field is

$$F(\psi) = F_B - \text{sgn}(\psi)\left(\frac{|e|N_c}{\varepsilon\varepsilon_o}\right)^{\frac{1}{2}}\left[\frac{kT}{|e|}\ln\left(1+\exp\left[\frac{\Delta E_f+|e|\psi}{kT}\right]\right) - \frac{\psi}{1+\exp\left[\frac{-\Delta E_f}{kT}\right]} - \frac{kT}{|e|}\ln\left(1+\exp\left[\frac{\Delta E_f}{kT}\right]\right)\right]^{\frac{1}{2}} \quad (5.17)$$

This is the first correction due to the bulk field that is necessary. The other thing that needs to be considered is the treatment of the thermionic emission over the barrier at the higher biases.

At low biases, with little of the applied voltage needed to drive the small current through the semiconductor bulk and therefore virtually all of the bias across the barrier region, the current is accurately described by equation (2.19) which is reproduced here for reference:

$$J_e = A^*T^2\exp\left(\frac{-|e|\phi}{kT}\right)\left[\exp\left(\frac{|e|V}{kT}\right) - 1\right] \quad (5.18)$$

where ϕ is now the aggregate barrier height. In deriving this result Henisch[5] sets an imaginary boundary, at a distance λ_B from the insulator-semiconductor interface, and assumes that any electron which crosses this boundary and is sufficiently energetic to surmount the barrier will reach the metal. This is an approximation equivalent to setting λ_B equal to the electron mean free path in the semiconductor. The derivation of equation (5.18) assumes that the Fermi level is constant

in the semiconductor. However, with high applied biases this is not the case and the Fermi level at $x = \lambda_B$ is increased by $\lambda_B F_B$ Volts and as it is the distribution of electrons at $x = \lambda_B$ that will govern the current over the barrier, the voltage V in equation (5.18) representing the potential across the insulator needs to be replaced by the potential across the insulator and up to $x = \lambda_B$ in the semiconductor, given by

$$V_{TE} = V_I + \lambda_B F_B \tag{5.19}$$

V_{TE} is an effective voltage for use in calculating the thermionic emission current and V_I is the voltage dropped across the insulator alone. If the total applied bias is V then it is straightforward to rewrite the field in the semiconductor bulk F_B as $(V-V_i)/W_B$, where W_B is the semiconductor thickness, and combine it with equations (5.18) and (5.19) to produce a revised expression for the thermionic emission current.

$$J_e = A^* T^2 \exp\left(\frac{-|e|\phi}{kT}\right)\left[\exp\left(\frac{|e|}{kT}\left(V_I\left(1-\frac{\lambda_B}{W_B}\right)+\frac{V\lambda_B}{W_B}\right)\right)-1\right] \tag{5.20}$$

5.3.3 Effective Barrier Height

The barrier height ϕ is given by the highest part of the insulator barrier. If the effects of image charge are included the barrier is modified somewhat with the potential barrier being rounded off by the Coulombic image charge field and resulting in a reduction in the barrier height. The basic theory of image charge barrier lowering is

reviewed in Chapter Two where the effect on ϕ is derived for a constant negative field in the barrier.

The profile of the insulator barrier depends on the thickness of the insulator as well as the bias applied to the device. The three possible profiles are illustrated in Figure 5.13. At low bias when the applied field across the insulator is negative, the profile can be either of those illustrated by Figures 5.13(a) and 5.13(b) depending on the insulator thickness. In Figure 5.13(a), corresponding to the case treated in Chapter Two, the insulator is wide enough to allow the image charge field to fall to a value equal and opposite to the applied field within its width and there is a distinct peak, whereas in Figure 5.13(b) this is not reached due to the thinner insulating barrier and the maximum barrier height is at the semiconductor-insulator interface. If the applied field is positive, however, only the situation in Figure 5.13(c) is possible, because the applied field is of the same sign as the image charge field, and the maximum is always at the semiconductor-insulator interface. In the last two cases it is straightforward to write the revised barrier height as

$$\phi = \phi_b + X_s - \frac{|e|}{4\pi\varepsilon_i\varepsilon_o(2\delta)} \tag{5.21}$$

where the last term is the correction due to the Coulombic image charge potential.

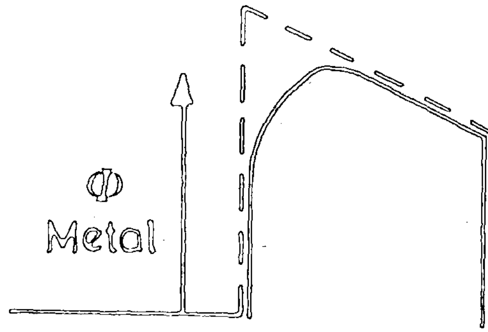

a)

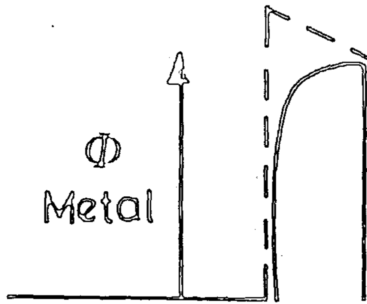

b)

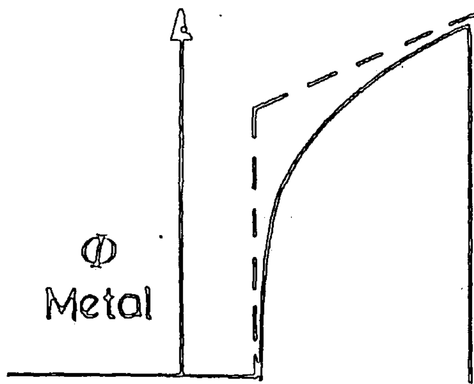

c)

Fig. 5.13 : Modification of the insulator barrier profile by image charge effects: a) and b) negative insulator field; and c) positive insulator field.

5.3.4 Effect of the Potential Step

Just as electrons entering the metal are funnelled into a narrow cone due to the conservation of momentum (see Chapter Two), so we can expect that majority carriers approaching the potential step at the insulator-semiconductor interface will need to be inside a similar cone if they are to be transmitted into the insulator. With a Maxwellian distribution, the mean energy of electrons crossing the insulator is $\frac{3}{2}$ kT above the barrier height. For an electr on of this energy to be transmitted throught the interface, it must be incident within a cone about the interface normal with half angle given by

$$\theta = \tan^{-1}\left[\left(\frac{m_i}{m_s X_s}\left(\frac{3}{2} kT + \phi - \phi_b - X_s + \frac{|e|}{8 \varepsilon_i \varepsilon_o \delta}\right)\right)^{\frac{1}{2}}\right] \tag{5.22}$$

The smallest values of θ will occur with the smallest clearance of the electrons over the potential step. This will occur when the maximum of the insulator barrier occurs at the insulator-semiconductor interface. In such a case, with the barrier height given by equation (5.21), the value of θ obtained is approximately 25° depending on the value of X_s. Assuming the distribution of electrons reaching the interface to be isotropic, the fraction of them in this cone will be $(1-\cos^2\theta)$ and using the value obtained above for θ it means that only about 20% of the electrons will be transmitted. This result can be seen to be supportive of the thermionic emission model, as the large number of carriers unable to cross the interface will be reflected back into the semiconductor helping to keep thermal equilibrium right up to the boundary. It

also supports the use of the effective voltage V_{TE}, defined in equation (5.19), as the only majority carriers transmitted will have to travel in a direction close to the normal of the interface and therefore the measurement of the mean free path back along the normal give a fair estimate of the point in the semiconductor at which the electrons actually being transmitted can be reasonably expected not to experience any further interactions. As in standard kinetic theory, it can be expected that the rate of carriers impinging on the interface from directions close to the normal will be greater than those at the larger angles, so bearing this in mind, no correction has been attempted in the following sections to account for the potential step.

At the metal-insulator interface, the electrons are focussed into a narrow cone, but in this case all electrons reaching the interface are able to be transmitted.

5.3.5 Current-Voltage Characteristics

We are now in a position to produce more realistic predictions of the behaviour of the semiconductor barrier height at high bias. The current across the barrier, given by equation (5.20), must be equal to the current in the bulk of the semiconductor. The bulk conduction is assumed to be ohmic, and hence:

$$\frac{(V-V_I)}{R_B} = A^*T^2 \exp\left(\frac{-|e|\phi}{kT}\right)\left[\exp\left(\frac{|e|}{kT}\left(V_I\left(\frac{1-\lambda_B}{W_B}\right) + \frac{V\lambda_B}{W_B}\right)\right) - 1\right] \tag{5.23}$$

Unfortunately this equation is trancendendal, and V_I is found numerically using the Newton Raphson technique. Equation (5.15), giving an expression for the change in semiconductor barrier height with voltage for low biases, can be readily adapted for use at higher voltages by using V_I, the voltages across the insulator, instead of the total voltage V. This is because the semiconductor Fermi level at the interface with the insulator only rises by V_I. Combining the revised form of equation (5.15) with equation (5.17), which defines the semiconductor field $F_s(V)$, we can now model the band behaviour at higher voltages as the effect of higher current on the barrier and bulk have been taken into account.

Figure 5.14 shows current density-voltage characteristics calculated using material constants consistent with the Au/Langmuir-Blodgett film/n-GaP devices for insulator film thickness of 1,7,9,11 monolayers, and assuming a constant surface state density of $10^{17}m^{-2}eV^{-1}$. Figure 5.15 shows similar curves for a surface state density of $5x10^{16}m^{-2}eV^{-1}$. In both cases there is barrier limited conduction at the lower voltages moving directly to the bulk limited case at an external bias of around 1.5Volts. These results obviously do not predict the region (b) in Figures 5.9 and 5.10. However, the work of Calandra and Santoro[7] shows that rather than having a continuous distribution of surface states GaP has a band of states beginning approximately 0.7eV above the valence band edge and with a width of about 0.7eV. Unfortunately the authors do not give the density of states. Their work is somewhat borne out by the experimental results of Straub et al[8] showing a sharp rise in the surface state density, starting at about the same point as predicted by Calandra and Santoro.

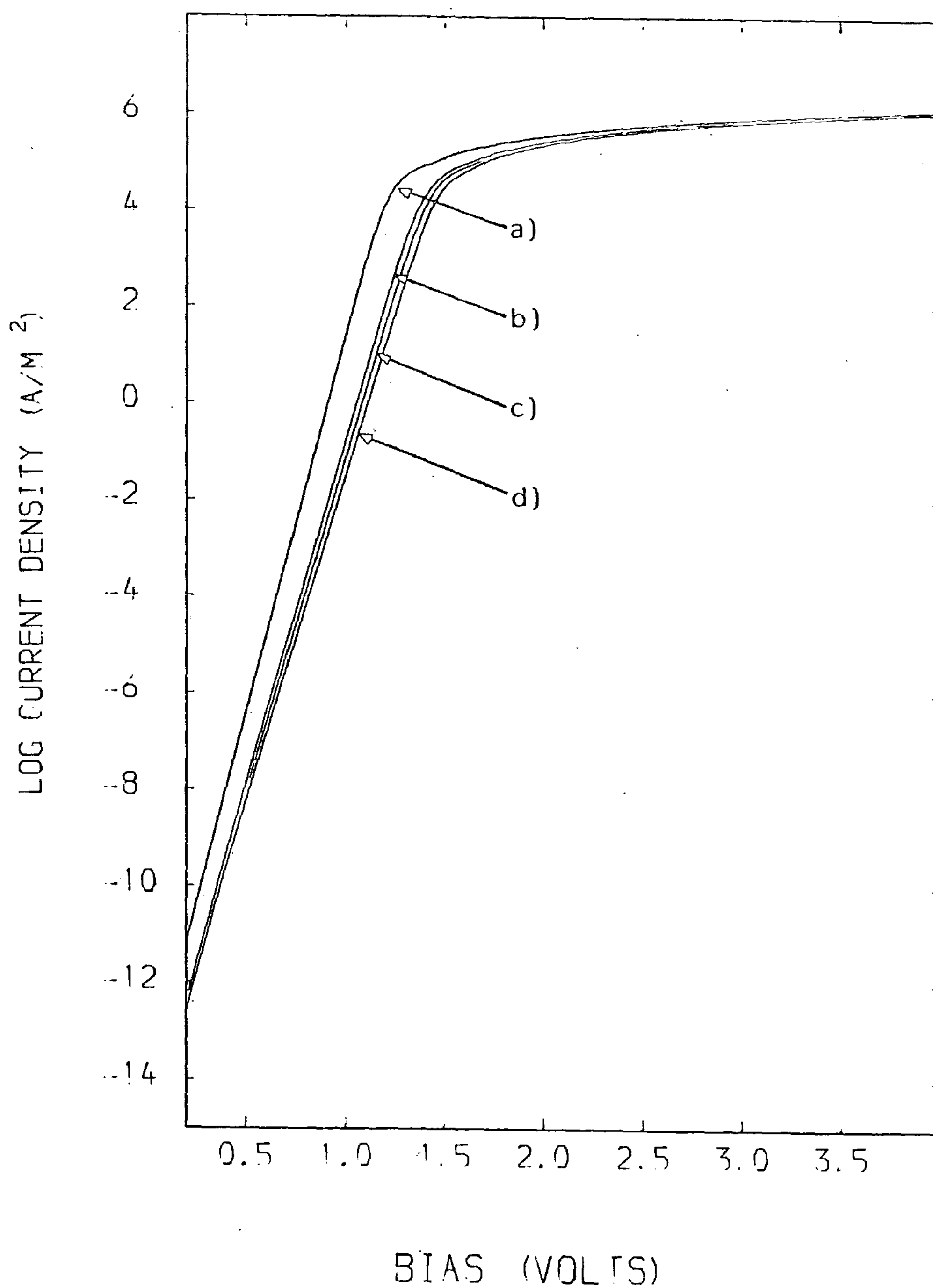

Fig. 5.14 : Theoretical J-V characteristic for an Au/Cadmium Stearate/n-GaP diode with unifrom density of surface states = $10^{17} eV^{-1} m^{-2}$ and incorporating a) one; b) five; c) seven and d) nine monolayers.

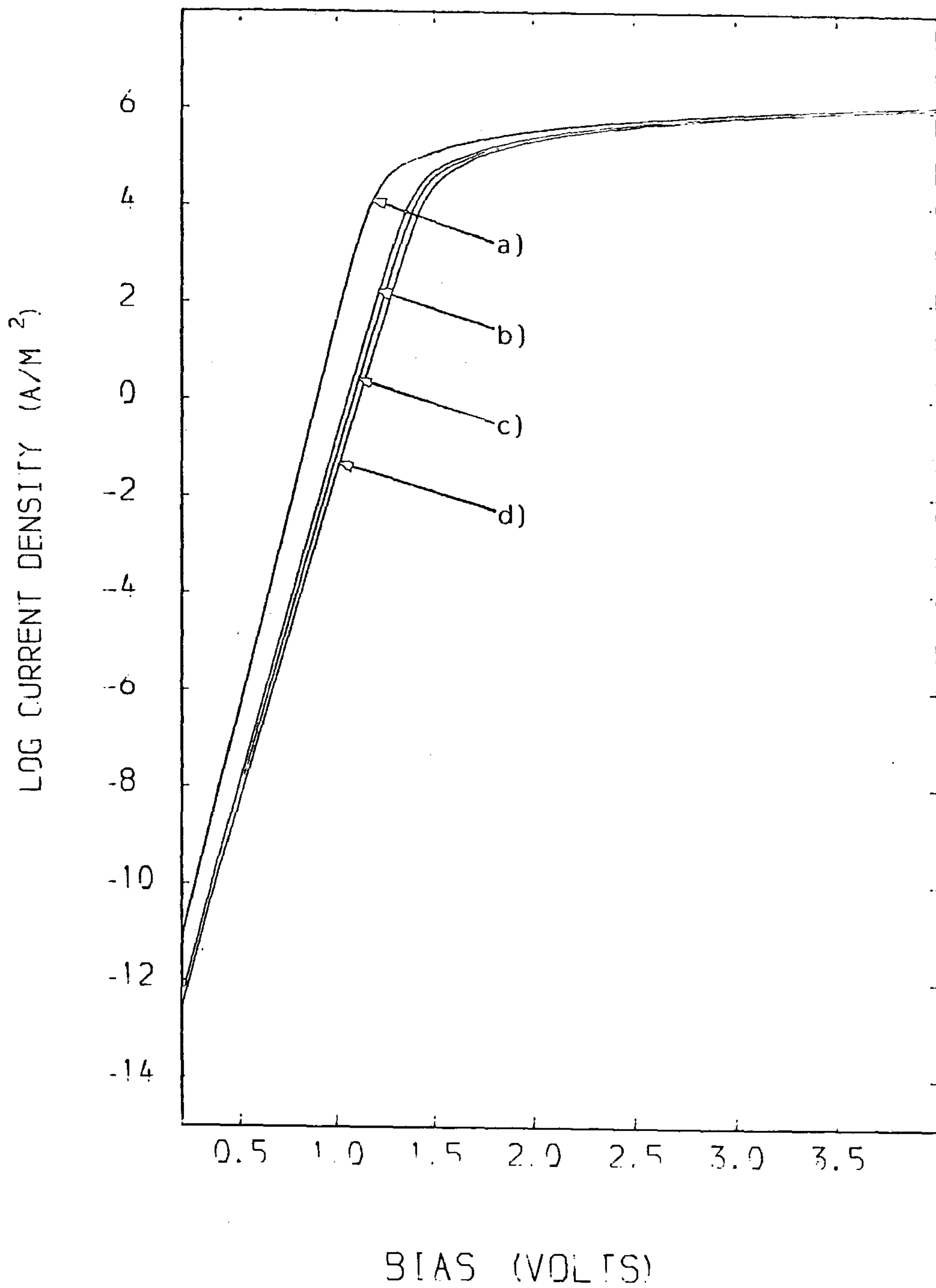

Fig. 5.15 : Theoretical J-V characteristic for an Au/Cadmium Stearate/n-GaP diode with uniform density of surface states = $5 \times 10^{16} eV^{-1} m^{-2}$ and incorporating a) one; b) five; c) seven and d) nine monolayers.

However, although a maximum is reached, the theoretically predicted fall off in the surface state band 1.4eV above the valence band edge, is not so pronounced. It is interesting that the band's lower edge, being 1.5eV below the conduction band edge, seems to correspond to a pinned Fermi level and a barrier height of 1.4eV.

Representing the intrinsic band by a region of constant surface state density of width 1.2eV, as suggested by the results of Straub et al, the current density-voltage characteristics now obtained are shown in Figures 5.16 and 5.17 for densities of $10^{17}m^{-2}eV^{-1}$ and $5x10^{16}m^{-2}eV^{-1}$ respectively. There are now three distinct regions to the curve, the first, at low voltages, is due to normal thermionic emission with the barrier height effectively constant. However, as the voltage rises, the barrier height gradually becomes larger until the second region is reached, where the metal Fermi level moves below the surface state band. Any change in surface charge is now entirely due to the behaviour of the semiconductor Fermi level, hence the barrier height rises more rapidly following E_{FS} in Figures 5.11. Also the diffusion potential is reduced more slowly and the rise in current is reduced. These conditions hold until the semiconductor Fermi level moves above the surface state band, and is no longer able to push up the barrier height. There is then a sudden rise in the current and finally the flattening off due to the bulk resistance effects.

Of the two sets of characteristics those more closely resembling the experimental curves are in Figure 5.17 and indeed the match seems to be quite good. The higher surface state density in Figure 5.15

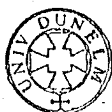

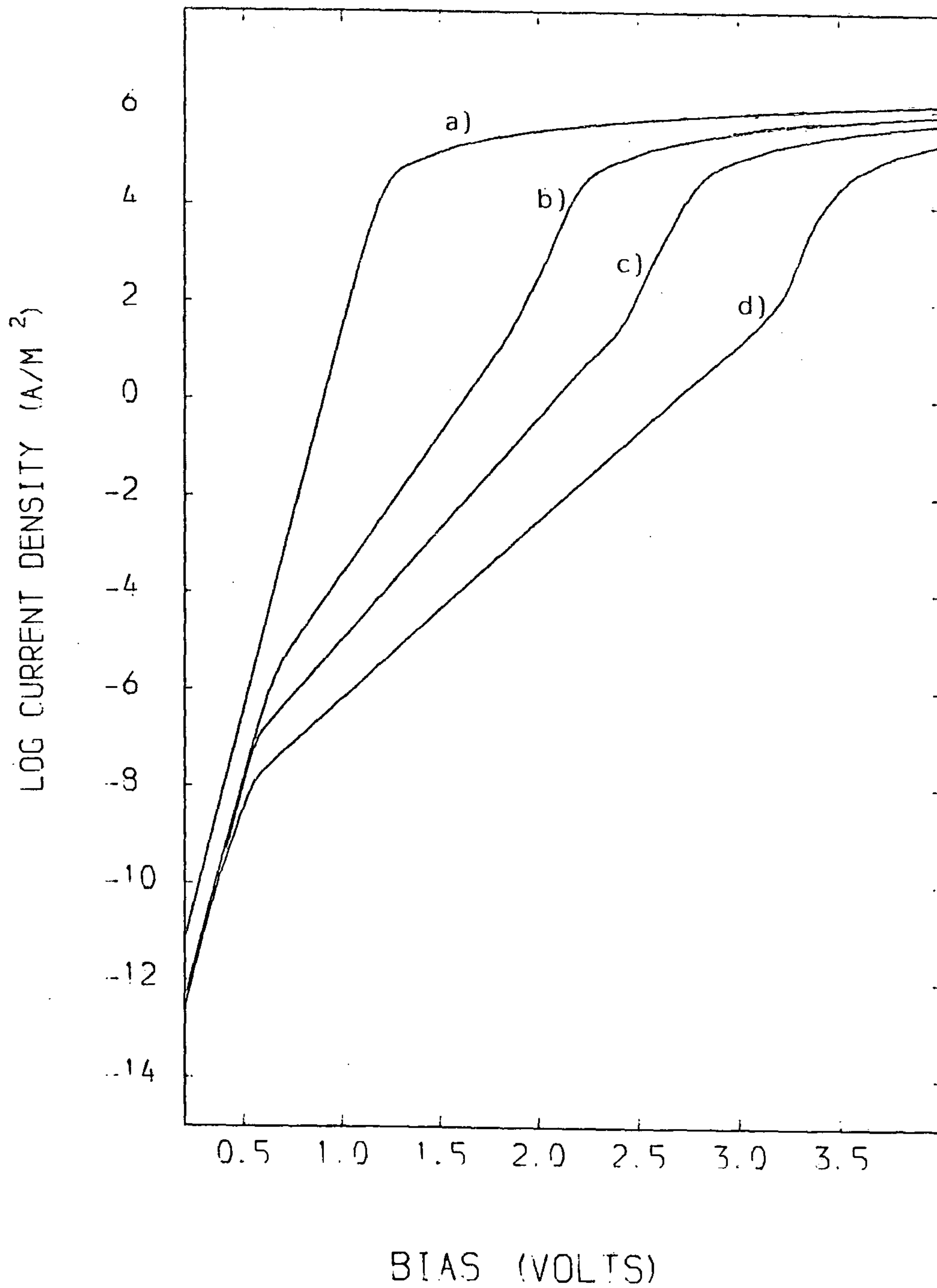

Fig. 5.16 : Theoretical J-V characteristic for an Au/Cadmium Stearate/n-GaP diode with $D_s = 10^{17} eV^{-1} m^{-2}$ and incorporating a) one; b) five; c) seven and d) nine monolayers.

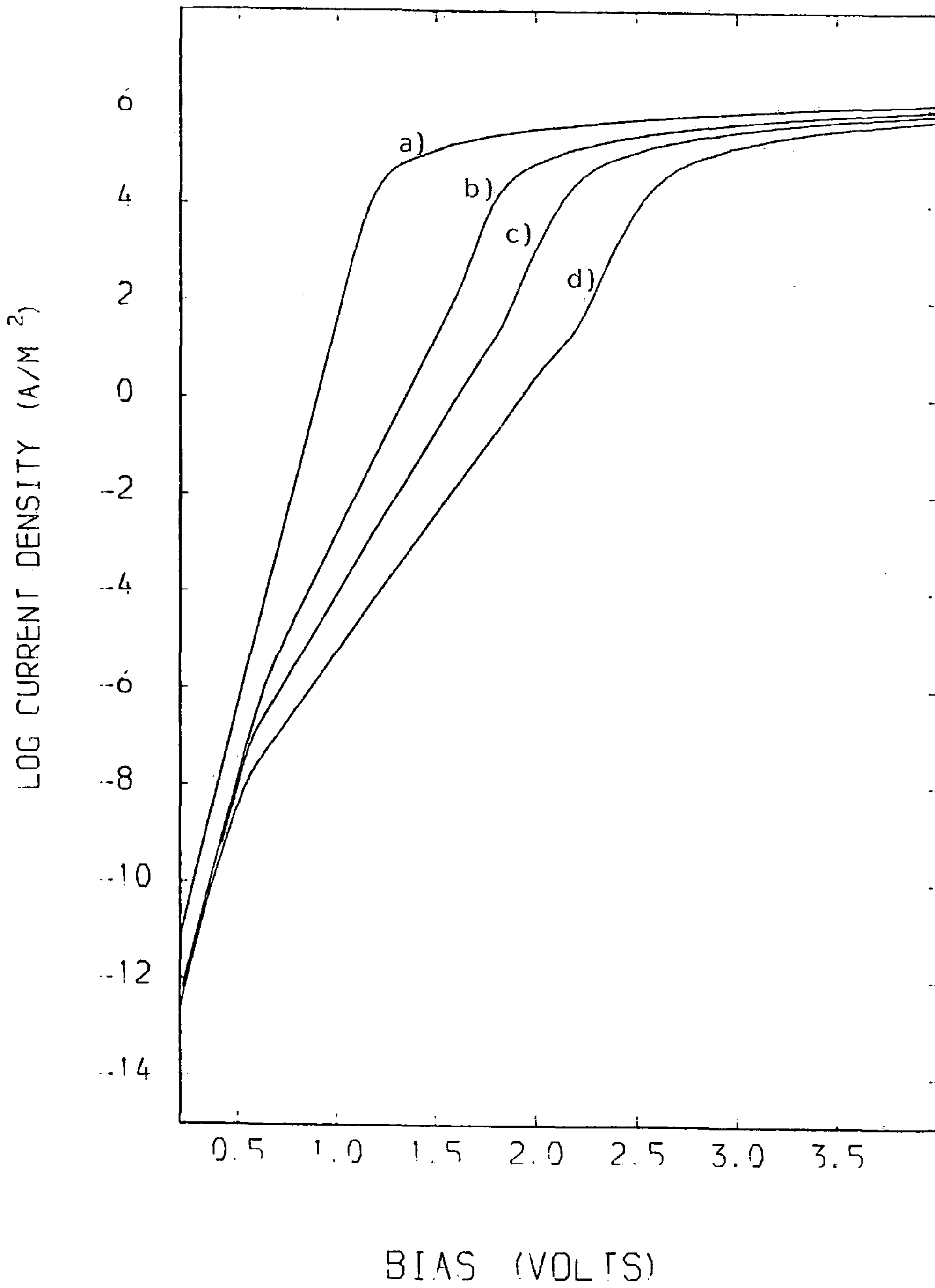

Fig. 5.17 : Theoretical J-V characteristic for an Au/Cadmium Stearate/n-GaP diode with $D_s = 5\times10^{16} eV^{-1} m^{-2}$ and incorporating a) one; b) five; c) seven and d) nine monolayers.

acts to push the barrier height up more in region (b) and the rise in the current is more markedly affected. It also means that the semiconductor Fermi level does not get above the interface state band until higher voltages.

5.3.6 Barrier Height Variations

Figure 5.18 shows the variations of the semiconductor barrier height in the calculation of the current voltages characteristics. The surface state density is $5 \times 10^{16} m^{-2} eV^{-1}$, the same as in Figure 5.17, which gives a good fit to the experimental results of Batey[3] reproduced in Figures 5.9 and 5.10. The curves, in Figure 5.18, are indicative of the fact that at the higher biases most of any additional external voltage is used in overcoming the bulk resistance, with the barrier resistance offering little impediment to carrier flow. Hence the barrier height is essentially constant.

The variation of the barrier height with insulator thickness is shown in Figure 5.19 for constant external biases of 1,2,3 and 4 Volts. The thicker the insulator the more of the external voltage it takes up, leading to the rise in ϕ_b, and eventually all of the bias is dropped across the barrier region. The point at which the applied bias is virtually all dropped across the insulator corresponds to a fairly sudden decrease in the gradient of the curve. The further increase in the semiconductor barrier height is due to the increase in the proportion of interface states communicating with the semiconductor with increasing insulator thickness and as a result ϕ_b being more effectively pushed up by E_{FS}.

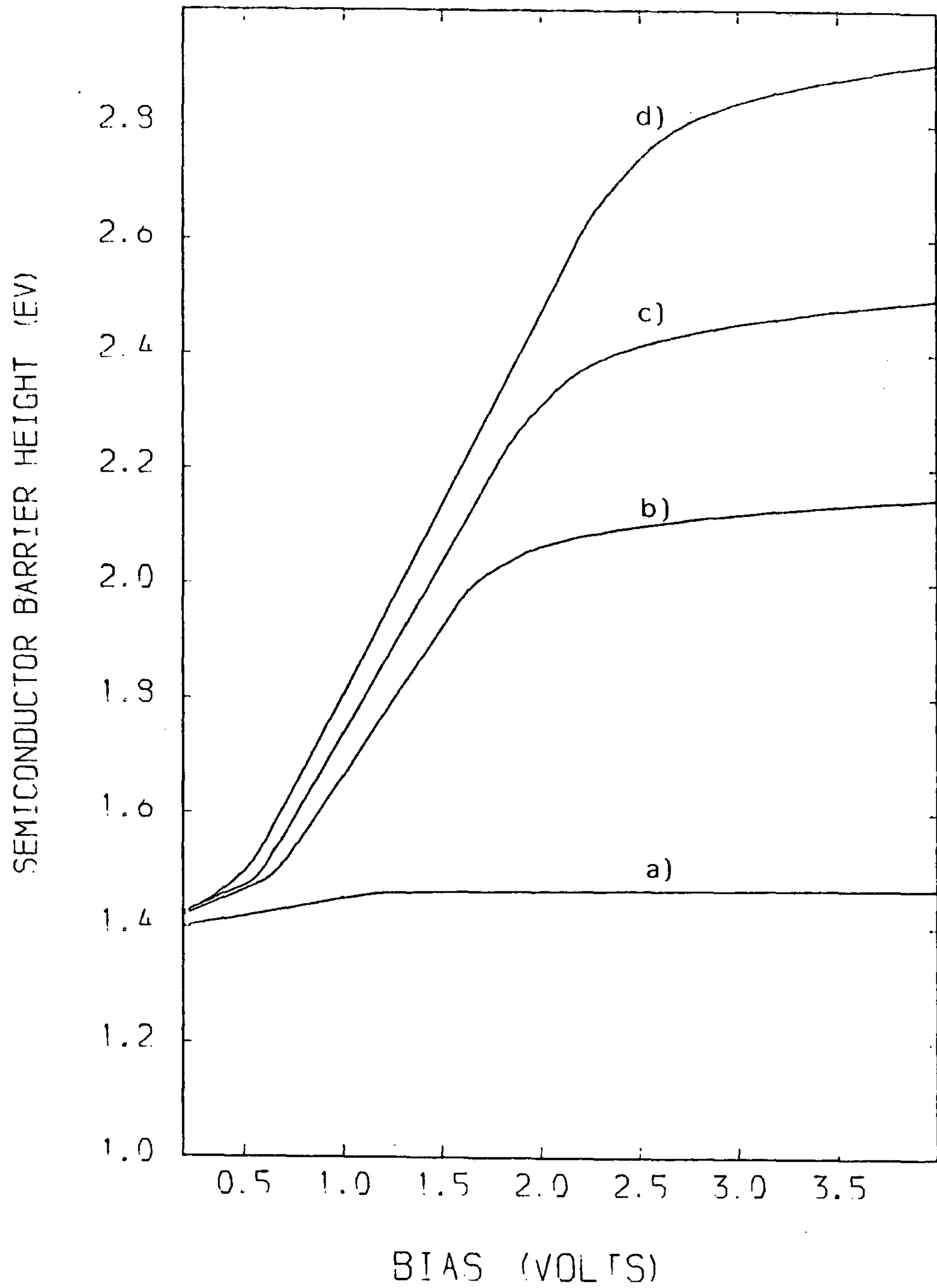

Fig. 5.18 : Theoretical variation of ϕ_b with external bias for an Au/Cadmium Stearate/n-GaP diode incorporating a) one; b) five; c) seven and d) nine monolayers.

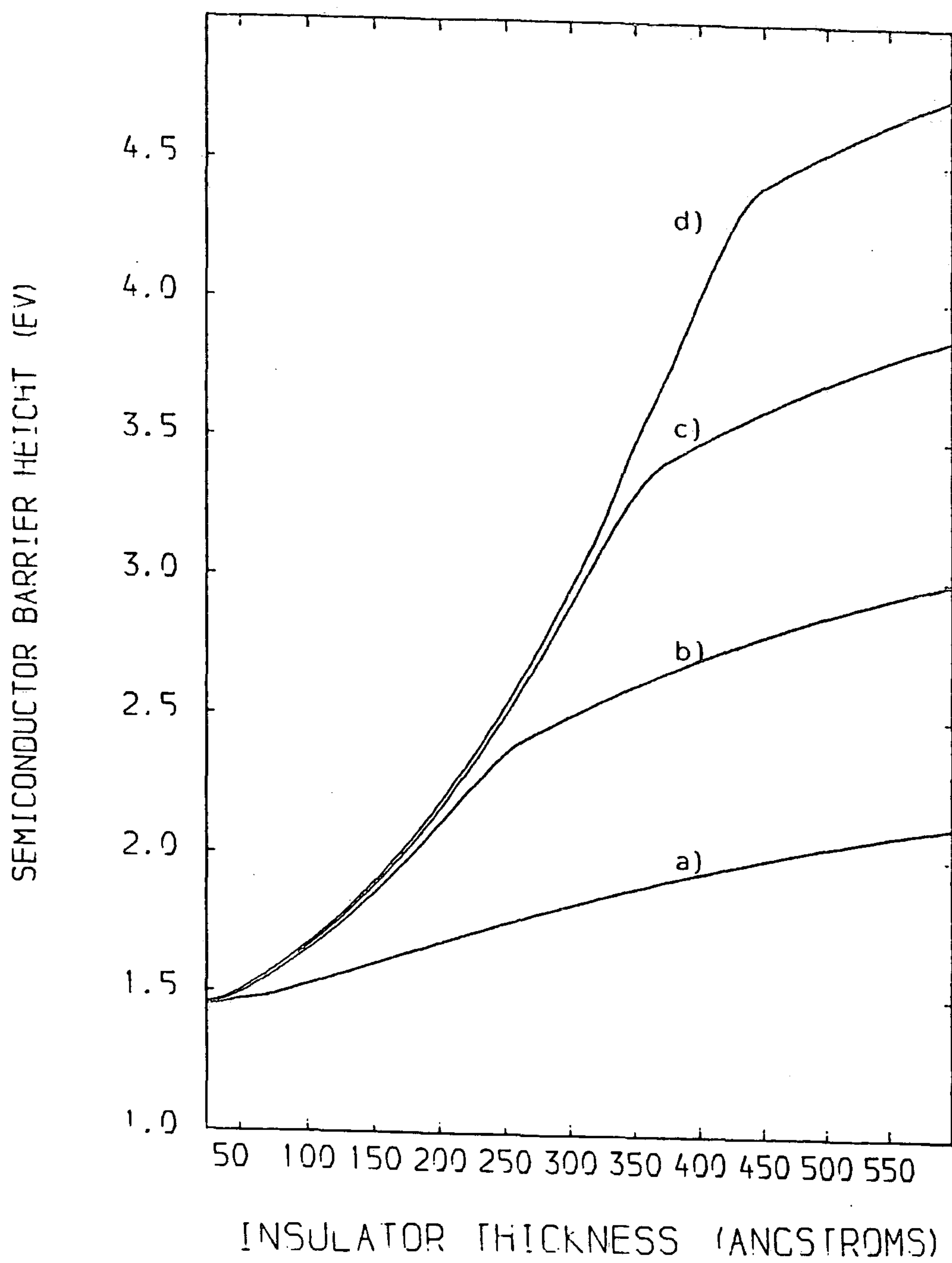

Fig. 5.19 : Theoretical variation of ϕ_b with insulator thickness for a constant applied bias of a) 1V; b) 2V; c) 3V and d) 4V.

If the current is kept constant rather than the voltage, the behaviour shown in Figure 5.20 results. There is an almost exponential rise in semiconductor barrier height with insulator thickness. This can be understood by considering the fact that as the insulator width increases more of the external voltage is across the barrier region, and there is less across the bulk, resulting in a lower current. To increase the current a higher voltage is required and this gives a larger barrier height. At these high currents any additional voltage is almost entirely dropped across the semiconductor bulk and this explains why the curves for the different currents are quite close together.

5.4 SUMMARY AND CONCLUSIONS

This chapter has discussed a model to describe the behaviour of the semiconductor conduction and valence bands when an MIS device is under forward bias. In particular it has attempted to explain the behaviour of the Au/Langmuir-Blodgett film/n-GaP devices fabricated by Batey et al[1,2,3] by assuming its behaviour to be dependent only on the majority electron current.

As suggested by Batey, the Langmuir-Blodgett insulating layer was given some form of conduction band producing a finite barrier to the electrons enabling the majority carriers to pass over the insulator by thermionic emission. A simple theory was produced to model the behaviour at the lower voltages when the thermionic current was negligible. However, the effects of the voltage dropped across the

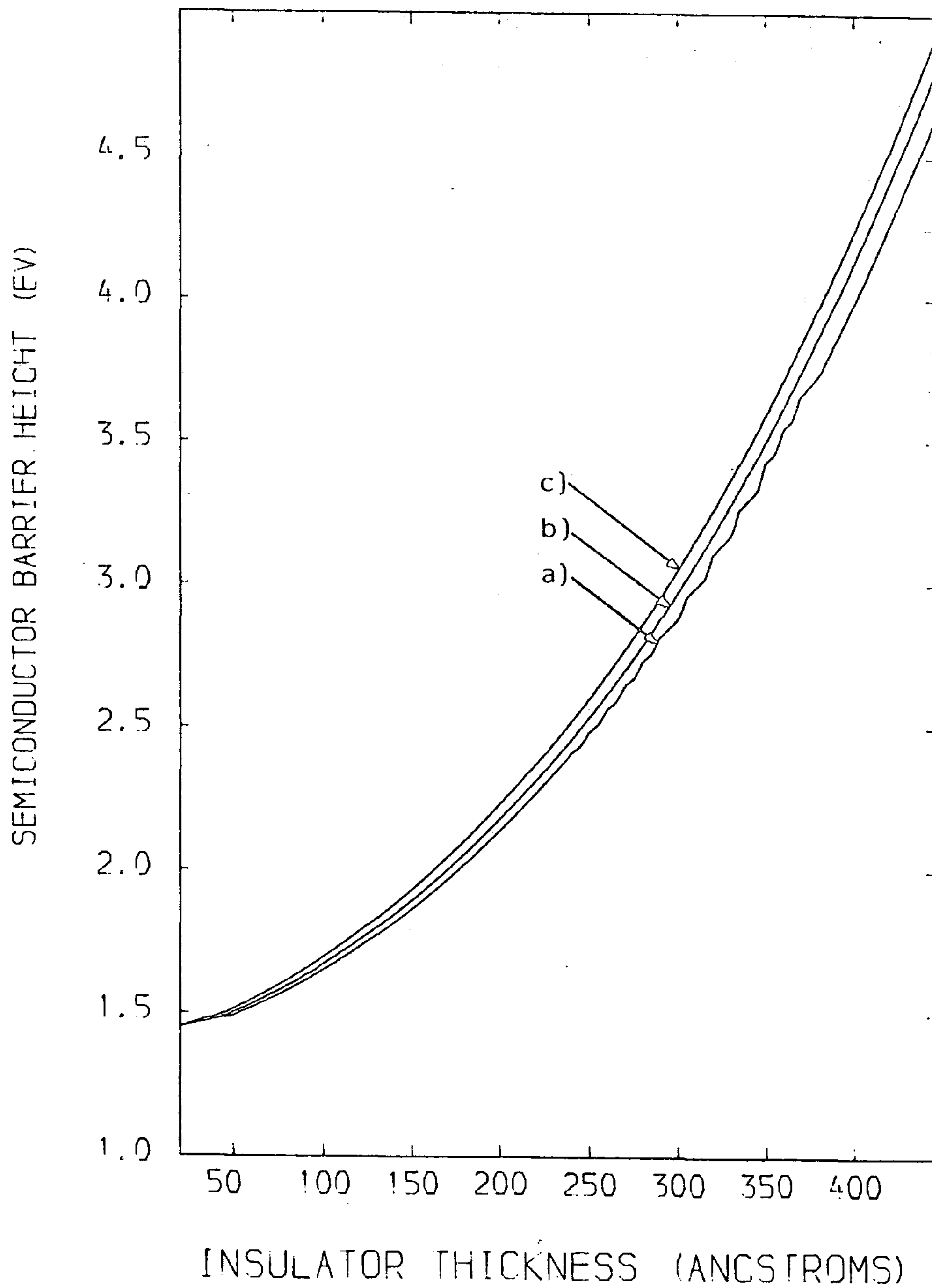

Fig. 5.20 : Theoretical variation of ϕ_b with insulator thickness for an Au/Cadmium Stearate/n-GaP diode at a constant majority carrier current of a) $10^3 Am^{-2}$; b) $10^4 Am^{-2}$ and c) $10^5 Am^{-2}$.

bulk of the semiconductor on the system had to be taken into account to understand the behaviour at higher voltages. The final stage in producing this model was to introduce a more realistic distribution of surface states for the semiconductor which included a band of states in the energy gap.

The accuracy of this model was tested by direct comparison of the current-voltage characteris tic with the experimental results produced by Batey[2,3]. The two sets of curves matched very well with current densities being comparable and with features of curves occcuring at approximately the same points. As can only be expected there are some discrepancies between theory and experiment, either due to inadequacies in the model, or possibly inconsistency in device fabrication, but these are not large enough to reduce confidence in the model.

Using the same parameters as those used to produce the current-voltages curves, we were then able to look at the variation of the semiconductor barrier height and valence band edge as a function of both applied voltage and insulator thickness. Of particular interest in this case is the variation with thickness, while the majority current is held constant. Figure 5.20 gives these characteristics for three different current densities. As described in Chapter Three, electroluminescent measurements on the two Langmuir-Blodgett devices incorporating Cadmium Stearate and w-Tricosenoic Acid, at a constant driving current of $10^5 Am^{-2}$, showed a maximum in the energy conversion efficiency at an insulator thickness of aroung 270Å. It is very interesting to note that in our model this corresponds to a

semiconductor barrier height of approximately the band gap or, in other words, to the valence band edge being at a similar energy to the metal Fermi level. The significance of this observation will be discussed in the next chapter when the minority carrier transport though the insulator is considered.

CHAPTER SIX

CARRIER TRANSPORT THROUGH THE INSULATOR OF THE MIS DIODE

6.1 INTRODUCTION

In the last two chapters we have dealt with important electronic processes in the metal and the semiconductor. To complete the description of the forward biased MIS diodes, it is necessary to look at the current transport mechanisms in the insulating region. In the preceding chapter it was explained how the majority carrier current in the Au/Langmuir-Blodgett film/n-GaP system could be adequately described in terms of thermionic emission theory. Similar conclusions have been drawn for diodes incorporating II-VI semi-insulators. This implies that electron transport through the insulator is relatively easy with emission from the semiconductor being the limiting factor.

Despite this last observation some attention will be paid to the majority carrier current in the Langmuir-Blodgett film device. The existence of sheets of interface states between the successive insulating layers can lead to some novel trapping mechanisms. These mechanisms will be investigated in the following sections.

The transport of holes through the insulator is less well understood so the main aim of this chapter will be to identify and investigate hole

tranport mechanisms in the respective devices.

6.2 TRAPPING OF ELECTRONS IN LANGMUIR-BLODGETT FILM INSULATORS

6.2.1 Interface States

Associated with successive layers in the insulator there will be two-dimensional sheets of states, which, if unoccupied, are available to play host to electrons passing through the insulator. These states could be particularly important in connection with the majority carrier current which appears to be the result of electrons in some conduction, or quasi-conduction, band in the Langmuir-Blodgett film (see Section 5.2.1) Later in this Chapter the possibility of the excitation of electrons from these traps as a hole creation mechanism will be discussed.

In investigating the trapping at these states we will make the usual simplifying approximation that the density of interface states is uniform over both area and energy. This approximation will enable the problem to be treated analytically.

6.2.2 The Trapping of Electrons

With the transport of electrons from the semiconductor into the metal there is always the possibility that some will be trapped at unoccupied interface states. One mechanisms for this, which is also a hole creation mechanism, is the trapping of an electron with the excitation of another

from a trap to the conduction band. In the following sections we will proceed to calculate the probability of such an event. This analysis will be similar in approach to the procedure used in Chapter Four with the use of perturbation theory.

Once an electron has entered the metal it is unlikely that it will interact with insulator interface states as the electron-electron interaction is heavily screened. An electron could only be expected to interact with interface states if it were within a few angstroms of the MI interface.

6.2.3 The Perturbing Potential

With the metal-insulator interface nearby it is expected that the metallic screening will have an important influence on the interaction potential. Describing this effect by an image charge leads to an interaction potential which is of the form of an electric dipole with its origin at the interface and given by

$$W(\underline{r}) = \frac{\underline{d}.\underline{r}}{4\pi\varepsilon\varepsilon_o r^3} \tag{6.1}$$

with $\underline{r}$ being the position vector of the injected electron relative to the centre of the dipole and $\underline{d}$ the dipole moment whose magnitude is expressed as

$$|\underline{d}| = x|e| \tag{6.2}$$

where x is the length of the dipole.

This potential, as opposed to a Coulombic perturbation will be used to described the perturbing effect of the injected electron on the system.

6.2.4 Transition Rate

Referring to Figure 6.2, if we consider an electron travelling through the insulator in a particular State 1, the transition rate for the interaction in which it is trapped at State 1' with the subsequent emission of another electron from State 2 (a trap) to State 2', is given by Fermi's Golden Rule No.2 as:

$$TR = \frac{2\pi}{\hbar}|\langle\psi'|W|\psi\rangle|^2\delta(E'-E) \tag{6.3}$$

ψ' and ψ are the final and initial wavefunctions of the system, W is the perturbing potential and the Dirac delta function ensures energy conservation.

6.2.5 Matrix Element

To proceed, it is necessary to evaluate the matrix element $\langle\psi'|W|\psi\rangle$. Assuming the insulator conduction band to be parabolic the incident electrons will have wavefunctions of the free particle form. To describe the wavefunction of trapped electrons is more difficult. The wavefunctions are expected to be short range, but there is no available information on them so it is reasonable to represent them as decaying exponentials.

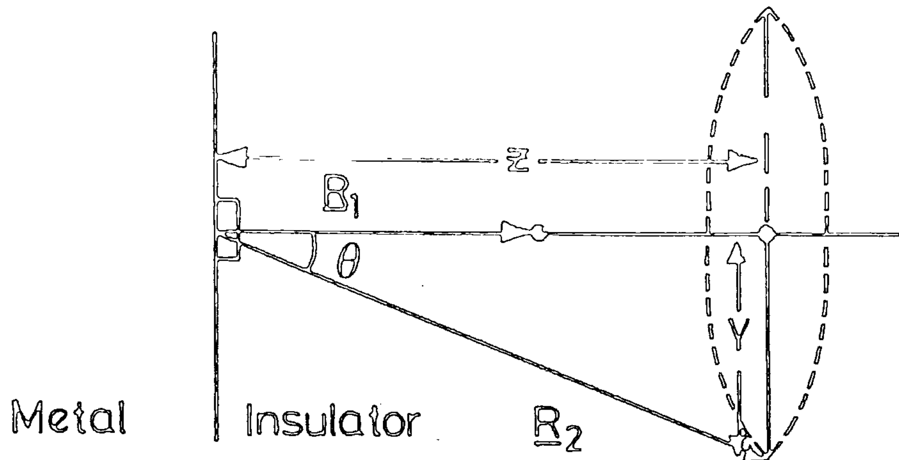

Fig. 6.1 : Co-ordinate system used in the calculation of trapping rates in Langmuir-Blodgett films.

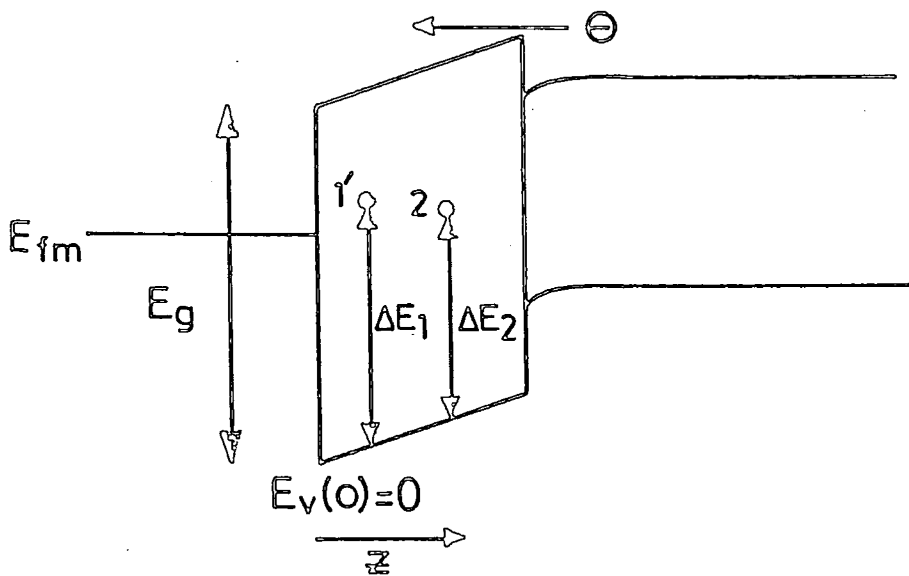

Fig. 6.2 : Position and energy of interface states involved in trapping in Langmuir-Blodgett films.

$$\phi = Ae^{-\alpha r} \tag{6.4}$$

where A is the normalisation constant. Calculating A in the normal way and assuming the wavefunction to be rapidly decaying, that is α relatively large, the wavefunction can be represented by a delta function with a prefactor chosen so that the delta function gives the same contribution as the exponential to overlap intergrals involving other slowly varying wavefunctions.

$$\phi = \frac{8\pi^{\frac{1}{2}}}{\alpha^{3/2}} \delta(\underline{r}) \tag{6.5}$$

The matrix element can be written as:

$$M = \frac{64\pi}{\Omega\alpha_1^{3/2}\alpha_2^{3/2}} \left\langle e^{i\underline{k}_{2'}\cdot\underline{r}_2} \delta(\underline{R}_a-\underline{r}_1) \middle| W(\underline{r}_1,\underline{r}_2) \middle| e^{i\underline{k}_1\cdot\underline{r}_1} \delta(\underline{R}_b-\underline{r}_2) \right\rangle \tag{6.6}$$

with the position vectors of the traps being given by $\underline{R}_a$ and $\underline{R}_b$. The origin of spatial co-ordinates is taken at the metal-insulator interface. The subscripts 1 and 2 refer to the incident and secondary electron respectively. Substituting for the perturbing potential from equation (6.1) it is straightforward to integrate over $\underline{r}_1$ and $\underline{r}_2$ to yield:

$$M = \frac{16|e|}{\varepsilon\varepsilon_0\Omega\alpha_1^{3/2}\alpha_2^{3/2}} \frac{\underline{d}\cdot\underline{R}_2}{R_2^3} e^{i(\underline{k}_1\cdot\underline{R}_1 - \underline{k}_{2'}\cdot\underline{R}_2)} \tag{6.7}$$

To produce a more useful form of $\underline{d} . \underline{R}_2 / R_2^3$ cylindrical polar co-ordinates are used with the origin chosen so that $\underline{R}_1$ is normal to the interface and defining the z axis. Referring to Figure 6.1 and using the fact that equation (6.2) becomes:

$$|\underline{d}| = 2z_1 \; |e| \qquad (6.8)$$

and the scalar product in equation (6.7) can be written as:

$$\underline{d}.\underline{r} = 2z_1 \; |e|^2 \; R_2 \cos\theta \qquad (6.9)$$

By writing $\cos\theta$ and R_2 in terms of z and y, where y is the radial distance from the z axis and is illustrated in Figure 6.1, equation (6.7) now becomes:

$$|M| = \frac{16\,|e|}{\varepsilon\varepsilon\;\Omega\alpha_1^{3/2}\,\alpha_2^{3/2}}\left(\frac{2z_1z_2}{(z_2^2+y_2^2)^{3/2}}\right) \qquad (6.10)$$

6.2.6 Mean Free Path of the Incident Electron

The transition rate for the process described, with the incident electron in State 1 interacting with a trapped electron in State 2, is found by substituting the matrix element from equation (6.10) into equation (6.3) to give the expression:

$$TR = \frac{2}{\hbar}\left(\frac{16\,|e|^2}{\varepsilon\varepsilon_0\;\alpha_1^{3/2}(\Delta E_1)\;\alpha_2^{3/2}\;(\Delta E_2)\;\Omega}\right)^2 \frac{4z_1^2z_2^2}{(z_2^2+y^2)^3}$$

$$\times \quad \delta(E_1 + E_2 - E_{1'} - E_{2'}) \qquad (6.11)$$

where E_1 and $E_{1'}$ are the energies of the incident electrons before and after the transition and E_2 and $E_{2'}$ are the initial and final energies of the excited electron. With the energies of the trapped electrons measured relative to the top of the insulator valence band at the metal-insulator interface, as illustrated in Figure 6.2, the Dirac delta function can be re-written as:

$$\delta(E_1+E_2-E_{1'}-E_{2'}) = \delta\left(\frac{\hbar^2}{2m}(k_1{}^2-k_{2'}{}^2) + \Delta E_2 - \Delta E_1\right) \tag{6.12}$$

Equation (6.11) only gives the transition rate between individual discrete states with the correct occupancy, so to find the overall transition rate of the electron from State 1 it is necessary to sum over all other possible transitions. First integrating over all states $k_{2'}$ (expressed in cylindrical polar co-ordinates, and assumed unoccupied):

$$TR = \sum_{1',2} \frac{m^*}{\pi\hbar^3\Omega}\left(\frac{2m^*}{\hbar^2}\right)^{\frac{1}{2}}\left(\frac{16|e|^2}{\varepsilon\varepsilon_0\,\alpha_1^{3/2}(\Delta E_1)\,\alpha_2^{3/2}(\Delta E_2)}\right)^2$$

$$\times\ \frac{4z_1{}^2z_2{}^2}{(z_2{}^2+y_2{}^2)^3}\left(\frac{\hbar^2k_i{}^2}{2m^*} + \Delta E_2 - \Delta E_1\right)^{\frac{1}{2}} \tag{6.13}$$

As a constant distribution of traps over area and energy is assumed, the summation can be rewritten as:

$$\sum_{1',2} = \sum_{z_1,z_2}\iint (D_s y_1\,d\theta_1\,dy_1\,d\Delta E_1)(D_s y_2\,d\theta_2\,dy_2\,d\Delta E_2) \tag{6.14}$$

where now the summation is just over the set of insulator interfaces. First perfroming the integration over y_2, it is a reasonable approximation to use the limits 0 to ∞ to produce:

$$TR = \sum_{z_1, z_2} \iint \frac{2m}{\hbar^3 \Omega} \left(\frac{16|e|^2 D_s}{\varepsilon\varepsilon_0 \alpha_1^{3/2} (\Delta E_1)\, \alpha_2^{3/2} (\Delta E_1)} \right)^2 \left(\frac{2m}{\hbar^2} \right)^{\frac{1}{2}}$$

$$\times \ \frac{z_1^{\,2}}{z_2^{\,2}} \left(\frac{\hbar^2 k_1^{\,2}}{2m} + \Delta E_2 - \Delta E_1 \right)^{\frac{1}{2}}$$

$$\times \ y_1 d\theta_1 dy_1 d\Delta E_1 d\Delta E_2 \qquad (6.15)$$

In general we might expect the value of α for a particular trap to depend on its energy, but the inclusion of that here would lead to intractable integrals. In the rest of the analysis we shall assume α to be constant over the energy range. This is by no means a drastic approximation in comparison to the assumptions already made about the wavefunction of the trapped electrons.

Before integrating over ΔE_2 it is necessary to establish the energy limits of suitable occupied states. It is proposed that there is some position dependent quasi-Fermi level above which the traps are empty and below which they are full. Writing this position dependent quantity as $L(Z_2)$ it is clear that it forms the upper energy limit for states from which electrons can be excited. The lower limit is the energy at which electrons are only just able to reach the conduction band edge and is given by $\Delta E_1 - \dfrac{\hbar^2 k_1^{\,2}}{2m^*}$. The limits of ΔE_1 can also be calculated in

a similar manner. The lower limit of ΔE_1 is given by $L(Z_1)$, because the state should be unoccupied and the upper limit is determined by the requirement that just enough energy is lost to allow the emission of another electron that is $L(Z_2) + \frac{\hbar^2 k_1^2}{2m^*}$.

The integration over ΔE_1 and ΔE_2 are straightforward and yield the result:

$$TR = \sum_{z_1, z_2} \int \frac{8m^*}{15\hbar^3 \Omega} \left(\frac{16|e|^2 D_s}{\varepsilon\varepsilon_0 \alpha^3} \right)^2 \left(\frac{2m}{\hbar^2} \right)^{\frac{1}{2}}$$

$$\times \frac{z_1^2}{z_2^2} \left(\frac{\hbar^2 k_1^2}{2m^*} + L(z_2) - L(z_1) \right)^{5/2} y_1 d\theta_1 dy_1 \qquad (6.16)$$

$y_1 d\theta_1 dy_1$ is simply the elemental unit of area and this just introduces a factor of A, the area of the interface. Replacing the system volume by $A\delta$, where δ is thetotal width of the insulator, gives:

$$TR = \sum_{z_1, z_2} \frac{8m^*}{15\hbar^3} \left(\frac{16|e|^2 D_s}{\varepsilon\varepsilon_0 \alpha^3} \right)^2 \left(\frac{2m}{\hbar^2} \right)^{\frac{1}{2}}$$

$$\times \frac{1}{\delta} \frac{z_1^2}{z_2^2} \left(\frac{\hbar^2 k_1^2}{2m^*} + L(z_2) - L(z_1) \right)^{5/2} \qquad (6.17)$$

The final summations over z_1 and z_2 can only be done numerically when applying equation (6.17) to a definite system with a given number of Langmuir-Blodgett layers (on the assumption that the behaviour of $L(z)$ can be modelled).

Equation (6.17) gives the transition rate electrons passing through the film. Dividing by the velocity of the incident electron gives the inverse mean free path for an electron. Hence:

$$\lambda = \sum_{z_1, z_2} \frac{15\hbar^4 k_1}{8m^*} \left(\frac{\varepsilon\varepsilon_0 \alpha^3}{16|e|^2 D_{ss}} \right)^2 \left(\frac{\hbar^2}{2m^*} \right)^{\frac{1}{2}}$$

$$\times \frac{\delta z_2^{\,2}}{z_1^{\,2}} \left(\frac{\hbar^2 k_1^{\,2}}{2m^*} + L(z_2) - L(z_1) \right)^{2/5} \qquad (6.18)$$

6.2.7 The Effect on the Majority Carrier Current

To investigate the effect of the electron trapping mechanism described, it is easier to work with the expression for the transition rate (equation (6.17)).

By substituting into equation (6.17) the numerical values of the physical constants, including the free electron mass for m^* and an estimate for $\alpha \cong 5\times10^9$, it is found that

$$TR \cong \sum_{z_1, z_2} (3.5\times10^{-29}) \frac{D_s^{\,2}}{\delta} \frac{z_1^{\,2}}{z_2^{\,2}} \left(\frac{1}{|e|} \frac{\hbar^2 k_1^{\,2}}{2m^*} + \frac{L(z_2)}{|e|} - \frac{L(z_1)}{|e|} \right)^{5/2}$$

(6.19)

where now D_s is the density of interface states in units of $m^{-2}eV^{-1}$. Unfortunately there is little published data on the density of states at the interface. Sugi et al[1] estimate that films produced using

cadmium stearate will have values of D_{ss} in the order of $10^{19}m^{-2}eV^{-1}$. This is equivalent to assuming that there is a state for each molecule in the Langmuir-Blodgett film. Lundstrom et al[2] predicted that with such a large density of interface states there would be a strong anisotropic conductivity parallel to the insulating layer. However, this has not been experimentally verified[3]. In their work on an InP MISFET, Roberts et al[4,5] produced MIS structures incorporating cadmium stearate and cadmium arachidate. The excellent results obtained for this device indicated that the interface state densities were quite low with the density at the Langmuir-Blodgett film-semiconductor interface being measured at $3 \times 10^{15} m^{-2}eV^{-1}$.

Expecting the interface density of states to be $\sim 10^{15}eV^{-1}m^{-2}$, an approximate value for the transition rate is given by:

$$TR \sim \sum_{z_1, z_2} \frac{35 z_1^2}{z_2^2} \sim \frac{35n}{\delta} \quad sec^{-1} \qquad (6.20)$$

where n is the number of monolayers.

As described in Chapter Two, the majority of the electrons emitted into the metal from the semiconductor will have an energy roughly $^3/_2kT$ above the peak of the barrier presented by the insulator. Therefore electrons have a typical velocity of $10^5 ms^{-1}$ and the time taken for them to travel through the insulator will be approximately $\delta/10^5$ secs. The probability that an electron will be trapped in the manner described is found by multiplying the transition rate by the transit time to give:

$$\text{prob} \sim 3.5n \times 10^{-4} \qquad (6.21)$$

This suggests that the rate of trapping by the mechanism will be negligible compared to the total current and will not adversely affect the validity of the thermionic emission model adopted in Chapter Five. However typical devices are driven at current densities of $10^5 Am^{-2}$ and the process might well affect the distribution of filled interface traps because as many as $2x10^{20}$ per second per square metre can be expected to take place.

6.2.8 Trapping as a Possible Hole Creation Process

The trapping mechanism described in the previous sections could also be an important hole creation mechanism. It is possible that an electron injected into the insulator will be trapped with a secondary electron being excited from below the semiconductor valence band edge at the insulator-semiconductor interface. There is also the possibility of an enhanced hole population in insulator interface states at energies below the semiconductor valence band edge. These processes have been illustrated in Figure 6.3.

One of the processes illustrated concerns the excitation of an electron from the semiconductor valence band to the conduction band. This requires the incident electron that this trapped in the insulator to lose an energy which is equal to or greater than the semiconductor band gap. As previously pointed out, the majority of electrons being injected into the metal are within $\sim {}^3/_2kT$ of the top of the insulator barrier. It is also expected that insulator trap states will be occupied by

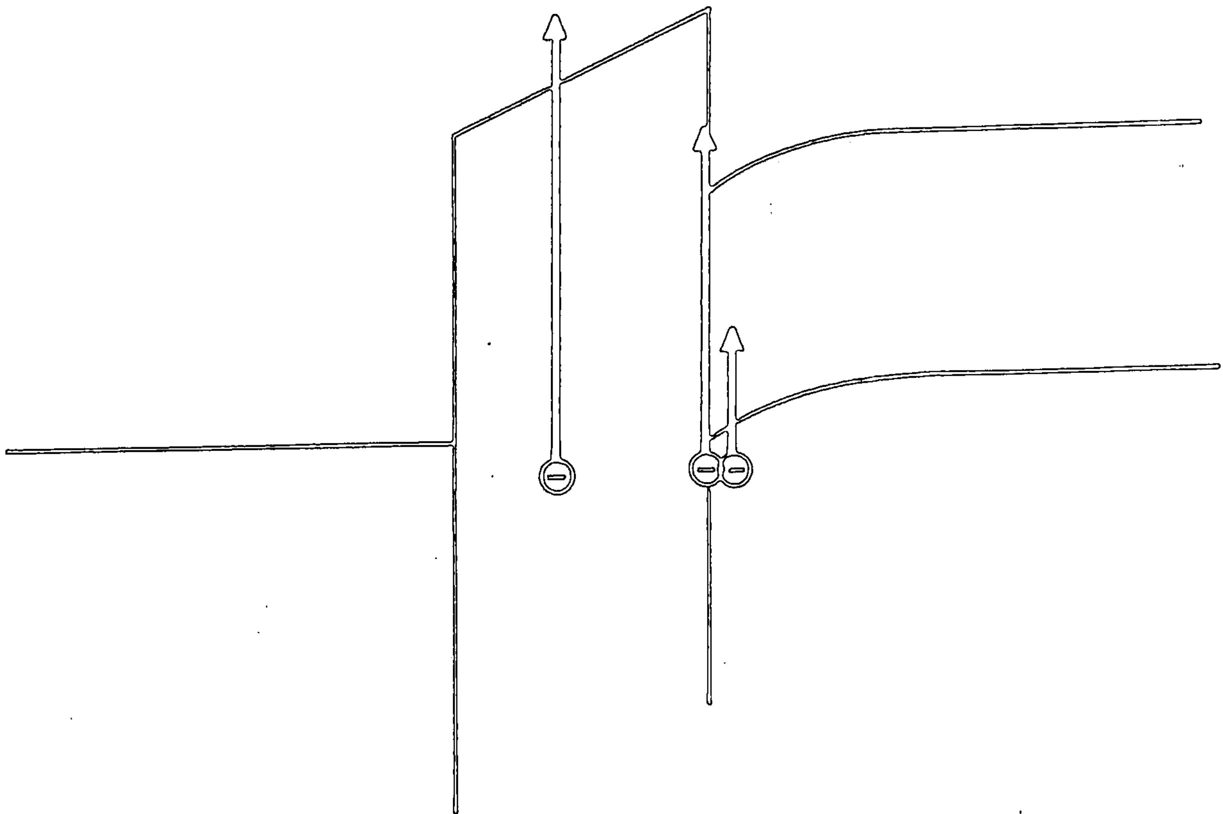

Fig. 6.3 : Possible holes creation mechanisms involving the trapping of a majority carrier.

electrons at least up to the Fermi level. This means that the top of the insulator barrier must exceed the metal Fermi energy by the semiconductor band gap energy or more, so that transitions of sufficient energy to unoccupied trap states are possible. Using the results of the model developed in Chapter Five, it can be seen in Figure 5.18 that we could only expect this threshold barrier height to be reached at an external bias of greater than 2V. This value is well in excess of the biases at which electroluminescence was observed experimentally in Au/cadmium stearate/n-GaP devices fabricated by Batey et al[6,7].

There will be a similar threshold voltage for hole creation at interface states below the level of the semiconductor valence band edge, although the exact value will be dependent on the position of the interface at which the hole is created. This is simply because of the change in potential across the width of the insulator. Therefore it appears that hole creation , at either the insulator-semiconductor interface or in the insulator itself, with an electron excited from a state below the level of the semiconductor valence band into the conduction band, is not a significant process in the MIS diodes investigated.

A third process, which is possible, is the excitation of an electron in the semiconductor valence band to an unoccupied interface state on the insulator-semiconductor boundary. As these interface states exist in the band gap there is no threshold bias for this process. For such a transition to produce holes systematically it would be necessary for the trapped electrons (incident and excited) to be removed to the semiconductor conduction band or the metal by further processes.

6.3 LANGMUIR-BLODGETT FILM HOLE TRANSPORT PROCESSES

6.3.1 Direct Tunnelling

The simplest mechanism for the transport of carriers through a thin insulator is quantum mechanical tunnelling. The theory developed by Card and Rhoderick[8] for an $Au/SiO_2/Si$ device, which was reviewed in Chapter Two, deals specifically with tunnelling and treats the insulator as perfect in all respects. These authors were successful in explaining the behaviour of the devices they had fabricated with thermally produced SiO_2[8]. In the review, given in Chapter Three, it was pointed out that the tunnelling theory of Card and Rhoderick[8] has been used to explain the behaviour of diodes fabricated by several groups. However it is very unlikely that direct tunnelling will be the dominant hole transport in devices incorporating Langmuir-Blodgett films because of the relatively large insulator thicknesses used in the devices with the highest efficiencies.

This can easily be demonstrated by using the WKB approximation[9] to give the tunnelling transmission coefficient as:

$$T = \exp\left[-2\int_0^{\delta} k(z)dz\right] \qquad (6.22)$$

where z is the direction normal to the metal-insulator interface and is measured from this interface. k(z) is the magnitude of the (imaginary) wavevector in the barrier region. For a typical majority carrier current of $10^5 Am^{-2}$ the electron concentration in the insulator will be approximately

$10^{18} m^{-3}$ which is not sufficiently high enough to affect the electric field significantly. Equation (6.22) can, therefore, be rewritten as the single parabolic band approximation as:

$$T = \exp\left[-2\int_0^{\delta} \sqrt{\frac{2m(E_c(z)-E)}{\hbar^2}}\, dz \right] \quad (6.23)$$

where $E_c(z)$ is the conduction band edge of the insulator given by:

$$E_c(z) = |e| \left[\phi_m - \left(\frac{\phi_m - (\phi_b + X_s)}{\delta} \right) z + E_{Fm} \right]$$

with the symbols being defined in Figure 5.1. We are primarily concerned with the rate at which electrons are able to tunnel from the semiconductor valence band into the metal. This is equivalent to holes tunnelling from the metal into the semiconductor. Assuming that the hole current is insulator controlled and that holes reaching the insulator-semiconductor interface are immediately removed to the bulk of the semiconductor, the only other factor affecting the minority carrier current will be the supply of holes at the metal-insulator boundary. As the semiconductor valence band moves upwards with respect to the metal Fermi level the number of available states in the metal occupied by the holes and at a suitable energy to receive valence band electrons increases and must be taken into account. If the hole occupancy of the states is described by Fermi-Dirac statistics the tunnelling rate will be approximately proportional to:

$$\text{Rate} \propto \int_{-\infty}^{E_v} \frac{\exp\left[-2\int_0^{\delta}\sqrt{\frac{2m\,(E_c(z) - E)}{\hbar^2}}\,dz\right]}{1 + \exp\left(\frac{E_{Fm} - E}{kT}\right)}\,dE \qquad (6.24)$$

The integral over z can be readily carried out to give

$$T = \frac{2\delta}{3(\phi_m - (\phi_b + X_s))}\left(\frac{2m|e|}{\hbar^2}\right)^{1/2}\left[(\phi_m + E_{Fm} - E)^{3/2} - (E_{Fm} + \phi_b + X_s - E)^{3/2}\right]$$

(6.25)

but, the integration over E needs to be done numerically. Figure 6.4 presents results for an Au/Langmuir-Blodgett film/n-GaP device under a constant current of $10^5 Am^{-2}$. Following the argument of Chapter Five the barrier height is taken to vary as shown in Figure 5.20. The three curves in Figure 6.4 are for different values of effective mass. Taking the effective mass to be the same as the free electron mass, curve (a) is obtained and it can be seen that a very sharp fall in the tunnelling current with insulator thickness is to be expected. An effective mass of $0.1m_e$, where m_e is the free electron mass, gives curve (b). Again there is a fall in tunnelling current, although in this case it is not as great as curve (a) and there is a shoulder around 225 Å. This is a result of the semiconductor barrier height rising faster at larger insulator thicknesses under the constant current conditions.

A peak can be reached when the valence band reaches the same energy as the metal Fermi level. If the rise in the semiconductor valence band edge with insulator thickness is sharp enough the increase in available

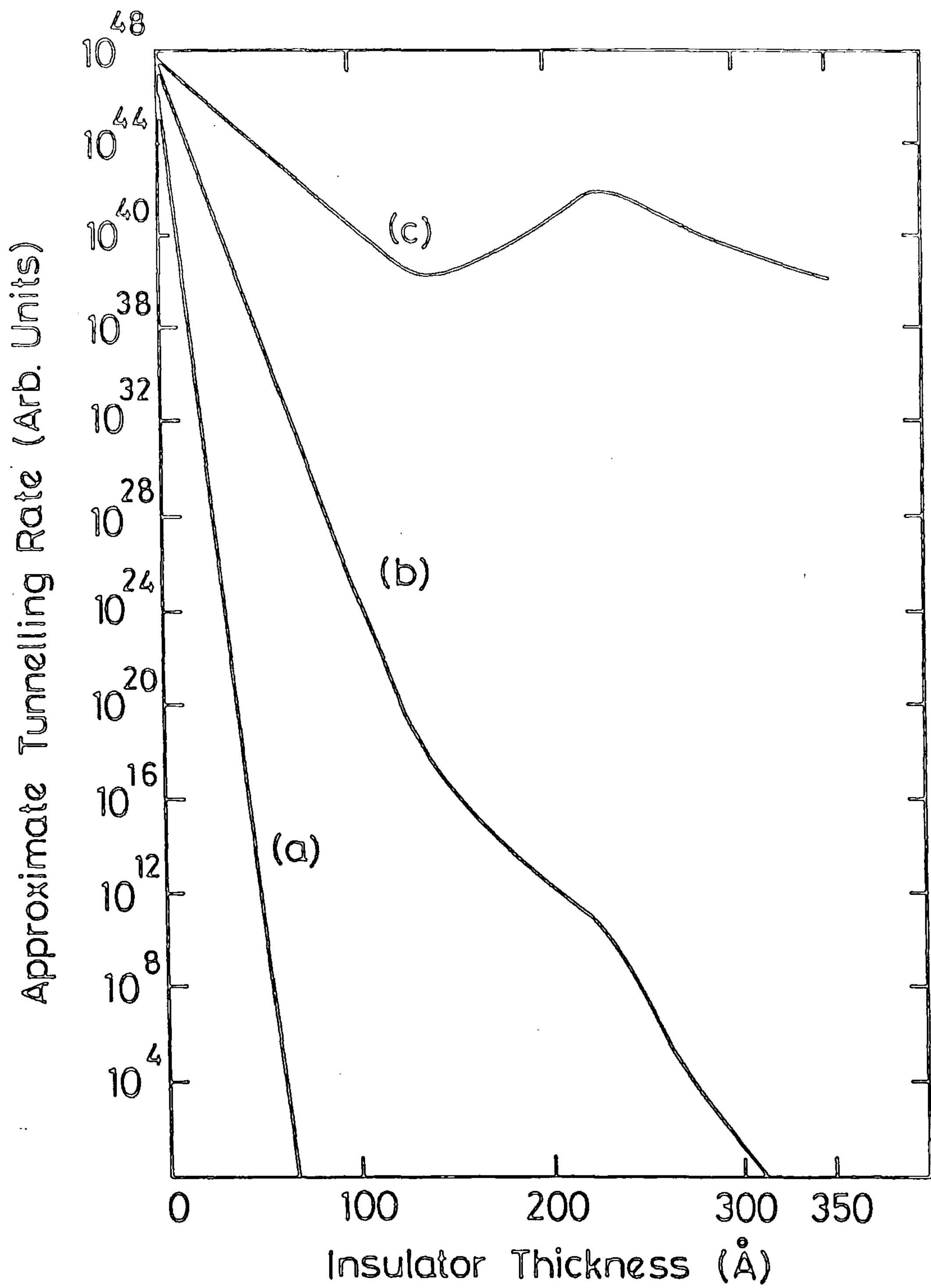

Fig. 6.4 : Quantum mechanical tunnelling rate for holes from the metal into the semiconductor valence band in a Langmuir-Blodgett MIS diode: a) $m = 1m_e$; b) $m = 0.1m_e$ and c) $m = 0.01\ m_e$.

holes at the metal-insulator interface will more than compensate for the reduced transmission coefficient of a range of insulator thickness. However, when the valence band edge and the E_{Fm} are aligned the rise in the available hole concentration will not be sustained. Above the metal Fermi level all the electron states are essentially empty so the rise in the available hole concentration is only proportional to the density of states (which is approximately linear). This is to be compared with an exponential rise below the Fermi level. The rise in the available hole concentration at the metal-insulator interface does not compensate for the decrease in transmission coefficient with insulator thickness unless the effective mass of the carriers is less than $10^{-2}m_e$ Curve (c) in Figure 6.4 shows the case when the effective mass is $10^{-2}m_e$.

What has not been taken into account in equation (6.24) and Figure 6.4 is the existence of holes at the metal-insulator interface which have been created by the impact ionisation process in the metal described in Chapter Four. As shown in Figure 4.18 (calculated for gold with a typical Schottky barrier height of 1.4eV) the hole flux at the metal-insulator interface is dominated by the impact ionisation process at energies approximately 0.6eV or more below the metal Fermi level. As the semiconductor valence band is an energy $\phi_b - E_g$ below the metal Fermi level, Figure 4.20 demonstrates that we can expect the impact ionisation created hole flux to be significant for the lower insulator thickness (that is for values of $\delta < 130$Å). Despite this it will not be included in the calculation at present because the increase in the available hole concentration produced by impact ionisation as the valence band rises is linear rather than exponential. This being the case,

the increase in the available hole concentration cannot be expected to compensate for the exponential decay with thickness in the transmission coefficient. However, what can be concluded from Figure 6.4 is that if a tunnelling mechanism is responsible for hole transport through the Langmuir-Blodgett film, the some enhancement of the transmission coefficient is necessary to produce the rise in the minority carrier injection ratio observed experimentally[6,7].

6.3.2 Poole-Frenkel Conduction

Poole-Frenkel conduction[10] is field activated and has been reported to be an important electron transport process in Langmuir-Blodgett films[11] especially at high fields.

The basic ideas behind the process can be explained with the aid of Figure 6.5. For clarity electron transport will be considered. Traps in the sample are assumed to attract the electrons with Coulombic potentials. When a field is applied (Figure 6.5(b)) there is a lowering of the barrier presented to a trapped electron and there is an enhanced probability of the electron escaping to the conduction band. With a higher concentration of conduction electrons the conductivity of the system is increased. For such a process the current can be expected to be of the form[10]

$$j_e \propto F_I \exp\left(\frac{|e|}{kT} (\beta F_I)^{\frac{1}{2}} \right) \qquad (6.26)$$

where β is the constant $(|e|/\pi\varepsilon\varepsilon_0)$.

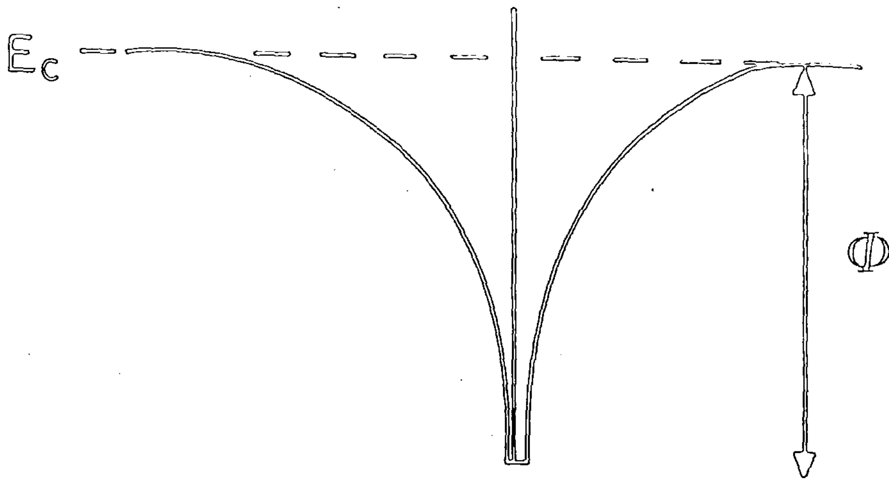

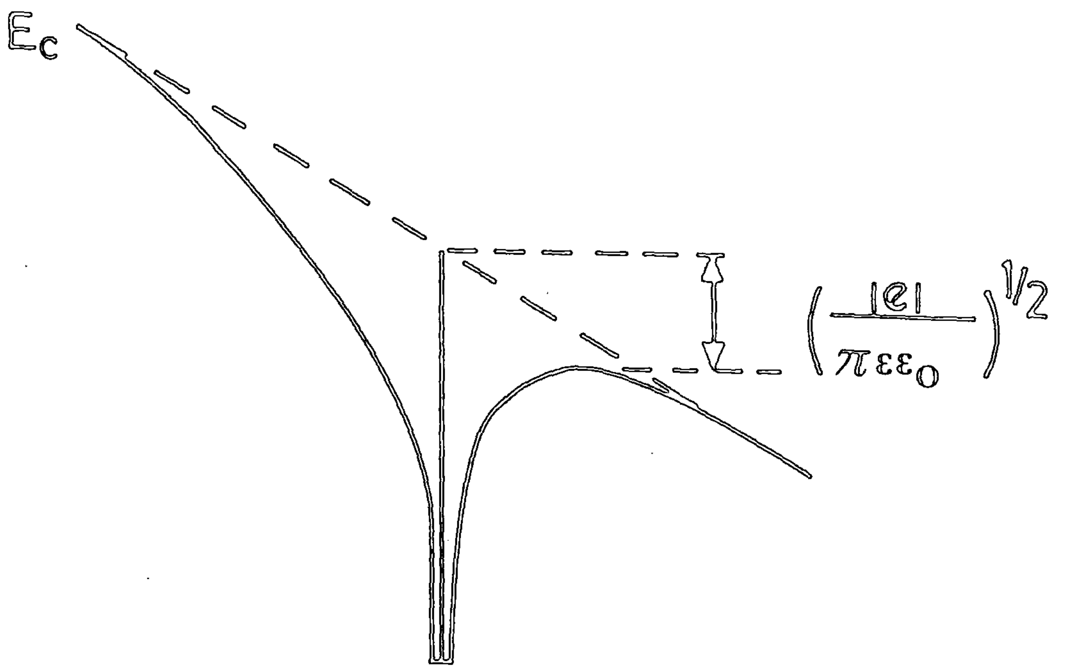

Fig. 6.5 : Schematic diagram of a Coulombic trap a) in zero field and b) under high field.

Under high field conditions and assuming a Langmuir-Blodgett film band structure it is to be expected that hole traps will affect the minority carrier transport in the way described above by enhancing the hole concentration in the valence band. Therefore the variation of hole current with field will also be given by equation (6.26).

The change in field with thickness for a cadmium stearate Langmuir-Blodgett film passing a constant majority current of $10^5 Am^{-2}$ is shown in Figure 6.6. This curve was calculated using the theory of Chapter Five and assuming the variation of the semiconductor barrier height illustrated in Figure 5.20. Thermionic emission from some conduction band, or quasi-conduction band, in the insulator was used to describe majority carrier conduction. The portion of the curve in Figure 6.6 corresponding to negative fields means that there is a threshold thickness for hole transport from the metal into the semiconductor by the Poole-Frenkel mechanism. Insulator widths less than this will have a field producing hole transport from the semiconductor into the metal.

For the change in field, shown in Figure 6.6, the expected variation of the Poole-Frenkel hole current with insulator thickness is shown in Figure 6.7. Assuming that the light emission from the device is directly proportional to the hole current J_h, and also noting that there is the condition of constant total current, the variation of the dc power conversion factor can be found to within a numerical factor by dividing the hole current by the total voltage across the device, V, to give:

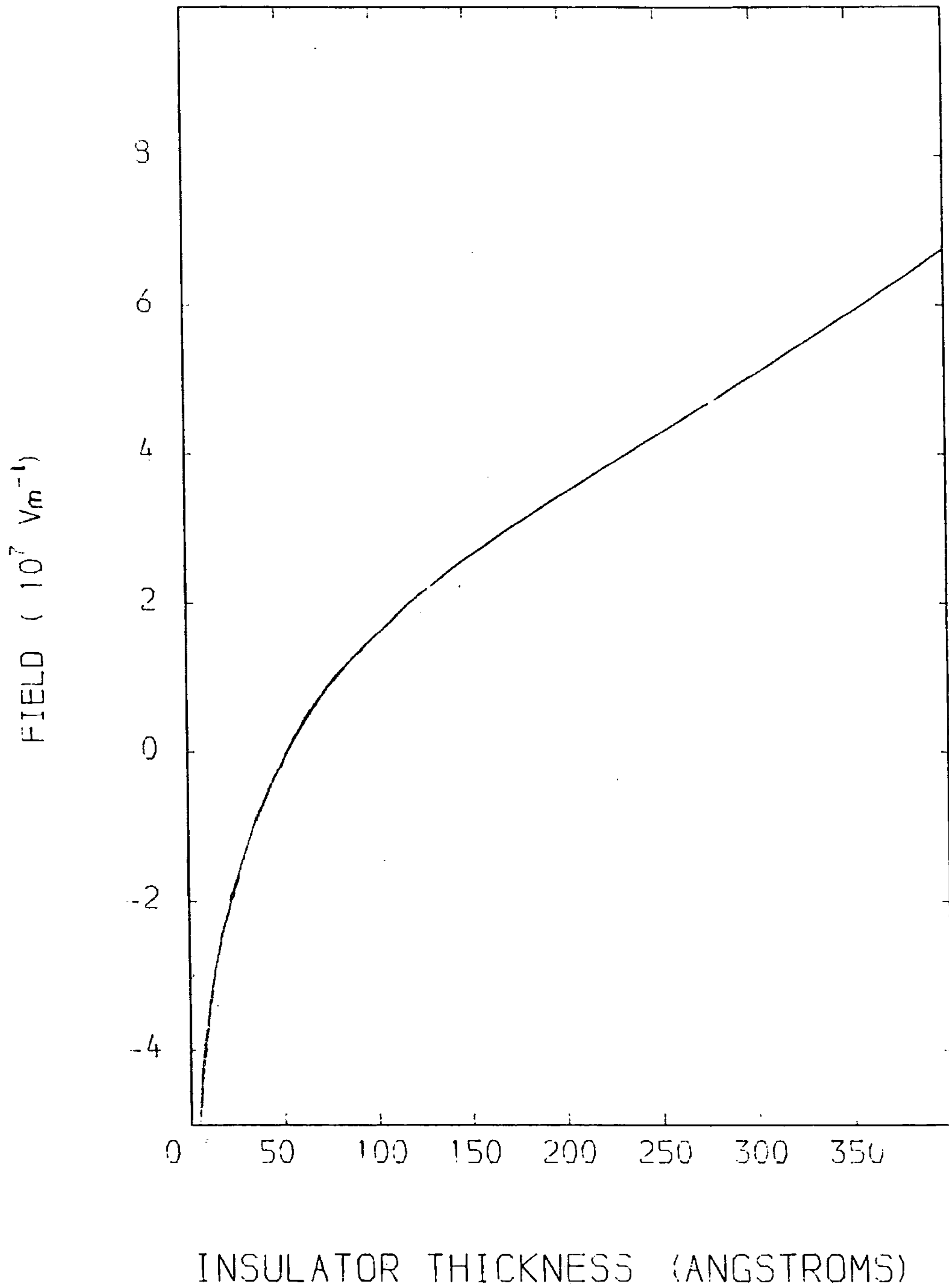

Fig. 6.6 : The variation in insulator field in the Langmuir-Blodgett MIS diode modelled in Chapter Five for a constant current of $10^5 Am^{-2}$.

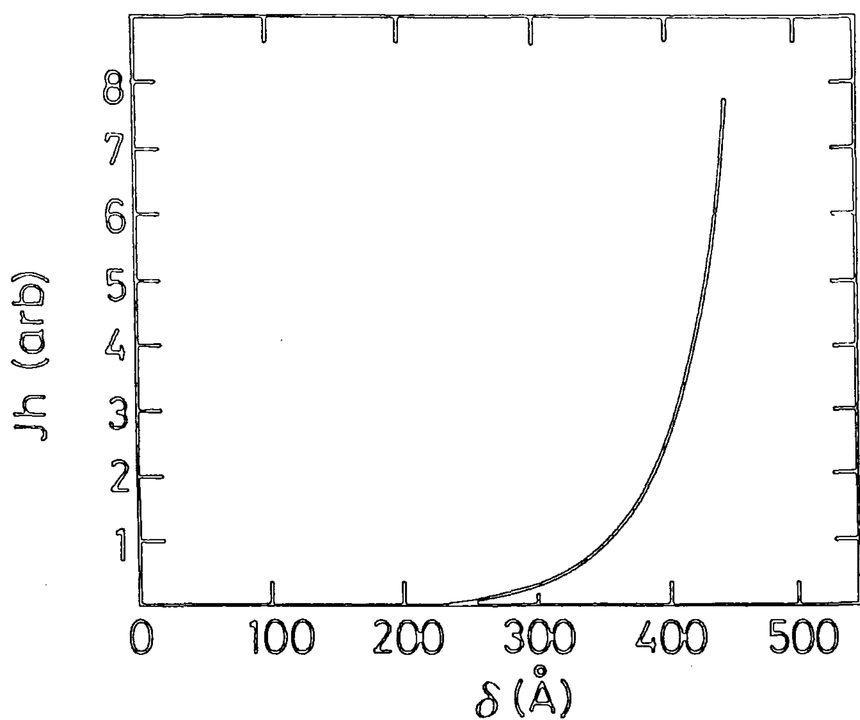

Fig. 6.7 : The expected variation in hole current due to Poole-Frenkel conduction assuming the insulator field variation in Fig. 6.6.

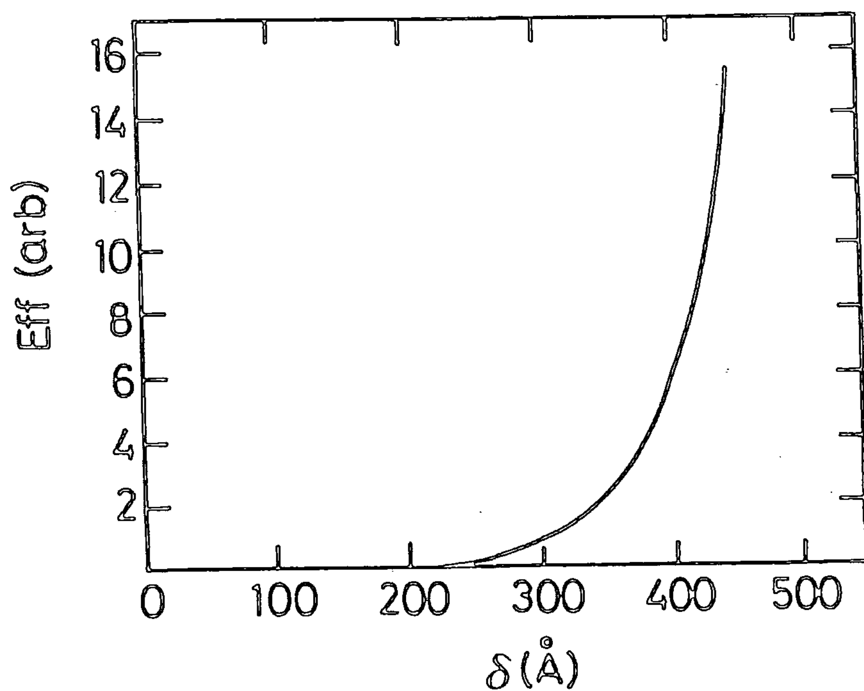

Fig. 6.8 : The expected variation in the dc power conversion ratio assuming insulator hole transport by Poole-Frenkel conduction.

$$E_{FF} \propto \frac{F_t}{V} \exp\left(\frac{|e|}{kT} (\beta F_I)^{\frac{1}{2}} \right) \qquad (6.27)$$

This expression is plotted in Figure 6.8 using the Au/Langmuir-Blodgett film/n-GaP device parameters. However, it can be seen that Figure 6.8 shows little resemblance to the experimentally obtained curves of Batey, reproduced in Figure 3.3 and it is clear that the theoretical model described above is not satisfactory.

Before leaving this section it should be emphasised that in the theory described above the hole current has been assumed to be insulator controlled. That is, there is an adequate supply of holes at the metal - insulator interface and that it is the transport through the insulator that is the limiting factor. With the results of Chapter Four, indicating that impact ionisation by electrons injected into the metal creates a relatively large hole concentration at energies well below the Fermi level, this is not an unreasonable assumption.

6.3.3 Linear Conduction

Several groups[13-15] have observed that at low fields, the electron current through Langmuir-Blodgett multilayers is proportional to the applied field. Taking Mann and Kuhn's[13] results in particular, it is interesting to note that the linear behaviour even occurred at insulator fields as high as $10^8 Vm^{-1}$. Their results also showed the conductivity varied little over a significant range of thicknesses (5-21 monolayers). This form of conduction has been attributed to hopping of carriers by thermally assisted tunnelling between the interface states of the

Langmuir-Blodgett films[13-15]. The mechanism is equally plausible for the transport of holes from the metal into the semiconductor valence band.

The variation of insulator field with insulator thickness for a fixed current of $10^5 Am^{-2}$ has already been illustrated in Figure 6.6. If the hole current is proportional to this then the dc power conversion ratio will be proportional to the quantitiy

$$\text{Eff} \propto \frac{F_I}{V} \tag{6.28}$$

The variation in the dc power conversion ratio to be expected from this form of conduction is shown in Figure 6.9. It can be seen that a plateau is reached at thicknesses of approximately 250Å or more. Unfortunately this does not correspond to the experimental results for the Au/cadmium stearate/n-GaP device[6,7]. However the hole current in the insulator is also expected to be influenced by lifetime effects.

The holes are injected into a set of localised states which are distributed in space and energy and are normally occupied by electrons. As a result there will be an attenuation with distance of the hole (minority carrier) current due to recombination with itinerant electrons (majority carriers) in the insulator conduction band as well as a thermalisation of the holes through localised states towards some quasi Fermi level in the insulator. The first process effectively removes the holes whilst the second process has the effect of reducing the number of holes energetically capable of entering the semiconductor valence band.

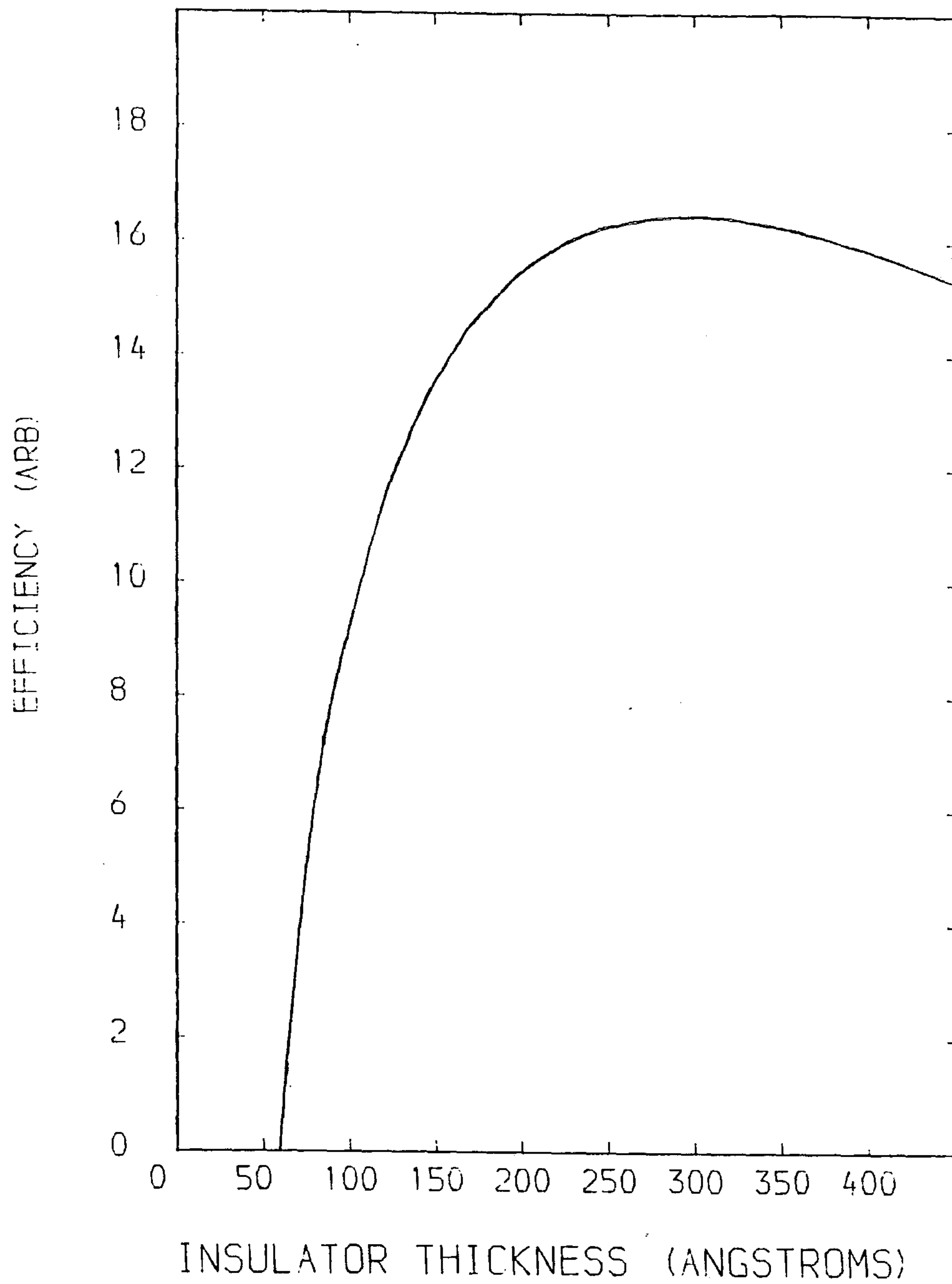

Fig. 6.9 : The expected variation in dc power conversion ratio assuming a hole current proportional to field.

Assuming these processes to be governed by an effective lifetime the attenuation in the hole current will be given by the factor $\exp(-\tau/\tau_o)$ where τ is the transit time across the insulator and τ_o is some mean lifetime. If the conduction is truly Ohmic and the drift velocity is proportional to field then, noting from Figure 6.6 that the field is proportional to thickness above approximately 200Å, the transit time will be constant at the larger thickness. Attenuation will not, therefore increase with thickness and the form of Figure 6.9 will not be greatly altered. If there is a saturation velocity however the transit time will vary and the attenutation will increase with thickness. Figure 6.10 shows a curve for such a situation with drift velocity proportional to field up to a threshold value of $4\times10^7 Vm^{-1}$. Above this value the velocity is constant. The threshold value was chosen in an attempt to reproduce the experimental curves illustrated in Figures 3.3 and 3.4. A value of $\mu\tau_o = 10^{15}$ was chosen using similar considerations.

If the current attenuation was due to some fixed, highly effective recombination centres then the probability of recombination would depend on the probability of a hole meeting such a centre. In this situation it would be more appropriate to describe the hole current attenuation by the factor $\exp(-\delta/\delta_o)$, where δ_o is the mean free path for hole-recombination centre collisions.

Multiplying equation (6.28) by the factor $\exp(-\delta/\delta_o)$, the results obtained for the efficiency of the device for different values of δ_o are presented in Figure 6.11. For all three curves shown, there is a well defined peak in the dc power conversion efficiency in the range 150Å to 200Å and there is a degree of similarity between the theoretical curves and

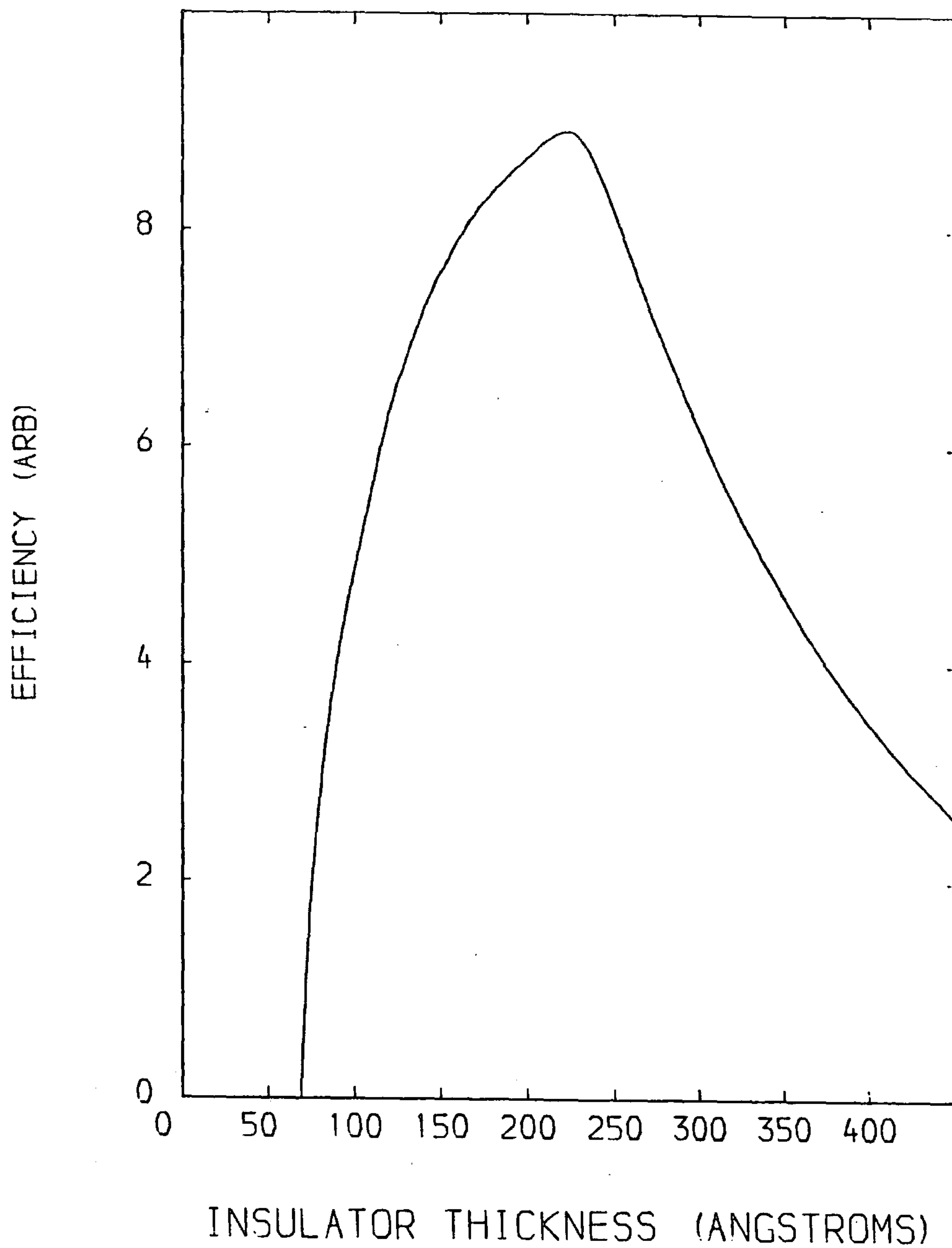

Fig. 6.10 : Variation in dc power conversion ration including the effects of a saturated hole velocity and a recombination lifetime. Values were chosen to produce a curve similar to experimental results.

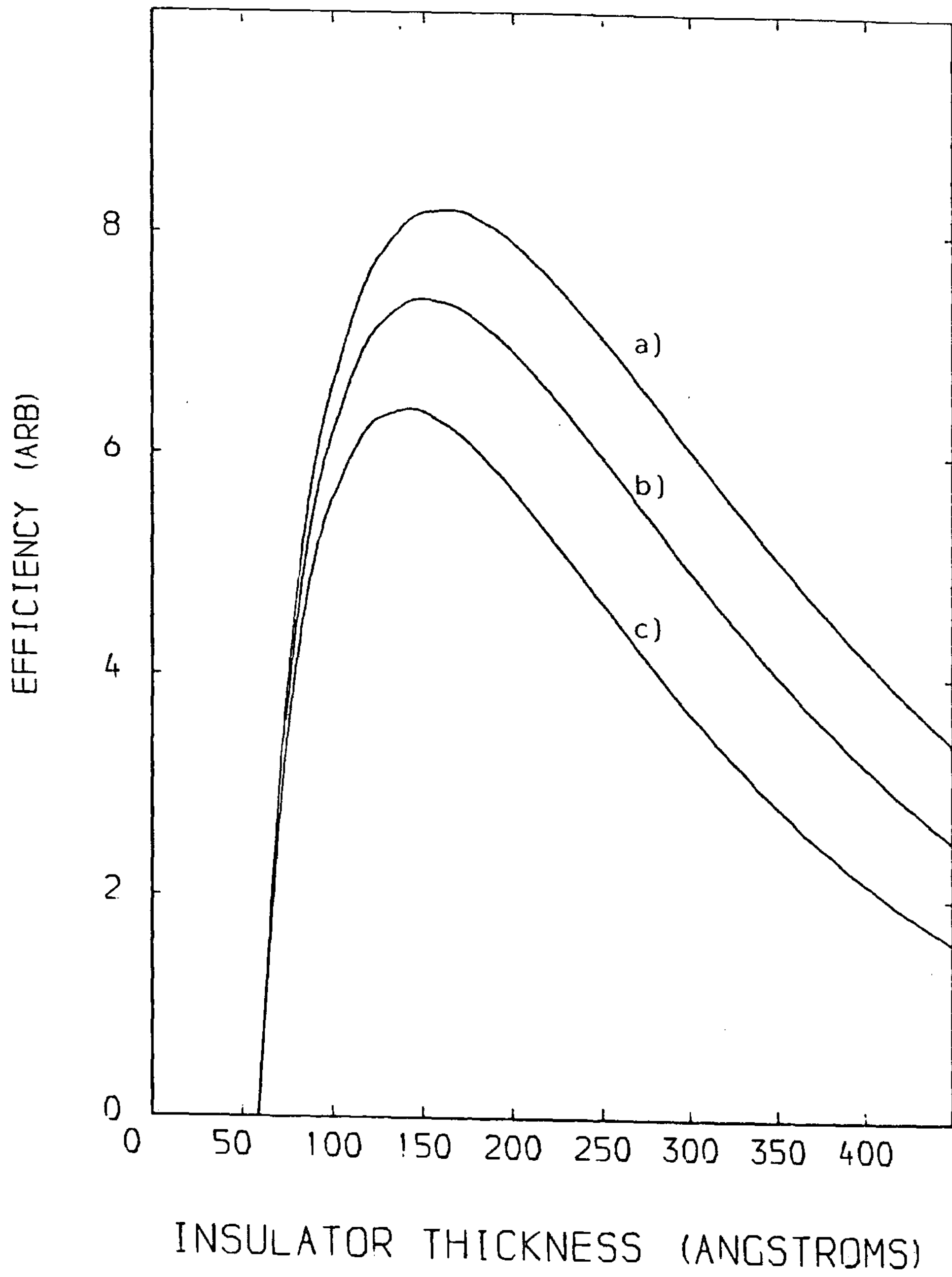

Fig. 6.11 : The expected variation in dc power conversion assuming a hole current proportional to field and a mean free path for recombination of a) 300Å b) 250Å and c) 200Å.

Batey et al's[6,7] experimental results.

Once again, it has been assumed in the treatment that there is an adequate supply of holes at the metal-insulator interface. At the smaller insulator thicknesses, with the semiconductor valence band edge well below the metal Fermi level, the population of thermally created holes that are energetically capable of entering the valence band, is extremely low. However, the population of holes created by the impact ionisation process (described in Chapter Four) will dominate at the energies close to the band edge ($\lesssim(E_{Fm}-0.5)$eV) with approximatley 15% of majority carriers injected into the metal creating holes capable of reaching the metal-insulator interface. Hence, in view of the typical values of the dc power conversion ratio ($\sim10^{-5}$%) [6,7], it would appear that there is a sufficient supply of holes at the interface.

By assuming that the hole current is always insulator limited, that it is attenuated by lifetime effects, and that it is proportional to field, as observed by other groups[13-15] for electron current, it has proved possible to identify a form of transport which gives similar characteristics to experimentally obtained ones. Before continuing, one final point should be made about the hole current at values of δ where the calculated insulator field is negative. The negative fields occur at very low thicknesses (1 and 3 monolayers only). These thicknesses are very small, with one monolayer only being 25Å. It therefore is quite plausible that there will be a significant contribution from quantum mechanical tunnelling leading to a measureable current in this regime.

The treatment of hole transport through the insulator in this section,

has been phenomenological in approach. This was necessitated by the lack of basic experimental work on the subject. Conductivity measurements have been made on MIM devices incorporating Langmuir-Blodgett films[13] and these were used as an indication of possible dependencies of the injected hole current. In the MIS device, however, the hole current is not in thermal equilibrium with the metal at the MI interface and apart from the uncertainty of the insulator transport mechanism for these carriers, there is the additional problem, as mentioned in the text, of lifetime effects. A detailed examination of these points would help to clarify the minority injection current mechanism.

6.4 HOLE TRANSPORT IN DIODES INCORPORATING II-VI SEMI-INSULATORS

6.4.1 Direct Tunnelling

Direct tunnelling in MIS devices incorporating Langmuir-Blodgett films was discussed in some detail in Section 6.3.1. It was shown then, that the quantum mechanical tunnelling process alone could not be responsible for the experimentally observed dc power conversion characteristics[6,7]. Devices incorporating undoped wide band gap II-VI compounds as the insulator, show enhanced dc power conversion ratios for insulator thicknesses which are even larger than those for the Langmuir-Blodgett film diodes. With insulator thickness in excess of 400Å it must be concluded, again, that the hole current due to direct quantum mechanical tunnelling is negligible.

6.4.2 Conduction via the Insulator Valence Band

A feature of the diodes incorporating II-VI semi-insulators is that in many cases the band gaps of the insulator and semiconductor are similar in value. Indeed, it is possible to use the same compound as the insulator and semiconductor by suitable doping. With the insulator having well defined conduction and valence bands it is a strong possibility that hole transport from the metal into the semiconductor will be by means of the insulator valence band.

In Chapter Five it was shown how the change in semiconductor barrier height in the Au/Langmuir-Blodgett film/GaP device could be modelled. The same techniques can be applied to devices incorporating different materials by a suitable choice of device parameters. To model the Au/i-ZnS/n-ZnS device produced by various groups, it was assumed that any interface states at the insulator-semiconductor boundary were uniform over both energy and area. It was also assumed that these states were only in communication with the semiconductor Fermi level. This last approximation is the most drastic. It is a reasonable assumption at large insulator thicknesses, however at lower values there might well be communication with the metal Fermi level through quantum mechanical tunelling or some trap transport mechanism. Such an effect, even if quite small, could be significant as the wide bandgap of the semiconductor means that large activation energies are needed for electrons in the semiconductor to occupy the interface states. Despite these short-comings, the model will be used in this form to give an indication of the device behaviour under forward bias.

Figure 6.12 shows the expected variation in field across the insulator. Any holes injected at the metal- insulator interface will be swept through the insulator into the semiconductor if the field is positive. This case is illustrated in Figure 6.13 . Incidentally, this band diagram, apart from being proposed by previous authors[17], is predicted by the model used here. Figure 6.12 shows that we can only expect a positive field when the insulator thickness is greater than about 200Å. Any communication of interface states with the metal will serve to increase this threshold thickness as the semiconductor barrier height will be pinned to the metal Fermi level in the manner described in Section 2.3.2.

Assuming that once the inversion in the insulator field has taken place all holes injected into the insulator valence band are swept through into the semiconductor, the minority carrier current will be controlled by the supply of holes at the metal-insulator interface. In Chapter Four we saw how an impact ionisation process (in which electrons below the Fermi level in the metal were excited by the electrions injected from the semiconductor) was an efficient hole production mechanism at energies well below the Fermi level. Applied to the Au/i-ZnS/n-ZnS system discussed above, with an MI barrier height of 2.2eV, this process is estimated to give a 1.6% probability that an injected electron will create a hole which is energetically capable of entering the insulator valence band. With the electron mean free path in ZnS being only 10Å the energy at which electrons are injected into the metal will not vary much with insulator field and the supply of holes at the metal-insulator interface will not vary significantly either. Assuming little impediment to hole transport through the insulator valence band, the minority carrier

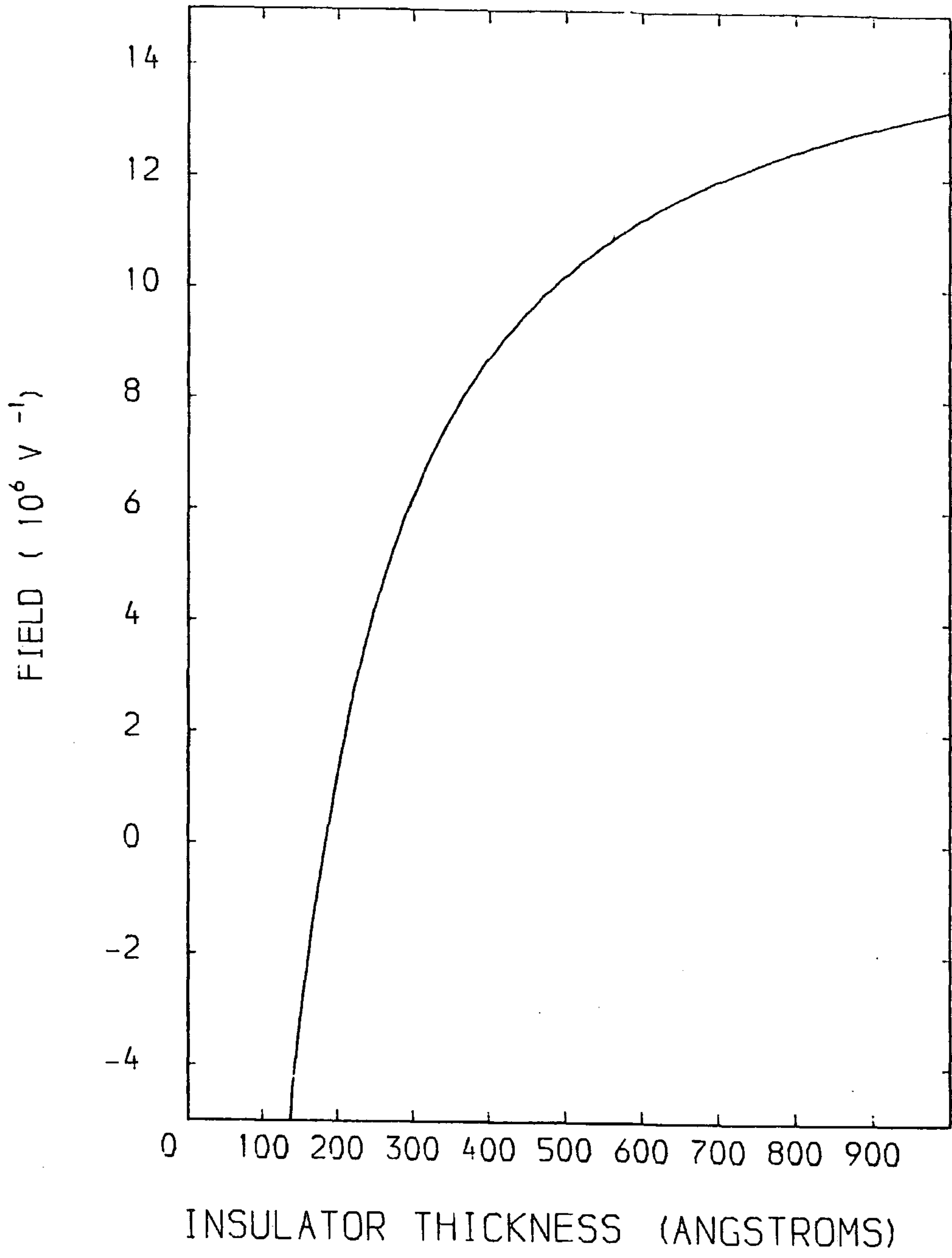

Fig. 6.12 : The change in insulator field calculated for an Au/i-ZnS/n-ZnS diode at a constant current of 10^3 Am^{-2}.

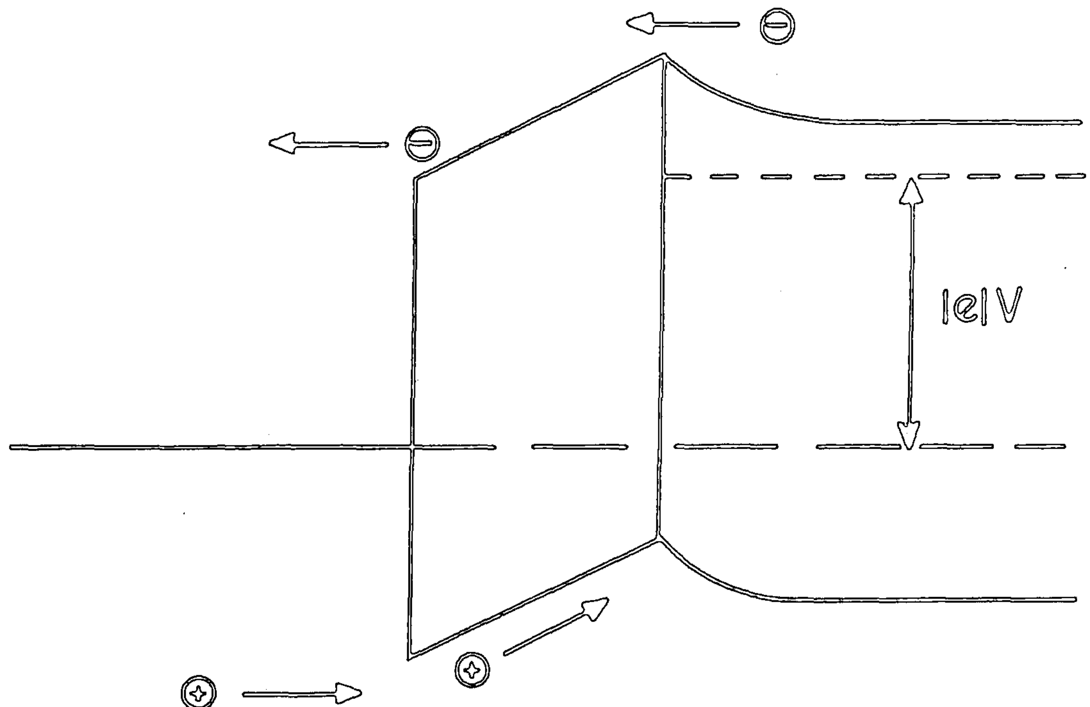

Fig. 6.13 : Proposed energy band diagram for an Au/i-ZnS/n-ZnS diode under forward bias.

current will be constant once a positive insulator field has been activated. This assumes that there is no recombination. This is not an unreasonable approximation as holes moving at thermal velocities ($\sim 10^5 ms^{-1}$) will pass through the insulator in times of the order of 10^{-13}secs. With the model presented here, it can be seen that there is approximately a 2% probability of an injected electron producing a hole capable of entering the n-ZnS valence band. II-VI materials are known to be efficient phosphors and it can be expected that as many as 1% of holes in the semiconductor valence band will recombine radiatively[18]. Therefore, using this model an efficiency of approximately 2×10^{-2}% can be expected. It is interesting to note that this result corresponds well with experimentally obtained values[19,20].

Even with the absence of the insulating layer there will be hole creation by the impact ionisation mechanism described. However the simple Schottky barrier will not be as efficient as the MIS diode for the following reasons. The first rests on the experimental evidence[17] that the barrier height of the MIS structure is larger than the Schottky barrier (2.2eV as opposed to 1.9eV). This means that more holes are created which are energetically capable of entering the semiconductor valence band. With reference to Figure 6.13 it can be seen that the insulator also fulfils another important role. Once a hole enters the insulator it is swept through into the semiconductor. In the Schottky barrier, driven at the same current density, the band bending in the semiconductor will be the same. In this case, then, the field will oppose the transport of holes from the metal into the semiconductor.

In the more widespread case of an insulator with a larger band gap,

there will be the additional advantage that the insulator will allow a "flat band" condition to be achieved in the semiconductor and under further forward bias the situation shown in Figure 6.14 will be reached. Any holes entering the semiconductor will now be swept, by the field, into the bulk where radiative recombination can take place. In a Schottky barrier it is not possible to reach this stage as bulk resistance effects will begin to dominate before "flat band" conditions are achieved. (Figure 6.15).

6.5 SUMMARY

In considering carrier transport through the insulator of an MIS diode much of this chapter has been devoted to the processes in the Au/Langmuir-Blodgett film/n-GaP device but II-VI diodes have also been considered.

First, considering the Langmuir-Blodgett films. it was demonstrated how sheets of interface states, expected at layer boundaries, could interact with the majority carrier or electron current. Calculations indicated that trapping was possible although it was not expected to affect the electron current significantly. The possibility of hole creation by electron-electron scattering at the trap sites was also discussed. It was concluded that this was not an important effect.

The two electron transport mechanisms found to dominate in Langmuir-Blodgett MIM devices, namely hopping and Poole-Frenkel conduction for low and high electric field regimes respectively, were used as the basis for investigating possible hole transport mechanisms. By using the model described in Chapter Five, the variation in the insulator field was

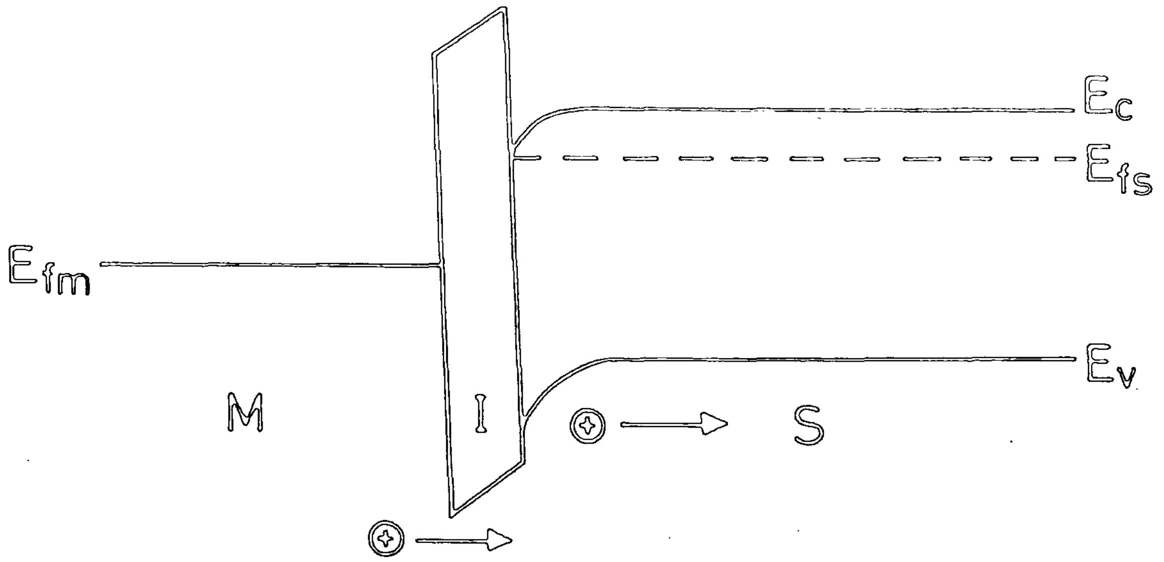

Fig. 6.14 : An MIS diode under forward bias.

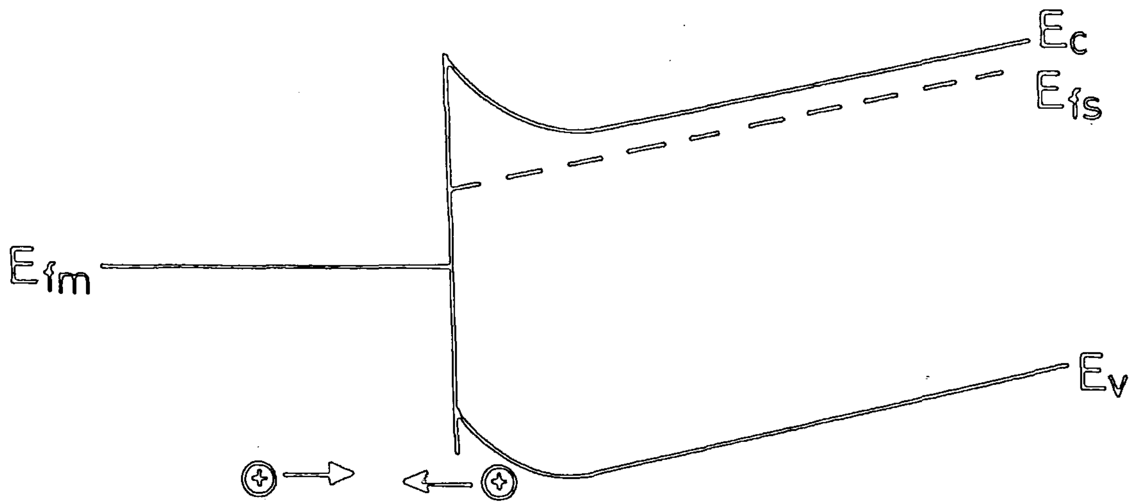

Fig. 6.15 : A Schottky barrier under forward bias.

predicted. It was found that hopping conduction, in which the hole current is proportional to field, was the more accurate in reproducing experimentally obtained results.

Hole conduction in devices incorporating II-VI semi-insulators was described in terms of transport via the insulator valence band. By assuming that this transport was unimpeded and that the conduction was limited by the supply of holes at the metal-insulator interface (this was investigated in Chapter Four), device efficiencies were calculated and found to be close to experimentally obtained results.

CHAPTER SEVEN

ELECTRICAL CHARACTERISTICS OF AN MIM ELECTROLUMINESCENT PANEL IN THE STEADY STATE

7.1 INTRODUCTION

This chapter considers an electroluminescent device rather different from the forward biased MIS diodes of the previous chapters as we look at the behaviour of an MIM structure which has been fabricated by a group at RSRE, Malvern[1]. Similar structures have been produced and investigated by other groups working in this area[2,3], and although the results presented in the chapter are primarily concerned with the RSRE device their usefulness is more general.

The RSRE structure is based on a thin layer of zinc sulphide doped with manganese with a transparent conductor (eg cadmium stannate) as one electrode and aluminium as the other. Cadmium stannate is, in fact, a degenerate semiconductor with an electron effective mass about equal to that of a free electron. The semi-insulating ZnS is normally prepared by sputtering in an atmosphere of hydrogen and argon and is then polycrystalline. It appears that hydrogen gives increased stability to the device by somehow limited the formation of high current filaments in the bulk. Only a thin layer near the cathode needs this hydrogen incorporation to give the desired stability.

The ZnS is doped with Mn[1,4] and those centres are responsible for the light emission by a process in which conduction electrons excite bound electrons in the orbitals of the manganese to higher states with subsequent light emission on de-excitation[5,6]. It is doped at a concentration of approximately ½ atomic percent. As the manganese mainly goes on the Zn sites in the material, about 1% of the zinc ions are replaced by the dopant.

As a precaution against the spread of high current filaments an additional control layer, shown in Figure 7.1(a), is also included. Two sorts of layer have been used, the first is a "cermet" consisting of a metal powder dispersed in a non conducting medium. This seems to act as an array of point contacts and any filament formed at one point is unable to spread to another as the current across the semi-insulator has in effect been broken up into distinct current paths, corresponding to the point contacts. Filaments burn out rather than expand and on each occasion there is a slight reduction in light output rather than catastrophic failure. A second type of control layer used is made of amorphous silicon. It is thought to act in a different way to the cermet by behaving more as a spreading resistance and not allowing the current in a filament to get so high that it burns out. Devices produced in this way are not as bright as those employing the cermet but they do have longer lifetimes.

Cattell, Inkson and Kirton[7] have suggested a model to explain the characteristics of the device and in particular the tendency to jump to higher currents with eventual failure. In section 7.2 the basis of this model is described. A set of equations are developed to describe

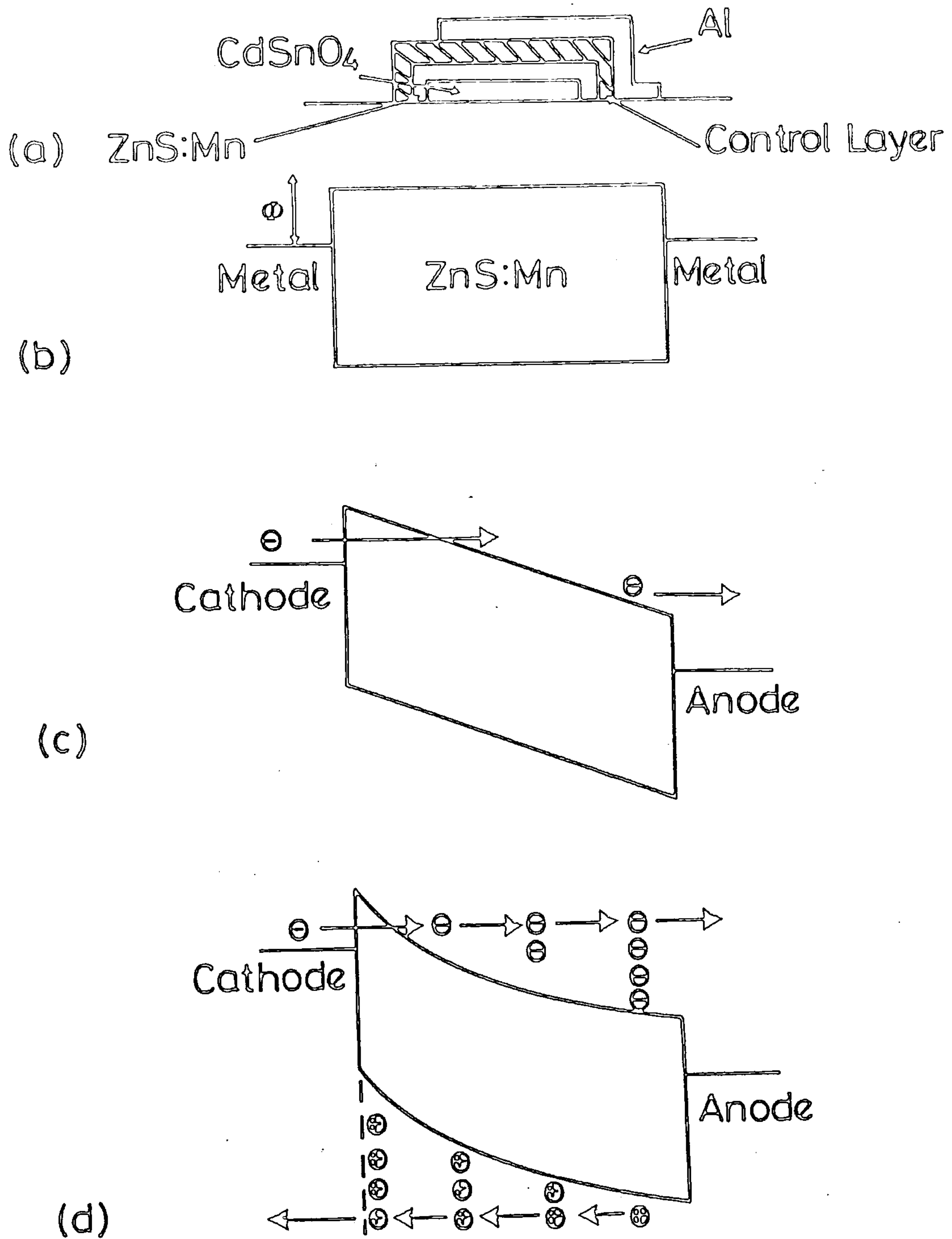

Fig. 7.1 : a) A schematic diagram of a typical directly coupled electroluminescent MIM device.

b) The idealised energy band diagram for an MIM device at zero bias.

c) The energy band diagram for an MIM device with a moderate electric field at the cathode.

d) The energy band diagram for an MIM device with a high electric field at the cathode.

the device once it has reached steady state conditions. It is shown that the model predicts an 'S' shaped curve for the current-voltage characteristic, a current controlled instability that is expected to lead to current filament formations.

7.2 MODELLING THE DEVICE

7.2.1 Band Alignment

In the absence of any bias the energy band diagram is expected to be as shown in Figure 7.1(b). The ZnS is taken to be insulating, with no free electrons in the conduction band. The fixed space charge due to impurities is assumed to be negligible, so the electric field is zero. ϕ is the barrier presented by the ZnS at its boundary with the metal. When a small voltage is applied across the device, all of it is dropped across the semiconductor and the current is barrier limited by the process of thermionic emission into the semiconductor. The triangular barrier, shown in Figure 7.1(c) is too thick for tunnelling to take place. The barrier height does not change with the field in the ZnS (except for small image charge effects) so the thermionic emission current remains constant as a function of voltage. ϕ is expected to be of the order of 0.5eV and the curent is small and has negligible effect on the electric field in the ZnS. As the field is increased to large values the barrier at the interface becomes thinner until it reaches a threshold value at which tunnelling through the barrier becomes significant. If the field is increased further the tunnelling current becomes quite large with the barrier becoming almost transparent to incident electrons. The large number of carriers in the ZnS conduction band now have a significant effect on the field. It is unlikely that the same argument can be applied

to hole injection into the valence band at the anode. The barrier height to holes is expected to be larger leading to a thicker barrier and the higher effective mass adversely affects tunnelling.

With high fields in the ZnS, holes can be created, in the valence band, by impact ionisation, which then travel with the field back to the cathode. The mobility of the holes is approximately two orders of magnitude less than that for electrons and the holes move relatively slowly to the cathode. This results in a build up of holes and hence positive charge near the cathode which causes band bending with the magnitude of the electric field becoming less away from the cathode. This flattening of the bands is illustrated in Figure 7.1(d) and is a further reason for neglecting hole injection at the anode. With their lower mobility the holes are unlikely to gain sufficient energy to cause impact ionisation and therefore their multiplication coefficient will be much less than that for the electrons so the effect of the process is neglected in our model. There is no reason to expect that the hole flow should be impeded at the cathode and it is reasonable to assume that the holes either pass into the metal or recombine as soon as they reach the boundary. However it should be noted that any blockage of the hole current will have a marked effect on the device characteristics because of the associated rise in the hole concentration at the cathode.

The basic mechanism of electroluminescence is one of impact excitation, of the Mn^{2+} ions by the electrons. Bound electrons in d orbitals are excited to higher bound states and subsequently emit light on de-excitation. The excited state is known to be about 2.2eV abcve the ground state[6]. We assume that the concentration of electrons losing energy in exciting these centres in negligible compared to the total concentration and that

the great majority of the electrons have sufficient energy to impact ionise.

7.2.2 Defining Equations

In the steady state the behaviour of the bands is governed by a set of equations relating the carrier concentrations to the electric field. There is Poisson's equations giving the first spatial derivative of the field in terms of the charge density, that is:

$$\frac{dF(x)}{dx} = \frac{|e|}{\varepsilon\varepsilon_o}(p(x) - n(x)) \qquad (7.1)$$

where F(x) is the field at a distance x from the cathode interface and p(x) and n(x) are the hole concentrations and electron concentration respectively.

We can also write down the condition of current continuity for the system. The total current consists of an electron current and a hole current:

$$\begin{aligned} J &= J_n(x) + J_p(x) \\ &= n(x)|e|\mu_e F(x) + p(x)|e|\mu_h F(x) \qquad (7.2) \end{aligned}$$

where μ_e and μ_h are the mobilities of the electrons and holes. The values of μ_e and μ_h may well be affected by the high fields in the device. This particular problem will be addressed in section 7.3.4.

Due to impact ionisation the electron current increases with x. If the

probability of an electron undergoing such an interaction is α per unit length then the change in the electron current is given by:

$$\frac{dJ_n(x)}{dx} = \alpha(F(x))\ J_n(x) \tag{7.3}$$

We do not need a similar equation for the holes as the current continuity in equation (7.2) will ensure the correct response. As mentioned in the last section it is not expected that the holes themselves will cause impact ionisation because of their lower mobility and smaller quantum mechanical ionisation rate.

Finally it is necessary to define the injection current through the triangular barrier at the cathode. This is given by Lampert and Mark[8] for a thermally assisted tunnelling current as:

$$J_n(0) = \frac{(|e|F(0))^2}{(4\pi)^2\ h\phi}\left[\frac{1+4\pi^2 m^*\ (kT)^2}{3h^2|e|F(0)^2}\right] \exp\left[-\frac{4(2m|e|)^{1/2}\phi^{3/2}}{3hF(0)}\right] \tag{7.4}$$

7.2.3 Method of Solution

We can incorporate current continuity into Poisson's Equation (equation (7.1)) by substituting for p(x) from equation (7.2) to give

$$\frac{dF(x)}{dx} = \frac{1}{\varepsilon\varepsilon_0 F(x)}\left(\frac{J}{\mu_h} - J_n(x)\left(\frac{1}{\mu_e} + \frac{1}{\mu_h}\right)\right) \tag{7.5}$$

Equations (7.3) and (7.5) form a set of two differential equations

with $F(x)$ and $J_n(x)$ as the unknown variables. If a cathode field $F(0)$ is chosen the electron current at the cathode $J_n(0)$ can be calculated using equation (7.4). The value of $J_p(0)$ which is needed to find $J(0)$ (equations (7.2)) is, however, unknown but it must be compatible with zero hole current at the anode. This is because it is assumed that there is no hole injection at that electrode.

It is necessary to guess the hole current density at the cathode and to combine it with the value obtained for the electrons to give the total current J. Then the differential equations can be solved numerically over the width of the ZnS and the value of $J_n(W)$ found. Since zero hole injection at the anode has been specified $J_n(W)$ must also be equal to the total current J. This will only turn out to be the case if the correct choice of $J_p(0)$ is made, so $J_p(0)$ must be continuously revised until $J_n(W) = J$. If $J_p(0)$ is too large then the excess positive charge at the cathode will reduce the magnitude of the electric field to such an extent that there will not be sufficient impact ionisation over the length of the ZnS to supply the holes and a finite hole current will be required at the anode (ie an injection current). If, however, $J_p(0)$ is too small then the electron current density at the anode is too large. These considerations give guidance on how the hole current density at the cathode should be modified to give convergence to the correct conditions at the anode.

To effect a numerical soultion a Runge Kutta routine was used to give an electric field profile across the thickness of the ZnS and using the values of the electric field, an integration routine was employed to find the potential difference across the device.

Different cathode fields give different potentials across the device and by varying the field it is possible to produce a current density-voltage characteristic for the device. This is best done by starting at the relatively low field where there is negligible band bending (essentially a constant electric field) and an approximate value of $J_p(0)$ can be found with little difficulty. With the constant field the multiplication of the electron current density is of a simple exponential form and the value at the anode is given by

$$J_n(W) = J_n(0)e^{\alpha(F(0))W} \tag{7.6}$$

Using this result it is straightforward to find the hole current density. Given J_p is zero at the anode

$$J_p(x) = J_n(W) - J_n(x) \tag{7.7}$$

The value of $\alpha(F)$ used is from an empirical expression for Schottky barriers by Allen[9]:

$$\alpha(F(x)) = \alpha_o \exp\left(-\left(\frac{F_o}{F(x)}\right)^2 \right) \tag{7.8}$$

with $\alpha_o = 1.2 \times 10^7 \ m^{-1}$

and $F_o = 2 \times 10^8 \ Vm^{-1}$

One reservation about this result is that it was deduced for relatively low fields ($\sim 10^6 Vm^{-1}$) and may not be valid for some of the higher field considered here.

On finding the approximate value of $J_p(0)$ the numerical method is used to obtain the associated value of the hole current density at the anode. Normally the numerical solution will show that the boundary conditions are not met precisely and $J_p(0)$ must be slightly modified and the procedure repeated until they are satisfied. Moving to higher fields the approximation of constant field used above will not be valid, but to give an indication of the hole current density at the cathode, it is possible to extrapolate from the previous values of $J_p(0)$ for lower contact fields.

7.2.4 Dead Space

It is worth mentioning here the concept of 'dead space'; the region adjacent to the cathode in which the injected electrons have not achieved sufficient energy to impact ionise. In Section 7.3.1 it will be shown that its existence doesnot affect the characteristics of the device to any great extent, but it is important that its presence is noted.

The applied potential must exceed the barrier height before a tunnelling current can enter the ZnS conduction band. In addition to this it must be larger again by $E_g/|e|$ volts (where E_g = 3.2eV) before the carriers have sufficient energy to impact ionise electrons from the valence band across the bandgap into the conduction band. So in total the potential needs to exceed $\phi + E_g/|e|$. As there is no carrier multiplication in dead space the electron and hole current densities individually remain unchanged and

$$n(x)F(x) = n(0)F(0)$$

$$p(x)F(x) = p(0)F(0) \tag{7.9}$$

$$0 < x < W_{DS}$$

where W_{DS} is the extent of the dead space. Using these equations to define the carrier concentrations at x in Poisson's Equation the spatial derivative of field at that point is given by

$$\frac{dF(x)}{dx} = \frac{|e|}{\varepsilon\varepsilon_o} (p(0) - n(0)) \frac{F(0)}{F(x)} \tag{7.10}$$

and the field itself is found by a simple integration

$$F(x) = - \left[F(0)^2 + \frac{2(p(0)-n(0))}{\varepsilon\varepsilon_o} |e|F(0)x \right]^{\frac{1}{2}} \tag{7.11}$$

If this is again integrated over x between the limits 0 and W_{DS} it gives the change in potential in the dead space. Equating the integral to $-(\phi + E_g/|e|)$ gives the length of the dead space which can be written as:

$$W_{DS} = \frac{\varepsilon\varepsilon_o}{2(p(0)-n(0))|e|F(0)} \left(\left[|F(0)|^2 + \frac{3F(0)(p(0)-n(0))|e|(\phi+Eg/|e|)}{\varepsilon\varepsilon_o} \right]^{2/3} - F^2(0) \right) \tag{7.12}$$

Equation (7.4) can be used to find the injected electron current density for a particular field and this also allows the cathode electron concentration to be calculated. If it is assumed that p(0) is within

two or three orders of magnitude of n(0) then

$$|F(0)|^2 \gg \left| \frac{3F(0)\ (p(0)-n(0))\ |e|\ (\phi+Eg/|e|)}{\varepsilon\varepsilon_o} \right| \qquad (7.13)$$

Using this condition, equation (7.12) can be greatly simplified to

$$W_{DS} = \frac{\phi + Eg/|e|}{|F(0)|} \qquad (7.14)$$

7.2.5 Mn Electroluminescent Centre

Given an excitation cross section σ (which is known to be of the order of $10^{-20}m^2$) the excitation rate of electroluminescent centres is given by:

$$R_{ex}(x) = Mn^g \sigma\mu_e\ |F(x)|n(x) \qquad (7.15)$$

where Mn_g is the density of centres in the ground state and the other symbols are as defined previously. In the steady state this excitation rate must be the same as the rate of decay of the excited centres back to the state described by a time constant $\tau_o(\sim 10^{-3}s)$. By equating the two rates, the rate of de-excitation (or excitation) is given by:

$$R_{de-ex}(x) = \frac{Mn}{\tau_o + \tau_1} \qquad (7.16)$$

where $\tau_1 = \dfrac{1}{\sigma\mu_e\ |F(x)|n(x)}$

and Mn is the total concentration of manganese electroluminescent centres. Calculating the electron current density at various points in the ZnS allows the calulation of the de-excitation rate at these positions and for the device as a whole.

It is interesting to note that the manganese excitation rate is relatively small compared to the impact ionisation rate with

$$(F(x)) \gg \frac{1}{\mu_e F(x)} \frac{Mn}{\tau_o + \tau_1} \tag{7.17}$$

where the right hand side is the rate of excitation per unit time (given by equation (7.16) divided by the electron velocity to give the rate per unit length).

The total light output can be obtained, if desired, directly from the total de-excitation rate.

7.3 CURRENT-VOLTAGE CHARACTERISTICS

With the band bending at high fields it is expected that there will be a region of differential negative resistance in the J-V characteristics, at which the voltage will actually fall with increasing field and current. With more that one value of J for a particular voltage there is the possibility of a device jumping from a low current state to a high current state with the destruction of the device. A central aim of the theory is to produce a J-V plot indicating the voltages at which this unfavourable process is possible and to investigate the influence of the material parameters.

In these calulations the material parameters used are the bulk values of ZnS, the barrier height ϕ (Cattell[1]) was taken as 0.5eV and the length of the ZnS was set at the typical value of $W = 1.5\mu m$.

7.3.1 Inclusion of Dead Space

If it is assumed that carrier multiplication does not occur in the dead space then equation (7.3) must be modified to

$$\frac{dJ_n(x)}{dx} = 0 \qquad 0 < x < W_{DS}$$

$$\frac{dJ_n(x)}{dx} = \alpha(F(x))J_n(x) \qquad W_{DS} < x < W \qquad (7.18)$$

Figure 7.2 illustrates the effect of this dead space comparing the log J-V characteristic obtained using the modification to the equivalent characteristic obtained by assuming that the electrons are capable of impact ionisation as soon as they enter the semiconductor. The most noticeable difference is at the lower current (corresponding to lower contact fields) and even then there is little difference. At low fields, although there will be a relatively large dead space (for example around 500 Å for a field of 10^7 Vm^{-1}) the low multiplication coefficient will mean that there is little multiplication anyway and so there is only a small effect. At the higher fields, with the large values of α, the dead space will be narrow and have only a small influence on device behaviour.

It must also be noted from these curves that the higher current branches,

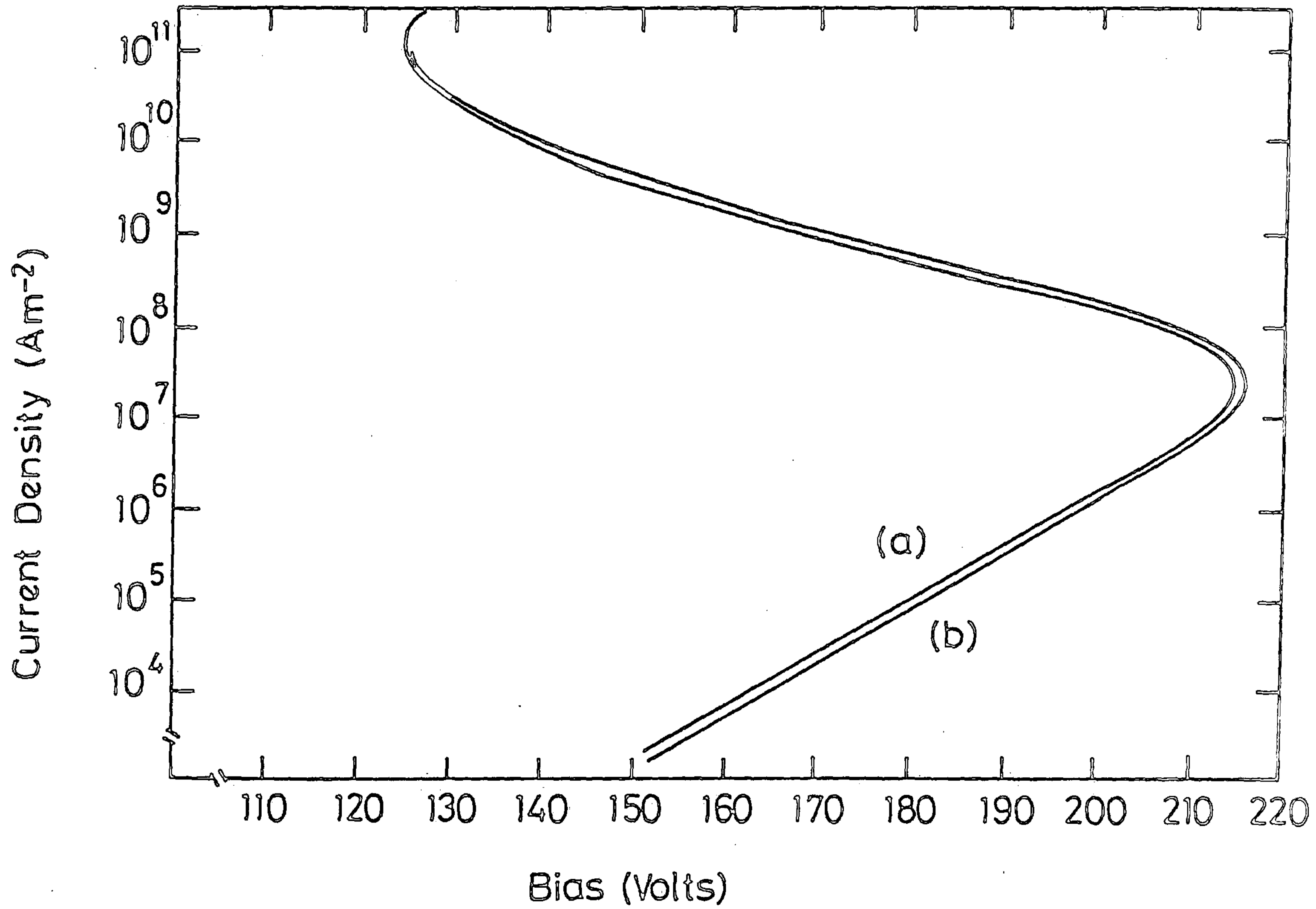

Fig. 7.2 : The current density - voltage characteristics with a) no dead space correction and b) dead space correction.

corresponding to the higher fields, have unrealistically large currents and under such conditions we would expect the device to burn out.

Figure 7.2 demonstrates that the inclusion of a dead space in the theory makes only a small difference to the characteristics and for this reason it is neglected in all subsequent calculations.

7.3.2 Carrier Concentration Profiles

It would be informative to know how the concentration of carriers varies across the sample for different contact field. Such figures are shown in Figures 7.3 to 7.7. Figures 7.3 shows the carrier concentrations profiles at the relatively low field of 10^8 Vm^{-1}. At these fields carrier multiplication and hole current are insignificant and the electron current dominates. The carrier concentrations are small and hence their effect on the field is only minor.

Figures 7.4 and 7.5 are the field and carrier profiles at a contact field of 2.9×10^8 Vm^{-1}. It can be seen that for a contact field of this size the holes are dominant and their large concentrations at the cathode leads to a sharp drop in the field with x. Towards the anode the carrier concentrations flatten out due to the lower multiplication rate in this region.

Figures 7.6 and 7.7 are for the very high field of 7×10^8 Vm^{-1}. Assuming that the device has not suffered breakdown (which is very likely at this magnitude of field), the field drops off very rapidly from the cathode and there is also a very sharp rise in the electron

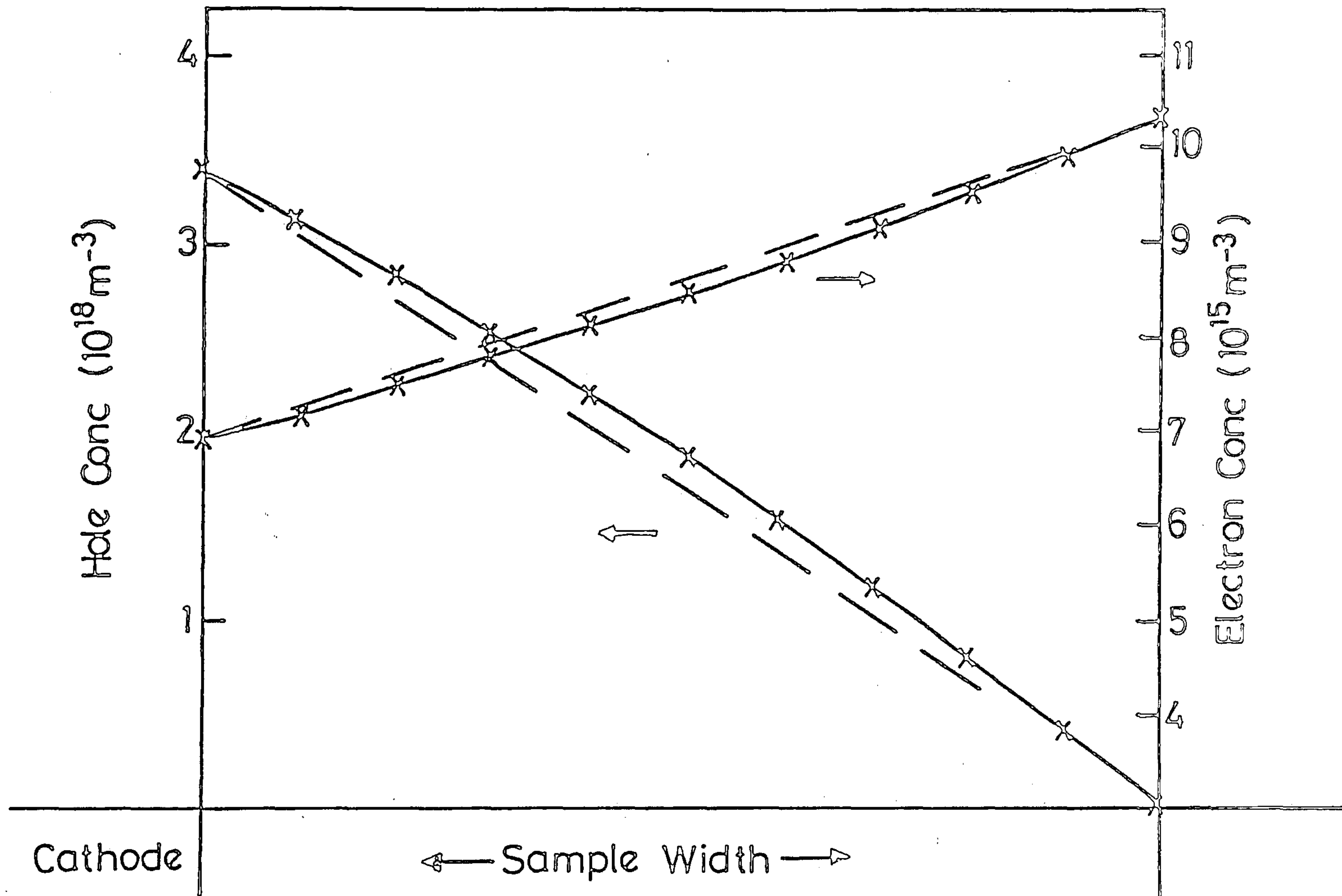

Fig. 7.3 : Carrier profile for a device with a cathode field of $10^8 Vm^{-1}$.

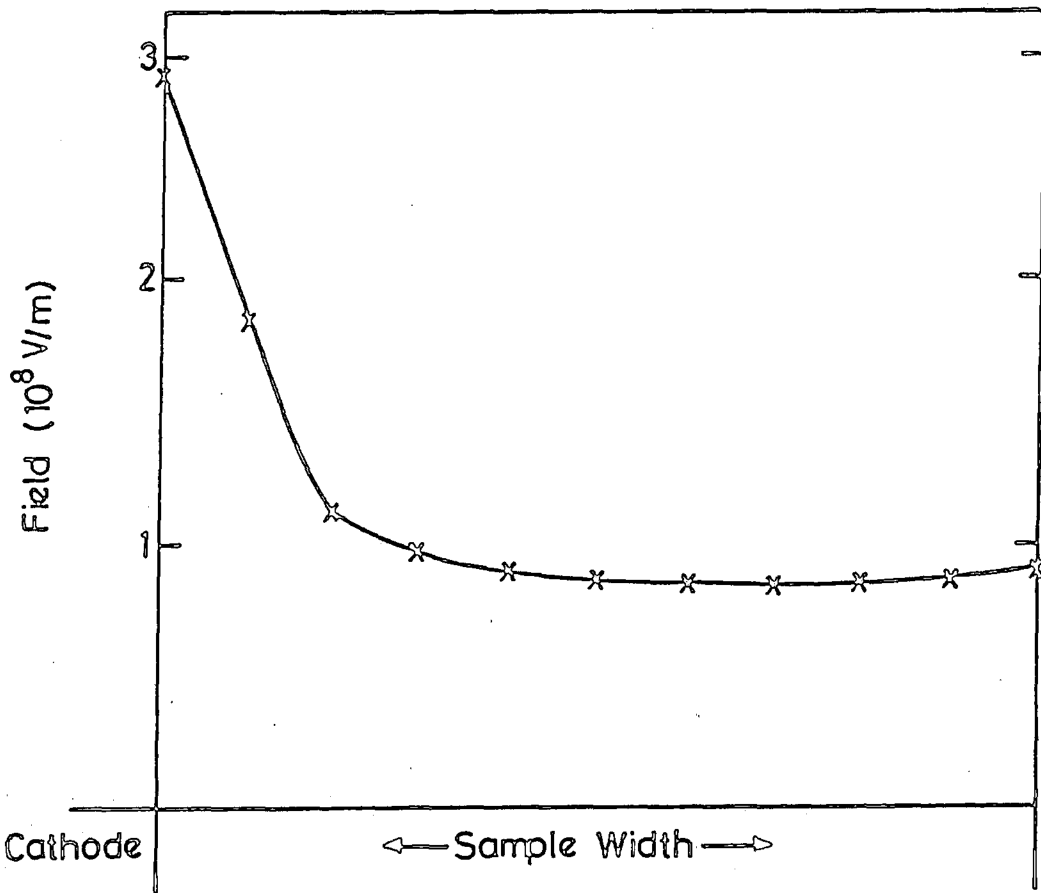

Fig. 7.4 : Field profile for a device with a cathode field of $2.9\times10^8 Vm^{-1}$.

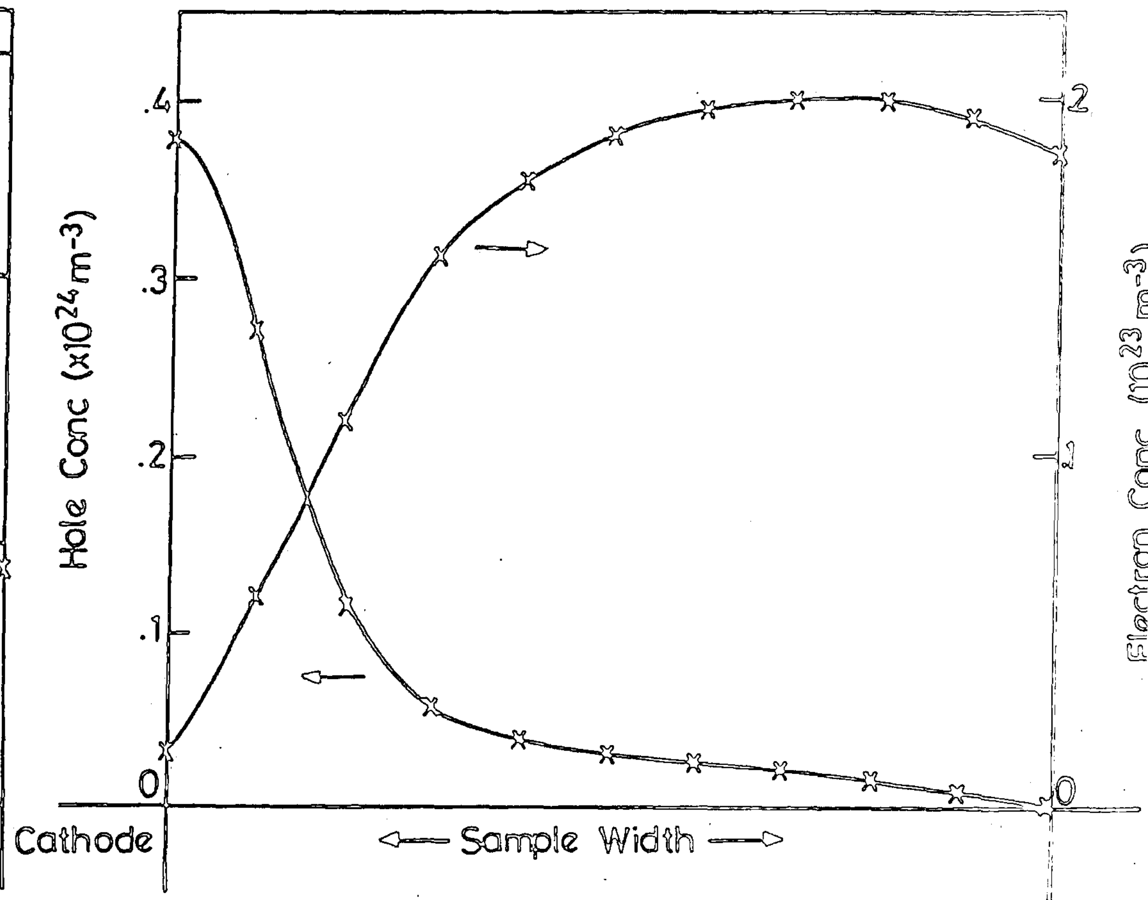

Fig. 7.5 : Carrier profile for a device with a cathode field of $2.9\times10^8 Vm^{-1}$.

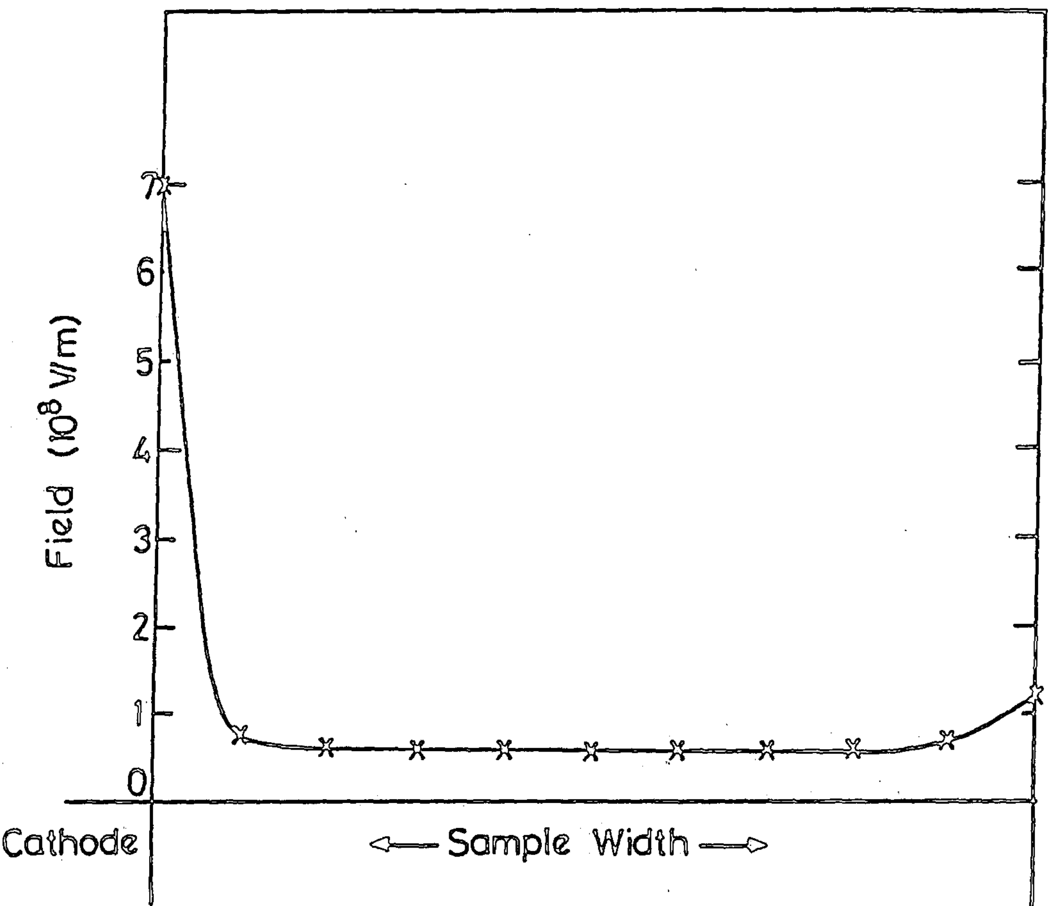

Fig. 7.6 : Field profile for a device with a cathode field of $7\times10^{8}Vm^{-1}$.

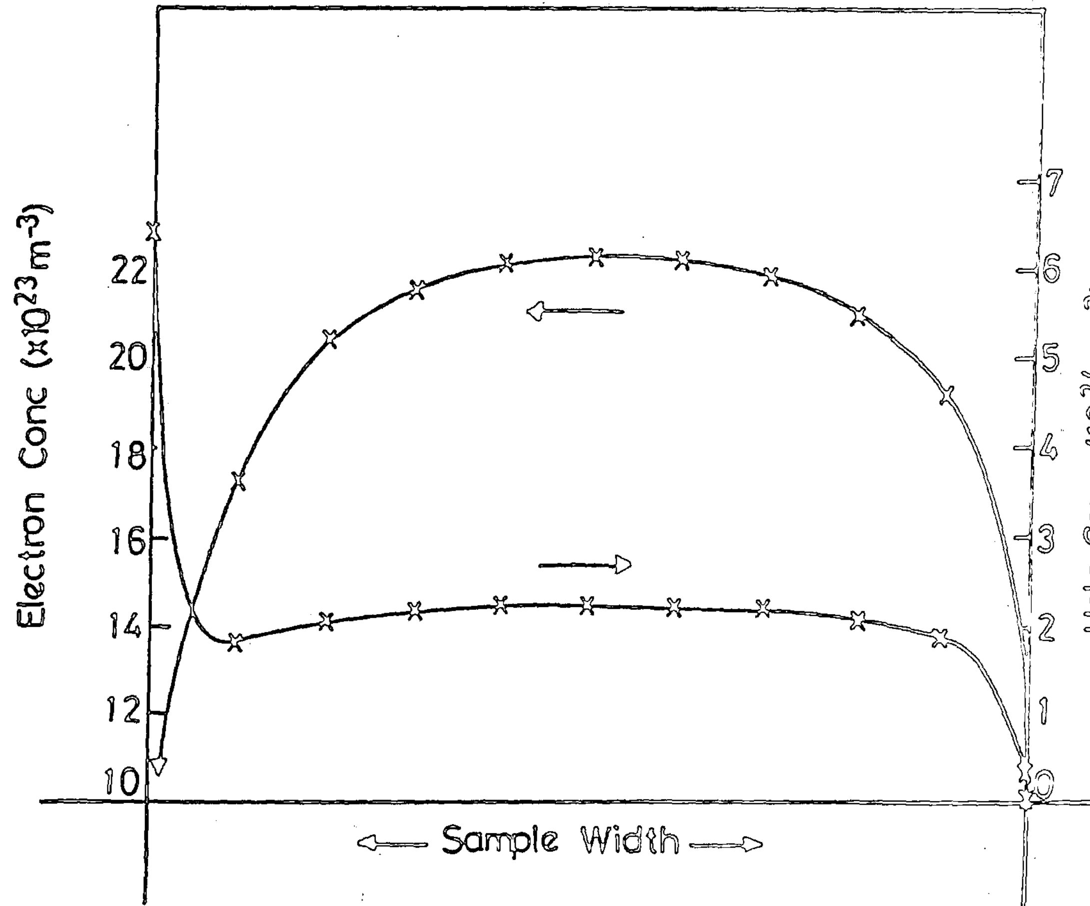

Fig. 7.7 : Carrier profile for a device with a cathode field of $7\times10^{8}Vm^{-1}$.

concentration . Towards the middle of the sample the field is reduced to such an extent that it is not sufficiently high to produce a significant multiplication rate. The rise in the electron concentration can be understood in terms of the requirement of constant current in the presence of a lower field. This also accounts for the rise in hole concentration. Both concentrations rise until a peak is reached at about the centre of the sample. From the centre of the sample the field begins to increase with x and this results in a larger value at the anode interface. This large increase in field at the anode is important as it leads to a rise in the potential across the sample with contact field and the higher branch of positive resistance in the current-voltage characteristics.

7.3.3 Effect of Temperature

At finite temperatures, electrons states above the Fermi level of the cathode can be occupied with a probability given by Fermi-Dirac statistics. For higher temperatures, the electron population above the Fermi level increases and as a result the average barrier thickness presented to them is reduced. With a reduction in the average barrier thickness there is an increase in the quantum mechanical tunnelling transmission rate and hence the injection current. Figure 7.8 shows that this is the case at the lower fields but that at higher values there is not significant effect. This is expected since the barrier will have become very thin and the impedance to electrons presented by the barrier will be negligible.

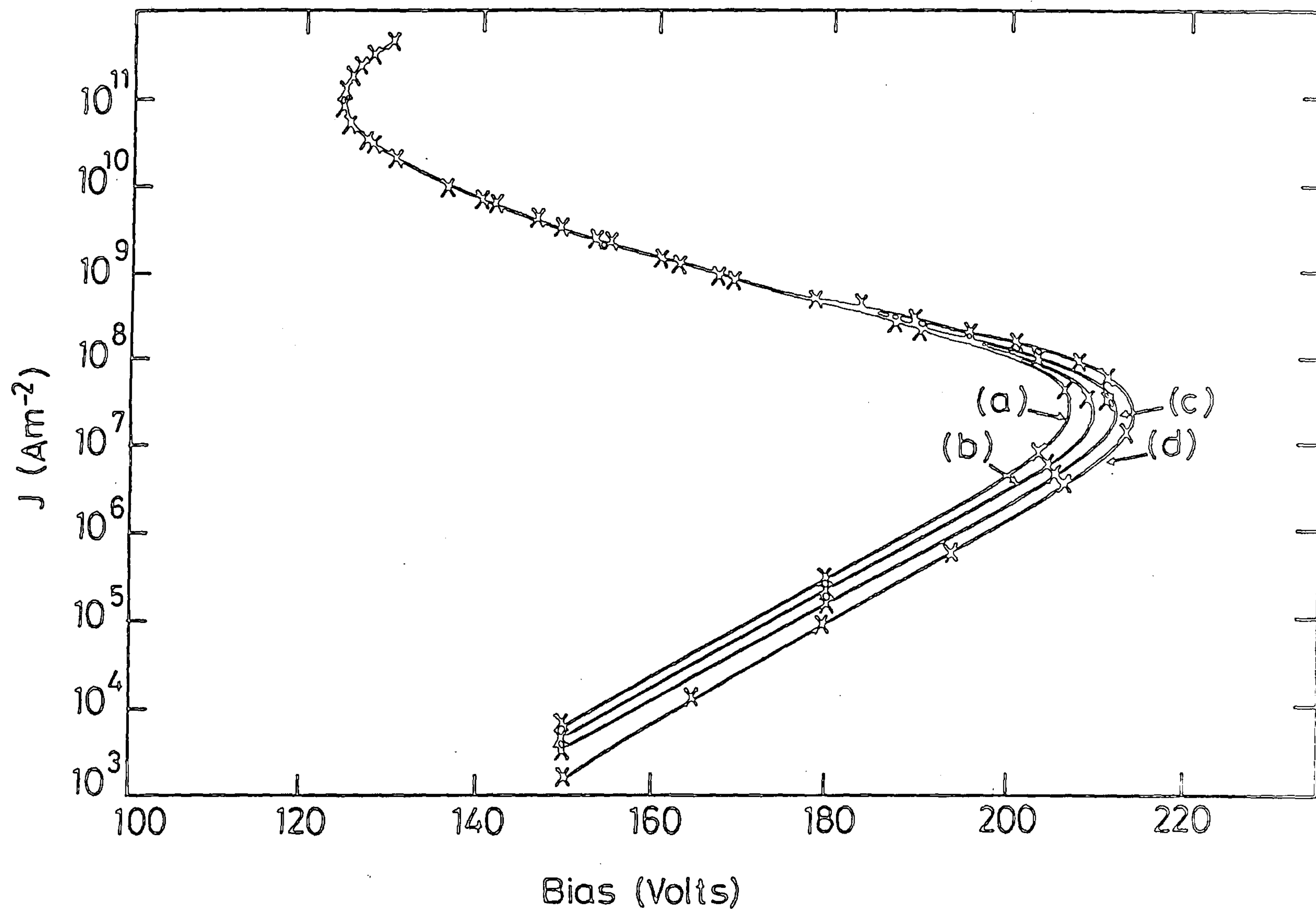

Fig. 7.8 : Current density-voltage characteristics for varying temperatures: a) 500°k; b) 400°k; c) 300°k and d) 0°k.

7.3.4 Carrier Mobilities

The bulk mobilities that have been used in the calculations are those appropriate for lower fields rather than those that exist in typical device conditions. It must also be taken into account that the ZnS is polycrystalline[1] rather than a single crystal and that additional effect due to, for example, grain boundaries might well affect the transport characteristics.. To gauge the importance of these points it is useful to look at the effect of the varying mobility values for both the electrons and holes. There is very little information in the literature on the mobilities at the relevant fields and the best indication of the variation of the electron mobility is given by the numerical calculations of Mukhopadhyay and Bhattacharya[10]. Their results are shown in Figure 7.9 (the normalised mobility versus electric field shows a reduction of approximately one order of magnitude on approaching typical fields). In our calculations reducing the electron mobility by an order of magnitude was found to produce very little change in the current-voltage characteristic principally because the concentration of holes in the valence band also changed to compensate for the increase in electrons.

To judge the effect that velocity saturation will have on the J-V characteristic a maximum value for the electron velocity (v_{max}) was set and an effective mobility used to limit the velocity to this value. For a low field mobility of μ_e the effective mobility was given by

$$\mu_{e\,eff}(x) = \mu_e \qquad v < v_{max}$$

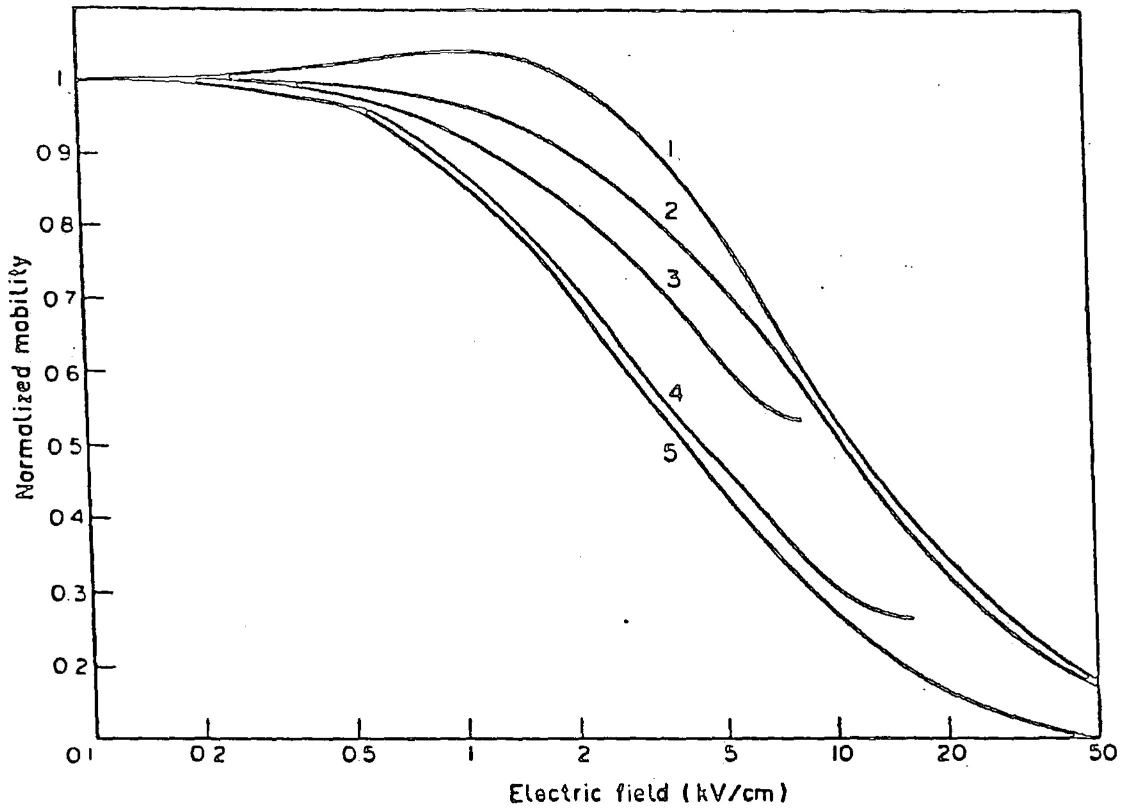

Fig. 7.9 : Variation of the normalised mobility with applied electric field at 77°k (with no impurity): 1) ZnS; 2) ZnS; 3) CdTe; 4) CdSe and 5) CdS (after Reference 10).

$$\mu_{e_{eff}}(x) = \frac{v_{max}}{F(x)} \qquad v > v_{max} \qquad (7.19)$$

Figure 7.10 shows the variationsin the device J -V characteristics using equations (7.19) for several values of v_{max}. This graph must be viewed with a certain amount of caution as the hole mobility is maintained at its low field value. In particular, curve (a) with $v_{max} = 10^3\ ms^{-1}$ is suspect as this velocity is, in fact, lower than the hole velocity under these fields and one might well expect the hole velocity to saturate too. Curves (b) and (c) are for v_{max} greater that the hole velocity and is a more plausible situation.

We now consider the hole mobility. Whereas the hole concentrations are dependent on these of the electrons, the opposite is not the case. We cannot expect some compensating effect by the negative charge. Figure 7.11 shows the kind of change expected with variation in μ_h. A lower hole mobility leads to a greater build up of positive charge, hence the greater band bending and negative differential resistance region at the lower fields. A higher hole mobility has the opposite effect. However, it is not expected that the hole mobility will vary as much as that for electrons because at low fields the holes have a velocity two orders of magnitude less that the electrons. So therefore, even at high fields, their velocity is not that great and less deviation from low field conditions can be expected. What must be noted, however, is that if there is some field activated trapping mechanism, such as Poole-Frenkel transport, there will be a fairly marked effect on the J-V characteristic.

One effect of the polycrystalline nature of the ZnS might be an overall

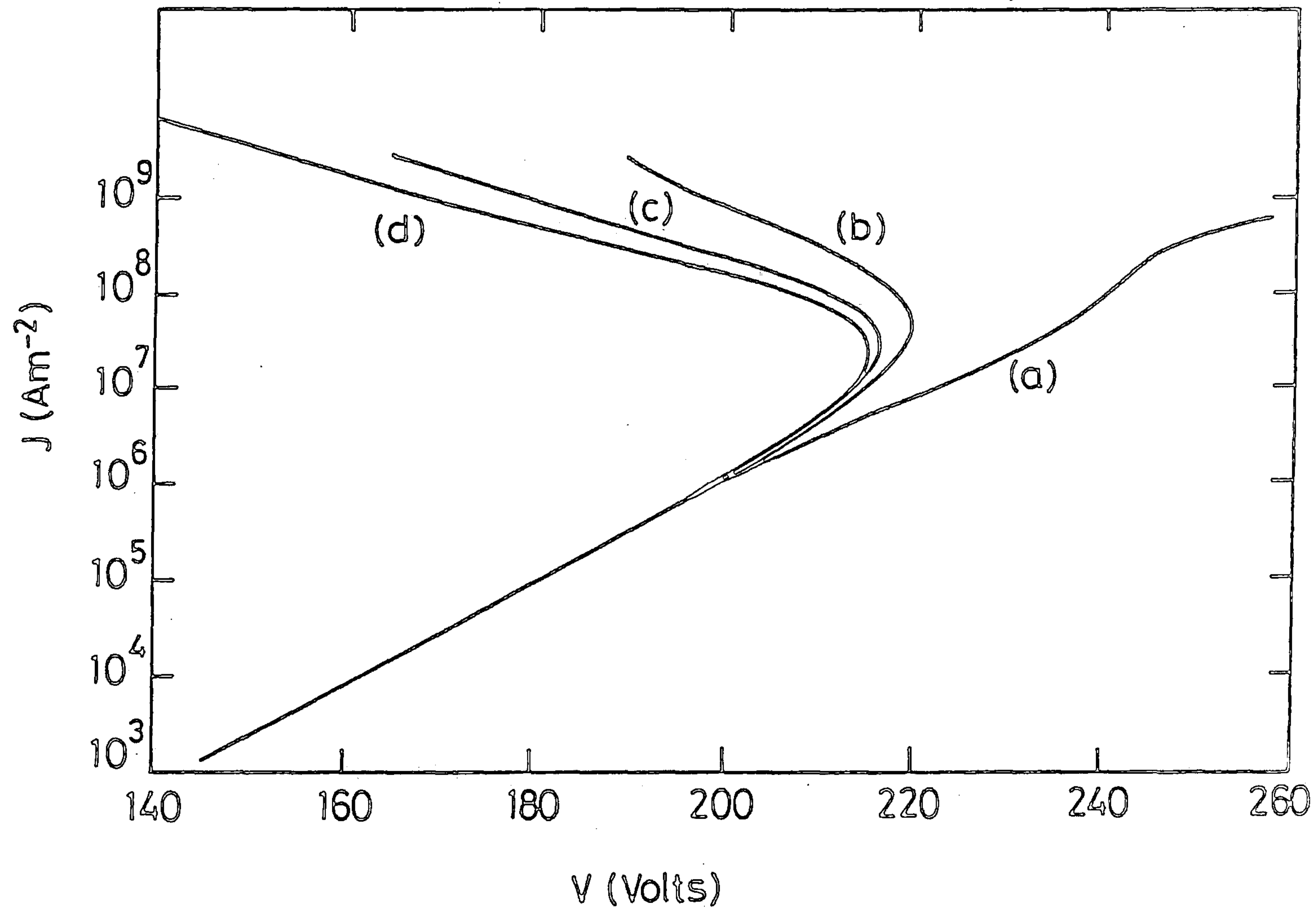

fig. 7.10 : Current density-voltage characteristics for an electron saturation current of a) $10^3 Vm^{-1}$; b) $10^4 Vm^{-1}$; c) $10^5 Vm^{-1}$ and d) no limit.

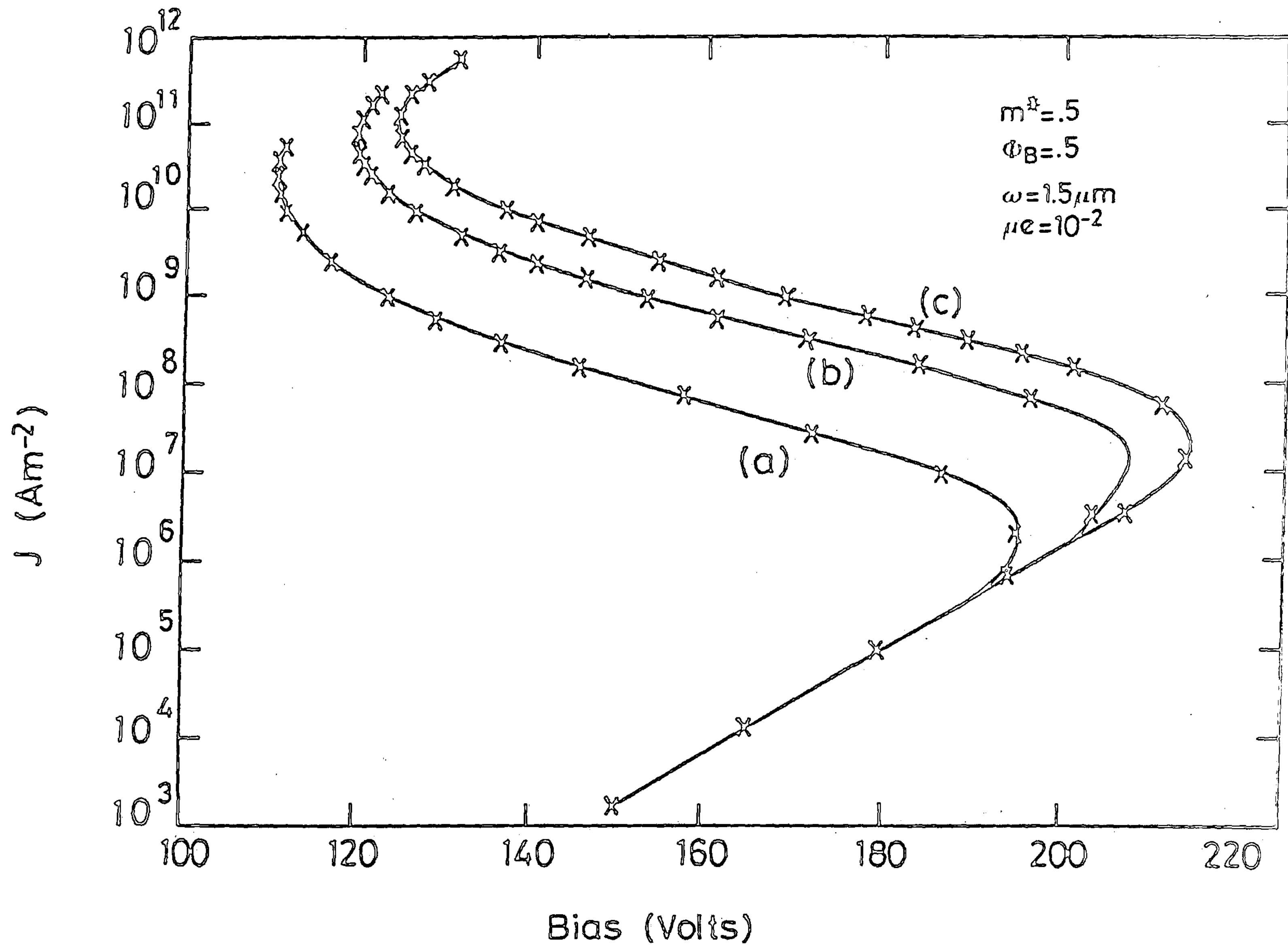

Fig. 7.11 : Current density-voltage characteristics for different hole mobilities a) $1 \times 10^{-5} m^2 V^{-1} s^{-1}$; b) $5 \times 10^{-5} m^2 V^{-1} s^{-1}$ and c) $1 \times 10^{-4} m^2 V^{-1} s^{-2}$.

reduction in both the electron and hole mobilities. Figure 7.12 illusrates the effect on the J-V curve when the mobilities are

(a) two orders of magnitude less

and

(b) one order of magnitude less than normal bulk values.

It should be noted that curve (b) is similar to to curve (a) in Figure 7.11 which itself corresponds to a fall, in the hole mobility only, of one order of magnitude.

7.3.5 Electron Barrier and Effective Mass

The value of the electron barrier height ϕ has a significant influence on the electron injection current and is expected to affect the device behaviour. Figure 7.13 shows the effect of this parameter and although, in this case, the difference is significant at all fields, the most observable difference is again at the lower fields. In normal operation the state of the device would correspond to a point on the lower positive resistance branch. It is clear that the voltage required for a certain current is strongly dependent on ϕ.

The effecti ve mass determines the ease with which carriers can tunnel and hence the injection current, so similar behaviour to Figure 7.13 is expected as indeed is the case in Figure 7.14, showing the effect of different values of m^*.

7.3.6 ZnS Thickness

An increase in the device thickness would be expected to lead to an

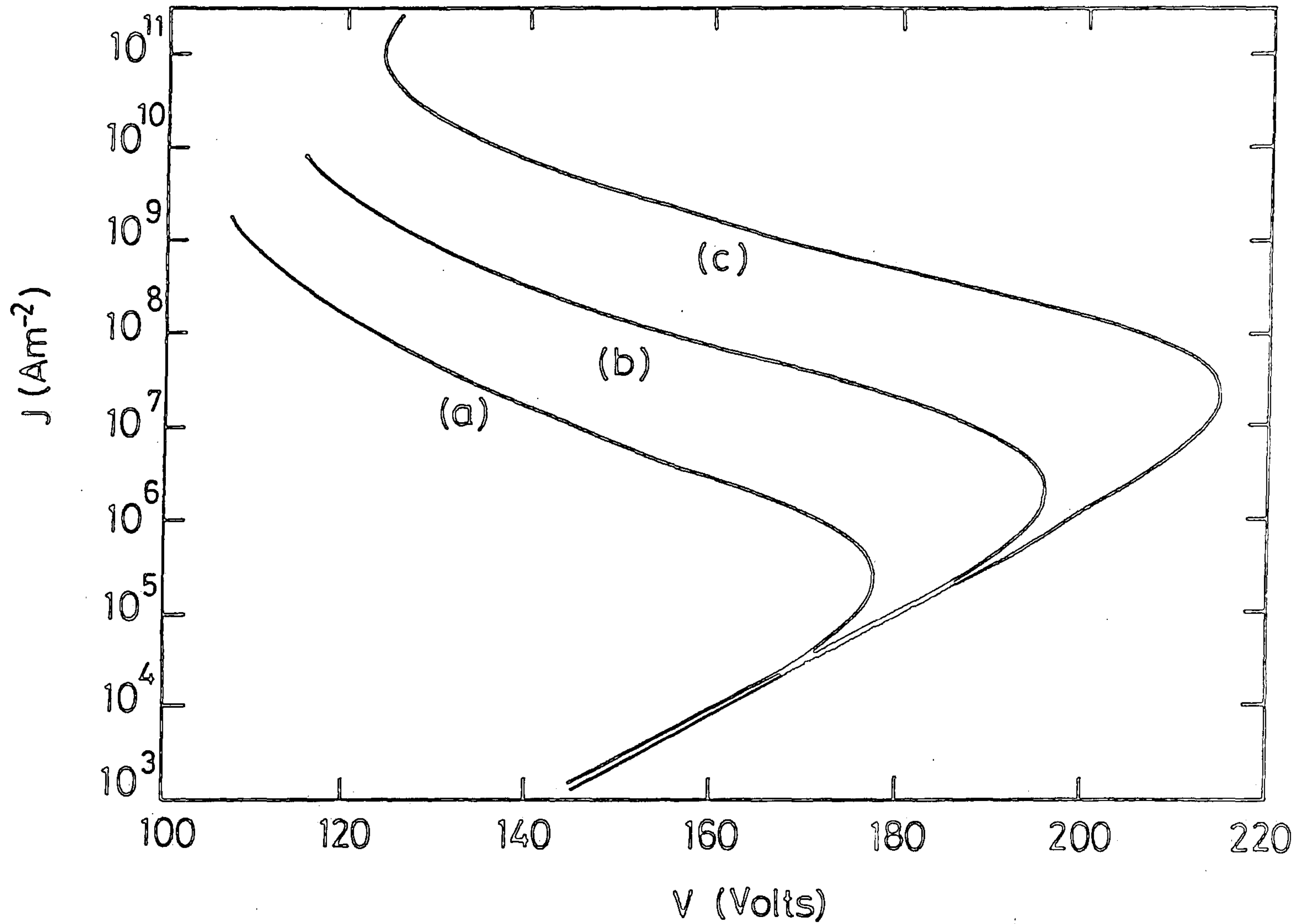

Fig. 7.12 : Current density-voltage characteristics when the normal bulk mobilities are reduced by a factor of a) 10^{-2}; b) 10^{-1} and c) no change.

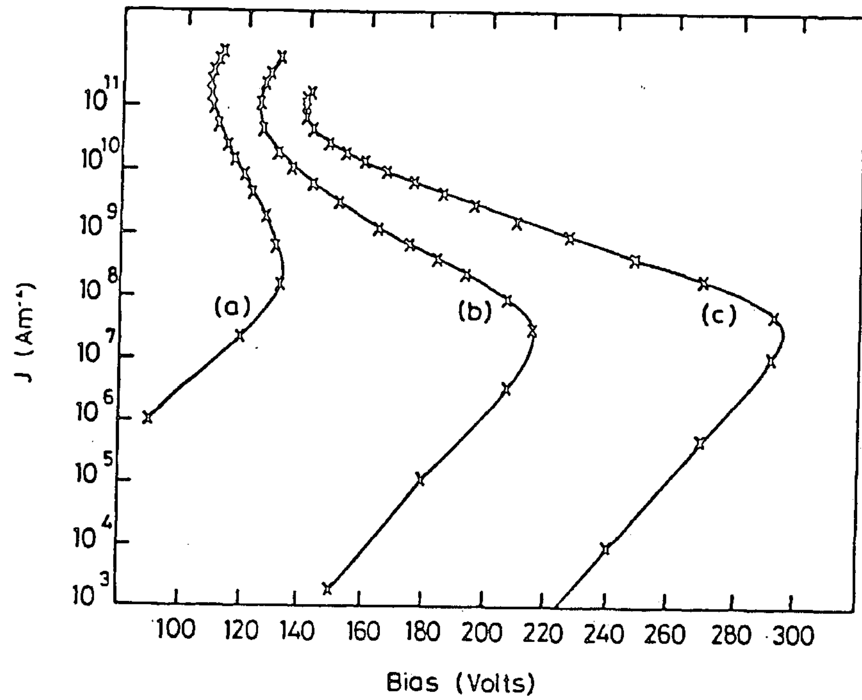

Fig. 7.13 : Current density-voltage characteristics for various barrier heights: a) 0.25eV; b) 0.5eV and c) 0.75eV.

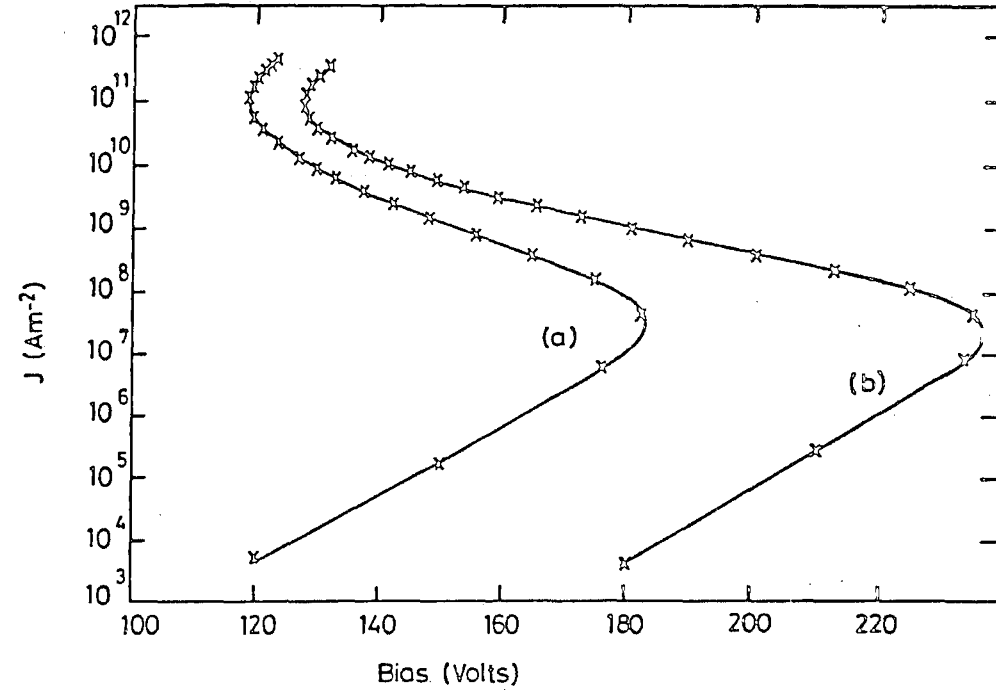

Fig. 7.14 : Current density-voltage characteristics for different effective masses: a) $0.25m_e$ and b) $0.75m_e$.

increase in total hole production and hence a more pronounced differential negative resistance region. This effect is illustrated in Figure 7.15. The thinner samples also require lower biases to achieve a particular current because less potential difference is required to produce a particular field across the ZnS. This tendency towards more band bending is further emphasised if voltage is plotted against thickness for constant current. In Figure 7.16 it can be seen that as W increases the rise in voltage at the higher currents is not as great as for the lower ones due to the increasing differential negative resistance region.

7.3.7 Inclusion of an N_D+ Region at the Cathode

In a real device it would be beneficial if the high field could be restricted to the cathode region where it would enhance the injection current. At the same time it would be desirable to have a low field over the rest of the sample to reduce the probability of breakdown. In this context it would seem that a layer of positive doping charge at the cathode would act to rapidly reduce the field to lower values and hence satisfy the above criteria. In considering the behaviour we have found that the type of solution depends strongly on the doping concentration N_D+. If N_D+ is too small then it has no effect but if it becomes too large the field will actually change sign. Figure 7.17 refers to a value of $N_D+ = 5 \times 10^{22}$ m^{-3} where a solution is possible. As in many previous instances the most marked effect is at the lower fields. In this regime the injected electron current and created hole current are not large enough to dominate the influence of the doped layer. The layer does bring on the differential negative resistance at lower fields, but this is also accompanied by a larger current.

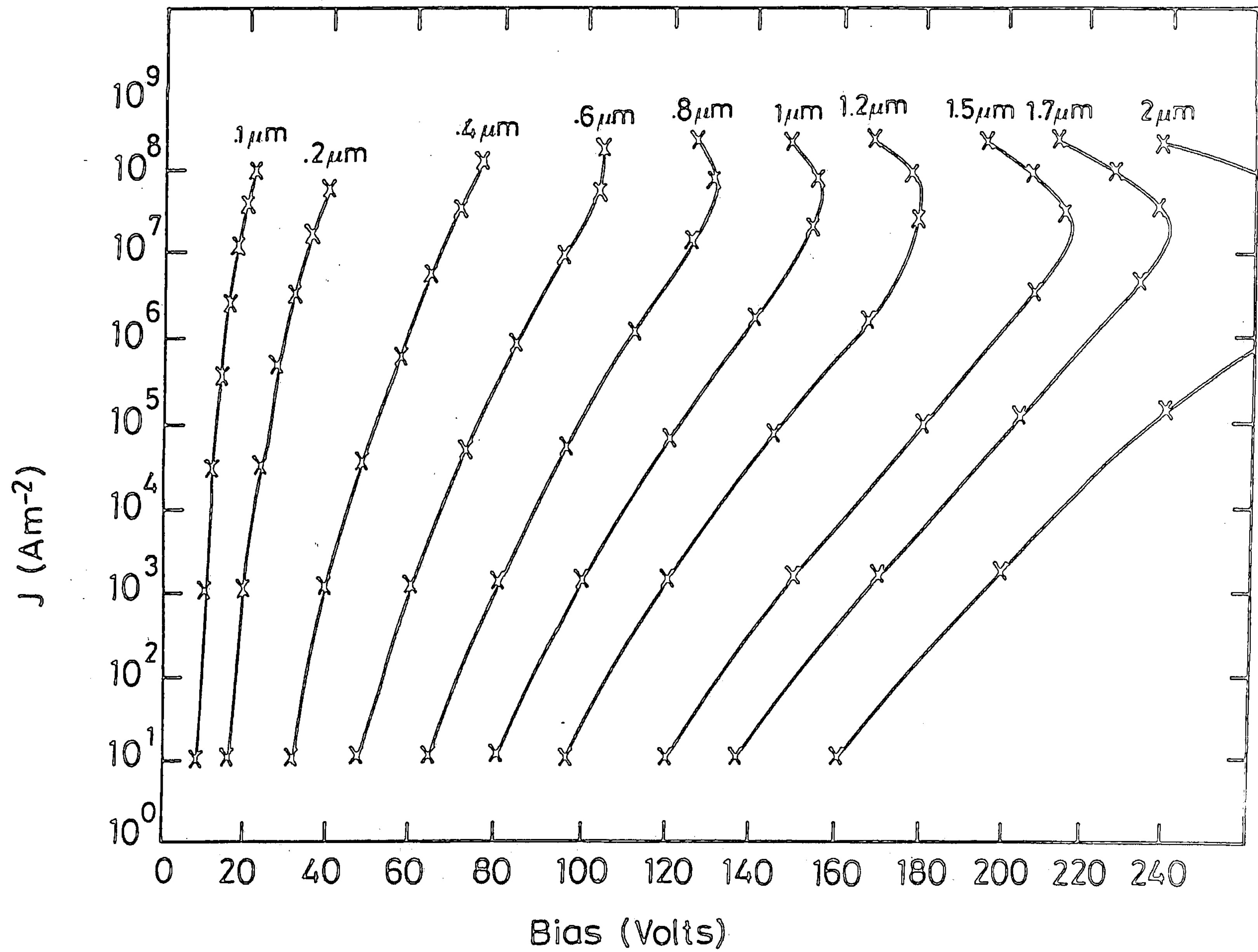

Fig. 7.15 : Current density-voltage characteristics for insulator samples of different widths.

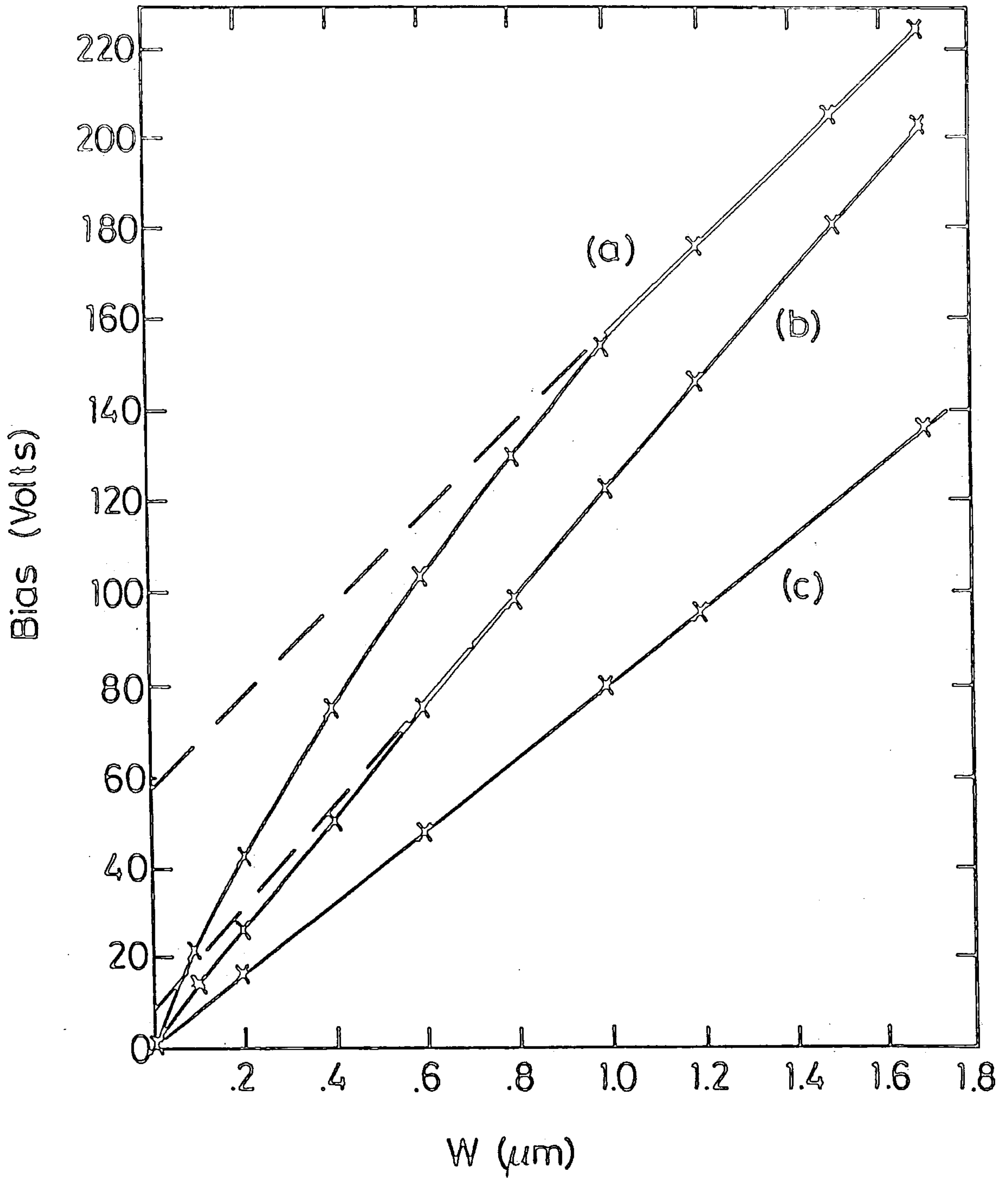

Fig. 7.16 : Variation of voltage with respect to insulator thickness for constant currents of a) $10^{8} Am^{-2}$; b) $10^{5} Am^{-2}$ and c) $10\ Am^{-2}$.

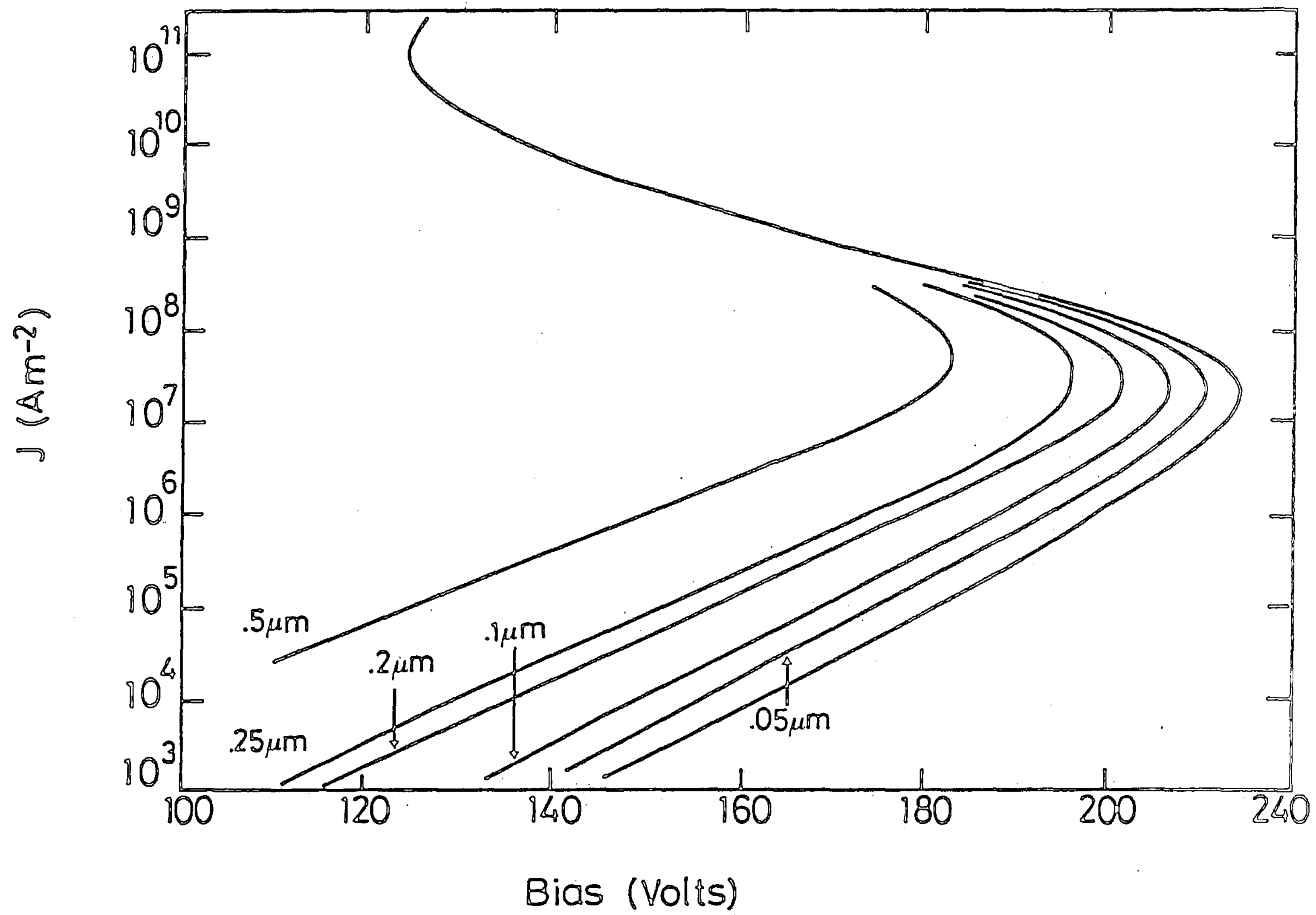

Fig. 7.17 : Current density-voltage characteristics for different thicknesses of a N_D+ doping layer (of concentration $5 \times 10^{22} m^{-3}$) adjacent to the cathode.

Figure 7.18 shows the behaviour of the device for a doped region of constant thickness (0.1μm) with varying donor concentrations. The larger concentrations have a similar effect to the wider doping layers in Figure 7.17 leading to more band bending and hence the earlier onset of the differential negative resistance region with electric field.

7.4 SUMMARY

The main conclusion from the steady state results for the MIM device is that there is a range of driving voltages over which there are three possible current density states. We have investigated the effect of various parameters on the current-voltages characteristics and identified the factors affecting the multi-current state voltage range. So far we have not considered what state the system is most likely to adopt and whether or not all the states are accessible. To achieve some understanding of these problems the next chapter is concerned with modelling the time dependent behaviour of the device as the applied voltage is increased to see how it approaches the steady state condition.

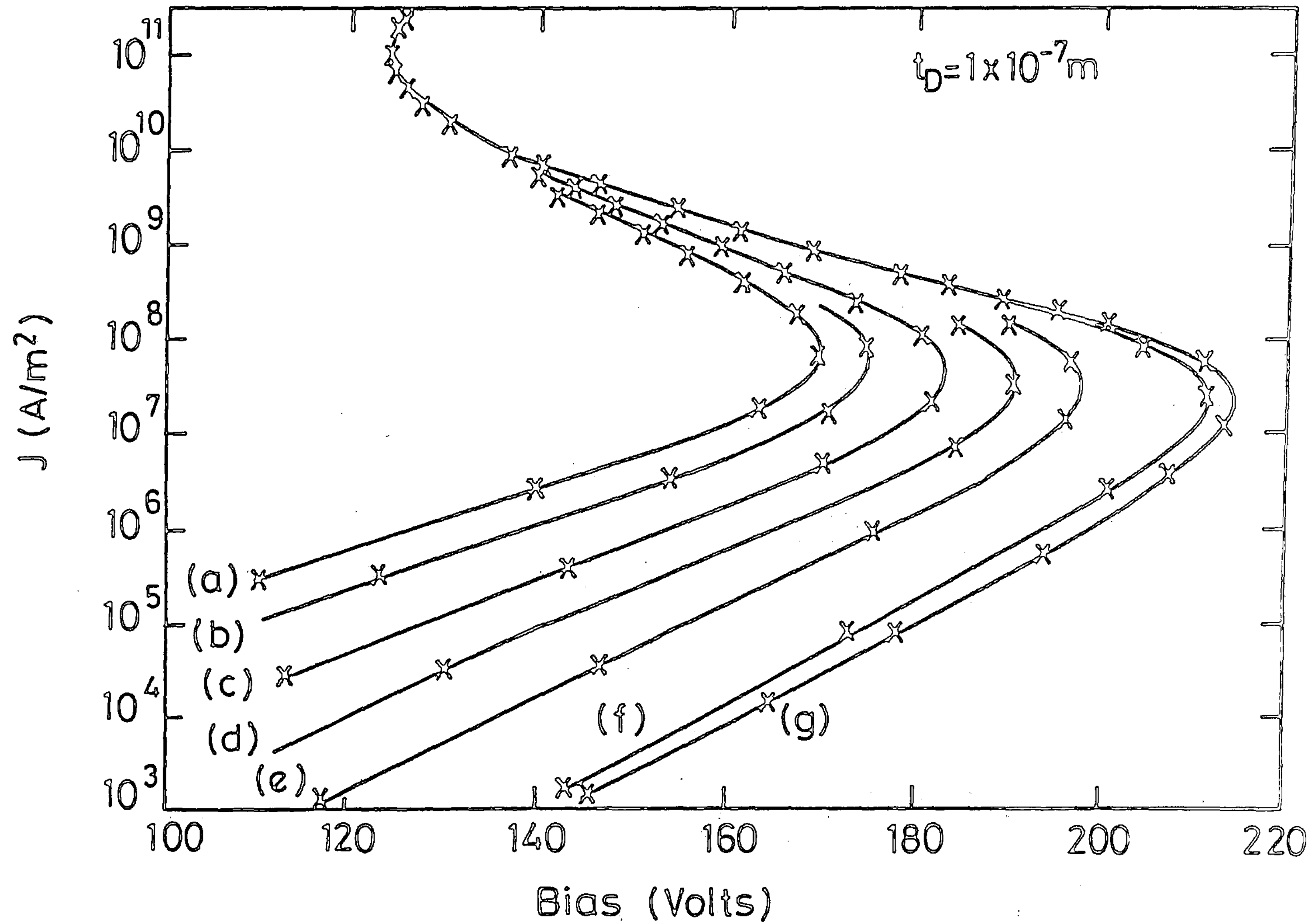

Fig. 7.18 : Current density-voltage characteristics for a N_D+ doping layers of thickness 0.1μm adjacent to the cathode for doping concentrations of a) 3×10^{23}m^{-3}; b) 2.6×10^{23}; c) 2×10^{23}; d) 1.5×10^{23}; e) 1×10^{23} ; f) 2×10^{23} and g) 0 .

CHAPTER EIGHT

TIME DEPENDENT CHARACTERISTICS OF AN MIM ELECTROLUMINESCENT PANEL

8.1 INTRODUCTION

Chapter Seven showed that we can expect S-shaped current-voltage characteristics for the devices produced by Cattell and Kirton[1], described in detail in the previous chapter. It was explained that with the current controlled, negative differential resistance it was possible to have more than one current state for a particular voltage. The aim of this chapter is to model the time dependent behaviour of the MIM electroluminescent panel after a bias is applied. This enables a study of the behaviour of the device as it approached a steady state and, when more than one current state is possible, to see which current state it tends to.

8.2 TIME DEPENDENT MODEL

8.2.1 The External Circuit

To consider the variation of voltage across the device it is important to know the external circuit and the constraints and conditions it imposes on the system. Cattell and Kirton[1] suggest that in their experiment there is a load resistance and a capacitive element to the voltage source. The bias at a time t after switching on is given by

$$V_T = V_o(1 - e^{-t/t_o}) \qquad (8.1)$$

with the time constant, being typically of the order of 0.1μs. The circuit is illustrated in Figure 8.1. Kirchoffs Law can be used to find an expression relating the total and device voltages to the current:

$$V_T = V_o(1 - e^{-t/t_o}) = RJ(t)A + V_D \qquad (8.2)$$

where R is the load resistance, J(t) is the total current at time t, A is device cross section area and V_D is the portion of the total voltage across the device.

8.2.2 Defining Equations

We can further modify equation (8,2) if the device's displacement current is explicitly included by writing

$$J(t) = J_n(x,t) + J_p(x,t) + \varepsilon\varepsilon_o \frac{\partial F(x,t)}{\partial t} \qquad (8.3)$$

and substituting for J(t) in equation (8.2) to give

$$\frac{\partial F(x,t)}{\partial t} = \frac{1}{\varepsilon\varepsilon_o}\left[\frac{1}{RA}(V_o(1 - e^{-t/t_0}) - V_D) - J_n(x,t) - J_p(x,t)\right] \qquad (8.4)$$

This is the first of the defining equations for the system. The second

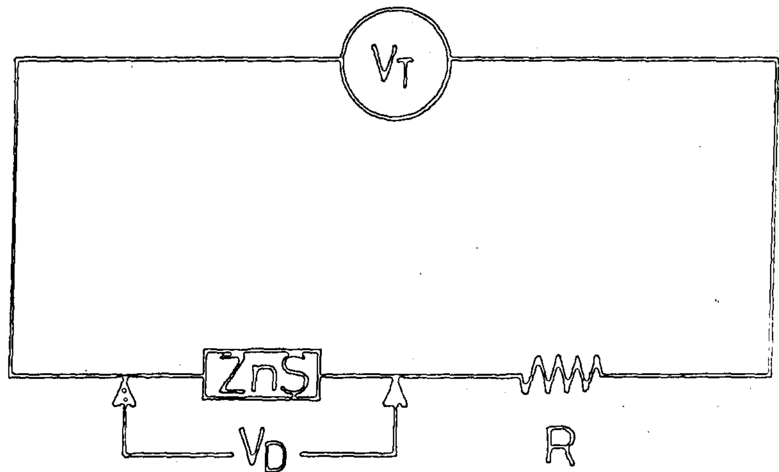

Fig. 8.1 : The circuit incorporating the ZnS electroluminescent panel.

is the spatial field variation given by Poissons equation

$$\frac{\partial F(x,t)}{\partial x} = \frac{|e|}{\varepsilon\varepsilon_0}(p(x,t) - n(x,t)) \tag{8.5}$$

Due to the inclusion of the displacement current, the carrier concentrations need to be considered separately. The two equations are

$$\frac{\partial J_n(x,t)}{\partial x} = |e| \frac{\partial n(x,t)}{\partial t} + \alpha(F(x,t)) J_n(x,t) \tag{8.6}$$

and

$$\frac{\partial J_p(x,t)}{\partial x} = -|e| \frac{\partial p(x,t)}{\partial t} - \alpha(F(x,t)) J_n(x,t)) \tag{8.7}$$

Equations (8.6) corresponds to equation (7.3) in the steady state case discussed in the previous chapter. The additional time derivative term is simply due to the equation of continuity

$$\text{div } J = -\frac{\partial \rho}{\partial t} \tag{8.8}$$

where ρ is the total charge. Four differential equations (ie equations (8.4) to (8.7)) have been produced which describe the system. In the next few sections, the method used to solve these equations is discussed.

8.3 METHOD OF COMPUTATION

As they stand it is not possible to solve the four defining equations ((8.4) to (8.7)) either analytically or numerically using standard integration routines. The inability to solve the equations numerically stems from the fact that they cannot be split into their separate spatial and temporal parts to define the problem in terms of ordinary differential equations. With this being the case, the method of solution adopted followed the lines of finite difference analysis.

8.3.1 Method 1 - Current Continuity Implied in System of Equations

The aim of this method is to increment time and at each step to solve over the length of the ZnS in a manner similar to that used in the last chapter for the time dependent case.

We assume that at some time t the field and carrier concentrations are known at all positions. The device is then considered at a time $t+\Delta t$ with the approximation

$$\frac{\partial F(x,t')}{\partial t} \approx \frac{F(x,t+\Delta t) - F(x,t)}{\Delta t} \qquad (8.9)$$

$$t < t' < t+\Delta t$$

t' can be any time over the range of the temporal step. Using this approximation in equation (8.4)

$$F(x,t+\Delta t) \approx \frac{\Delta t}{\varepsilon\varepsilon_o}\left[\frac{1}{RA}(V_o(1-e^{-t/t_o})-V_D)-J_n(x,t)-J_p(x,t)\right]+F(x,t)$$

(8.10)

This equation can be used to define the new field at the cathode and then the expression given by Lampert and Mark[2] employed to find the injection current at the cathode due to thermionic field emission.

$$J_n(O.t+\Delta t) = \frac{(|e|F(O,t+\Delta t))^2}{(4\pi)^2 h\phi}\left[\frac{1+4\pi^2 m^*\phi(kT)^2}{3h^2|e|F(O,t+\Delta t)^2}\right] \times \exp\left[\frac{4(2m|e|\phi)^{\frac{1}{2}}\phi}{3hF(O,t+\Delta t)}\right] \quad (8.11)$$

This expression corresponds to equation (7.4) in the last chapter.

By employing a small spatial step Δx to find an approximation to $\partial J_p(x,t)/\partial x$, (in a manner similar to the use of Δt in equation (8.9)) equation (8.7) can be utilised to find an approximation to the hole concentration at the cathode at time $t+\Delta t$. This is done by setting

$$\frac{\partial J_p}{\partial x}(x',t) \approx \frac{J_p(x+\Delta x,t) - J_p(x,t)}{\Delta x} \quad (8.12)$$

$$x < x' < x+\Delta x$$

and

$$\frac{\partial p(x,t')}{\partial t} \approx \frac{p(x,t+\Delta t) - p(x,t)}{\Delta t} \qquad (8.13)$$

$$t < t' < t+\Delta t$$

Substituting these two expressions into equation (8.7) and rearranging to give an approximate expression for the cathode hole concentration as

$$p(0,t+\Delta t) \approx p(0,t) + \frac{\Delta t}{|e|}\left[\frac{J_p(0,t) - J_p(\Delta x,t)}{\Delta x} - \alpha(F(0,t))J_n(0,t)\right] \qquad (8.14)$$

We now have boundary conditions for the field and carrier concentrations at the cathode. Rewriting equations (8.6) and (8.7) as

$$\frac{\partial J_n}{\partial x}(x,t+\Delta t) \approx |e|\left(\frac{n(x,t+\Delta t)-n(x,t)}{\Delta t}\right) + \alpha(F(x,t+\Delta t))J_n(x,t+\Delta t) \qquad (8.15)$$

and

$$\frac{\partial J_p}{\partial x}(x,t+\Delta t) \approx -|e|\left(\frac{p(x,t+\Delta t)-p(x,t)}{\Delta t}\right) - \alpha(F(x,t+\Delta t))J_n(x,t+\Delta t) \qquad (8.16)$$

they can be used along with equation(8.5) to find the solution over the length of the ZnS for the new time using a Runge-Kutta routine in what is now a quasi time independent problem. Using a shooting method $J_p(0,t+\Delta t)$ is adjusted, in computation, from its original estimate in equation (8.11) to ensure the condition of no hole injection at the anode. Ideally equation (8.11) should give the correct cathode hole

concentration, but in the finite difference technique there are inevitably small numerical discrepancies. To correct for this, it is assumed that equation (8.13), the corresponding one for the electron concentration, and equation (8.9) are accurate and that it is equation (8.12) that is responsible for the inconsistencies. By chosing equation (8.12) as the least reliable expression it is not necessary to obtain fine accuracy over the spatial step because equation (8.12) is only used to obtain an estimate for the cathode hole concentration in equation (8.11) and it is this estimate that is modified in the computation, However a sufficicently small temporal step Δt is required to ensure that equations (8.10), (8.15) and (8.16), which are not modified in the computation, are accurate.

The carrier concentration profiles can be adequately represented by arrays of ten points across the sample and an interpolation routine used to provide the values needed in the spatial calculations.

8.3.2 Method 2 - Current Continuity Explicit in System of Equations

The current for a system developing in time is given by:

$$J(t) = J_n(x,t) + J_p(x,t) + \varepsilon\varepsilon_0 \frac{\partial F}{\partial t}(x,t) \qquad (8.17)$$

where the last term is the displacement current and the omission of any x dependence in the total current J indicates the current continuity across the sample.

Equation (8.17) provides another way of obtaining the hole concentrations as an alternative to using equation (8.16) in Method 1. By substituting equation (8.9) into equations (8.17) and rearranging the hole current density it can be written as:

$$J_p(x,t+\Delta t) = J(t+\Delta t) - J_n(x,t+\Delta t) - \varepsilon\varepsilon_0 \left(\frac{F(x,t+\Delta t) - F(x,t)}{\Delta t} \right) \tag{8.18}$$

where the total current J is computed at the cathode using the known values for field and electron injection current and the values for the hole concentration either estimated from equation (8.14) or modified in the computation to ensure zero hole injection at the anode.

The spatial problem has now been reduced to a system of two differential equations, namely equations (8.5) and (8.15), with equations (8.18) supplying the hole concentrations needed for Poisson's equation (equation (8.5)). The change in the contact field is calculated in an identical manner to Method 1.

8.3.3 The Choice Between Methods

The relative accuracy of the two techniques depends very much on the stage of the time development. If t is small and most of the current is displacement current then Method 1 is the more accurate with the particle currents and concentrations in equations (8.15) and (8.16) being small and therefore any error due to the approximations for $\partial n(x,t)/\partial t$ and $\partial p(x,t)/\partial t$ also being small.

However at larger values of t the particle currents dominate and it is the displacement current that becomes negligible and then Method 2 is the more accurate.

8.3.4 Starting Conditions

At the time t = 0 the change in field with respect to time is also zero, so equation (8.10) cannot be used as defined to find the field after the time step Δt. In this case it is assumed that the actual particle current is negligible and an analytical result , with the particle currents set to zero, is used to calculate the new field. This calculation is carried out in Section 8.4 but the result is quoted here for $t = \Delta t$.

$$F(\Delta t) = \frac{V_o\left(\frac{1}{W_D} + \frac{e^{-\Delta t/t_o}}{\varepsilon\varepsilon_o R A} - \frac{e^{-W_D \Delta t/\varepsilon\varepsilon_o R A}}{t_o W_D}\right)}{\frac{1}{t_o} - \frac{W_D}{\varepsilon\varepsilon_o R A}} \tag{8.19}$$

8.3.5 Electroluminescent Centres

As described in Section 7.2.5 , we can expect the excitation rate of Mn^{2+} centres to be $Mn^g(x,t)\ \mu_e|F(x,t)|n(x,t)$ and the decay rate to be given by $Mn^{ex}(x,t)/\tau_o$. Now that we are not in the steady state, these two values will not necessarily be equal and in general there will be a change in the number of excited centres given by

$$\frac{\partial Mn^{ex}(x,t)}{\partial t} = (Mn - Mn^{ex}(x,t)\sigma\mu_e|F(x,t)|n(x,t)) - \frac{Mn^{ex}}{\tau_o} \tag{8.20}$$

If, for the purpose of the finite difference analysis, we make the approximation

$$\frac{\partial Mn^{ex}(x,t')}{\partial t} \approx \frac{1}{2}\left[\frac{\partial Mn^{ex}(x,t)}{\partial t} + \frac{\partial Mn^{ex}(x,t+\Delta t)}{\partial t}\right] \tag{8.21}$$

$$t < t' < t+\Delta t$$

which gives the average value of $\partial Mn^{ex}(x,t)/\partial t$ at either end of the time step, and use this expression in equation (8.20) the density of excited states at time $t+\Delta t$ can be written as

$$Mn^{ex}(x,t+\Delta t) = \frac{1}{\left(1 + \frac{\Delta t}{2t_o} + \frac{\Delta t\sigma\mu_e}{2}|F(x,t+\Delta t)|n(x,t+\Delta t)\right)}$$

$$\times\left[M^{ex}(x,t) + \frac{\Delta t}{2}\left((Mn - Mn^{ex}(x,t))\sigma\mu_e|F(x,t)|n(x,t)\right.\right.$$

$$\left.\left. + Mn\sigma\mu_e|F(x,t+\Delta t)|n(x,t+\Delta t) - \frac{Mn^{ex}(x,t)}{\tau_o}\right)\right] \tag{8.22}$$

Hence, knowing the density of excited states at time t and solving for

field and electron contraction at time $t+\Delta t$, $Mn^{ex}(x,t+\Delta t)$ can be calculated using equation (8.22). By finding values as functions of position across the length of the ZnS the total number of excited centres can be found numerically using an integration routine and the total rate of decay will simply be that number divided by the decay time constant τ_o.

8.4 ANALYTICAL TREATMENT FOR NO CURRENT INJECTION

As mentioned in Section 8.3.3, it should be possible to assume, at small t, that the electron and hole currents are negligibly small due to the small initial voltage and the large displacement current. It seems reasonable that it should be possible to derive an expression which is valid over part of the time range and can be compared to results obtained using the finite difference technique.

If there is zero particle current, there will be a constant field across the device and so the voltage drop will be given by $F(t)W_D$. Setting $J_p(x,t) = 0$ and $J_n(x,t) = 0$, equation (8.4) gives:

$$\frac{dF(t)}{dt} = \frac{1}{\varepsilon\varepsilon_o}\left(\frac{1}{RA}\left(V_o(1 - e^{-t/t_o}) - F(t)W_D\right)\right) \qquad (8.23)$$

and by differentiating with respect to time we obtain

$$\frac{d^2F(t)}{dt^2} = \frac{1}{\varepsilon\varepsilon_o RA}\left(\frac{V_o}{t_o}\, e^{-t/t_o} - W_D\frac{dF(t)}{dt}\right) \qquad (8.24)$$

This has a solution of the type

$$F(t) = B + Ce^{-W_D t/\varepsilon\varepsilon_o RA} + De^{-t/t_o} \qquad (8.25)$$

with

$$B = \frac{V_o}{W_D}$$

$$C = \frac{V_o}{t_o W_D} \Bigg/ \left(\frac{1}{t_o} - \frac{W_D}{\varepsilon\varepsilon_o RA}\right)$$

and

$$D = \frac{V_o}{\varepsilon\varepsilon_o RA} \Bigg/ \left(\frac{1}{t_o} - \frac{W_D}{\varepsilon\varepsilon_o RA}\right)$$

This expression for the field is expected to be accurate at low fields, when the ZnS is still acting as a conventional insulator. It will fall short of the true value at higherfields when carrier injection occurs. This approximation is compared with the numerical calculations in Section 8.5.

8.5 DEVELOPMENT OF SYSTEM WITH TIME

We now present some of the important characteristics produced using this model. In calculating these results, Method 1 was used for lower values of the time t, when the displacement current dominated, while Method 2 was used for the higher values.

Figure 8.2 shows the type of results obtained using a total external voltage of 200V with an external load resistance of 1kΩ and a device of cross-sectional area $1mm^2$. There is the expected sharp rise in voltage across the device in the early stages with a flattening out as the steady state is approached. The current shows a pronounced peak at a small time due to the displacement current caused by the

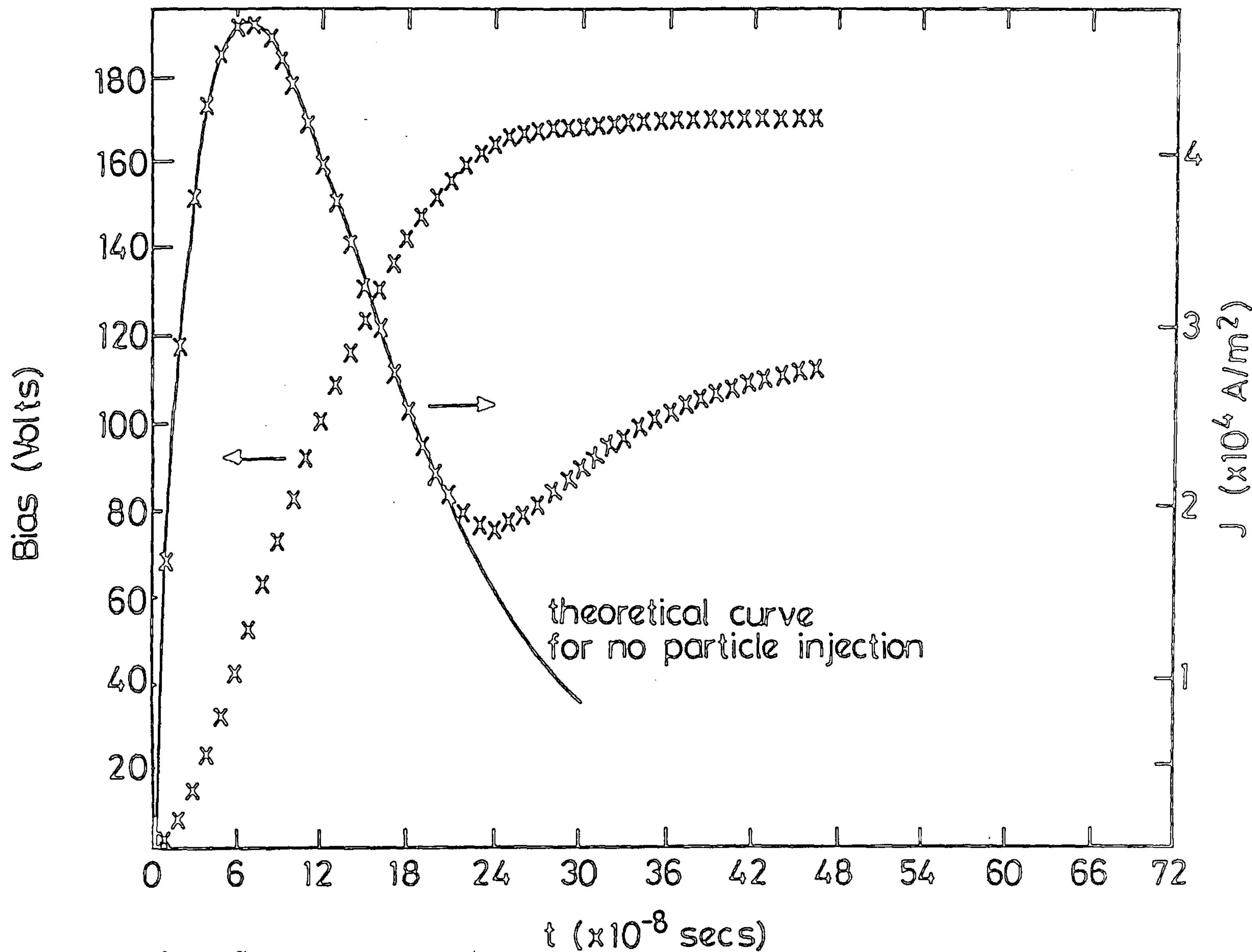

Fig. 8.2 : The development of the device voltage and current density over time for values of R = 1000Ω and V_0 = 200 V.

changing voltage and field. This displacement current falls off as the voltage steadies, but there is another rise due to the particle current which also saturates at its steady state value. It should be pointed out that these saturation values of voltage and current correspond to a point on the lower branch of the steady state current-voltage characteristic calculated in the previous chapter and shown in Figure 7.2.

The analytical results given by equation (8.25) can be substituted into equation (8.23) and multiplied by $\varepsilon\varepsilon_0$ to give the displacement current at time t assuming zero carrier injection. This curve is also shown in Figure 8.2 for the same parameters. It shows close agreement at the lower values of t, where we would expect it to be accurate, and gives added confidence in the numerical methods adopted.

Figure 8.3 is for the same parameters as used in Figure 8.2 and shows the development of the hole concentration across the sample with time. With the hole concentration profiles shown at various time intervals it can be seen how the concentration rises across the whole sample with time, as more charge is injected from the cathode, finally tending to the steady state profile.

For a higher voltage of 300V and a reduced load resistance of 600Ω it was expected that a larger bias would be dropped across the device itself and a higher current would result. This is demonstrated in Figure 8.4. The curve shows the same general characteristics as Figure 8.2, but in this case the particle current is saturating at a value greater than the maximum displacement current.

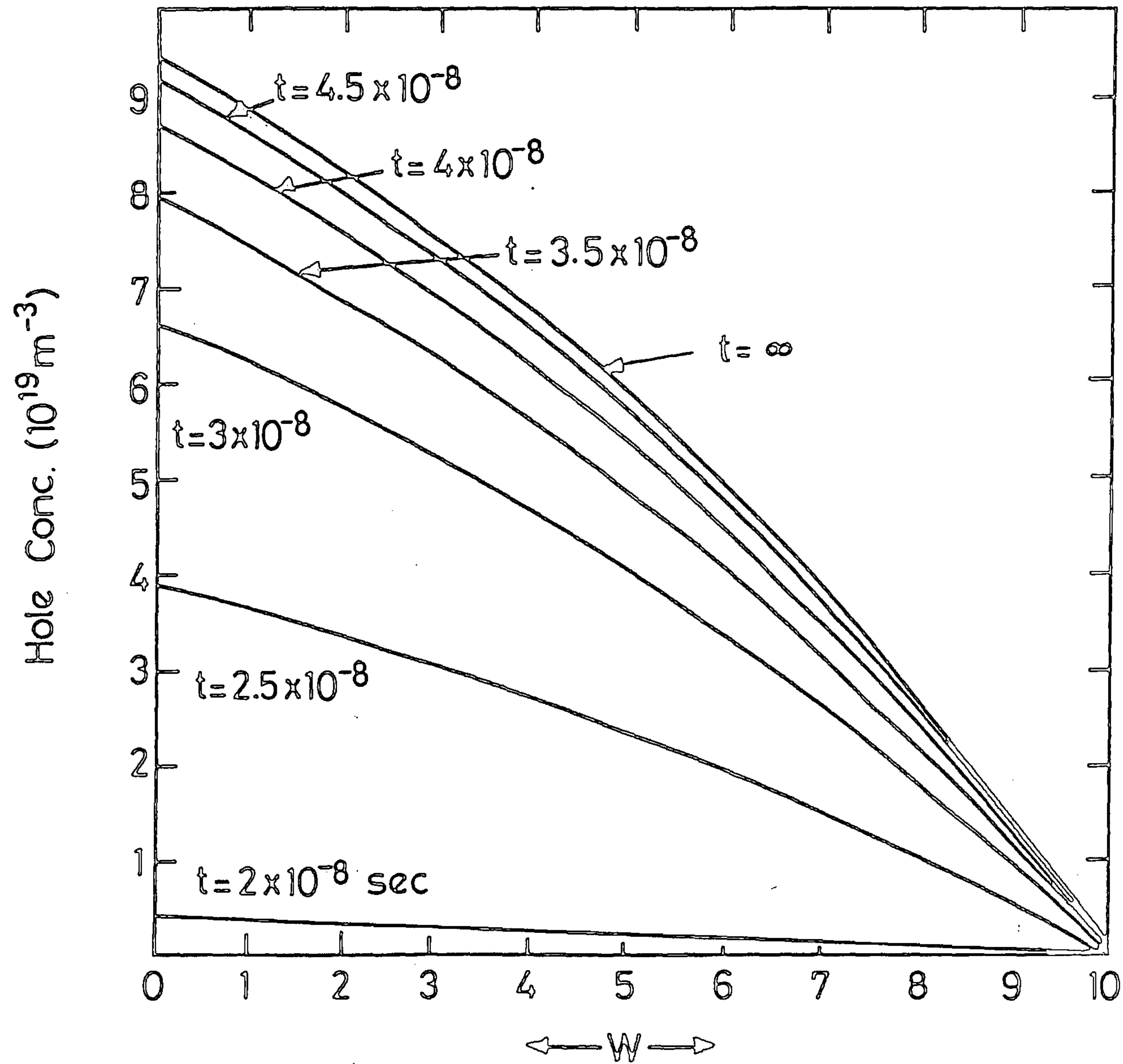

Fig. 8.3 : The development over time of the hole concentration profile in the ZnS device for the same parameters as Fig. 8.2.

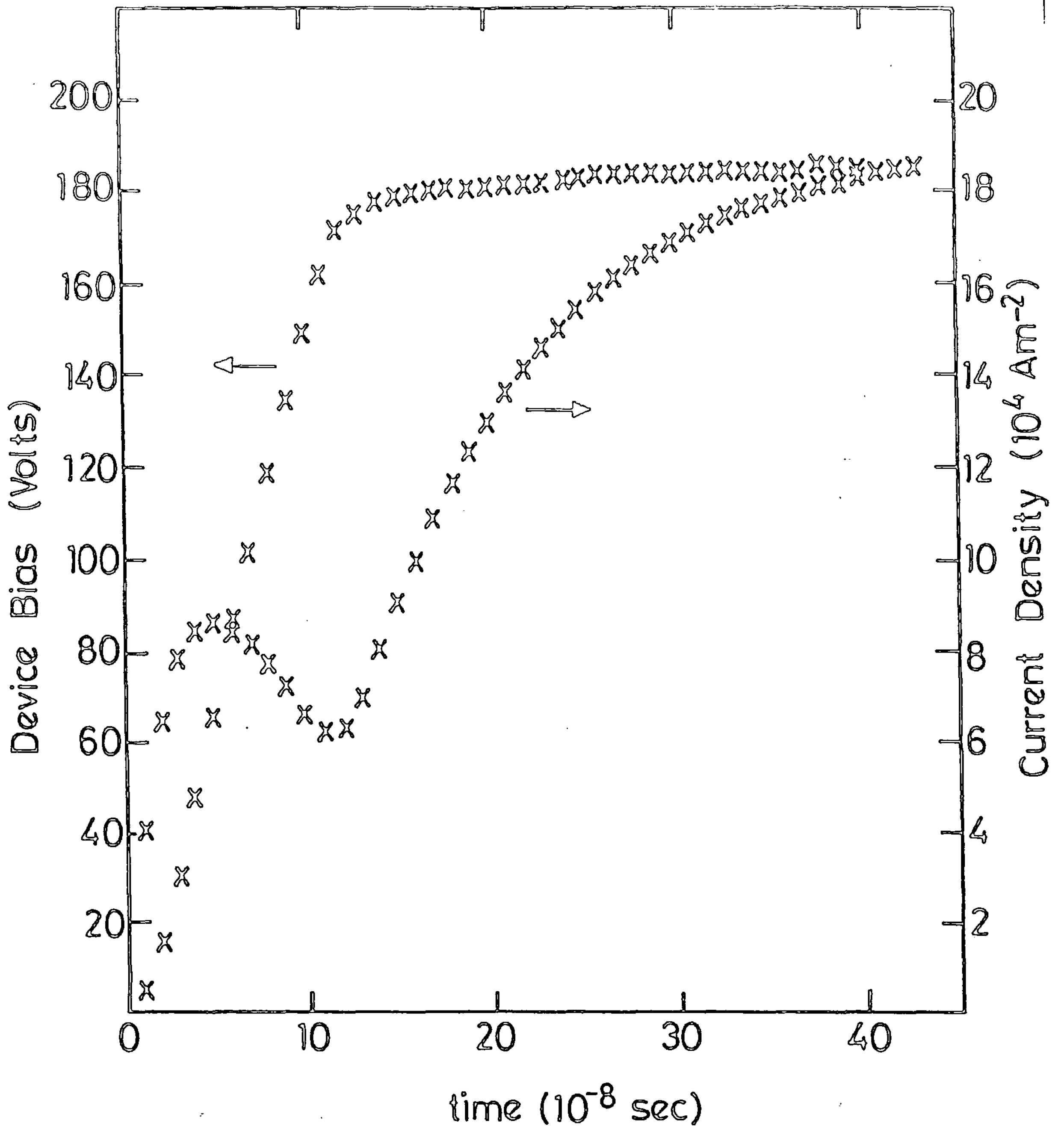

Fig. 8.4 : The development of the device voltage and current density over time for values of $R = 600\Omega$ and $V_o = 300V$.

By choosing the suitable voltage and load resistance it is possible to produce similar curves corresponding to a steady state on any point of the lower forward resistance branch characteristic. By showing the time dependent problem in this way the steady state to which the device tends is always found to be on the lower branch of the characteristic and there is no tendency to go to the higher, potentially destructive, region of the characteristic.

Attempts were made to model a situation in which the applied bias and load resistance were such that the only steady state solution would be the higher forward resistance region of the steady state J-V characteristic (Figure 7.2). This required a very low load resistance to enable the load line to reach the higher values of J.

Unfortunately, under these circumstances, the modelling program was unable to proceed satisfactorily, with solutions being unstable, convergence slow and finally overflow problems.

8.6 SUMMARY AND DISCUSSION

In these calculations we have shown that given a steadily rising external voltage and a current uniform across the device cross-section, there seems no reason why the current should reach a point on the higher forward bias region of the current-voltage characteristic. In the actual model we have not constrained the current in any way except that it is required to be uniform across the cross-section of the device.

We must conclude from these results that any jumping to a higher current state must be due to some local variation in field or in inhomogeneity in the current. A suggestion for further work is to investigate the behaviour of the device, when either powering up or in the steady state, if some sharp and indiscriminate variation is modelled into the voltage supply, and to test the stability of any solution under such conditions.

In his treatment of current controlled negative resistance, Ridley[3] argues, using the principle of least entropy production, that a high current filament, once formed, will be limited in size, and will not spread across the whole cross-section of the device. The filament itself, he suggests, is produced by some local fluctuation in field at, for example, some inhomogeneity in the device. This limit to the cross-section of the filament was borne out by the early work of Barnett and Milnes[4] using semi-insulating silicon and, more importantly for this work, has been observed by Cattell[1] in the breakdown of the RSRE ZnS device. It is suggested then that in the time dependent model developed in this chapter, the creation of the high current state is inhibited by the assumption of constant current density over the cross-section. Therefore to study realistic device behaviour it would appear necessary to treat the device in a 2-dimensional model.

CHAPTER NINE

SUMMARY AND CONCLUSIONS

The work reported in this thesis is an attempt to identify important electronic processes in two kinds of electroluminescent device. The two structures investigated are the MIS diode, incorporating a thick insulator and the high field MIM electroluminescent panel. In each case the experimental characteristics of the devices had not been satisfactorily explained and there was a clear need for further theoretical work.

9.1 THE "THICK" MIS DIODE

Two forms of this device were considered. These were the "II-VI" diodes, which incorporate semi-insulating II-VI materials as the insulator and "Langmuir-Blodgett film" devices using Langmuir-Blodgett film technology to create insulating layers of well regulated thickness. The operation of such devices depends on the injection of minority carriers (holes) into the semiconductor valence band where they can recombine radiatively. Calulations were performed to investigate the possibility of majority carriers, injected into the metal, creating a significant hole population well below the metal Fermi level in an impact ionisation type of process. Results showed that this was a viable process with approximately 15% of the injected electrons producing holes capable of reaching the metal-insulator interface. Due to energy conservation holes cannot be created in electron states at energies less

than $E_{fm}-|e|\phi_b$, where E_{fm} is the metal Fermi energy and ϕ_b is the electron barrier height. However above this energy the distribution of created holes with energy is approximately linear. Therefore the impact ionisation process was seen to be capable of producing a significant hole flux at the interface, compared to minority carriers created thermally, at energies well below the metal Fermi level (ie $> E_{fm}-2eV$).

Considering the Au/cadmium stearate/n-GaP Langmuir-Blodgett film device first, it proved possible to model the J-V characteristics using a modified thermionic emission theory which took account of the potential dropped in the semiconductor bulk at high current densities. Using typical insulator-semiconductor interface state densities a good degree of agreement with experimental characteristics was achieved. This calculation is particularly valuable because it describes how the band structure of the device alters under forward bias.

The mechanism by which holes pass through the Langmuir-Blodgett film from the metal into the semiconductor remains unclear largely as a result of a lack of fundamental experimental research in this area. With this in mind transport mechanisms known to be important in electron conduction in Langmuir-Blodgett film MIM structures were considered as possible models for hole transport. Calculating the variation of the dc power conversion efficiency using these different possible transport mechanisms and comparing to experimentally obtained results it was concluded that holes most probably travelled across the insulator by hopping between interface states on the successive insulating layers.

In the Au/cadmium stearate/n-GaP device it was assumed that the limiting

process for hole injection was the transport through the insulator. However, in the II-VI devices and in particular the Au/i-ZnS/n-ZnS structure, the limiting process was assumed to be the hole creation mechanism in the metal. This was because the bandgap of the semi-insulator is similar in value to the n type semiconductor and it was expected that minority carrier transport would be in the semi-insulator valence band. For a constant current it was shown that there would be a threshold insulator thickness above which any hole entering the insulator valence band would be swept into the semiconductor by the insulator field. Below this threshold thickness the insulator field would oppose the injection. The quantum efficiency of the Au/i-ZnS/n-ZnS device was estimated by calculation the probability of holes being created (in the impact ionisation process) which were capable of entering the insulator valence band and then assuming that the holes were swept into the semiconductor. The results were seen to be close to the experimentally obtained values.

9.2 MIM ELECTROLUMINESCENT PANEL

In considering the high field dc electroluminescent panel, with i-ZnS as the insulator, it was demonstrated how hole creation in the ZnS valence band by impact ionisation coupled with a hole mobility two orders of magnitude less than the value for electrons, can lead to a build up of positive charge at the cathode. As a result there can be a region of current controlled negative differential resistance in the calculated J-V characteristics. This in turn means that, in a certain voltage range, there can be three possible current states, the highest of which might be as high as $10^{11}\,Am^{-2}$, which would lead to the device burning out.

In the absence of accurate data on the material and device parameters, the effect of these values on the J-V characteristic was investigated. The characteristics calculated over the various ranges of parameters all showed the same general trends.

As these devices are usually driven by a pulsed signal, their behaviour when a voltage was first applied, was also modelled. In all cases the current was found to approach smoothly the lowest steady state current state. However it was pointed out that the method of solution adopted for the system enforced the condition of constant current density over the device cross-section and precluded the possibility of local high current filament formation in the ZnS. Therefore it would be a sensible extension of this work to model the device in two, or three, dimensions and include local inhomogeneities to see if filament formation can be predicted.

APPENDIX ONE

STANDARD INTEGRALS

where

$$R = a + bx + cx^2$$

$$\int_0^{2\pi} \frac{dx}{(a + b\cos x)^{n+1}} = \frac{2}{(a^2 + b^2)^{n+1}} P_n\left(\frac{a}{\sqrt{(a^2 - b^2)}}\right) \qquad A1.1$$

$$\int \frac{dx}{R^{3/2}} = \frac{2(2cx + b)}{\sqrt{R}} \qquad A1.2$$

$$\int \frac{xdx}{R^{3/2}} = - \frac{2(2a + bx)}{\sqrt{R}} \qquad A1.3$$

$$\int \frac{dx}{R^{\frac{1}{2}}} = \frac{1}{\sqrt{c}} \ln(2\sqrt{cR} + 2cx + b) \qquad A1.4$$

REFERENCES

CHAPTER TWO

1. Sze, S.M., "Physics of Semiconductor Devices", 2nd edition. Wiley (1981).

2. Ray, B., "II-VI Compounds ". Pergamon Press (1969).

3. e.g. Deskriau, G., J. Chem. Phys., 33 620 (1936), and see also references 4, 5 and 6 below.

4. Howard, W.E.J., Luminesc 24/25 835 (1981).

5. Mach, R. and Muller, G.O., Phys. Stat. Sol.(a), 69 11 (1982).

6. Alder, C.J., Fray, A.F., Hilsum, C. and Lloyd, P., Displays, 1 191 (1980).

7. Cattell, A.F., Cockayne ., B., Dexter, K., Kirton, J. and Wright, R.J., IEEE Trans. Electron. Dev., ED-30 471 (1983).

8. Hanak, J.J., Jap. J. Appl. Phys. Suppl., 2 809 (1974).

9. Cattell, A.F. and Kirton, J. - private communication.

10. Mott, N.F., Proc. Cambridge. Phil. Soc., 34 568 (1938).

11. Schottky, W., Naturwiss , 26 843 (1938).

12. See e.g. Mead, C.A., Solid State Electron., 9 1023 (1966).

13. Bardeen, J., Phys. Rev., 71 717 (1947).

14. Cowley, A.M. and Sze, S.M., J. Appl. Phys. 36 3212 (1965).

15. Harper, F.G. and Bertram, W.J., IEEE Trans. Elec. Dev., 16 641 (1969).

16. Crowell, C.R. and Rideout, V.L., Solid State Electron., 12 89 (1969).

17. Wagner, C., Phys. Z., 32 641 (1931).

18. Schottky, W. and Spenke, E., Wiss. Veoff. Siemens-Werken, 18 225 (1939).

19. Bethe, H.A., MIT Rad. Lab. Rpt., 43-12 (1942).

20. Rhoderick, E.H., "Metal-Semiconductor Contacts", (1978) Oxford.

21. Henisch, H.K. "Semiconductor Contacts", (1984) Oxford.

CHAPTER TWO (continued)

22. Crowell, C.R. and Sze, S.M., Solid State Electron., 9 1035 (1966).

23. e.g. see Bleany, B.I. and Bleany, B., "Electricity and Mangetism", 3rd edition, Oxford (1978).

24. Fowler, R.H., Phys. Rev., 38 45 (1931).

25. Rhoderick, E.H., J. Phys. D., 5 1920 (1972).

26. Yu, A.Y.C., and Snow, E.H., J. Appl. Phys., 37 3008 (1968).

27. Scharfetter, D.L. Solid State Electron.,8 299 (1965).

28. Green, M.A. and Shewchum J., Solid State Electron., 16 1141 (1973).

29. Card, HC and Rhoderick,E.H., J. Phys. D. 4 1589 (1971).

30. e.g. see Cassells, J.M. "Basic Quantum Mechanics", 2nd edition, MacMillan (1982).

31. Cowley, A.M., J.Appl. Phys. 37 3024 (1966).

32. Chen, C.L. and Wise, K. D. , IEEE Trans. Electron. Devices, 29 1522 (1982).

33. Fonash, S.J., J. Appl. Phys. 54 1966 (1983).

34. Lawther, C., Jpn. J. Appl. Phys. 18 849 (1979).

35. Card, H.C. and Rhoderick, E.H. Solid State Electron., 16 365 (1973).

36. Stratton, R., J. Phys. Chem. Solids., 23 1177 (1962).

CHAPTER THREE

1. Card, H.C. and Rhoderick, E.H., Solid State Electron., 16 365 (1973).

2. Card, H.C. and Rhoderick, E.H., J. Phys. D. 4 1589 (1971).

3. Fischer, A.G. and Moss, H.I., J. Appl. Phys., 34 2112 (1963).

4. Jaklevic, R.C., Donald, D.K., Lambe, J. and Vassell, W.C., Appl. Phys. Letts., 2 7 (1963).

5. Card, H.C. and Smith B.L., J. Appl. Phys., 42 5863 (1971).

6. Chybicki, M., Acta. Phys. Pol. A48 575 (1975).

7. Walker, L.G. and Pratt. R.E.Jnr., J. Appl. Phys. 47 2129 (1976).

8. Nicollian, E.H., Schwartz, B., Coleman, D.J. Jnr., Ryder, R.M. and Brews, J.R., J. Vac. Sci. Tech., 13 1047 (1976).

9. Pankove, J.I., IEEE Trans. Electron. Devices, ED-22 721 (1975).

10. Lagersdedt, O., Manemar , B. and Gilslason, H., J. Appl. Phys., 49 2953 (1978).

11. Livingstone, A.W., Turvey,K. and Allen, J.W., Solid State Electron., 16 351 (1973).

12. Watanabe, H., Chikamura, T. and Wada, M., Jpn. J. Appl. Phys., 13 357 (1974).

13. Yamaguchi. M and Yamamoto, A., Jpn. J Appl. Phys., 16 77 (1977).

14. Lawther, C. and Woods, J., Phys. Stat. Sol.(a), 44 693 (1977).

15. Lukyanchikova, Pekar, G.S., Tkachenko, N.N., Hoang Mi Shin and Sheinkman, Phys. Stat. Sol.(a), 41 299 (1977).

16. Lawther, C. and Woods, J., Phys. Stat. Sol.(a), 50 491 (1978).

17. Fischer, A.G., Phys. Letts., 12 313 (1964).

18. Thomas, A.E., Woods, J. and Haupman, Z.V., J. Phys. D., 16 1123 (1984).

19. Labes, M.M., Love, P. and Nichols, L.F., Chemical Reviews, 79 1 (1971).

20. Blodgett, K.B. and Langmuir, I., Phys. Rev., 51 964 (1937).

21. Vincett, P.S. and Roberts, G.G., Thin Solid Films, 68 135 (1980).

22. Batey, J., PhD Thesis, Durham (1983).

23. Batey, J. Roberts, G.G. and Petty, M.C. Thin Solid Films, 99 283 (1983).

24. Batey, J., Petty, M.C. and Roberts, G.G., Proc. Infos. Conf. (Elseuier), Durham (1983).

25. Batey, J, Petty, M.C., Roberts, G.G. and Wight, D.R., Electronics Letts., 20 489 (1984).

26. Polymeropoulos, E.E., J. Appl. Phys., 48 2404 (1977).

27. Mann, B. and Kuhn, H., J. Appl. Phys., 42 4398 (1971).

CHAPTER FOUR

1. Watanabe, H., Chickemura, T. and Wada, M., Jpn. J. Appl. Phys., 13 357 (1974).
2. Lawther, C. and Woods, J., Phys. Stat. Sol. (a), 44 693 (1977).
3. Ritchie, R.H., Phys. Rev., 114 644 (1959).
4. Quinn, J.J., Phys. Rev., 126 1453 (1962).
5. Ritchie, R.H. and Ashley, J.C., J. Phys. Chem. Solids, 26 1689 (1965).
6. Batey, J., PhD Thesis, Durham (1983).
7. Eisberg, R.M., "Fundementals of Modern Physics" (1961) Wiley.
8. Kittel, C., "Introduction to Solid State Physics", (1971) Wiley.
9. Ashcroft, N.W. and Mermin, N.D., "Solid State Physics" (1976) Holt, Rinehart and Winston.
10. Crowell, C.R. and Sze, S.M., Physics of Thin Films, 4 325 (1967).
11. Wilson, A.H., "Theory of Metals", (1955) Cambridge University Press.
12. Mott, N.F., Proc. Cambridge Phil. Soc., 32 281 (1936).
13. Mott, N.F. and Jones, H., "The Theory of the Properties of Metals and Alloys", (1958) Dover.

CHAPTER FIVE

1. Batey, J., Petty, M.C. and Roberts, G.G., Proc. Infos. Conf. Durham (Elseuier), 141 (1983).
2. Batey, J., Roberts, G.G. and Petty, M.C., Thin Solid Films, 19 283 (1983).
3. Batey, J. PhD Thesis, Durham (1983).
4. Sze, S.M., "Physics of Semiconductor Devices", 2nd edition, Wiley (1981).
5. Card, H.C. and Rhoderick, E.H., Solid State Electron., 16 365 (1973).
6. Henisch, H.K., "Semiconductor Contacts", Oxford (1984).
7. Calandra, C. and Santoro, G., J. Phys. C., 9 L51 (1976).
8. Straub, D., Skibowski, M. and Himpsel, F.J., J. Vac. Sci. Tech. A. 3 1484 (1985).

CHAPTER SIX

1. Sugi, M., Fukui, T. and Iizima, S., ?Appl. Phys. Letts., 27 559 (1975).

2. Lundström, I., Löfgren, H. and Stenberg, M., Solid State Comm., 18 457 (1976).

3. Roberts, G.G., McGinnity, M., Barlow, W.A. and Vincett, P.S., Solid State Comm., 32 683 (1979).

4. Roberts, G.G., Pande, K.P. and Barlow, W.A., Electron. Letts., 13 581 (1977).

5. Roberts, G.G., Pande, K.P. and Barlow, W.A., Solid State Electron Devices, 2 169 (1978).

6. Batey, J. PhD Thesis, Durham (1983).

7. Batey, J., Petty, M.C. and Roberts, G.G., Proc. Infos. Conf. Durham (Elsevier), 141 (1983).

8. Card, H.C. and Rhoderick, E.H., Solid State Electron. 16 365 (1973).

9. see e.g. Cassells, J.M. "Basic Quantum Mechanics" 2nd edition MacMillan (1982).

10. O'Dwyer, J.J., "The Theory of Electrical Conduction and Breakdown in Dielectric Solids" Clarendon Press(1973).

11. Careem, M.A. and Hill, R.M., Thin Solid Films, 51 363 (1978).

12. Vincett, P.S. and Roberts, G.G., Thin Solid Films, 68 135 (1980).

13. Mann, B. and Kuhn, H., J. Appl. Phys., 42 4398 (1971).

14. Honig, E.P., Thin Solid Films, 33 231 (1976).

15. Jonscher, A.K. and Nathoo, M.H., Thin Solid Films, 12 515 (1972).

16. see Chapter Three, e.g. Livingstone, A.W., Turvey, K and Allen, J.W., Solid State Electron., 16 351 (1973).

17. Lawther, C. and Woods, J., Phys Stat. Sol.(a) 50 491 (1978).

18. Ray, B., "II-VI Compounds" (1969) Pergamon.

19. Lukyanchikova, N.B., Pekar, G.S., Tkachenko, N.N., Hoang Mi Shin and Sheinkman, M.K., Phys. Stat. Sol. (a), 41 299 (1977).

20. Katayama, H., Oda, S. and Kukimoto, H., Appl. Phys. Letts, 27 697 (1975).

CHAPTER SEVEN

1. Cattell, A.F. and Kirton, J., Private Communication.

2. Warren, A.J., Thomas, C.B., Reehal, H.S. and Stevens, P.R.C. J Lumin., 28 147 (1983).

3. Krier, A. and Bryant, F.J., J. Phys. D., 17 1093 (1984).

4. Wright, P.J., Cockayne, B., Cattell, A.F., Dean, P.J., Pitt, A.D. and Blackmore, G.W., J. Crys.Growth, 59 155 (1982).

5. Cattell, A.F. and Cullis, A.G., Thin Solid Films, 92 211 (1982).

6. Ray, B., "II-VI Compounds", Pergamon Press (1969).

7. Cattell, A.F., Inkson, J. and Kirton, J., Private Communication.

8. Lampert, M.A. and Mark, P., "Current Injection in Solids", Academic Press (1970).

9. Allen, J., Cattell, A.F. and Kirton, J., Private Communication.

10. Mukhopadhyay, D. and Bhattacharya, D.P., J. Phys. Chem. Solids, 45 393 (1984).

11. Torpey, P.A., J. Appl. Phys. 56 2284 (1984).

12. Klein, N., J. Appl. Phys., 53 5828 (1982).

13. Cattell, A.F., Cockayne, B., Dexter, K., Kirton, J. and Wright, P.J., IEEE Trans. Elec. Rev., ED-30 471 (1983).

CHAPTER EIGHT

1. Cattell, A.F. and Kirton, J., Private Communication.

2. Lampert, M.A. and Mark, P., "Current Injection in Solids", Academic Press (1970).

3. Ridley, B.K., Proc. Phys. Soc., 82 954 (1963).

4. Barnett, A.M. and Milnes, A.G., J Appl. Phys., 37 4215 (1966).

5. Ray, B., "II-VI Compounds" Pergamon Press, (1969).

APPENDIX ONE

Gradshteyn, I.S. and Ryzhik, I.M., "Table of Integrals, Series and Products", Academic Press (1980).

LIST OF FIGURES

CHAPTER ONE

Fig. 1.1 : An MIS diode under forward bias.

CHAPTER TWO

Fig. 2.1 : Schematic diagram of a p-n homojunction a) at zero bias b) under forward bias.

Fig. 2.2 : Formation of a Schottky barrier.

Fig. 2.3 : A Schottky barrier under a) reverse bias b) forward bias.

Fig. 2.4 : An MIS diode under a) zero bias b) forward bias.

Fig. 2.5 : Various forms of electroluminescent panel devices a) ac device b) composite thin film-powder dc device, and c) dc thin film device.

Fig. 2.6 : a) Charge distribution b) field and c) potential in a Schottky barrier using the depletion approximation.

Fig. 2.7 : A Schottky barrier incorporating a thin interfacial layer.

Fig. 2.8 : Quasi Fermi levels proposed to explain current mechanisms in a Schottky barrier a) thermionic emission of electrons b) diffusion of electrons and c) diffusion of holes.

Fig. 2.9 : The effect of image charge on the electron barrier of a Schottky diode.

Fig. 2.10 : The influence of the Schottky effect on the bandgap at the metal-semiconductor interface.

Fig. 2.11 : The MIS diode under forward bias.

CHAPTER THREE

Fig. 3.1 : The variation of quantum efficiency with insulator thickness in Au/ZnO/ZnSe diodes (reference 11).

Fig. 3.2 : The hole creation mechanism proposed for II-VI MIS diodes.

Fig. 3.3 : dc power conversion ratio versus insulator thickness for Au/$CdSt_2$/GaP MIS diodes (reference 23).

Fig. 3.4 : dc power conversion ratio versus insulator thickness for Au/$CdSt_2$/GaP MIS diodes (reference 24).

CHAPTER FOUR

Fig. 4.1 : The final (1' and 2') and initial (1 and 2) electron states of the impact ionisation process in relation to the Fermi sphere.

Fig. 4.2 and Fig 4.3 : Illustration of variables used in impact ionisation transition rate calculations.

Fig. 4.4a) Maximum value of $\theta_{1'}$ corresponding to $\underline{k}_{1'}$ lying on the Fermi surface.

Fig. 4.4b) Minimum value of $\theta_{1'}$ corresponding to $\underline{k}_{2'}$ lying on the Fermi surface.

Fig. 4.5 : Hole distribution over θ_2, for an incident electron of energy E_F+1.4eV, at the Fermi surface.

Fig. 4.6 : Hole distribution over θ_2, for an incident electron of energy E_F+1.4eV, at an energy of E_F-1.05eV.

Fig. 4.7 : Hole distribution over θ_2, for an incident electron of energy E_F+1.4eV, at energies of a) 5.5eV b) 5.15eV c) 4.8eV and d) 4.45eV.

Fig. 4.8 : Available scattering states for hole creation at the Fermi surface with $\theta_2 = 0$.

Fig. 4.9 : Available scattering states for hole creation at the Fermi surface with $\theta_2 = \pi$.

Fig. 4.10 : Available scattering states for hole creation below the Fermi surface with $\theta_2 = 0$.

Fig. 4.11 : Available scattering states for hole creation below the Fermi surface with $\theta_2 = \pi$.

Fig. 4.12 : Hole distribution over E_2, for an incident electron of energy E_F+1.4eV, at $\theta = 0$ and π.

Fig. 4.13 : The initial and final wavevectors for an Auger type transition.

Fig. 4.14 : The path of a hole created in an impact ionisation process.

Fig. 4.15 : The variation of the mean free path of the incident electron over energy for direct transitions only compared to previous theoretical and experimental results (from reference 10).

Fig. 4.16 : Distribution, over E_2, of holes incident at the MI interface in a 5° cone to the normal assuming an injection current of 10^4 Am^{-2} and a) $\lambda_p = \infty$ b) λ_p = 300Å c) λ_p = 50Å and d) isotropic scattering with $\lambda_e = \lambda_h$.

CHAPTER FOUR (continued)

Fig. 4.17 : Distribution, over E_2, of holes incident at the MI interface in a 5° cone for an injection current of $10^4 Am^{-2}$ compared to the thermal hole flux.

Fig. 4.18 : The total distribution, over E_2, of holes incident at the MI interface in a 5° cone.

Fig. 4.19 : The distribution, over E_2, of holes incident at the MI interface at all angles a) created by impact ionisation b) created thermally.

Fig. 4.20 : The probability of an incident electron of energy E_F+1.4eV creating a hole capable of reaching the interface below energy E_2 (a) compared to the results for isotropic scattering (b).

Fig. 4.21 : Curve (a) in Figure 4.20 using a logarithmic scale.

CHAPTER FIVE

Fig. 5.1 : Schematic energy band diagram for an MIS diode under a small forward bias.

Fig. 5.2 : $F_s(0)$ plotted against diffusion potential for $N_D = 10^{22}m^{-3}$ a) depletion approximation b) equation (5.10).

Fig. 5.3 : $F_s(0)$ versus diffusion potential for $N_D = 10^{24}m^{-3}$ a) depletion approximation b) equation (5.10).

Fig. 5.4 : $F_s(0)$ versus diffusion potential for $N_D = 10^{20}m^{-3}$ a) depletion approximation b) equation (5.10).

Fig. 5.5 : (a) Communication between surface states and the metal (b) Communication between surface states and the semiconductor.

Fig. 5.6 : Variation of ϕ_b with V for $N_D = 10^{22}m^{-3}$ and $D_S = 10^{17}eV^{-1}m^{-2}$ assuming no injection current a) 125Å b) 275Å c) 375Å and d) 525Å.

Fig. 5.7 : Variation of ϕ_b with V for $N_D = 10^{22}m^{-3}$ and $D_S = 10^{16}eV^{-1}m^{-2}$ assuming no injection current a) 125Å b) 275Å c) 375Å and d) 525Å.

Fig. 5.8 : Variation of ϕ_b over insulator thickness for $N_D = 10^{22}m^{-3}$ and applied voltage and D_S of a) lV and $10^{17}eV^{-1}m^{-2}$ b) iV and $10^{16}eV^{-1}m^{-2}$ c) 2V and $10^{17}eV^{-1}m^{-2}$ and d) 2V and $10^{16}eV^{-1}m^{-2}$.

Fig. 5.9 : Experimental J-V characteristic for a five monolayer Au/Cadmium Stearate/n-GaP MIS diode (reference 3).

CHAPTER FIVE (continued)

Fig. 5.10 : Experimental J-V characteristic for an Au/ω-Tricosenoic Acid/ n-GaP MIS diode incorporating i) one ii) five iii) seven and iv) nine monolayers (reference 3).

Fig. 5.11 : Schematic diagram of an MIS diode under high bias with depletion at the IS interface.

Fig. 5.12 : Schematic diagram of an MIS diode under high bias with accumulation in the semiconductor.

Fig. 5.13 : Modification of the insulator barrier profile by image charge effects a) and b) negative insulator field and c) positive insulator field.

Fig. 5.14 : Theoretical J-V characteristic for an Au/Cadmium Stearate/ n-GaP diode with uniform density of states = $10^{17}eV^{-1}m^{-2}$ and incorporating a) one b) five c) seven and d) nine monolayers.

Fig. 5.15 : Theoretical J-V characteristics for an Au/Cadmium Stearate/ n-GaP with uniform density of states = $5x10^{16}eV^{-1}m^{-2}$ and incorporating a) one b) five c) seven and d) nine monolayers.

Fig. 5.16 : Theoretical J-V chracteristic for an Au/Cadmium Stearate/ n-GaP diode with $D_s = 10^{17}eV^{-1}m^{-2}$ and incorporating a) one b) five c) seven and d) nine monolayers.

Fig. 5.17 : Theoretical J-V characteristic for an Au/Cadmium Stearate/ n-GaP with $D_s = 5x10^{16}eV^{-1}m^{-2}$ and incorporating a) one b) five c) seven and d) nine monolayers.

Fig. 5.18 : Theoretical variation of ϕ_b with external bias for an Au/Cadmium Stearate/GaP diode incorporating a) one b) five c) seven and d) nine monolayers.

Fig. 5.19 : Theoretical variation of ϕ_b with insulator thickness for a constant applied bias of a) 1V b) 2V c) 3V and d) 4V.

Fig. 5.20 : Theoretical variation of ϕ_b with insulator thickness for an Au/Cadmium Stearate/n-GaP diode at a constant majority carrier current of a) 10^3Am^{-2} b) 10^4Am^{-2} and c) 10^5Am^{-2}.

CHAPTER SIX

Fig. 6.1 : Co-ordinate system used in the calculation of trapping rates in Langmuir-Blodgett films.

Fig. 6.2 : Position and energy of interface states involved in trapping in Langmuir-Blodgett films.

Fig. 6.3 : Possible hole creation mechanisms involving the trapping of a majority carrier.

CHAPTER SIX (continued)

Fig. 6.4 : Quantum mechanical tunnelling rate for holes from the metal into the semiconductor valence band in a Langmuir-Blodgett MIS diode a) $m = 1m_e$ b) $m = 0.1m_e$ and c) $m = 0.01m_e$.

Fig. 6.5 : Schematic diagram of a Coulombic trap a) in zero field b) under high field.

Fig. 6.6 : The variation in insulator field in the Langmuir-Blodgett MIS diodes modelled in Chapter Five for a constant current of $10^5 Am^{-2}$.

Fig. 6.7 : The expected variation in hole current due to Poole-Frenkel conduction assuming the insulator field variation in Fig.6.6.

Fig. 6.8 : The expected variation in the dc power conversion ratio assuming insulator hole transport by Poole-Frenkel conduction.

Fig. 6.9 : The expected variation in dc power conversion ratic assuming a hole current proportional to field.

Fig. 6.10 : Variation in dc power conversion ratio including the effects of a saturated hole velocity and a recombination lifetime. Values were chosen to produce a curve similar to experimetal results.

Fig. 6.11 : The expected variation in dc power conversion ratio assuming a hole current porportional to field and a mean free path for recombination of a) 300Å b) 250Å and c) 200Å.

Fig. 6.12 : The change in insulator field calculated for an Au/i-ZnS/n-ZnS diode at a constant current of $10^3 Am^{-2}$.

Fig. 6.13 : Proposed energy band diagram for an Au/i-ZnS/n-ZnS diode under forward bias.

Fig. 6.14 : An MIS diode under high bias.

Fig. 6.15 : A Schottky barrier under high bias.

CHAPTER SEVEN

Fig. 7.1 : (a) A schematic diagram of a typical directly coupled electroluminescent MIM device.
(b) the idealised energy band diagram for an MIM device at zero bias.
(c) The energy band diagram for an MIM device with a moderate electric field at the cathode.
(d) The energy band diagram for an MIM device with a high electric field at the cathode.

CHAPTER SEVEN (continued)

Fig. 7.2 : The current density-voltage characteristics with a) no dead space correction and b) dead space correction.

Fig. 7.3 : Carrier profile for a device with a cathode field of $10^8 Vm^{-1}$.

Fig. 7.4 : Field profile for a device with a cathode field of $2.9 \times 10^8 Vm^{-1}$.

Fig. 7.5 : Carrier profile for a device with a cathode field of $2.9 \times 10^8 Vm^{-1}$.

Fig. 7.6 : Field profile for a device with a cathode field of $7 \times 10^8 Vm^{-1}$.

Fig. 7.7 : Carrier profile for a device with a cathode field of 7×10^8 Vm^{-1}.

Fig. 7.8 : Current density-voltage characteristics for varying temperatures a)500°K b) 400°K c) 300°K and d) 0°K.

Fig. 7.9 : Variation of the normalised mobility with applied electric field at 77°K (with no impurity) 1) ZnO 2) ZnS 3) CdTe 4) CdSe and 5) CdS (after reference 10).

Fig. 7.10 : Current density-voltage characteristics for an electron saturation current of a) $10^3 Vm^{-1}$ b) $10^4 Vm^{-1}$ c) $10^5 Vm^{-1}$ and d) no limit.

Fig. 7.11 : Current density-voltage characteristics for different hole mobilities a) $1 \times 10^{-5} m^2 V^{-1} s^{-1}$ b) $5 \times 10^{-5} m^2 V^{-1} s^{-1}$ and c) $1 \times 10^{-4} m^2 V^{-1} s^{-1}$.

Fig. 7.12 : Current density-voltage characteristics when the normal bulk mobilites are reduced by a factor of a) 10^{-2} b) 10^{-1} and c) no change.

Fig. 7.13 : Current density-voltage characteristics for various barrier heights of a) 0.25eV b) 0.5eV and c) 0.75eV.

Fig. 7.14 : Current density-voltage characteristics for different effective masses a) $0.25m_e$ and b) $0.75m_e$.

Fig. 7.15 : Current density-voltage characteristics for insulator samples of different widths.

Fig. 7.16 : Variation of voltage with respect to insulator thickness for constant currents of a) $10^8 Am^{-2}$ b) $10^5 Am^{-2}$ and c) $10 Am^{-2}$.

CHAPTER SEVEN (continued)

Fig. 7.17 : Current density-voltage characteristics for different thicknesses of a N_D+ doping layer (of concentration $5\times10^{22}m^{-3}$) adjacent to the cathode.

Fig. 7.18 : Current density-voltage characteristics for a N_D+ doping layer of thickness 0.1μm adjacent to the cathode for doping concentrations of a) $3\times10^{23}m^{-3}$ b) 2.6×10^{23} c) 2×10^{23} d) 1.5×10^{23} e) 1×10^{23} f) 2×10^{23} and g) 0.

CHAPTER EIGHT

Fig. 8.1 : The circuit incorporating the ZnS electroluminescent panel.

Fig. 8.2 : The development of the device voltage and current density over time for values of R = 1000Ω and V_o = 200V.

Fig. 8.3 : The development over time of the hole concentration profile in the ZnS device for the same parameters as Fig. 8.2.

Fig. 8.4 : The development of the device voltage and current density over time for values of R = 600Ω V_o = 300V.